

Optimisation of a New Class of Peptide- Based MRI Contrast Agent

Sarah Lauren Newton

A thesis submitted to

The University of Birmingham

For the degree of

DOCTOR OF PHILOSOPHY



PSIBS Doctoral Training Centre

School of Chemistry

College of Engineering and Physical Sciences

The University of Birmingham

August 2017

UNIVERSITY OF
BIRMINGHAM

University of Birmingham Research Archive

e-theses repository

This unpublished thesis/dissertation is copyright of the author and/or third parties. The intellectual property rights of the author or third parties in respect of this work are as defined by The Copyright Designs and Patents Act 1988 or as modified by any successor legislation.

Any use made of information contained in this thesis/dissertation must be in accordance with that legislation and must be properly acknowledged. Further distribution or reproduction in any format is prohibited without the permission of the copyright holder.

Abstract

To determine the effect rotational correlation time (τ_R) has on relaxivity, peptides of different lengths were investigated. Extending the length of the peptide had a negligible impact on folding, stability and inner-sphere water coordination. The relaxivity was found to be the same indicating that τ_R is not the limiting factor in this class of contrast agent.

A peptide was designed with the potential to increase secondary sphere water coordination to the peptide exterior. No change in relaxivity was observed, compared to MB1-2, due secondary sphere H₂O being located at too far from the paramagnetic Gd(III).

Secondary sphere water coordination was further investigated when a water channel was identified. The channel allows water to come within close proximity of Gd(III), with the potential to increase relaxivity. D-amino acids were introduced in an attempt to block the water channel, but this had little impact.

Finally, the biological activity of the peptides in biological systems was investigated. It was found that increased transmetalation occurred when the Gd(III) binding site was located at the N-terminus of the coiled coil. Cell lines were treated with Gd(MB1-1)₃ at MRI relevant concentrations and cell death occurred when treated with clinically relevant concentrations of the metallo peptide.

Acknowledgments

Firstly I would like to thank my supervisors, Anna Peacock, Melanie Britton and Iain Styles, without your support and guidance this PhD would not have been possible. Your passion for science has driven me to achieve my scientific goals and I appreciate the time and effort you have put in to help me with all aspects of my PhD.

Thank you to the PSIBS Doctoral Training Centre for the opportunity to undertake a PhD and for your continual support. I would like to say a big thank you to my PSIBS buddy Becky for your friendship, guidance and encouragement throughout the last four years.

Thank you to the members of the Peacock and Britton groups, to the past members for your guidance and advice, and to the current members - it has been a pleasure working with you. Thank you to Josh, your knowledge and passion for science is inspirational and I am so appreciative of the help you have given me in the lab and with writing my thesis. A massive thank you to Louise, I will never forget the support you have given me both in academia and life outside the lab; I couldn't have done it without you.

To Mum, Dad and Jamie, thank you for your enthusiasm and encouragement throughout my education, I hope I have made you proud with what I have achieved. Dad, I am so pleased to follow in your footsteps to become the next Dr Newton. Finally, I have been lucky to meet my boyfriend and best friend, Chris, at the University of Birmingham. Thank you for always being there for me and encouraging me to reach the finish line.

Table of Contents

| | |
|--|-----|
| Acknowledgments | i |
| Abbreviations | vi |
| Amino Acids..... | vii |
| Peptide Sequences | x |
| Awards and Publications | xi |
| Chapter 1: Literature Review | 1 |
| 1.1 Introduction..... | 1 |
| 1.2 The Lanthanides | 1 |
| 1.3 Relaxation Theory in MRI | 2 |
| 1.3.1 T_1 Specific Contrast Agents | 6 |
| 1.3.2 T_2 Specific Contrast Agents | 7 |
| 1.4 Current Gd(III) Contrast Agents..... | 7 |
| 1.5 Approaches to Enhanced Contrast..... | 8 |
| 1.5.1 Water Coordination | 9 |
| 1.5.2 Water Residency Time and Exchange | 11 |
| 1.5.3 Rotational Correlation Time | 13 |
| 1.6 Lanthanides as MRI Contrast Agents | 16 |
| 1.7 The Use of Manganese(II) in MRI Contrast Agents | 18 |
| 1.8 Peptide-Based Contrast Agents..... | 20 |
| 1.9 <i>De Novo</i> Design and Coiled-Coil Peptides | 21 |
| 1.10 Metal Binding in Coiled-Coil Peptides | 22 |
| 1.11 Lanthanide Binding Coiled-Coil Peptides | 23 |
| 1.12 <i>De Novo</i> Designed Lanthanide Coiled-Coils for MRI | 25 |
| 1.13 Project Aims | 27 |
| Chapter 2: Experimental Techniques | 30 |
| 2.1 Peptide Synthesis and Purification..... | 30 |
| 2.2 High Performance Liquid Chromatography | 32 |
| 2.3 Mass Spectrometry | 33 |
| 2.4 Ultra Violet-Visible Spectroscopy | 34 |
| 2.5 Circular Dichroism | 34 |
| 2.6 Emission Spectroscopy | 36 |
| 2.7 Nuclear Magnetic Resonance..... | 37 |
| 2.8 Relaxation..... | 40 |

| | |
|--|----|
| 2.9 Magnetic Resonance Imaging | 41 |
| 2.9.1 Frequency and Phase Encoding..... | 42 |
| 2.9.2 Resolution and Field of View | 43 |
| 2.9.3 Spin Echo Imaging Sequence | 43 |
| 2.9.4 Image Contrast | 44 |
| Chapter 3: Effect of Peptide Length on Relaxivity and the Effectiveness of MRI Contrast Agents | 45 |
| 3.1 Introduction..... | 45 |
| 3.2 Aims..... | 46 |
| 3.3 Results and Discussion | 47 |
| 3.3.1 Secondary Structure..... | 47 |
| 3.3.2 Ln(III) Binding | 50 |
| 3.3.3 Peptide Stability | 52 |
| 3.3.4 Ca(II) Displacement | 54 |
| 3.3.5 Water Coordination | 56 |
| 3.3.6 Relaxivity and MRI Contrast Agent Efficiency | 57 |
| 3.3.7 Prediction of the Rotational Correlation Time | 60 |
| 3.3.8 Prediction of the Water Residence Time | 61 |
| 3.3.9 Experimental Water Residence Time in Gd(MB1-1) ₃ | 62 |
| 3.4 Conclusions..... | 63 |
| Chapter 4: Investigation of the Importance of Water Coordination to the Exterior of a Coiled-Coil MRI Contrast Agent | 65 |
| 4.1 Introduction..... | 65 |
| 4.2 Aims..... | 67 |
| 4.3 Results and Discussion | 70 |
| 4.3.1 Secondary Structure..... | 70 |
| 4.3.2 Calculation of a Binding Constant using CD and Luminescence | 71 |
| 4.3.3 Determining the Oligomeric State of Mo1-2..... | 74 |
| 4.3.4 Effect of Oligomeric State on the Rotational Correlation Time | 79 |
| 4.3.5 Effect of Amino Acid Substitutions on Peptide Stability | 85 |
| 4.3.6 Computational Analysis of Water Coordination to the Peptide Exterior..... | 87 |
| 4.3.7 Water Coordination | 89 |
| 4.3.8 Relaxivity and Contrast Agent Efficiency..... | 90 |
| 4.4 Conclusions..... | 91 |
| Chapter 5: Investigating the Presence of Water Located in the Hydrophobic Core of a Coiled-coil Peptide | 93 |
| 5.1 Introduction..... | 93 |

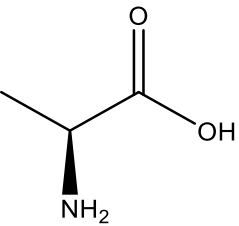
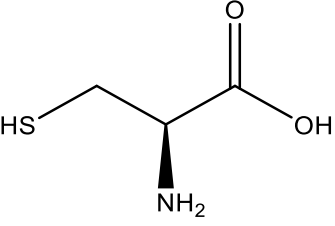
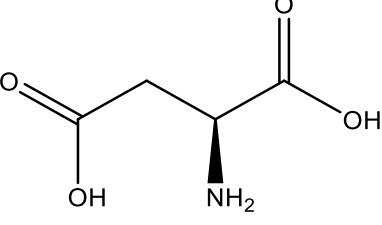
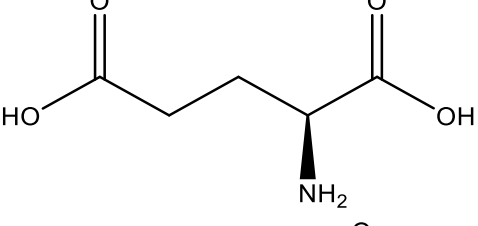
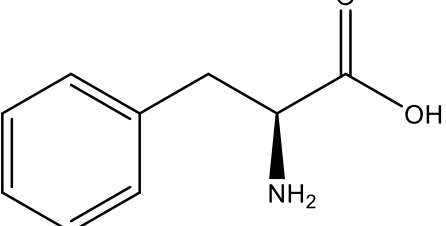
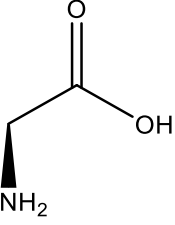
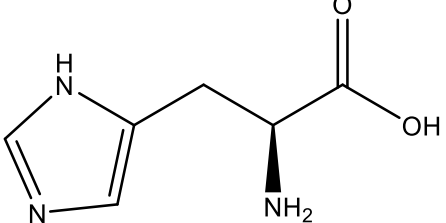
| | |
|---|-----|
| 5.2 Aims..... | 94 |
| 5.3 Results and Discussion | 96 |
| 5.3.1 Investigation into Water Location in MB1-2 | 96 |
| 5.3.2 Analysing Water Distances and SN1-2 Design | 98 |
| 5.3.3 Secondary Structure..... | 103 |
| 5.3.4 Tb(III) Binding and Luminescence | 105 |
| 5.3.5 Water Coordination | 106 |
| 5.3.6 Relaxivity and MRI Contrast Agent Efficiency | 107 |
| 5.3.7 SN1-3L and MB1-3L Peptide Design..... | 108 |
| 5.3.8 Secondary Structure..... | 110 |
| 5.3.9 Tb(III) Binding and Luminescence | 113 |
| 5.3.10 Thermal Stability | 114 |
| 5.3.11 Water Coordination | 116 |
| 5.3.12 Relaxivity and MRI Contrast Agent Efficiency | 117 |
| 5.4 Conclusions..... | 119 |
| Chapter 6: Investigating the Introduction of Ln(III) Coiled Coils into Biological Systems | 121 |
| 6.1 Introduction..... | 121 |
| 6.2 Aims..... | 124 |
| 6.3 Results and Discussion | 124 |
| 6.3.1 Displacement of Ln(III) with Medically Relevant Metals..... | 124 |
| 6.3.2 Lanthanide Binding under Physiological Conditions | 129 |
| 6.3.3 Initial Cell Toxicity Testing..... | 132 |
| 6.3.4 Investigation of MB1-1 in Cancerous Brain Cells | 134 |
| 6.4 Conclusions..... | 136 |
| Chapter 7: Concluding Remarks and Future Work..... | 138 |
| 7.1 Conclusions..... | 138 |
| 7.2 Future Work | 140 |
| 7.2.1 Use of Alternative Lanthanides for MRI PARACEST | 140 |
| 7.2.2 Mn(II) MRI Contrast Agents..... | 141 |
| 7.2.3 Improvement in Binding Constant | 142 |
| Chapter 8: Materials and Methods | 143 |
| 8.1 Materials | 143 |
| 8.2 Peptide Synthesis and Purification..... | 143 |
| 8.3 Sample Preparation and Concentration Determination | 145 |
| 8.4 Circular Dichroism (CD) Spectroscopy..... | 146 |

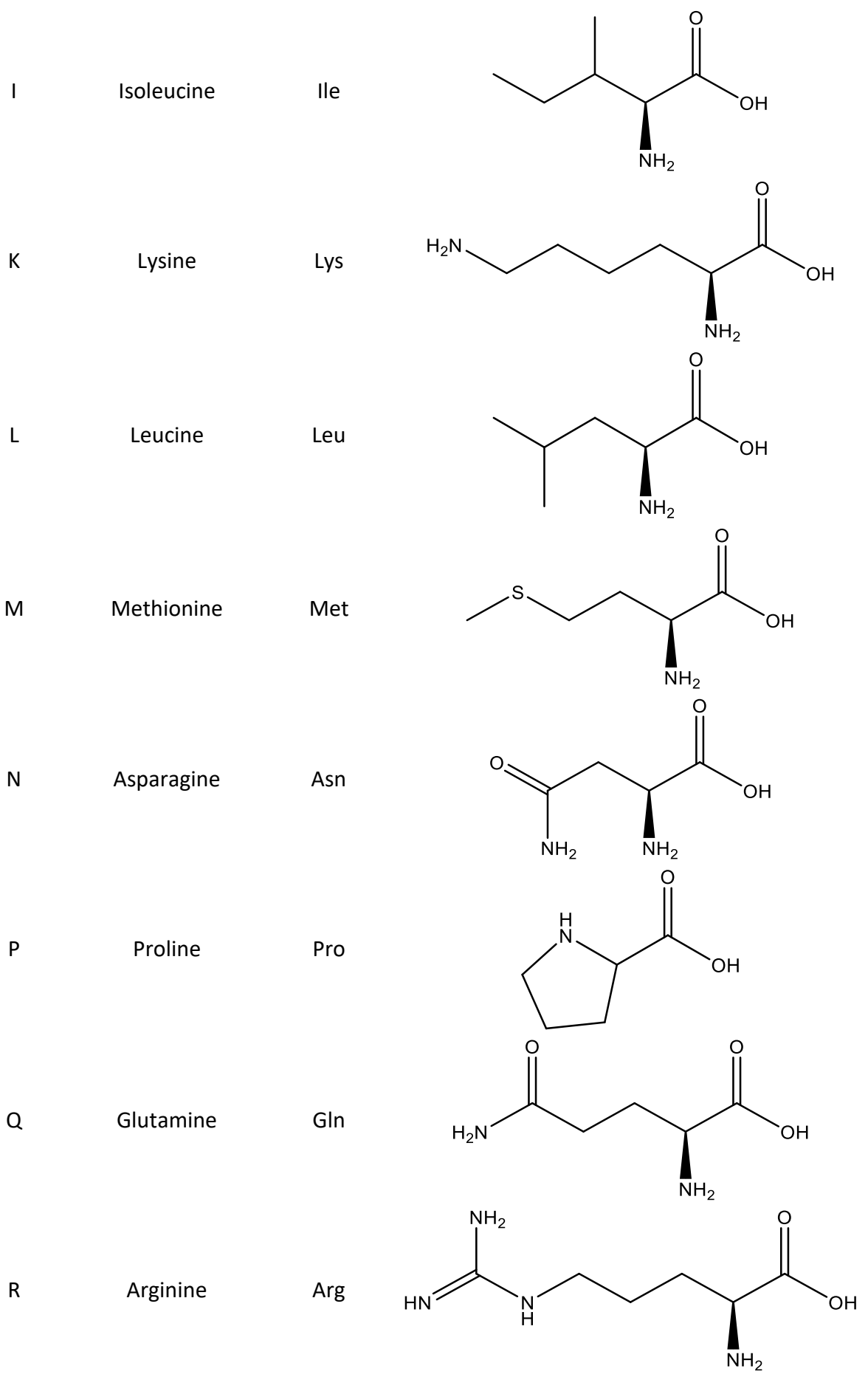
| | |
|--|-----|
| 8.5 Luminescence..... | 148 |
| 8.6 NMR Spectroscopy | 149 |
| 8.7 Molecular Dynamics Simulations | 151 |
| 8.8 Cell Culture | 152 |
| References..... | 154 |
| Appendix | 160 |

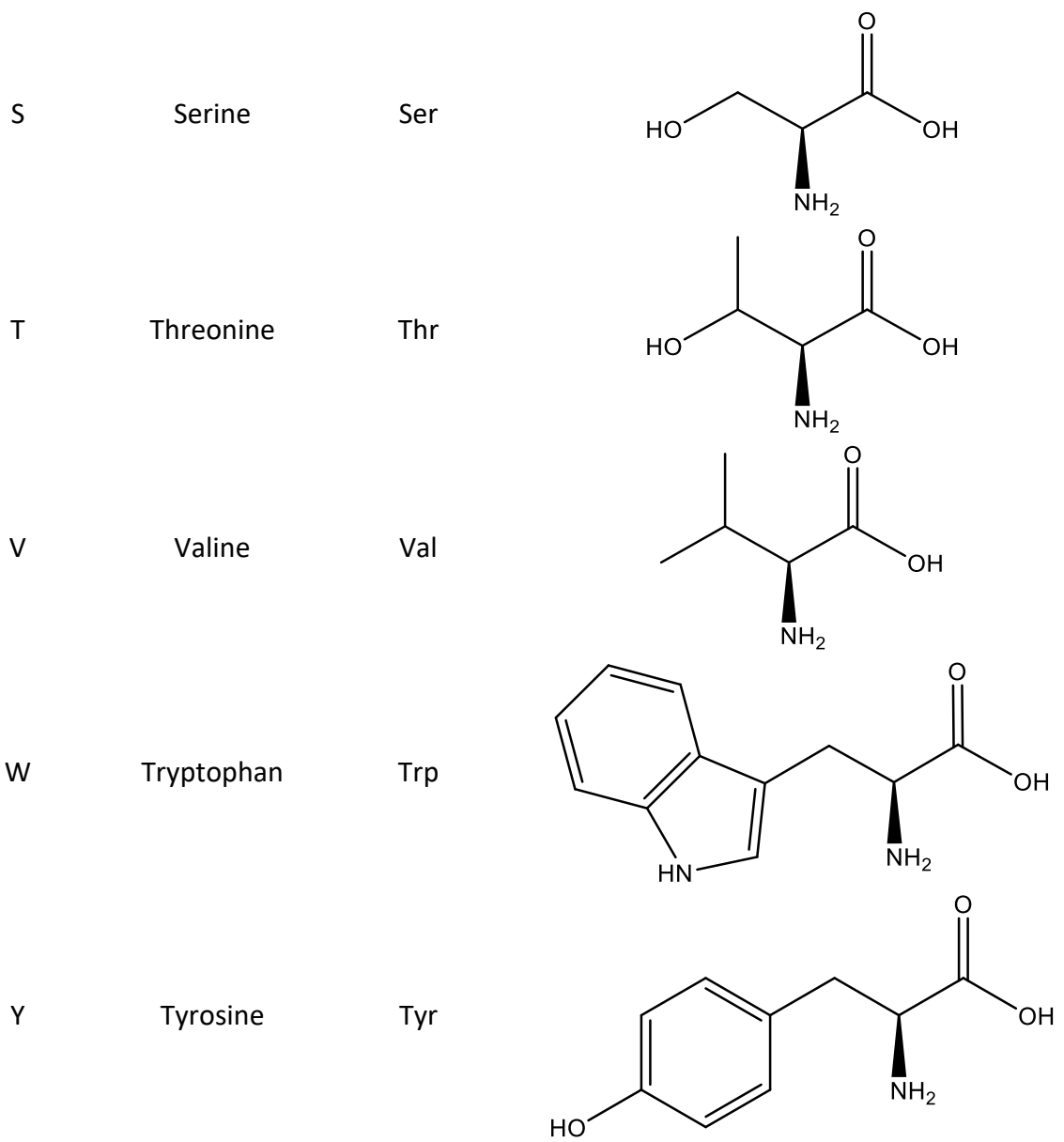
Abbreviations

| | |
|---------|--|
| 2D | Two Dimensional |
| 3D | Three Dimensional |
| CA | Contrast Agent |
| CC | Coiled Coil |
| CD | Circular Dichroism |
| CPMG | Carr-Purcell-Meiboom-Gill |
| CS | Curie Spin |
| DCM | Dichloromethane |
| DIPEA | N,N-diisopropylethylamine |
| DMF | N,N-dimethylformamide |
| FID | Free Induction Decay |
| Fmoc | Fluorenylmethyloxycarbonyl |
| GuaHCl | Guanadinium hydrochloride |
| GdCA | Gadolinium(III) Contrast Agent |
| HBTU | N,N,N',N'-Tetramethyl-O-(1H-benzotriazol-1-yl)uroniumhexafluorophosphate |
| HEPES | 4-(2-Hydroxyethyl)piperazine-1-ethanesulfonic acid |
| HoBT | Hydroxybenzotriazole |
| HPLC | High Performance Liquid Chromatography |
| HSA | Human Serum Albumin |
| Ln(III) | Lanthanide (III) |
| MALDI | Matrix Assisted Laser Desorption Ionisation |
| MRI | Magnetic Resonance Imaging |
| NMR | Nuclear Magnetic Resonance |
| NSF | Nephrogenic Systemic Fibrosis |
| SC | Scalar Coupling |
| SPPS | Solid Phase Peptide Synthesis |
| TFA | Trifluoroacetic acid |
| UV-Vis | Ultraviolet-Visible |

Amino Acids

| | | | |
|---|---------------|-----|---|
| A | Alanine | Ala |  |
| C | Cysteine | Cys |  |
| D | Aspartate | Asp |  |
| E | Glutamate | Glu |  |
| F | Phenylalanine | Phe |  |
| G | Glycine | Gly |  |
| H | Histidine | His |  |





Peptide Sequences

A table of the peptide sequences used in this thesis. Ln(III) binding site and tryptophan sensitiser are shown in bold. **X** symbolises D-isoleucine.

| Peptide Name | Sequence |
|--------------|--|
| MB1-1S | Ac – G – IAANE W DAAIEQK IAAIEQK IAAIEQK – G – NH ₂ |
| MB1-1 | Ac – G – IAANE W DAAIEQK IAAIEQK IAAIEQK IAAIEQK – G – NH ₂ |
| MB1-1L | Ac – G – IAANE W DAAIEQK IAAIEQK IAAIEQK IAAIEQK IAAIEQK – G – NH ₂ |
| MB1-2 | Ac – G – IAAIEQK IAANE W DAAIEQK IAAIEQK IAAIEQK – G – NH ₂ |
| Mo1-2 | Ac – G – IKAIEEK IKENE W DKAIEEK IKAIEEK IKAIEEK – G – NH ₂ |
| SN1-2 | Ac – G – IAAIEQK X AANE W DAAIEQK IAAIEQK IAAIEQK – G – NH ₂ |
| SN1-3L | Ac – G – IAAIEQK IAAIEQK X AANE W DAAIEQK IAAIEQK IAAIEQK – G – NH ₂ |
| MB1-3L | Ac – G – IAAIEQK IAAIEQK IAANE W DAAIEQK IAAIEQK IAAIEQK – G – NH ₂ |

Awards and Publications

Publications

- S. L. Newton, A. Franke, A. Kenwright, I. Styles, D. J. Smith, I. Ivanovic-Burmazovic, M. M. Britton, A. F. A. Peacock; Investigating the impact of rotational correlation time and water residence time on the MRI relaxivity of *de novo* designed gadolinium coiled coils; Manuscript in Progress
- M. R. Berwick, L. N. Slope, C. F. Smith, S. M. King, S. L. Newton, R. B. Gillis, G. G. Adams, A. J. Rowe, M. M. Britton, A. F. A. Peacock; Location dependent coordination chemistry and MRI relaxivity, in *de novo* designed lanthanide coiled coils. *Chemical Science*; 2016; **7**: 2207–16.

Awards

- Best Research Award at the University of Birmingham Graduate School Poster Conference, 2015
- Nature Chemistry Flash Presentation and Poster Prize at the 5th Annual Postgraduate Symposium on Nanoscience, University of Birmingham, 2015
- RSC NMR DG funding to complete a research collaboration at the University of Durham, 2015
- Society of Bio-Inorganic Chemistry (SBIC) scholarship to attend the EuroBIC Conference in 2016
- Three RSC scholarships to attend: the Joliot-Curie conference in 2015, the 4th Berliner Chemie Symposium in 2015 and the Portuguese Young Chemists Conference in 2016
- Winner of European and RSC funding to attend the EuCheMS Conference in 2014
- European Young Chemists' Network elected board member, 2015-2017

Chapter 1: Literature Review

1.1 Introduction

Magnetic resonance imaging (MRI) is a technique at the forefront of medical diagnosis.¹ MRI was developed in the 1950's as an *in vivo* imaging technique, building on nuclear magnetic resonance (NMR) methodology.² MRI uses radio frequency waves as a source of excitation; this is a non-invasive technique that has been shown to have no detrimental effects on the patient.³ This makes it more attractive than other imaging techniques, for example, computed tomography (CT) which uses X-rays, and positron emission tomography (PET) which uses radioactive markers.⁴ This chapter will introduce and review MRI contrast agents (CAs), with specific focus on lanthanide metallopeptides.

1.2 The Lanthanides

The lanthanides are becoming more and more popular in biomedical research because of their interesting chemical, magnetic and photo-physical properties, which have led to uses in medical imaging. They are most stable in their +3 oxidation state.⁵ Because of the poor shielding of the nucleus by *4f* electrons, as the atomic number increases across the series, the distance between outer electrons decreases and the atomic radii decreases. This is known as lanthanide contraction.⁵⁻⁷

Despite their differences in size across the series, the lanthanides have comparable chemical properties, because of the *5s* and *5p* shielding of the outer *4f* electrons. This allows a general lanthanide binding site to be developed. An ideal binding site will have a coordination number of more than six, be made of hard oxygen and nitrogen atoms, and will facilitate electrostatic bonding.^{5,7}

The photo-physical properties of the lanthanides are due to electronic transitions and results in luminescence. Due to the Laporte Rule, $f-f$ transitions are spin forbidden, resulting in weak emission. In order to overcome this, a sensitizer can be used. A sensitizer works by transferring energy from a strongly absorbing chromophore to the lanthanide, resulting in increased emission.⁸ The sensitizer often contains an aromatic ring, as this will have a high extinction coefficient for absorption in the UV region.⁸ In order for sensitisation to take place the sensitizer and lanthanide must have an overlap in energy emission and absorption. Organic fluorophores such as the amino acid tryptophan, shown in Figure 1.1, are often used and can be characterised by a high molar absorption, short lived excited state, and a neutral charge.⁹

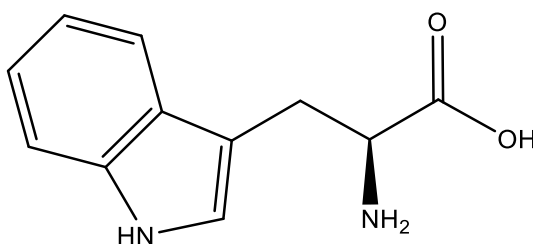


Figure 1.1: The amino acid tryptophan.

Ln(III) emission is long lived (millisecond) due to Laporte forbidden transitions. This is advantageous in biological samples as it leads to better signal to noise and resolution. Tb(III) emission is most commonly studied as its low lying excited states lead to emission in the visible region.¹⁰ Gd(III) has a high energy excited state which results in emission in the UV region. Tb(III) is often used as a model for Gd(III) luminescence as it is hard to find sensitizers with excited states of a high enough energy to allow for energy transfer to Gd(III).^{6,7}

1.3 Relaxation Theory in MRI

NMR was first discovered in 1946 (Bloch, Hansen, Packard and Purcell, Torrey, Pound), and led to Bloch and Purcell sharing the Nobel Prize in physics for their work in 1952.^{11,12} To

understand the process of how MR images are formed, a basic understanding of the theory of NMR is required.¹³ See Chapter 2 for further information.

Most commonly, MRI uses NMR to image ^1H nuclei in water and organic molecules, such as lipids and proteins, inside the body.³ Contrast in MRI is related to the relaxation times (longitudinal relaxation time (T_1) and transverse relaxation time (T_2)) of *in vivo* protons, proton density and instrument parameters.³ T_1 describes the process by which net magnetisation returns to its initial maximum value.¹³ T_2 describes the process by which the transverse components of magnetisation decay.¹³ Relaxivity is defined as the change in relaxation rate of bulk water protons upon addition of a CA; this is normalised to the concentration of the CA and reported as r_1 and r_2 , respectively. T_1 and T_2 vary depending on the type of tissue being studied. For example, fat has a short T_1 and T_2 compared to water. Metal complexes can enhance contrast by shortening the T_1 and T_2 relaxation times of water through electron-proton dipolar coupling. Contrast agents that primarily reduce T_1 are called positive, whereas those that mostly affect T_2 are called negative.³

The Solomon-Bloembergen-Morgan (SBM) equations, established in the 1960's, define the interaction of paramagnetic metals with bulk water in MRI.¹⁴ The equations consist of a number parameters, three of which can be synthetically modified when designing a CA: the hydration of the metal ion (q), the rotational correlation time (τ_R) and the mean residence time of water (τ_m).^{15,16}

In the SBM equations, water interactions can be divided into two mechanisms. The inner-sphere relaxation mechanism (r_i^{IS}) takes advantage of interactions between the Gd(III) ion and the water molecules directly coordinated to the ion.¹⁷ The outer sphere mechanism (r_i^{OS}) uses the interactions between the water located in the second and outer sphere which is diffusing in proximity to the CA construct, these interactions are shown in Figure 1.2.¹⁸

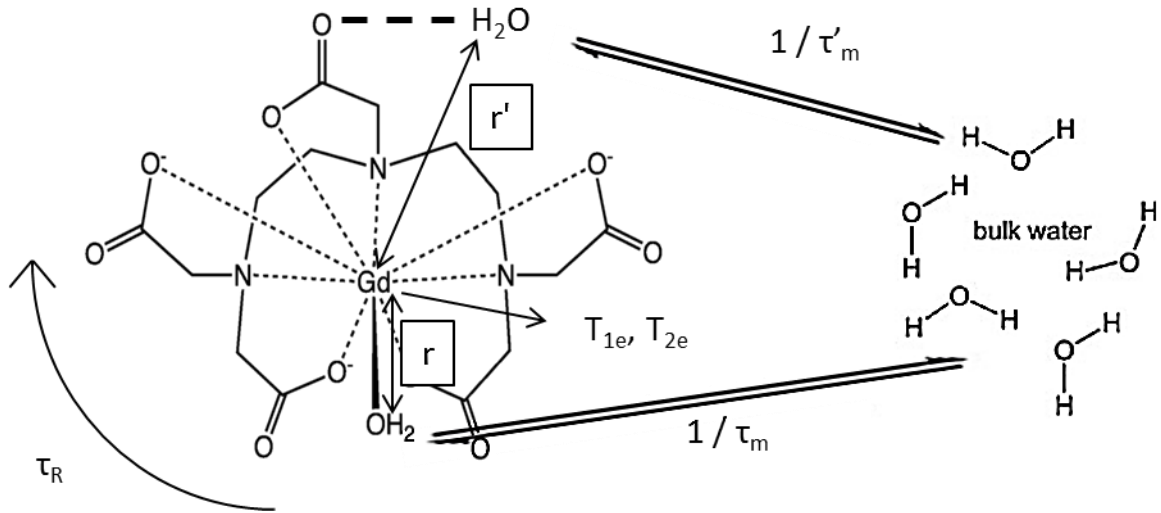


Figure 1.2: Factors influencing solvent water relaxation based on [Gd(DOTA)]. The metal complex has one coordinated water molecule distance r away from Gd(III). Primary water exchange occurs with the bulk water at a rate of $1/\tau_m$ and the rotational correlation time is indicated by τ_R . Properties of the Gd(III) ion such as the primary and secondary electronic relaxation time (T_{1e} , T_{2e}) also influence relaxivity. Secondary sphere effects also influence relaxivity such as secondary water exchange ($1/\tau'_m$) and the Gd(III) H₂O' distance (r').

The inner-sphere relaxivity (r_i^{IS}) of a CA is controlled using the inner-sphere relaxation mechanism. This takes into account the number of bound water molecules (q), the molar concentration of bulk water ($[H_2O]$), the longitudinal relaxation time of bound water (T_{im}), and the water residence time (τ_m),¹⁹ as given in Equation 1.1.

Equation 1.1:

$$r_i^{IS} = \frac{q/[H_2O]}{T_{im} + \tau_m} \quad i = 1, 2$$

When considering the longitudinal relaxation time (T_{1m}) at fields higher than 1.5 T, the dipolar relaxation mechanism (T_1^{DD}) will dominate for Gd(III) contrast agents (GdCAs).^{20,21} This is represented in Equation 1.2, where μ_0 is the permittivity of the vacuum, γ_H is the magnetogyric ratio of a proton, g_e is the electronic G-factor (2 for Gd(III)), μ_B is the Bohr magneton, S is the spin quantum number, r_{MH} is the ion-proton distance, τ_C is given in Equation 1.7, and ω_H is the Larmor frequency of a proton.

Equation 1.2:
$$\frac{1}{T_1^{DD}} = \frac{2}{15} \left(\frac{\mu_0}{4\pi} \right) \frac{\gamma_H^2 g_e^2 \mu_B^2 S(S+1)}{r_{MH}^6} \left[\frac{3\tau_C}{1+\omega_H^2 \tau_C^2} \right]$$

The SBM theory failed to accurately describe the transverse relaxation time (T_{2m}) so the SBM equations were adapted by Gueron and the mechanism of Curie spin relaxation (T_2^{CS}) was introduced.²² Three mechanisms contribute to T_{2m} and $1/T_{2m} = 1/T_2^{DD} + 1/T_2^{SC} + 1/T_2^{CS}$, shown further in Equations 1.3 – 1.10, where τ_{SC} is the scalar coupling correlation time, τ_{CS} is the Curie spin correlation time, τ_R is the rotational correlation time, τ_m is the water residency time, τ_{ie} is the electronic relaxation time, (A/\hbar) is the hyperfine coupling constant, Δ is determined from crystal field effects, ω_S is the Larmor frequency of an electron and τ_V is the correlation time related to the zero field splitting. A detailed review of the explanation of these factors has been published by Aime and co-workers.¹⁶

Equation 1.3:
$$\frac{1}{T_2^{DD}} = \frac{1}{15} \left(\frac{\mu_0}{4\pi} \right) \frac{\gamma_H^2 g_e^2 \mu_B^2 S(S+1)}{r_{MH}^6} \left[4\tau_C + \frac{3\tau_C}{1+\omega_H^2 \tau_C^2} \right]$$

Equation 1.4:
$$\frac{1}{T_2^{SC}} = \frac{1}{3} \left(\frac{A}{\hbar} \right) S(S+1) (\tau_{SC})$$

Equation 1.5:
$$\frac{1}{T_2^{CS}} = \frac{1}{5} \left(\frac{\mu_0}{4\pi} \right)^2 \frac{\omega_H^2 g_e^4 \mu_B^4 S^2(S+1)^2}{(3k_B T)^2 r_{MH}^6} (4\tau_{CS})$$

Where:

Equation 1.6:
$$\frac{1}{\tau_C} = \frac{1}{\tau_R} + \frac{1}{\tau_m}$$

Equation 1.7:
$$\frac{1}{\tau_{SC}} = \frac{1}{\tau_m} + \frac{1}{\tau_{ie}} \quad i = 1, 2$$

Equation 1.8:
$$\frac{1}{\tau_{CS}} = \frac{1}{\tau_R} + \frac{1}{\tau_m}$$

Equation 1.9:
$$\frac{1}{T_{1e}} = \frac{\Delta^2(4S(S+1)-3)}{25} \left(\frac{\tau_V}{1+\omega_S^2 \tau_V^2} + \frac{4\tau_V}{1+\omega_S^2 \tau_V^2} \right)$$

Equation 1.10:
$$\frac{1}{T_{2e}} = \frac{\Delta^2(4S(S+1)-3)}{50} \left(\frac{5\tau_V}{1+\omega_S^2 \tau_V^2} + \frac{2\tau_V}{1+4\omega_S^2 \tau_V^2} + 3 \right)$$

CAs are able to enhance relaxivity when $q = 0$, therefore, outer sphere water coordination must be important.²³ This can take two forms (1) second sphere water relaxation, described in Equation 1.11, with prime indicating second sphere, and (2) outer sphere water relaxation, i.e. bulk water.^{15,16}

Equation 1.11:

$$r_i^{SS} = \frac{q'/[H_2O]}{T_{im}' + \tau_m'} \quad i = 1,2$$

Outer sphere relaxivity is estimated using the equations proposed by Freed,²⁴ and is dictated by water exchange and the distance between Gd(III) and the water molecule.^{15,16} A thorough explanation of outer sphere contributions can be found in the works of Freed,²⁴ Aime¹⁶ and Caravan.¹⁵

1.3.1 T_1 Specific Contrast Agents

Magnevist was first designed in the 1980's as a T_1 specific CA. It is made up of diethylenetriaminepentaacetic acid (DTPA) as a chelate around Gd(III),^{25,26} shown in Figure 1.3(a). By using eight of the available donating sites of DTPA to coordinate to Gd(III), a single site remains, allowing for primary water coordination and exchange. This exchangeable water is used to transfer T_1 relaxation of Gd(III) to the bulk water. Gd(III) has the ability to reduce T_1 of 1H nuclei substantially because of the large magnetic moment of the seven unpaired electrons.^{25,26}

The acquisition of a T_1 weighted image is enhanced by GdCAs due to the shortening of the T_1 relaxation rate of the water that interacts with the GdCA. Water located in different tissues will not interact with a GdCA in the same way due to different compositions of tissue and concentrations of water, and so relaxation times will differ. A MRI pulse sequence can be designed to image only the fast relaxing nuclei, allowing for specific tissue imaging.²⁷

1.3.2 T_2 Specific Contrast Agents

T_2 based CAs are most typically based on superparamagnetic iron oxide (SPIO) particles. The field inhomogeneity of SPIOs alters the magnetic field, dephasing the water signal and altering the T_2 of associated water.^{28,29} All SPIO CA have been removed from the clinics due to concerns regarding toxicity.

In this work, the focus is on new Ln(III) based CAs for use as T_2 CA. Gd(III) can be used for T_2 contrast, in addition to those Ln(III) that produce a hyperfine shift, such as Dy(III), Tm(III) or Tb(III). A hyperfine shift is the difference in chemical shift between the nucleus of a paramagnetic molecule and that in a diamagnetic analogue. For example, primary sphere water that has been influenced by the paramagnetic Ln(III) and bulk water. The large difference in frequency between bound and bulk water creates a powerful T_2 CA because of the dephasing which occurs during water exchange.²⁹

1.4 Current Gd(III) Contrast Agents

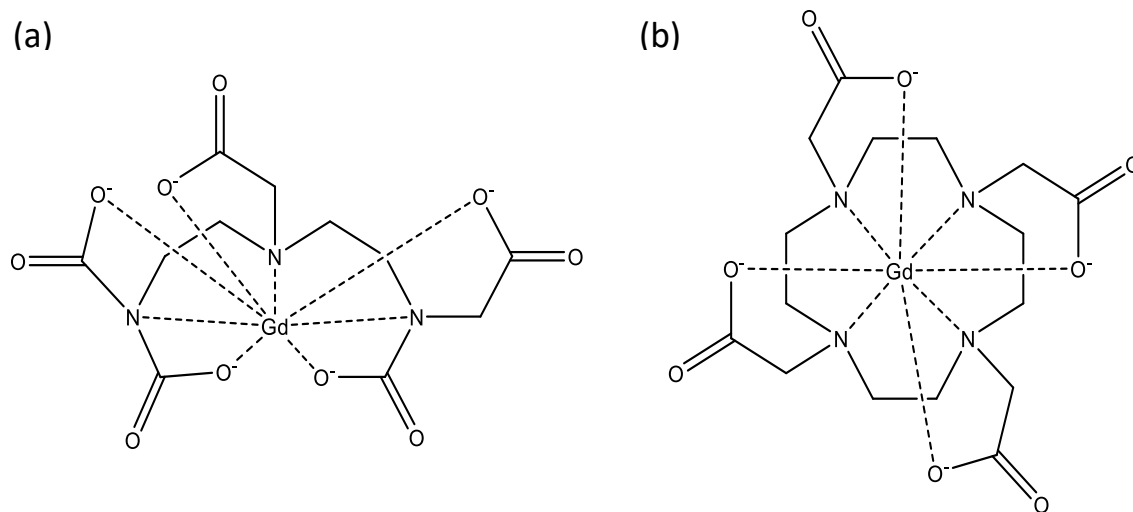


Figure 1.3: Structures of the MRI CAs, (a) $[\text{Gd}(\text{DTPA})]^{2-}$ and (b) $[\text{Gd}(\text{DOTA})]$.

Commercial CAs consist of a Gd(III) metal centre with an octadentate heteroatom organic chelator. The octadentate structure allows for $q = 1$. There are currently nine CAs on the market, listed in Table 1.1, all based on Gd(III) with slight structural differences of the

ligand. These approved CAs are injected at hundred millimolar concentrations, required due to their low efficiencies.³⁰

Table 1.1: The 9 clinically approved GdCAs currently on the UK market

| Contrast Agents | Clinical Name |
|-------------------------------|-------------------------------|
| Gadoterate | Dotarem |
| Gadodiamide | Omniscan |
| Gadobenate | MultiHance |
| Gadopentetate | Magnevist |
| Gadoteridol | ProHance |
| Gadoversetamide | OptiMARK |
| Gadobutrol | Gadovist [EU] / Gadavist [US] |
| Gadopentetic acid dimeglumine | Magnetol |
| Gadofosveset | Ablavar / Vasovist |

The negatively charged $[\text{Gd}(\text{DTPA})]^{2-}$ (Magnevist) and $[\text{Gd}(\text{DOTA})]$ (Dotarem) were the first GdCAs to be used in the clinics; their structures are shown in Figure 1.3.³¹ The DTPA ligand is commercially available, however, the preparation of DOTA is time consuming.³² These first generation CAs are extremely useful in medical diagnostics and have accounted for the increased use of MRI. They distribute in the intravascular space and are non-specific, however, they can concentrate in the kidneys due to the elimination process of glomerular filtration.²⁸

1.5 Approaches to Enhanced Contrast

Since the introduction of a range of different imaging techniques during the twentieth century, medical applications have been of high importance in imaging research. Different techniques have been optimised for various uses, for example, increasing the resolution of CT, increasing depth penetration of optical imaging and improving the sensitivity of MRI.³³ Ultimately all imaging modalities have turned to CAs, to increase the effectiveness of the technique in the clinics.⁴

A MRI CA is most effective when it has a high relaxivity and a high kinetic and thermodynamic stability. This means that a lower dose can be administered and the CA safely excreted, intact after imaging.³⁰ It has proven difficult to find a CA with all of these properties.³⁴ Many CAs have problems with solubility in blood, which is a challenging obstacle for administration.

Gd(III) is highly toxic in its aqueous form⁵ and is similar in size to Ca(II), allowing Gd(III) to move easily through Ca(II) channels in cell membranes and disturbing Ca(II) pathways and cell messaging. Gd(III) toxicity is linked to Nephrogenic Systemic Fibrosis (NSF).^{35,36} This is a disease of fibrosis of the skin and internal organs and is caused by Gd(III) exposure in patients who have renal failure. NSF can occur due to imaging with a GdCA, therefore, Gd(III) must remain coordinated to a ligand to avoid toxicity.³⁷

The ability of a CA to influence magnetic resonance relaxation times is categorised by its corresponding relaxivities, r_1 and r_2 . The aim of optimising a new CA is to maximise these values. This can be achieved by modifying the parameters defined in the SBM equations: water coordination (q), water residence time (τ_m) and rotational correlation time (τ_R).^{14,15,38}

1.5.1 Water Coordination

There are three water spheres that can be defined in a GdCA.³⁹ The inner, or primary, sphere comprises of water which is directly coordinated to Gd(III). The secondary sphere contains water hydrogen bonded to the CA construct or primary water, where the residency time is longer than the diffusional correlation time of bulk water. The outer sphere is less organised and water freely diffuses.⁴⁰

The importance of q has previously been highlighted through the analysis of a complex, based on DTPA, with the ability to conjugate to human serum albumin (HSA) through a

diphenyl phosphate group. In the absence of HSA, the metallo complex had $q = 1$. When HSA bound to the complex, water coordination was blocked leading to $q = 0$. This reduction in q was accompanied by a reduction in r_1 from 6 to 2 $\text{mM}^{-1} \text{s}^{-1}$.⁴¹ The difference in rotational correlation time, due to the binding of a large protein, was shown to have no impact on relaxivity in this example.

Many of the CA's currently on the market have $q = 1$.¹⁴ It was proposed that when more water is located in the inner-sphere, relaxivity would increase and the CA would be less stable. Additionally Gd(III) would become less shielded and more likely to transmetalate.¹⁵ There have been examples of stable CAs with $q = 2$, attractive as the coordination of more inner-sphere water molecules enables the relaxivity of the CA to be enhanced.¹⁶ By using hexa- or hepta-coordinate ligands, complexes with $q = 2$ or 3 can be developed, this is often associated with a decrease in thermodynamic and kinetic stability. In one example, a derivative of DOTA, [Gd(DO3A)] with three pendant arms and $q = 2$, led to a r_1 of twice that of [Gd(DOTA)] (where $r_1 = 4.74 \text{ mM}^{-1} \text{ s}^{-1}$) whilst maintaining a high stability constant.⁴² Another example is a $q = 3$ complex of hydroxypyridinone (HOPO) ligands capped with triazacyclonane groups. The r_1 was found to be three times higher (9.9 compared to 3.3 $\text{mM}^{-1} \text{ s}^{-1}$) than that of [Gd(DTPA)]²⁻. This can be attributed to fast water exchange and a high q . In comparison, r_2 was found to be four times higher (16.0 compared to 3.5 $\text{mM}^{-1} \text{ s}^{-1}$) due to the additional influence of outer sphere effects. In this example, despite the increase in q , the stability constant remains high enough for clinical use.⁴³

Secondary sphere water also plays a significant role in relaxivity. Secondary sphere water effects arise from water which can interact with inner-sphere water or the CA scaffold. Secondary sphere water is influenced by the paramagnetic effect of the Ln(III), and its contribution is predominantly due to the exchange rate of secondary sphere water and its

distance from Gd(III).^{20,21} Using an analogue of [Gd(DTPA)]²⁻ with $q = 0$, [Gd(TTHA)]³⁻,³⁹ it was determined that a third of the relaxivity at low fields and a quarter of the relaxivity at high fields could be attributed to secondary sphere water.⁴⁴

Botta and co-workers found that through the careful selection of hydrogen bond acceptor groups on a GdCA it is possible to: promote the formation of a strong interactions; increase the number of water molecules in the second hydration shell; and decrease their average distance from the paramagnetic metal centre.⁴⁵ They concluded that despite secondary sphere water playing only a small role in determining the relaxivity of GdCA, it is important to consider for a more realistic interpretation of relaxation data and for a better understanding of the structure-relaxivity relationship.⁴⁵ Large increases in relaxation are possible due to secondary sphere water interactions and can be optimised through exploiting strong interactions with suitable side chains such as phosphonate and carboxoamide ligands.⁴⁵

Botta and co-workers also concluded that secondary sphere water effects play an important role when small GdCA interact with macromolecules, such as BSA, which results in an increase in relaxivity. The increase could not be attributed to inner or outer sphere water spheres but was instead attributed to the exchangeable protons close to the interaction site of the complex and from a network of hydrogen bonded water molecules in the second sphere of the GdCA.⁴⁵ This contribution is only detected in the presence of the protein because of the reduced mobility of its well-structured hydration layer.

1.5.2 Water Residency Time and Exchange

Water residency time (τ_m) is defined as the average time an individual water molecule is coordinated to the metal centre before it exchanges with the bulk.^{40,46} τ_m directly impacts τ_c and determines the total number of water molecules that are influenced by the metal centre. If τ_m is too long, there will only be a small effect on the bulk water. If τ_m is too short, water

molecules will not be sufficiently relaxed before they exchange, with both scenarios leading to poor relaxivity. Therefore, there is an optimum τ_m window which changes with τ_R , as shown in Figure 1.4. At high fields, relaxivity is largest when τ_m is equal to the inverse of the Larmor frequency.

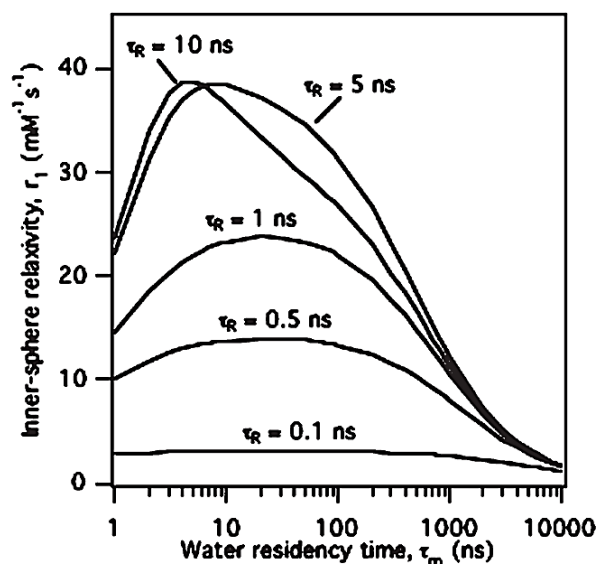


Figure 1.4: An optimum window for water residency time occurs for varying rotational correlation times. Figure reproduced with permission from Caravan, P. Chem. Soc. Rev. 2006, 3, 512–523.

τ_m is dependent on complex charge and solvent accessibility. This was demonstrated by replacing acetate oxygen ligands with amine groups to decrease τ_m , or in another example, using phosphate oxygens to increase τ_m .³⁹ By using hydrophilic or hydrophobic side chains, or conjugating proteins to the CA, τ_m can be slowed due to hydrogen bonding of water to the complex, or sterically blocking water access.^{47,48} This was also demonstrated in the work by Lukes and co-workers, where a carboxylic acid group was substituted with a phenyl containing a phosphate group on one arm of DTPA.⁴⁹ This reduced τ_m from 303 to 90 ns. The same was observed when a monophosphonic acid group was introduced into a macrocyclic DOTA complex. This reduced τ_m from 37 to 14 ns. In this example, the decrease in water residency

time was thought to be due to the steric conformation of the ligand forcing the DOTA analogue into a conformer which allowed better solvent access to the metal centre.^{50,51}

The direct observation of water exchange at a Cd(II) binding site within a *de novo* designed coiled-coil has recently been performed by Hemmingsen and co-workers, using ¹¹³Cd NMR spectroscopy.⁵² The water residency time was calculated to be on the scale of 10 ns and was the first direct experimental observation of the residence time of water coordinated to Cd(II) in any system.⁵² It was found that a substitution of leucine for alanine, 10 Å below the metal binding site, resulted in a change in the equilibrium constant and the water residence time, despite the metal binding site remaining unchanged. By using *de novo* designed proteins and NMR, it was established that nanosecond water exchange times can be determined for water binding to metals within coiled coils and that these exchange reactions can be controlled by amino acid substitutions that occur several residues away from the metal binding site.⁵²

1.5.3 Rotational Correlation Time

Large CAs normally exhibit slow rotational correlation times (τ_R), which can increase inner-sphere relaxivity. This has been observed when large Gd(III) complexes are used, with a τ_R of 10 ns, compared to τ_R of 0.1 ns for [Gd(DOTA)], and an increase in relaxivity is observed.⁴⁰ The rotation of a molecule is defined by its size and shape. For a spherical molecule τ_R can be determined by considering viscosity (η), radius (r^3), the Boltzmann constant (k_B) and temperature (T), as shown in Equation 1.12.

Equation 1.12:
$$\tau_R = 4\pi\eta r^3 / 3k_B T$$

τ_R is increased by increasing the size of the molecule, for example through the conjugation of a macromolecule. Examples of such work include dendrimers,⁴⁸ proteins⁵³ and

nanoparticles.⁵⁴ The addition of such macromolecules provides a large degree of synthetic versatility which can be taken advantage of for multimodal imaging, drug delivery and therapeutics.⁵⁵

When used in biological applications, dendrimers often have functionalised terminal groups such as hydroxyl groups which allow for increased solubility,⁵⁶ Raymond and co-workers described a Gd(hydroxypyridinone)-based chelate coordinated to a dendrimer which contained 12 hydroxyl groups, allowing for adequate solubility.⁵⁷ A relaxivity three times higher than commercial agents was reported. The dendrimer based CA was most efficient at a field strength of 90 MHz, which makes it one of the first published CAs which features fast water exchange and high relaxivity when used at higher magnetic fields.

A significant amount of research has been conducted using $[\text{Gd}(\text{DTPA})]^{2-}$ derivatives conjugated to HSA.¹⁵ There are a number of examples of small molecule contrast agents that bind to HSA, resulting in an increase of the rotational correlation time and an increase in relaxivity, for example, MS-325 (7 times increase in relaxivity on binding) and MP-2269 (3 times increase in relaxivity on binding), structures shown in Figure 1.5.¹⁵ When using MP-2269 it was calculated that the rotational correlation time was 1 ns, 7 times longer than the unbound complex and that the water residence time did not change upon binding. It has also been shown that increasing the number of benzyloxymethyl (BOM) groups onto DTPA in the presence of HSA increases relaxation. Two derivatives of $[\text{Gd}(\text{DTPA})]^{2-}$, one with one BOM group and the other with three, both showed an increase in relaxivity. The derivative with three BOM groups had a higher relaxivity and was more rigidly bound; reducing internal motion. Additionally, on binding to HSA the relaxivity of the complex increased from $8 \text{ mM}^{-1} \text{ s}^{-1}$ to $54 \text{ mM}^{-1} \text{ s}^{-1}$.

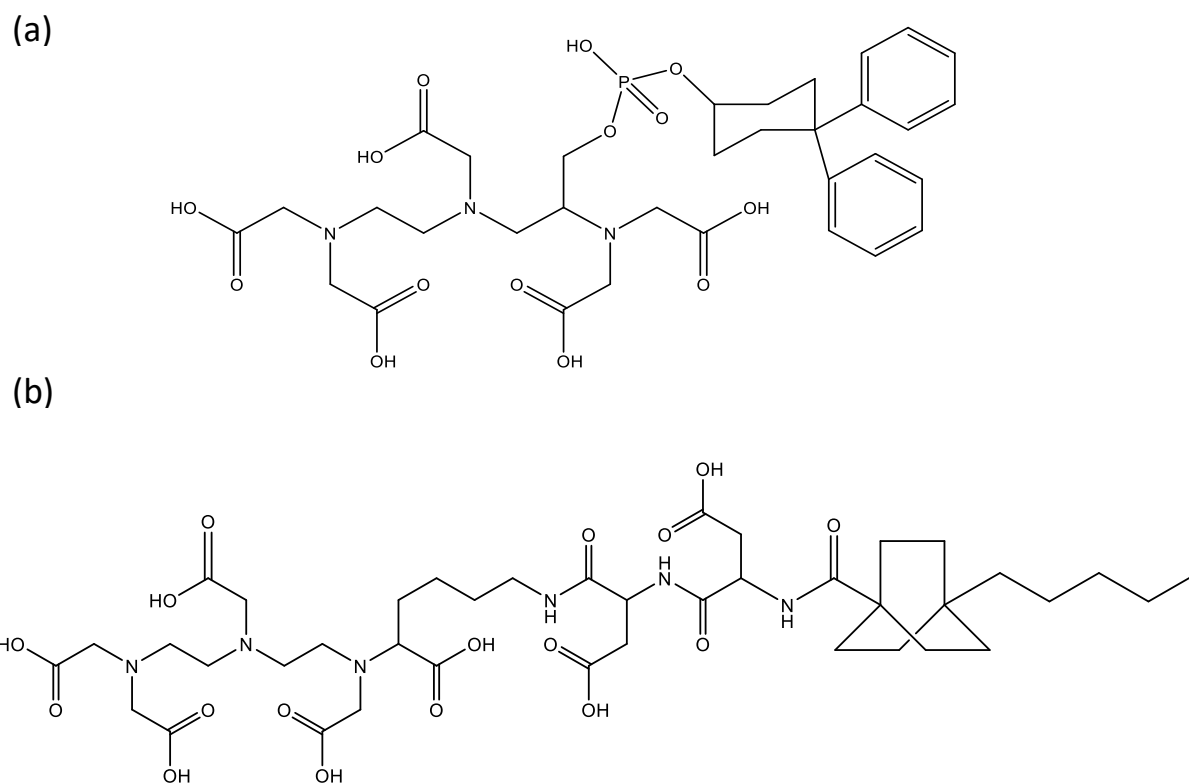


Figure 1.5: (a) MS-325 and (b) MP-2269 ligands.

When increasing τ_R , for example by coordination to a polymer, dendrimer, or macromolecule, there may be fast internal motion, for example, side chain rotation, coupled with the overall rotation of the macromolecule.⁵⁸ In the SBM equations, τ_C is a function of the overall motion of the macromolecule and the internal motion.¹⁵ This may be approximated using a model free approach where a second spectral density term is added to account for the fast motion.

Magnetic field strength impacts the effect of changing τ_R . At low field slowing the rotation increases relaxivity, however, at higher fields r_1 and r_2 are impacted differently. This was demonstrated by Uppal and co-workers who simulated the effects of different τ_R at different field strengths, as shown in Figure 1.6. It was found that r_2 was consistent over a range of field strengths (1 - 15 T), and a dramatic decrease in r_1 was demonstrated when τ_R was slow.⁴⁰

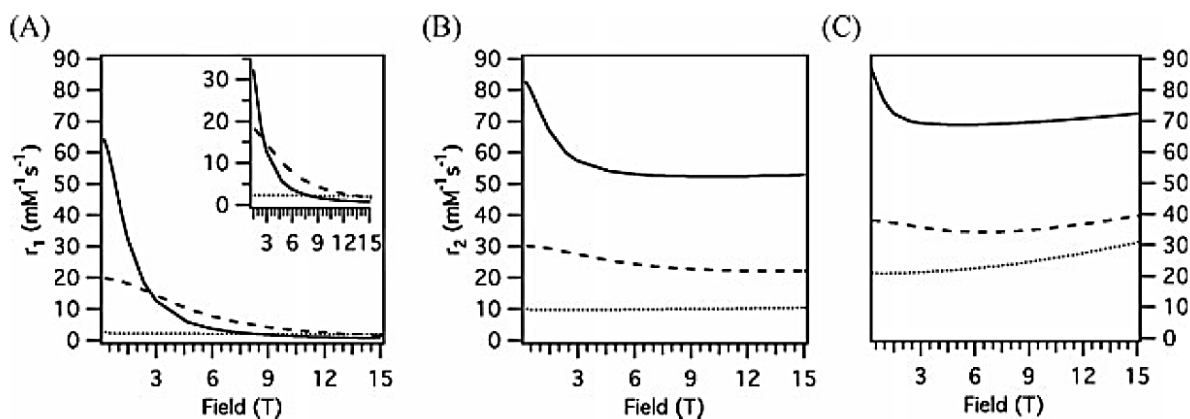


Figure 1.6: The change in (A) r_1 and (B,C) r_2 as a function of field strength. r_2 is highly dependent on water residence times, due to a scalar contribution, but there is no effect on r_1 . Rotational correlation times of 0.1 ns (dashed), 1.0 ns (grey line) and 10 ns (black line) with a water residency time of (B) 5 ns or (C) 100 ns. Figure reproduced with permission from Caravan, P.; Farrar, C. T.; Frullano, L.; Uppal, R. *Contrast Media Mol. Imaging* 2009, 4 (2), 89–100.

1.6 Lanthanides as MRI Contrast Agents

Gd(III) is the most common Ln(III) used in MRI, however some of the other Ln(III)'s also have the ability to enhance signal. In one example, the magnetic field dependence of r_1 and r_2 was investigated in Dy(III) analogues of Gd(III) complexes.^{59–61} Dy(III) has a highly efficient transverse relaxivity at high field strengths.⁶² Clinical MRI is constantly using higher magnetic fields, therefore new CAs need to be developed and optimised for higher field strengths where current GdCAs may fail. Dy(III) based complexes are becoming more popular as they display long water residence times resulting in an increase in relaxivity.⁶²

Dy(III) is not the only Ln(III) which has the potential to be used in MRI, however, the mechanism by which contrast occurs is different. For Gd(III), T_1 and T_2 are due to water exchange between the CA and bulk water, described in the inner-sphere relaxation. The inner-sphere mechanism is also responsible for T_1 of Dy(III), Ho(III), Er(III) and Tb(III).⁶³ However, T_2

is caused by the diffusion of water in the field inhomogeneities created by the CA, described in the outer-sphere relaxation mechanism.⁶³

The T_1 relaxation induced by Dy(III), Ho(III), Er(III) and Tb(III) is almost 100 times less efficient than for Gd(III).⁶³ This is due to the different electron relaxation times of the ions: long for Gd(III), 176 ps, and short for the remaining lanthanides ($\ll 20$ ps).⁶³ As the inner-sphere relaxation rate is proportional, at low field, to the shortest correlation time, which is the electronic relaxation time for Dy(III), Ho(III), Er(III) and Tb(III), the r_1 is negligible. This can be compared to Gd(III) which has r_1 of 4 - 40 $s^{-1} mM^{-1}$ at 1.5 T.⁶⁴

Gd(III) has a high T_2 relaxation rate, where the inner-sphere water mechanism is the dominant process.⁶³ However, for Dy(III), Ho(III), Er(III) and Tb(III) T_2 relaxation is due to the outer sphere mechanism. When using the outer sphere mechanism, r_2 increases quadratically with increasing field strength, making these lanthanides most efficient at high fields.⁶³ Additionally, the outer sphere mechanism for T_2 is proportional to the square of the radius; very small CAs (radius < 5 nm) containing Dy(III), Ho(III), Er(III) and Tb(III) will be inefficient, ($r_2 < 20 s^{-1} mM^{-1}$) even at high fields.

It is thought that the outer sphere mechanism dominates for T_2 of Dy(III), Ho(III), Er(III) and Tb(III) because of the difference in the electron relaxation times, which cause negligible inner-sphere relaxation rates for these compounds compared to the outer-sphere contribution, due to the mean magnetic moment of the CA. One major drawback of using these Ln(III) is their toxicity. Without strong binding, the Ln(III) could be released *in vivo* causing a toxic response.⁶⁵ A summary of the properties of the lanthanides of interest is shown in Table 1.2

Table 1.2: A summary of the properties of a number of different lanthanide salts relevant for MRI

| Ln(III) | Gd | Tb | Dy | Ho | Er |
|---------------------------------|---|--|------|------|-----|
| Atomic radius / pm | 233 | 225 | 228 | 226 | 226 |
| Electronic relaxation time / ps | 176 | << 20 | | | |
| Number of unpaired electrons | 7 | 6 | 5 | 4 | 3 |
| Magnetic moment | 7.9 | 9.6 | 10.4 | 10.7 | 9.5 |
| Relaxivity mechanism | T_1 and T_2 are dominated by the inner-sphere mechanism | T_1 is negligible and T_2 is dominated by the outer sphere mechanism | | | |

1.7 The Use of Manganese(II) in MRI Contrast Agents

Due to the toxicity attributed to GdCA, especially in patients with renal failure, manganese(II) contrast agents (MnCAs) can be used as an alternative. MnSO_4 was first reported as a potential MRI CA in 1973.³ Mn(II) features all the physical attributes that make Gd(III) highly effective as an MRI CA, especially in T_1 imaging. Both ions have long longitudinal electronic relaxation times, high spin quantum numbers and fast water exchange.⁶⁶ Mn(II) complexes can be cleared from the body through biliary excretion which is extremely attractive for patients suffering from renal failure.

$[\text{Mn}(\text{DPDP})]^{3-}$ (Telescan) is the only Mn(II) CA to have been approved for clinical use. It was designed by Lissner and co-workers and was approved in the 1990s, with the structure shown in Figure 1.7.^{67,68} It was used as a liver imaging agent and was found to undergo partial dechelation in plasma, with Mn(II) being taken up rapidly by surrounding cells.^{69,70}

$[\text{Mn}(\text{DPDP})]^{3-}$ has $q = 0$ which gives rise to low relaxivity.³ However, a large enhancement of T_1 was observed in the liver and was thought to be due to free Mn(II) interacting with proteins.³ The use of $[\text{Mn}(\text{DPDP})]^{3-}$ demonstrated both the success and weaknesses attributed to using MnCAs; the complex was highly efficient yet the lability of Mn(II) highlights the challenge of designing a stable MnCA.

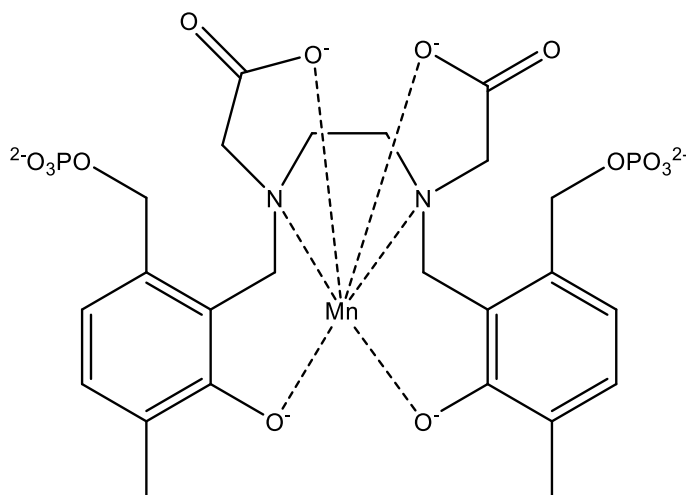


Figure 1.7: Structure of $[\text{Mn}(\text{DPDP})]^{3-}$, clinical name Telescan.

Caravan and co-workers⁶⁶ developed a series of Mn(II) complexes to be used as MRI CAs and replace current GdCAs. The most successful featured a PyC3A chelator which formed a stable, inert complex with Mn(II), as shown in Figure 1.8. It has been reported that $[\text{Mn}(\text{PyC3A})]^-$ is one of the most stable Mn(II) complexes at physiological pH.^{66,71} The stability was further investigated by a transmetalation study with Zn(II). On addition of 25 molar equivalences of Zn(II) to comparable solutions of $[\text{Mn}(\text{PyC3A})]^-$ and $[\text{Gd}(\text{DTPA})]^{2-}$, the MnCA was found to be 20 times more resistant to dissociation than the GdCA.⁶⁶ When comparing relaxivity, $[\text{Mn}(\text{PyC3A})]^-$ was found to be comparable to commercial GdCAs. In further work, a bi-functional analogue of the chelator allowed for the development of a targeted probe for molecular imaging of thrombosis.⁶⁶ Such Mn(II) complexes have optimal thermodynamic stability and kinetic inertness whilst still achieving high relaxivity.⁶⁶

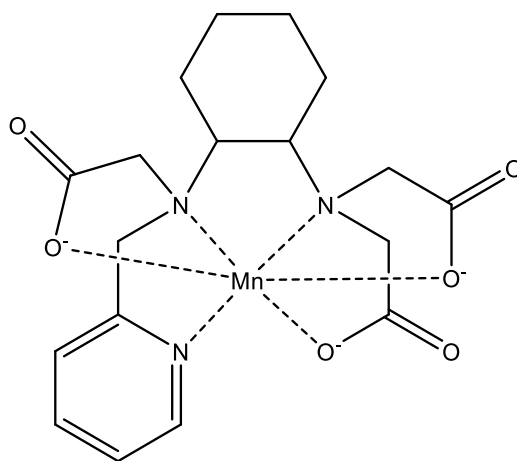


Figure 1.8: Structure of Manganese contrast agent $[\text{Mn}(\text{PyC3A})]^-$.

1.8 Peptide-Based Contrast Agents

Macromolecular CAs have the potential for high relaxivity, due to their slow rotational correlation time in solution.⁷² Because of their large size, it is possible to optimise the water coordination time and water exchange to generate even higher relaxivities.⁷³ Macromolecules can be adapted for ideal biodistribution and localisation, through chemical modifications to their exterior.⁷³

Peptides can be used as scaffolds for MRI CAs due to their wide variety of structures, bioavailability and non-toxicity. They are most commonly used for localisation into a specific tissue, for example a tumour. An example of this is the work by Sherry and co-workers where a short peptide was used to provide greater binding specificity.⁷⁴ A DOTA chelate, coupled to the N-terminus of a 12 amino acid peptide (G80BP), was designed to bind to the yeast transcription factor Gal80. The DOTA-peptide complex had a two fold increase in r_1 (at 20 MHz) compared to $[\text{Gd}(\text{DOTA})]$ due to reduced tumbling.⁷⁴

Self-assembling peptides can be used to conjugate to Gd(III). Upon addition of Gd(III), the peptide self-assembles into a larger structure. This allows for an enhancement of relaxivity because of the slower rotational correlation time. Meade and co-workers demonstrated this

through the development of a poly-Lys₃-Ala₃ peptide, which they conjugated to DOTA. In this example, nanofibres were formed upon self-assembly and a relaxivity three times higher than [Gd(DOTA)] was observed.⁷⁵

1.9 *De Novo* Design and Coiled-Coil Peptides

De novo design^{76,77} continues to become more and more popular as a method of designing novel proteins.⁷⁸ *De novo* is defined as “from first-principles” and involves the careful selection of a linear sequence of amino acids which will yield a peptide with the desired secondary and tertiary structure.⁷⁹ These designs are most frequently based on the α -helix.⁸⁰ Previous work has involved using coiled-coil structures which consist of two or more α -helices that wrap around each other in a left handed super helix.⁸¹ Coiled coils created by *de novo* design have the advantage of combining the simplicity of an α -helix with the complexity of a cooperatively stabilised structure. The complex, assembled from short polypeptide chains, exhibits globular protein characteristics such as inter-chain interactions that promote coiled-coil folding.⁸⁰

Three-stranded coiled-coils are well understood structures that are common in nature. They occur in fibrous proteins and cell-surface receptors,⁷⁸ with the most well-known example being keratin.⁸² The structural principles that dictate the folding of coiled coils have been discovered through biophysical characterisation and crystallographic studies of both natural and designed peptides.^{83–85}

The trimeric coiled-coil structure features a seven-residue repeat, allowing for a full turn of the α -helix, termed a heptad, where the residues are labelled **a-g**. Apolar residues at the **a** and **d** position stabilise the coiled coil by packing their hydrophobic side chains into the centre of the structure. Charged side chains at the interfacial **e** and **g** positions have the ability to shield the hydrophobic core with their side chains and form stabilising electrostatic and

hydrogen bonding interactions. Positions **b** and **c** are normally occupied by hydrophilic residues which aid with solubility and the **f** position accommodates highly polar and charged residues.⁷⁸

The formation of a three-stranded coiled-coil, in comparison to different oligomeric states, is dependent on the position and nature of hydrophobic residues.^{86,87} For a trimeric structure these residues must be restricted to the **a** and **d** position.^{84,88,89} A single residue change has the ability to change the oligomeric state of the coiled coil. For example, an asparagine residue at a single **a** position of a coiled coil can change the structure from a trimeric to dimeric coiled coil.^{84,85} Three-stranded coiled-coils are versatile scaffolds for protein design. They can be exploited for the introduction of functional sites: the hydrophobic core can bind small ligands or contain metal binding sites. The exterior can also be modified to bind transition metals or complex organic ligands.⁷⁸

1.10 Metal Binding in Coiled-Coil Peptides

Metals are commonplace in biology and are found in a third of all naturally occurring proteins.⁹⁰ They are important for functions such as enzyme catalysis, electron transfer and structure stabilisation.^{79,91} The incorporation of a metal binding site is useful for enhancing peptide stability, folding and function.⁸⁰ Metal binding is attractive for the construction of *de novo* designed peptides because metal ions can play an important role in determining protein structure and can also be used in the catalytic centres of proteins. As such, many coiled-coil peptides have been designed with the ability to bind transition metals.

Of the 20 naturally occurring amino acids, a number can be used for metal binding. The most common are the carboxylate groups of aspartic acid (Asp) and glutamic acid (Glu), the imidazole of Histidine (His) and the thiolate group of cysteine (Cys). Each functional group has the ability to bind to a number of biologically relevant metals.^{90,92} The hard oxygen donors

of Asp and Glu prefer binding to hard metals such as Ca(II) and Mg(II), whereas the soft thiolate groups of Cys will bind to softer metals such as Cd(II) preferentially. His shows little preference and can bind to either hard or soft metals.⁹²

Dieckmann and co-workers used coiled-coil peptides to investigate metal binding site geometry.⁹³ Metal binding sites can be identified as structural or functional. Structural sites fulfil the coordination of the metal; they have a common geometry and are well defined in crystal structures. Here, the metal can act as a template around which the peptide will fold. In comparison, functional metal binding sites can have a more unusual geometry which are enforced in folded coiled coils.⁷⁸ Dieckmann and co-workers used a trimeric coiled-coil to investigate the structure of a cysteine Hg(II) binding site.⁹³ A cysteine residue was located at position α of the coiled coil. Metal binding was examined using spectroscopic and physical methods. In the apo peptide a dimeric structure formed at low pH, but became a trimer above pH 7. At low pH the peptide bound Hg(II) in a two coordinate complex. Upon increasing pH a trigonal geometry was formed when peptide was in excess.

1.11 Lanthanide Binding Coiled-Coil Peptides

Except for one rare example,⁹⁴ lanthanides are not bound in native proteins. Due to the similarities between Ca(II) and Ln(III) coordination chemistry, Ln(III) binding sites can be developed using natural Ca(II) binding sites as a motif. Resulting Ln(III) metallopeptides have a variety of applications such as optical imaging agents, MRI CAs and catalysts.

Ln(III) binding requires hard oxygen or nitrogen donor groups. These are often attached to hydrophilic amino acids with negative charges such as Asn, Asp, Glu and Gln. The introduction of these groups in the hydrophobic core can be highly destabilising.

Hodges and co-workers designed the first Ln(III) coiled-coil, which consisted of a disulphide bridged, two-stranded coiled-coil, capable of binding La(III) and Ca(II) at the helical

interface. The coiled coil used the non-natural amino acid (γ -carboxyglutamic acid) which has two carboxylate groups in its side chain, structure shown in Figure 1.9. These two negative groups repel each other, however, on the addition of a metal, a transition occurred leading to a folded two-stranded coiled-coil.⁸⁰ Kashiwada and co-workers built upon this work through the design of a three-stranded coiled-coil which has the ability to selectively bind Ln(III) over other metals. The peptide featured a trigonal planar binding site located within the hydrophobic core of the coiled coil, made up of γ -carboxyglutamic acid.⁹⁵ Upon addition of a Ln(III) a trimeric structure forms.^{81,96} Non-natural amino acids can be expensive and their use is limited to peptides that can be readily synthesised. Therefore, the *de novo* design of coiled coils using natural amino acids to create a Ln(III) binding site would be much more desirable.

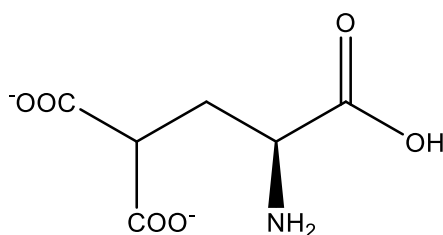


Figure 1.9: The non-natural amino acid, γ -carboxyglutamic acid.

In *de novo* designed coiled coils, each amino acid is selected for its structural or functional contribution to the overall peptide. Peptides developed previously in the Peacock group include the MB1 series designed by Berwick and co-workers.⁹⁷ The peptides incorporate a lanthanide binding site, with the ability to bind gadolinium. This was the first example of a Gd(III) coiled-coil to be reported. The coiled coil uses the sequence Ac-G-(I_aA_bA_cI_dE_eQ_fK_g)_x-G-NH₂.⁹⁷

By changing the residues in the *a* and *d* positions of a heptad, a Ln(III) binding site is formed. This was achieved by inserting asparagine at position *d* of the second heptad and aspartate at position *a* of the third heptad. This generated a hard oxygen binding site to bind

Ln(III) ions.⁹⁷ Tryptophan was introduced into the *f* position of the second heptad, next to the lanthanide binding site. Tryptophan has two main advantages; the first is its ability to absorb light at 280 nm so that the peptide concentration can be calculated using UV-Vis spectroscopy. The second is its ability to sensitise lanthanide luminescence allowing the binding site to be probed. This sequence of amino acids creates a metal binding site with a possible 9 coordination using the oxygen atoms from three asparagine residues and three aspartate residues on the internal core of the coiled coil.⁹⁷

1.12 *De Novo* Designed Lanthanide Coiled-Coils for MRI

The MB1 series of coiled-coil peptides are shown in Figure 1.10 and have been optimised for use in MRI by changing *q*. The relaxivity of the MB1 peptides was investigated at 7 T due to the trend towards the use of high field instruments in clinical MRI.

The four peptides in the MB1 series contain the same Ln(III) binding site, but differ in its linear translation along the coiled coil. The most apparent difference between the four MB1 peptides is their difference in folding, measured using CD spectroscopy, in the absence and presence of Ln(III), with the data shown in Table 1.3. When the Ln(III) binding site is located towards either termini of the peptide, an increase in folding is observed compared to when it is located in the centre of the peptide, suggesting the destabilising binding site is better tolerated when the core heptads remain unchanged.⁹⁵

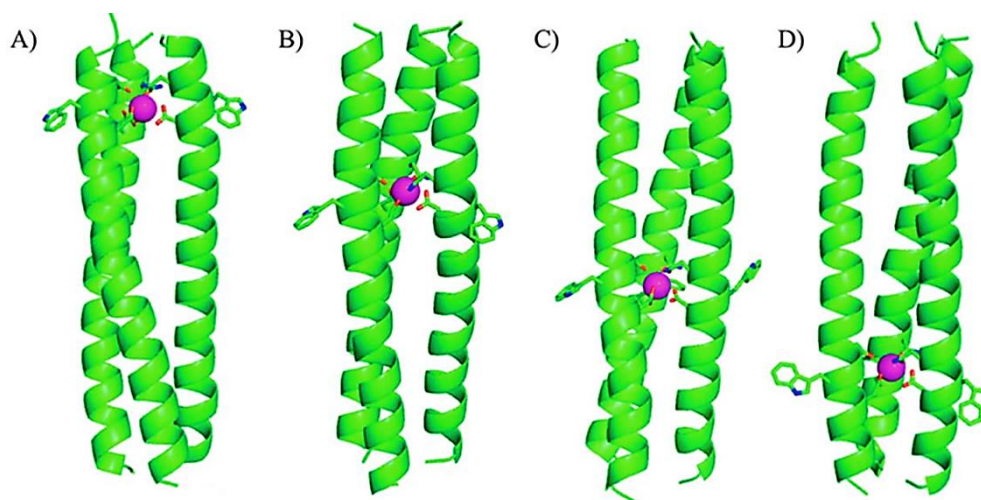


Figure 1.10: Pymol figures of the MB1 series of peptides A) Ln(MB1-1)₃, B) Ln(MB1-2)₃, C) Ln(MB1-3)₃ and D) Ln(MB1-4)₃. Peptide backbone is represented as a cartoon, the metal binding site and Trp sensitizer represented as sticks and the Ln(III) ion as a sphere. Reproduced with permission from Berwick, M. R.; Slope, L. N.; Smith, C. F.; King, S. M.; Newton, S. L.; Gillis, R. B.; Adams, G. G.; Rowe, A. J.; Harding, S. E.; Britton, M. M.; Peacock, A. F. A. *Chem. Sci.* 2016, 7, 2207–2216. - Published by The Royal Society of Chemistry.

An increase in folding was observed for each peptide on addition of Ln(III) in a 1:3 Ln(III) to peptide monomer ratio, indicating that binding is possible despite the position of the Ln(III) binding site.⁹⁵ This was confirmed using luminescence studies where addition of one equivalent of Tb(III) per trimer showed characteristic Tb(III) emission peaks with the emission enhancement attributed to the sensitisation of Tb(III) by the tryptophan sensitizer. A binding constant for each peptide was extrapolated, with the $\log K_a$ values given in Table 1.3. The binding constants were shown to be the same within the experimental error, despite the differences in peptide folding and stability.⁹⁵ The stability of the metallo coiled coils displayed the same trend as folding, with the free energy of folding given in Table 1.3.

Luminescence lifetime decay experiments were used in order to determine q for each peptide in the MB1 series. q was found to be zero when the Ln(III) binding site was located in the centre of the coiled coil but increased when the binding site was positioned at either

terminus, due to water being unable to penetrate the hydrophobic core of the coiled coil. When $q = 0$, in the MB1-2 and MB1-3 peptides, the r_1 relaxivity was found to be comparable to that of [Gd(DOTA)], compared to r_2 which was found to be significantly higher.⁹⁷ This was thought to be due to an outer sphere water mechanism, involving the coordination of water to the exterior of the peptide construct, in addition to the proposed reduction in rotational correlation time compared to [Gd(DOTA)].

By translating the Ln(III) binding site towards the C-terminus of the coiled coil and increasing the inner-sphere water coordination, $q = 2$, the relaxivities (both r_1 and r_2) were shown to increase significantly. By increasing the inner-sphere even more, $q = 3$, by translating the binding site to the N-terminus of the coiled coil, maximum relaxivities for the MB1 series of peptides was observed, data given in Table 1.3.⁹⁵

These results demonstrate the control that can be accomplished through the translation of a Ln(III) binding site along a *de novo* designed coiled coil and that the location of the Ln(III) binding site can enhance the relaxivity of the MRI CA through the use of inner-sphere and outer sphere water coordination and dynamics.

Table 1.3: Data collected through analysis by CD, luminescence and MRI by Berwick and co-workers.⁹⁵

| | % Folding Apo | % Folding Metallo | Metallo- $\Delta G_{H_2O}^{\circ} /$ $kcal\ mol^{-1}$ | $\log K_a$ | q | $r_1 /$ $mM^{-1}\ s^{-1}$ | $r_2 /$ $mM^{-1}\ s^{-1}$ |
|-------|---------------|-------------------|---|------------|-----------|------------------------------|------------------------------|
| MB1-1 | 80 ± 6 | 83 ± 7 | 22.4 ± 1.5 | 5.3 ± 0.2 | 3.1 ± 0.2 | 9.9 ± 1.5 | 88.3 ± 16.8 |
| MB1-2 | 21 ± 3 | 62 ± 3 | 15.3 ± 2.0 | 5.5 ± 0.2 | 0.0 ± 0.1 | 4.1 ± 1.2 | 24.4 ± 2.6 |
| MB1-3 | 15 ± 1 | 41 ± 4 | 16.7 ± 3.9 | 5.2 ± 0.3 | 0.0 ± 0.1 | 4.0 ± 1.0 | 20.9 ± 1.0 |
| MB1-4 | 55 ± 6 | 70 ± 5 | 19.3 ± 4.8 | 5.3 ± 0.4 | 1.8 ± 0.4 | 7.5 ± 4.1 | 37.6 ± 4.0 |

1.13 Project Aims

The coiled coil is a common peptide motif and has been extensively used as a scaffold for metal binding. Through the design of the MB1 series of peptides, it has been observed that

metal hydration can be tuned through translation of the Gd(III) binding site. This has allowed for the first steps into the optimisation of this class of peptides for use as MR imaging probes.

In this thesis the MB1 peptides will be further investigated, and optimised for use as MRI CAs. This will involve the principles of the SBM equations, which provide important information allowing for the optimisation of a CA. This work will include investigation into rotational correlation time, water coordination and water residence time in order to provide further insight into CA optimisation.

Rotational correlation time, in comparison to MB1-1, will be investigated through the synthesis and characterisation of two new peptides of differing length (4, and 6 heptads). Increasing peptide length from 5 to 6 heptads was proposed to slow the rotational correlation time and increase relaxivity. The effect of rotational correlation time and the MRI efficiency will be discussed in Chapter Three.

Secondary sphere water interactions, in comparison to MB1-2, will be analysed through the synthesis of a new peptide with side chains predicted to coordinate more water to the peptide exterior. Increasing secondary sphere water coordination was proposed to cause an increase in MRI relaxivity. This will be discussed in Chapter Four.

The presence of a water channel in the MB1-2 peptide will be investigated in Chapter Five. This will be achieved through the design, synthesis and characterisation of two new peptides containing D-amino acids which were proposed to block water access to the hydrophobic core of the coiled coil, thereby decreasing secondary sphere water interactions and decreasing relaxivity. This will allow for a proof of concept and greater understanding into secondary sphere water interactions in the MB1 peptides.

Finally, the toxicity and biological effects of the MB1-1 and MB1-2 peptides will be investigated in Chapter Six. Here, transmetalation studies were undertaken, using luminescence spectroscopy, and two cell types were incubated with $\text{Gd}(\text{MB1-1})_3$ in order to assess the toxicity of the CA within biological systems.

Chapter 2: Experimental Techniques

2.1 Peptide Synthesis and Purification

Solid-phase peptide synthesis (SPPS) was introduced by Merrifield in 1963⁹⁸ and is used to synthesise a peptide on a resin. Normally, the C-terminus of the peptide is coupled to the resin through a carboxyl group and the N-terminus is protected to avoid polymerisation reactions. This protective group can be selectively removed to allow for the next amino acid to couple, forming a peptide bond. An excess of amino acid is used to drive the synthesis to completion and any unreacted reagent can be washed away. An amino acid with a protecting group at the N-terminus is then added to the solution with an activator for the carboxyl group. The amino acid couples with the amine on the N-terminus of the amino acid currently attached to the support. Any unreacted amino acid is washed away. The deprotection and coupling procedures can be repeated until the desired sequence is produced. This method of peptide synthesis can lead to incomplete reactions and there is a chance that side reactions may take place. There is also the possibility of reagent impurities residing on the resin. This can lead to a lower yield of peptide and, therefore, this method is generally used for peptides up to 50 amino acids in length, depending on the sequence.^{9,98,99} A diagram showing the peptide synthesis cycle is shown in Figure 2.1. Deprotection and coupling can be assisted by the use of a microwave. Microwave irradiation allows more complex sequences to be constructed, as it prevents aggregation and secondary structure formation.^{100,101}

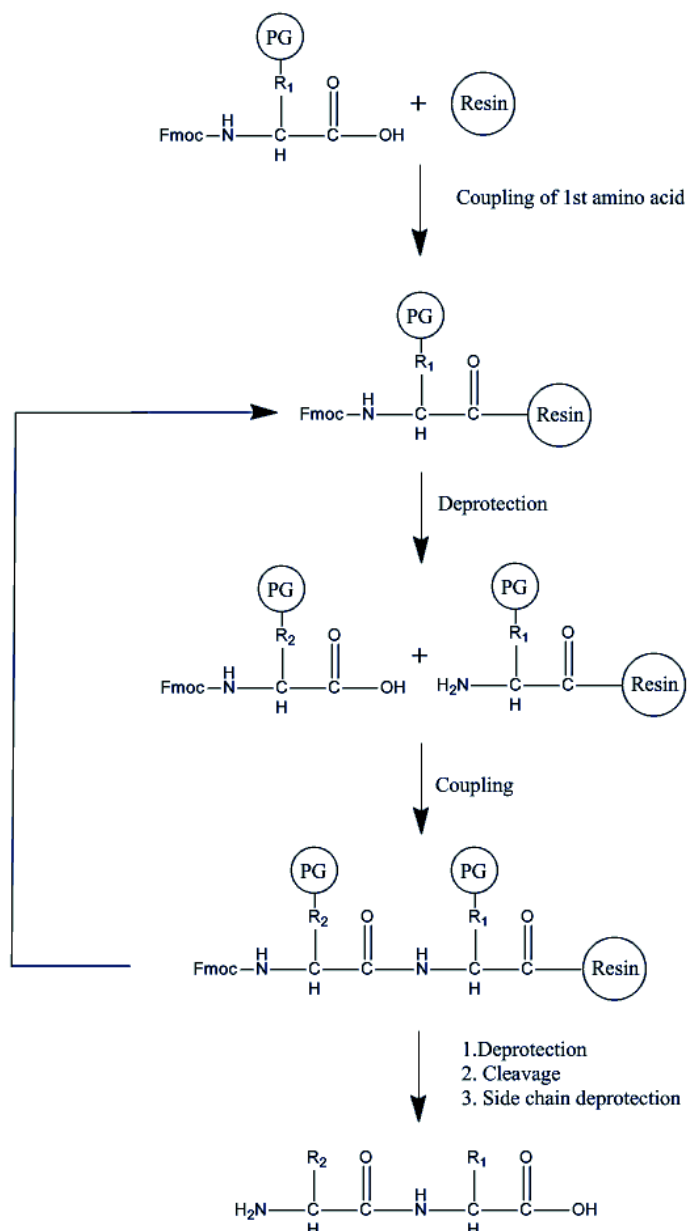


Figure 2.1: A schematic diagram of Fmoc SPPS illustrating the coupling procedure for the first amino acid on the solid support, the deprotection and coupling cycle and the final deprotection and cleavage to form the desired peptide.

Fluorenylmethoxycarbonyl (Fmoc) is commonly used to protect the N-terminus of an amino acid during SPPS and is readily removed using an organic base, for example, piperidine. Amino acid side chains often need to be protected to avoid side reactions during synthesis. A wide selection of reagents and resins can be used in SPPS; the following were used in this work. A rink amide 4-methylbenzhydrylamine (MBHA) resin was used as a solid support, (O-

(benzotriazol-1-yl)- N,N,N',N',-tetramethyluronium) hexafluorophosphate (HBTU) and diisopropylethylamine (DIPEA) activate the carboxyl and amine groups allowing for the formation of amide bonds. The final amino acid in the desired peptide sequence is acetylated, using acetic acid and DIPEA, at the N-terminus to prevent any further reactions taking place. The peptide is cleaved from the resin, and the amino acid protecting groups removed using a mixture of TFA, TIPS and H₂O.^{9,99,102} The resulting peptide can then be dissolved in a mix of acetic acid and water, and purified using HPLC.

2.2 High Performance Liquid Chromatography

Liquid chromatography (LC) separates molecules by charge, mass and hydrophobicity.^{103,104} The sample is injected onto a stationary phase and the chosen mobile phase is passed over, causing the sample to flow through the stationary phase, with a rate determined by the sample's affinity for the two phases. Separation of the mixture will occur due to the different chemical properties of the components of the sample.¹⁰⁵ When using HPLC, the polar stationary phase is contained in a tightly packed column and the mobile phase is pumped through under high pressure. This allows for better separation and better resolution of the chromatogram.¹⁰³ Reversed phase HPLC differs in that the stationary phase is non-polar.^{103,104} The non-polar stationary phase is frequently formed of aliphatic carbon chains, for example C₁₈, as used in this work, which are secured onto a silica support. The mobile phase is made up of a mixture of solvents, for example, acetonitrile and water, and the polarity of the mobile phase is controlled by changing the ratio of the two solvents as a function of time. Ion pairing reagents such as TFA can be added to the solvents in order to aid solubility and create an acidic pH, which increases hydrophobic interactions between the peptide and the column, allowing for an improvement in resolution. The polarity of the mobile

phase can be changed in order to separate the peptide species by size and hydrophobicity. Peptides, or peptide fragments, with a low molecular weight commonly elute first.^{102–104}

2.3 Mass Spectrometry

Mass spectrometry is a commonly used gas-phase technique where a sample is ionised and separated by a magnetic field, based on its mass to charge ratio (m/z). Many different ionisation techniques, separation methods and detection methods are possible and are selected depending on the properties of the sample. The most common ionisation methods for the analysis of peptide samples are electrospray ionisation (ESI) and matrix assisted laser desorption ionisation (MALDI). This is because a high energy focused beam of electrons, such as in electron impact, can be too harsh for biological samples.^{103,106,107}

In ESI, a liquid containing the sample of interest travels through a charged capillary at high pressure and enters a vacuum. This results in a fine spray of charged droplets which evaporate to give ionised molecules. This is a soft ionisation method as it does not cause fragmentation. ESI produces a range of charged species, giving the species of interest a characteristic charge envelope.^{103,106,107}

MALDI is a soft ionisation technique which uses a matrix to form a co-crystal with the sample of interest. The matrix must be able to absorb in the UV region, as it is through the crystals being irradiated with a high energy laser beam, that the matrix absorbs energy and transfers it to the sample, generating single charged ions of the sample of interest.^{106,107}

Time of flight detectors, which can be coupled with both of these ionisation techniques, measure the time taken for the ions of interest to travel along the drift tube, determining the mass to charge ratio.^{106,107}

2.4 Ultra Violet-Visible Spectroscopy

Certain molecules have the ability to absorb energy; this is most commonly observed as electromagnetic radiation. In a given chemical system, this has the potential to result in an electronic transition, occurring between the ground and excited state.¹⁰⁸ The difference in energy between these two levels (ΔE) is related to the frequency (ν) and wavelength (λ) of the absorbed electromagnetic radiation, where h is Planck's constant and c is the speed of light in a vacuum, as given in Equation 2.1. When considering biological molecules, such as peptides, absorption often occurs in the UV region.^{103,108}

Equation 2.1:
$$\Delta E = h\nu = \frac{hc}{\lambda}$$

In UV-Visible spectroscopy, the transmittance of light travelling through a sample of interest is measured.¹⁰³ This is the ratio between the intensity of light measured and that of a blank. This can be converted to absorbance (A), which is related to the extinction coefficient (ϵ), concentration of the peptide (c) and the path length of the cuvette (l), as identified by the Beer Lambert law, as given in Equation 2.2.

Equation 2.2:
$$A = \epsilon cl$$

The amino acid tryptophan absorbs at 280 nm with an extinction coefficient of 5690 $M^{-1} cm^{-1}$.¹⁰⁸ By using the intensity of absorbance at this wavelength, the exact concentration of tryptophan in solution, and therefore the peptide concentration, can be calculated.

2.5 Circular Dichroism

Circular dichroism (CD) measures the optical activity of asymmetric molecules using the basic principles of absorption spectroscopy.¹⁰⁹ Differently oriented circularly polarised light (A_L and A_R) is passed through a sample of interest and the difference in absorbance, (θ_{obs}), is recorded as a function of wavelength, reported in milidegrees. For peptides this can

then be converted to molar ellipticity per residue, which is calculated from the number of amino acids in the peptide of interest (n), the peptide concentration (c) and the cuvette pathlength (l), as shown in Equations 2.3 – 2.4.¹¹⁰

Equation 2.3:
$$\theta_{obs} = A_L - A_R$$

Equation 2.4:
$$[\theta] = \frac{\theta_{obs}}{n \times c \times l \times 10}$$

Peptides are characterised using CD as they consist of chiral amino acids and fold to generate chiral secondary structures. The emission of the peptide backbone gives rise to a CD signal which can then be assigned to a specific secondary structure, for example, α -helix or β -sheet, as shown in Figure 2.2.¹⁰⁸ For coiled-coil peptides, a minimum is observed at 208 and 222 nm and a 1:1 ratio of the two minima is representative of an α -helical structure. The minimum at 208 nm is indicative of a single stranded helix, with a decrease in this band representing a more coiled structure.

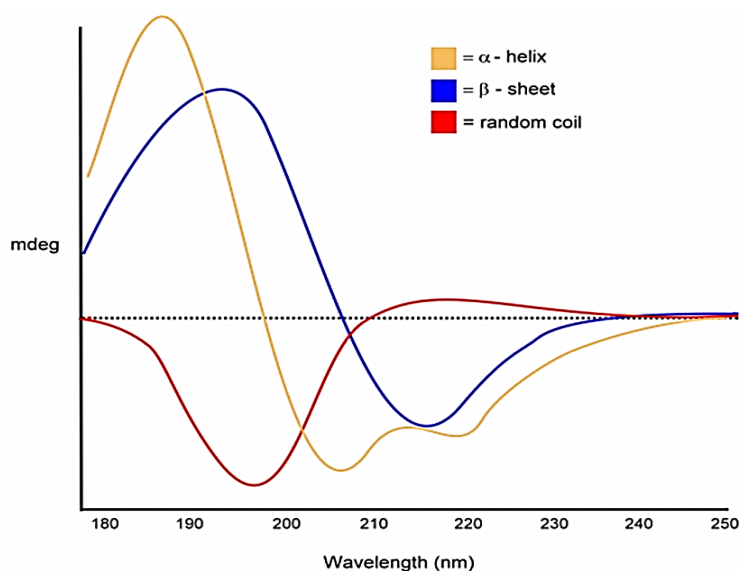


Figure 2.2: CD spectra illustrating different secondary structures of proteins.¹¹¹

The minimum at 222 nm can be used to calculate the percentage folding of a coiled coil, with 100% folding being representative of every amino acid being in its preferred position

in the helix.^{80,112–114} This can be calculated using Equation 2.5, based on the molar ellipticity per residue at 222 nm, $([\theta]_{222\text{ nm}})$, and the number of amino acids in the peptide sequence (n).¹¹⁰

Equation 2.5:
$$\text{percentage folded} = \frac{([\theta]_{222\text{ nm}} - 640)}{\left(\left(-42500 \times \left(1 - \frac{3}{n}\right)\right) - 640\right)} \times 100$$

2.6 Emission Spectroscopy

The electromagnetic radiation which is emitted from a sample can be measured, and categorised as either fluorescence or phosphorescence. During the process of fluorescence, emission will occur from an excited singlet state. Here, the electrons in the excited and ground states are spin paired. The transition is spin allowed and has a short lifetime. In phosphorescence emission occurs from an excited triplet state. An electron in the excited state will be in the same spin orientation as the electron in the ground state. This means that the transition is spin forbidden and the emission rate is slower. In the case of emissive metal complexes, emission can often occur from both singlet and triplet excited states, and is referred to as luminescence.^{108,115}

An excited electron can follow a number of non-radiative decay pathways, as shown in Figure 2.3. Non-radiative intersystem crossing (ISC) can occur, followed by relaxation to the lowest vibrational level. Here, an electron can transfer from a singlet to a triplet state, allowing phosphorescence to take place. Quenching can also occur through non-radiative pathways involving collisions or interactions with other molecules. Importantly for lanthanides, water has the ability to quench luminescence by transferring high energy vibrations from OH bonds.¹¹⁶

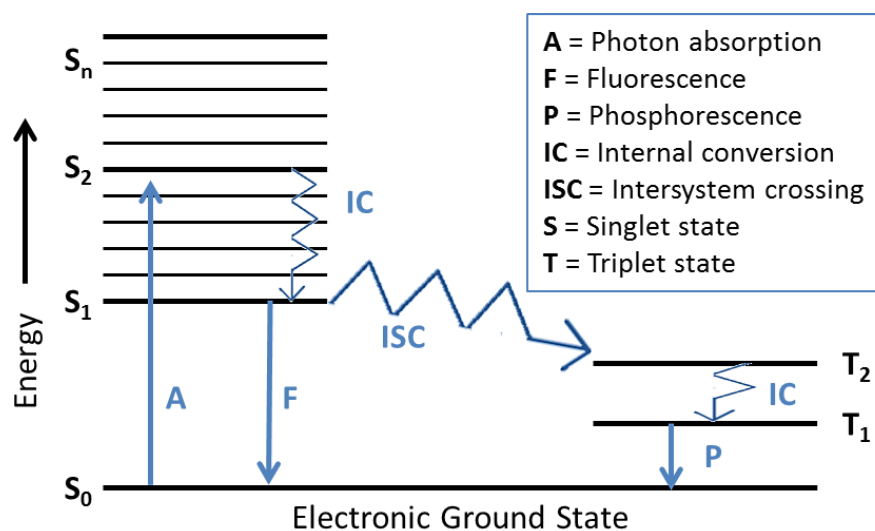


Figure 2.3: Jablonski diagram showing excitation from the ground to excited state. Energy is transferred between different energy levels through internal conversion and intersystem crossing.

This leads to fluorescence or phosphorescence.

Terbium emission is commonly studied due to its low lying excited state which leads to emission at a wavelength located in the visible spectrum.⁵ The amino acid tryptophan is often used as a sensitizer for terbium emission as it has a large molar absorptivity and a short excited state. The tryptophan sensitizer can be excited to a higher energy singlet state. From here, the energy can be transferred through intersystem crossing to an excited triplet state. The excited triplet state can then pass energy to the 5D_4 excited terbium state, leading to luminescence emission to the 7F_j ground state.⁵

2.7 Nuclear Magnetic Resonance

NMR can be used to measure the intrinsic magnetic properties of nuclei with a spin quantum number (I) that does not equal zero. This nucleus will possess intrinsic angular momentum which, in turn, imparts a magnetic moment (μ). When located in a static magnetic field (B_0), the magnetic moment will align with the magnetic field, shown in Figure 2.4(a). For a nucleus of spin = I there are $2I + 1$ available orientations, represented by the magnetic

quantum numbers (m), with the lowest energy state being preferred, shown in Figure 2.4(b).^{13,117}

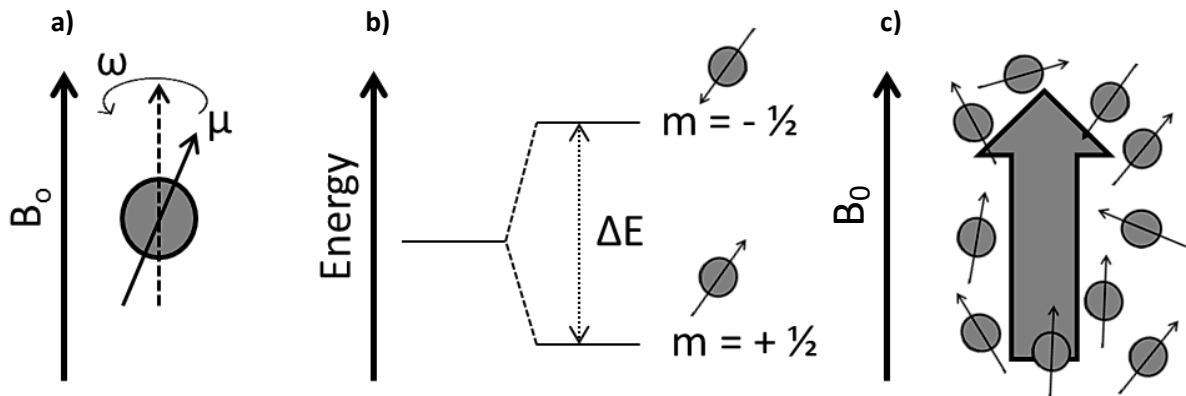


Figure 2.4: Schematic to show (a) a nucleus and magnetic moment, (b) energy levels of an $I = \frac{1}{2}$ nucleus and (c) the Boltzmann distribution of spins leading to macroscopic magnetisation.

For hydrogen nuclei, the spins will orientate in the lowest energy state, $m = +\frac{1}{2}$, where the spin direction is aligned with the magnetic field, and a high energy state, $m = -\frac{1}{2}$, where the spin direction is opposite to the magnetic field. These two energy levels can be labelled as spin up and spin down. The energy difference between the two levels is defined by Planck's constant (h), frequency of electromagnetic radiation (ν), magnetogyric ratio (γ), and field strength (B_0) as shown in Equation 2.6.

Equation 2.6:
$$\Delta E = h\nu = \frac{h\gamma B_0}{2\pi}$$

When a magnetic field is applied, the spins will precess around the B_0 axis at the Larmor frequency (ω). This will be dependent on the gyromagnetic ratio (γ) and the strength of the magnetic field strength (B_0) as shown in Equation 2.7.^{13,117}

Equation 2.7:
$$\omega = \gamma B_0$$

After a radio frequency (RF) pulse, transitions occur between energy levels. Transitions occurring from the low to high energy levels correspond to the absorption of energy. As the

population is higher in the lower energy level, this is the major transition. The transitions which occur in the reverse direction, lead to the emission of energy. These transitions are detected as a signal with the intensity proportional to the population difference.^{13,117} A 90° pulse will position the net magnetisation in the x-y plane where it will precess with the Larmor frequency, shown in Figure 2.5(a). The precession will induce an oscillating current in the RF coil, which is detected as an NMR signal. The signal will decay with time due to relaxation producing an FID, shown in Figure 2.5(b). By using a Fourier transform, a spectrum can be created.

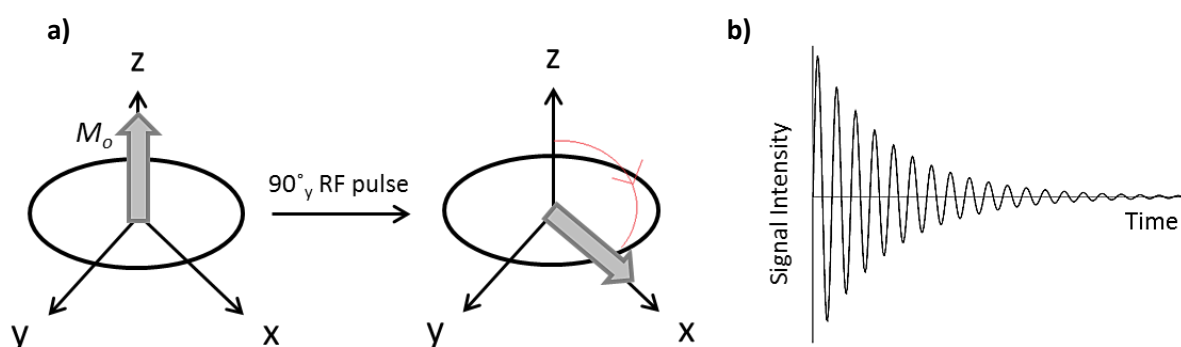


Figure 2.5: Schematic diagram to show (a) the application of a 90° pulse which causes the net magnetisation to move into the transverse plane and (b) the FID produced due to the precession of magnetisation in the transverse plane.

Multiple nuclear environments in a single sample will result in a number of different precession rates which, once Fourier transformed, will produce a spectrum with multiple peaks. The difference between the peaks of the sample and that of a reference is called the chemical shift. Splitting can occur within a NMR peak due to the influence of neighbouring spins on the Larmor frequency. By analysing the position and splitting of the peaks, information regarding the structure and chemical environment can be obtained.^{13,117}

2.8 Relaxation

When a RF pulse is turned off, the magnetisation vector moves from its equilibrium position. The spin system relaxes due to a loss in energy, which can be described as longitudinal or transverse relaxation.¹¹⁷ The longitudinal relaxation time (T_1) is associated with the net magnetisation returning to its initial position. T_1 relaxation is exponential and can be calculated using the magnetisation located in the z-direction during thermal equilibrium, using Equation 2.8.

Equation 2.8:
$$M_z = M_0 \left(1 - 2e^{-t/T_1}\right)$$

One method for measuring T_1 is the inversion recovery experiment. In this method a number of spectra are recorded using an $180^\circ - \tau - 90^\circ$ - FID pulse sequence, shown in Figure 2.6. The 180° pulse rotates the magnetisation vector to a negative z-axis position. A range of evolution times, τ , are used throughout the experiment. By creating an experiment with increasing τ times, the signal will increase and the data can be fit to give a T_1 relaxation constant.^{13,117}

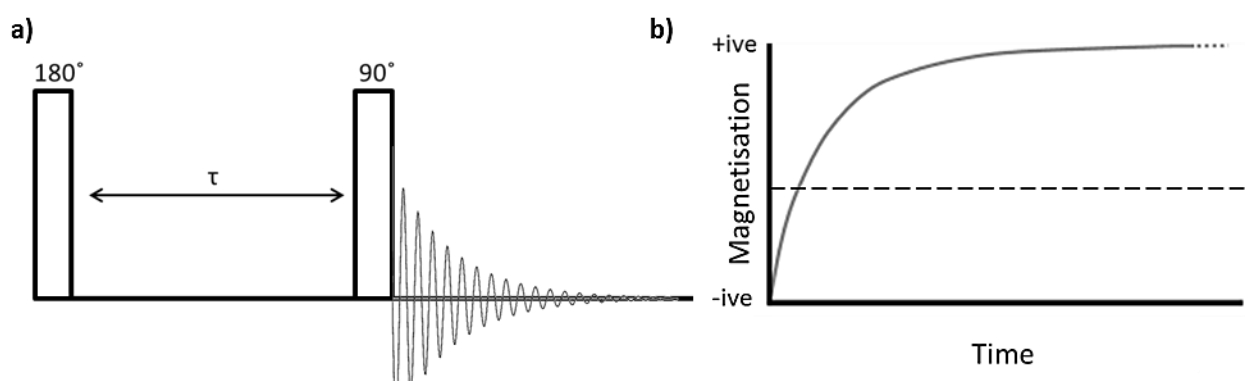


Figure 2.6: Schematic to show (a) the inversion recovery pulse sequence, (b) graph of signal intensity over time.

Transverse relaxation (T_2) describes how rapidly the transverse magnetisation components decay. After the 90° pulse, the precessing nuclear spins gradually lose their phase

coherence and the magnetisation reduces to zero. Again, an exponential relationship is observed between the evolution time and the magnetisation in the transverse plane ($M_{x,y}$). This allows the T_2 relaxation constant to be determined, using Equation 2.9.^{13,117}

Equation 2.9:
$$M_{x,y} = M_0 e^{-2t/T_2}$$

T_2^* results primarily from inhomogeneity in the magnetic field. The measured T_2 relaxation time is a combination of these field inhomogeneities and molecular interactions intrinsic to the sample. To separate the data of interest, the field inhomogeneities are eliminated using a CPMG pulse sequence, shown in Figure 2.7. Following excitation by a 90° pulse, spins begin to dephase during the mixing time τ . An 180° pulse refocuses the signals, creating an echo. Multiple 180° pulses are used with a constant mixing time and the echoes are repeated a defined number of times before data collection. The intensity and decay of the acquired echoes can be fit to obtain the intrinsic T_2 value. By using a short echo time, relative to diffusion of the spins, only the intrinsic T_2 is measured.^{13,117}

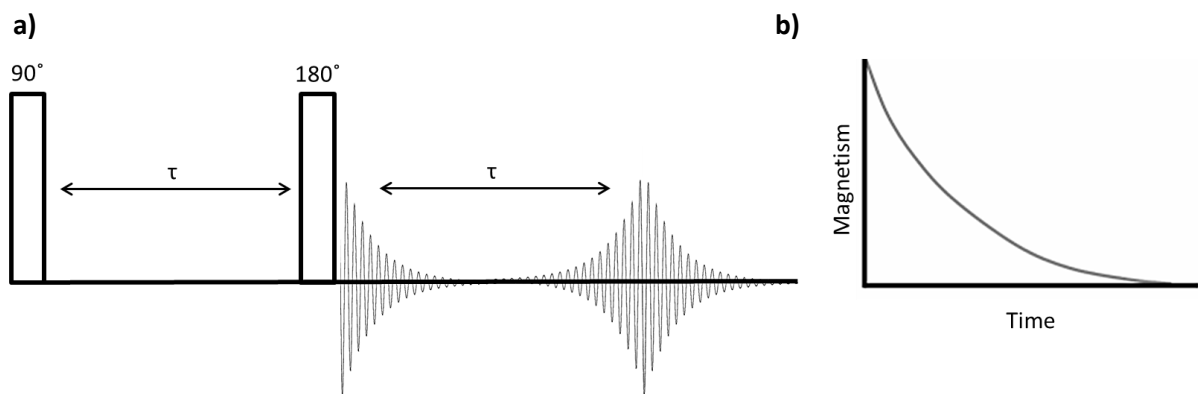


Figure 2.7: Schematic to show (a) CPMG pulse sequence (b) a graph of the change in signal intensity over time.

2.9 Magnetic Resonance Imaging

In MRI, the application of magnetic field gradients causes the magnetic field to no longer be uniform. Spins experience position-dependent field strength, which causes

precession at varying frequencies, producing a helix of phase. The Larmor frequency (ω) of the nuclei becomes spatially encoded with respect to the x , y and z direction (r). The wavelength (λ) is determined by the strength (G) and duration (t) of the gradient and the reciprocal space vector (k), as given in Equations 2.10 and 2.11.^{27,118}

Equation 2.10:
$$\omega_r = \gamma B_0 + \gamma G \cdot r$$

Equation 2.11:
$$k = \frac{1}{\lambda} = \frac{\gamma G t}{2\pi}$$

2.9.1 Frequency and Phase Encoding

K-space is used in order to gain spatial information by increasing the gradient strength (phase encoding) or time (frequency encoding). To generate a 2D image, frequency and phase encoding gradients are generally used in the x and y direction and slice selection in the z direction, in order to determine the slice thickness and z position. When creating a 2D image, the NMR signal at each location in a **K**-space map is collected.²⁷

During phase encoding, a gradient pulse with a constant duration is used. The gradient is switched off before the start of the acquisition. This means that the frequency of the spin packets will be identical but their phase will be different. This allows for spatial encoding in the phase direction. Here **K**-space is traversed by varying the gradient strength (**K_y**).

During frequency encoding, a magnetic field gradient is applied with constant field strength during signal acquisition and the acquisition time is varied (traverse through **K_x**). Spins at different positions will have different frequency dependence and so the signal intensity across the spectra is proportional to the number of spins located at each position.²⁷ In order to obtain spatial information in the third dimension an additional slice encoding gradient can be used which, when used with a soft RF pulse, selectively excites spins in a slice of the sample.²⁷

2.9.2 Resolution and Field of View

Resolution in an MR image is dependent on $K(\max)$, which is ΔK multiplied by the total number of data points collected. The resolution in the frequency encoding direction is influenced by the NMR signal linewidth and pixel size, with the linewidth limiting the resolution. The field of view is defined by ΔK . If some of the sample is outside of the field of view, aliasing will occur leading to image fold-over and artefacts.¹¹⁹

2.9.3 Spin Echo Imaging Sequence

A spin echo imaging sequence can be used to produce two dimensional images. A slice-selective gradient is used in the z-direction in order to spatially encode spin packets. Through the use of a soft, frequency selective, 90° , RF pulse, a narrow band of frequencies is excited and this corresponds to the selected slice of the sample. Often sinc or Gaussian functions are used for the soft pulse.^{27,119} Following slice selection, a phase encoding gradient step is used to spatially encode spin packets along the y-direction. An 180° pulse is required to focus the magnetisation, allowing for the production of an echo. The frequency encoding gradient will be applied and the resulting data encoded in both the frequency and phase directions. The echo time, T_E , is defined as the time between the middle of the excitation pulse and the centre of the echo, which is at the centre of the positive part of the read gradient. The above sequence is repeated with a repetition time of T_R . By using a number of varying phase encoding gradients, all the required values of K_y will be obtained. The consequent array will be Fourier transformed in order to produce a 2D image.^{27,119}

The spin echo sequence can be modified using RARE (Rapid Acquisition with Relaxation Enhancement), shown in Figure 2.8.¹²⁰ Here, multiple pulses are used to create many echoes. By applying a different phase encoding gradient to each echo, multiple K -space lines can be attained from a single excitation. This can dramatically decrease experiment time.¹²⁰

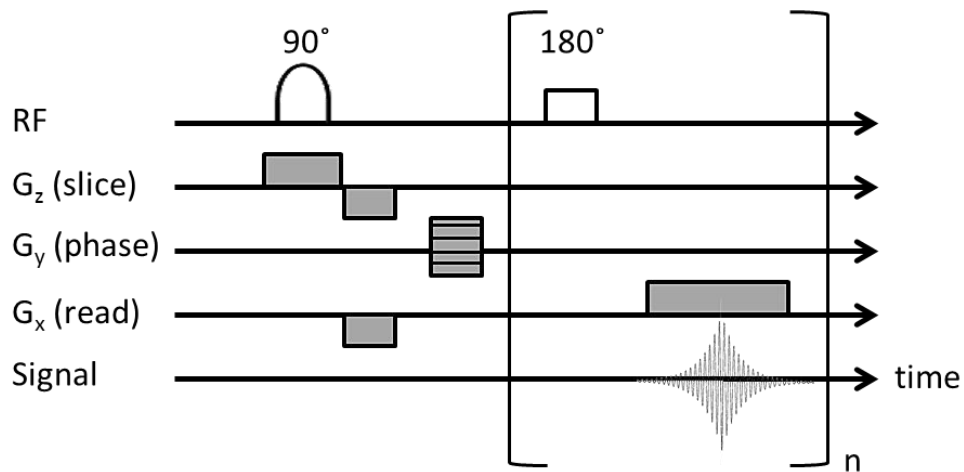


Figure 2.8: A pulse program diagram for imaging sequence with n echoes.

2.9.4 Image Contrast

Image contrast occurs due to variations in signal intensity across the pixels which form the image. These variations can be attributed to differences in relaxation time, spin density, chemical shift, and molecular displacement. By choosing the correct imaging sequence, optimal contrast will be observed. A spin density image can be produced if the echo time is short, in comparison to the T_2 time, and the repetition time is long in comparison to the T_1 time. By varying the repetition time or the echo time, T_1 -weighted or T_2 -weighted images can be obtained. A series of T_1 or T_2 images, with difference signal intensities can be collected and the changes in signal intensity can be used to produce maps which give T_1 or T_2 values at a specific position in a 2D image.¹¹⁸

Chapter 3: Effect of Peptide Length on Relaxivity and the Effectiveness of MRI Contrast Agents

3.1 Introduction

The relaxivity of an MRI contrast agent (CA), is dependent on the number of coordinated water molecules, the distance between water and Gd(III), the water residence time and the rotational correlation time of the complex.⁴⁶ The majority of CAs used in the clinic do not exhibit optimal relaxivity, due to, amongst other things, their small size and rapid rotational correlation time.¹⁵

One popular strategy for enhancing relaxivity is to slow down the rotational correlation time of the CA through the design of macromolecular Gd(III) complexes. These can be based on linear polymers⁷², nanotubes,^{121,122} dendrimers,¹²³ carbohydrates,¹²⁴ viral capsids,¹²⁵ liposomes¹²⁶ and peptides.^{15,25,122} One approach involves the preparation of Gd(III) peptide hybrid complexes, in which a small Gd(III) complex is conjugated to a peptide or protein fragment, resulting in an increase in rotational correlation time and an enhancement in relaxivity.^{127,128} An example of this is the small molecule CA [Gd(MS-325)] (gadofosveset trisodium), a derivative of [Gd(DTPA)]²⁻, which is designed to bind to HSA, thereby increasing the rotational correlation time.^{40,46} When conjugated to HSA, the observed relaxivity was 42.0 mM⁻¹ s⁻¹ (at 20 MHz). This can be compared to the relaxivity of [Gd(MS-325)] in PBS which is 6.6 mM⁻¹ s⁻¹ under the same conditions.¹⁵ This represents a 7 times increase in relaxivity.⁴⁰

In other work,¹²⁹ a Gd(III) binding site was engineered onto the surface of a rat cell adhesion protein. The Gd(III) complex showed promising MRI relaxivity with $q = 2$. Additionally, the protein had a slow rotational correlation time of 10 ns, giving a high relaxivity for the protein complex.¹²⁹

3.2 Aims

It has previously been reported that the MB1 series of Gd(III) coiled-coils display promising MRI relaxivity,⁹⁷ and that the introduction of the Gd(III) binding site towards the N-terminus, Gd(MB1-1)₃, yielded the highest relaxivity complex ($r_1 = 9.9 \pm 1.5 \text{ mM}^{-1} \text{ s}^{-1}$, $r_2 = 88.3 \pm 16.8 \text{ mM}^{-1} \text{ s}^{-1}$ at 7 T) by increasing q to 3.⁹⁵ This second generation design was adopted for subsequent optimisation, specifically to evaluate whether the dependence of relaxivity on molecular rotation could be exploited to further modulate the MRI efficiency of the Gd(III) complex. A series of three peptides based on the MB1-1 design; MB1-1S, MB1-1 (original design⁹⁵) and MB1-1L, were studied in order to investigate the importance of peptide length and rotational correlation time on MRI relaxivity.

With the Gd(III) binding site located at the N-terminus, the shorter (MB1-1S) and longer (MB1-1L) designs were achieved by removal or addition of a heptad at the C-terminus, see Figure 3.1 and Table 3.1. By altering the length of the peptide, the role of rotational correlation time of Gd(III) coiled-coils on MRI relaxivity could be interrogated. This could provide insight into the mechanism of this class of Gd(III) coiled CA.

Table 3.1: The peptide names and sequences used in this chapter

| Peptide | Sequence |
|---------|---|
| MB1-1S | Ac – G IAAN <u>EW</u> K <u>D</u> AAIEQK IAAIEQK IAAIEQK G – NH ₂ |
| MB1-1 | Ac – G IAAN <u>EW</u> K <u>D</u> AAIEQK IAAIEQK IAAIEQK IAAIEQK G – NH ₂ |
| MB1-1L | Ac – G IAAN <u>EW</u> K <u>D</u> AAIEQK IAAIEQK IAAIEQK IAAIEQK IAAIEQK G – NH ₂ |

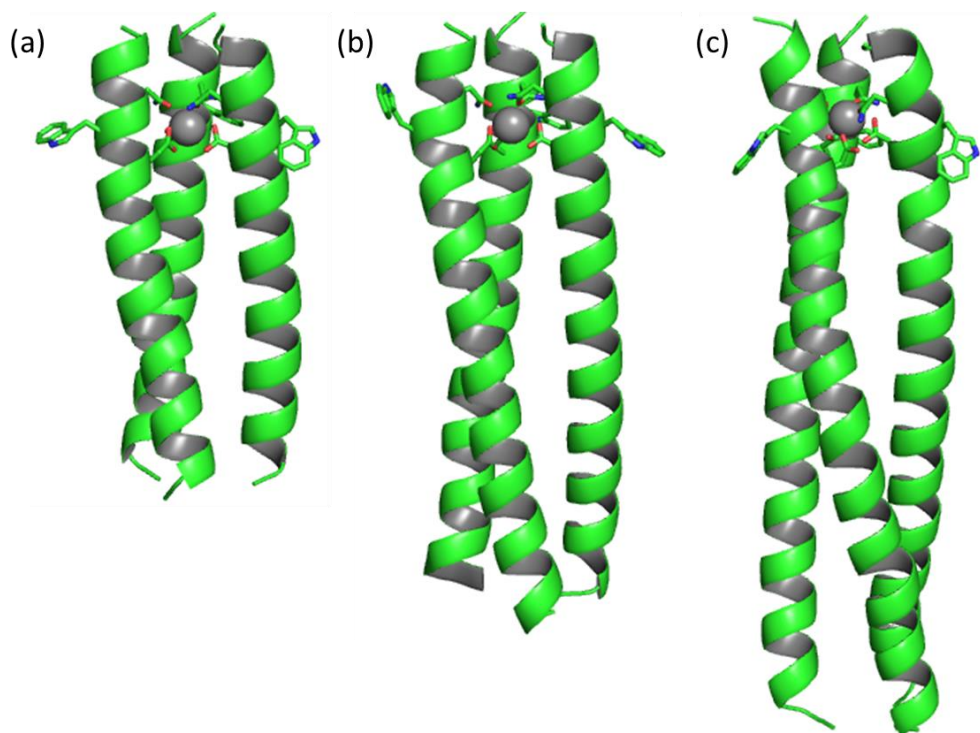


Figure 3.1: Schematic diagram of (a) MB1-1S, (b) MB1-1 and (c) MB1-1L. The peptide backbone is represented as a cartoon, binding site (Asn, Asp) and sensitizer (Trp) shown as sticks and Ln(III) as a sphere.

3.3 Results and Discussion

3.3.1 Secondary Structure

It was first of interest to investigate how the secondary structure of the peptide was affected when the length of the peptide was changed. Secondary peptide structure refers to the regular structure of the peptide backbone. This can be defined as α -helical or a β -sheet and is stabilised by hydrogen bonding. The secondary structure of MB1-1S, MB1-1 and MB1-1L was investigated using CD spectroscopy. A 30 μ M solution of MB1-1L monomer forms an α -helical coiled-coil, represented by the intense minimum at 208 and 222 nm in the CD spectrum, see Figure 3.2(c). The intensity at 222 nm ($\Theta_{222} = -31992 \text{ deg dmol}^{-1} \text{ cm}^2$), which is an indication of the extent of folding, is consistent with that of a well-folded α -helical coiled-coil peptide ($84 \pm 2\%$).

In contrast, MB1-1S yielded instead a CD spectrum more consistent with a poorly folded, random coil ($\Theta_{222} = -5928 \text{ deg dmol}^{-1} \text{ cm}^2$; $20 \pm 1\%$ folded), see Figure 3.2(a). This can be compared to the previously investigated MB1-1 which was calculated to be $80 \pm 6\%$ folded in the absence of metal.⁹⁵

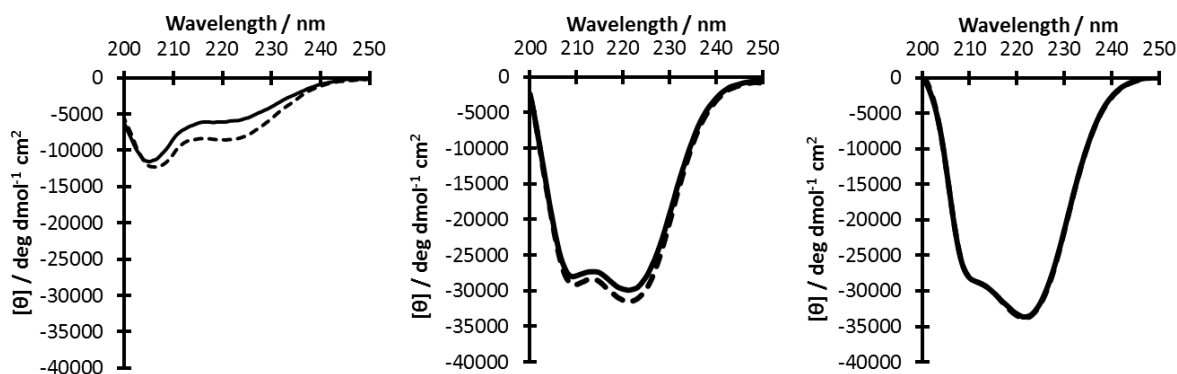


Figure 3.2: CD profile of 30 μM monomer peptide (a) MB1-1S, (b) MB1-1 and (c) MB1-1L in the presence (dashes) and absence (full) of 10 μM GdCl_3 ran in 10 mM HEPES buffer pH 7.0.

The addition of 10 μM GdCl_3 into a 30 μM MB1-1L monomer solution led to a very small increase in the negative intensity of the minimum at 222 nm ($\Theta_{222} = -33757 \text{ deg dmol}^{-1} \text{ cm}^2$, $85 \pm 2\%$). A greater change was observed with MB1-1S, with the resulting spectrum resembling more of an α -helix ($\Theta_{222} = -8470 \text{ deg dmol}^{-1} \text{ cm}^2$, $33 \pm 4\%$). This can again be compared to the previously investigated MB1-1 ($83 \pm 7\%$). The addition of a heptad, from five to six, has no significant impact on the degree of peptide folding, as determined from the CD spectra of MB1-1⁹⁵ and MB1-1L. This observation applies to both the apo state and in the metallo complex, with the degree of folding being the same within error. In comparison, MB1-1S remains poorly folded on addition of 1 equivalent of Gd(III).

Titration of aliquots of GdCl_3 (1 mM stock) into a 30 μM solution of MB1-1S monomer were monitored by CD, with the data shown in Figure 3.3(a). The addition of Gd(III) initially led to an increase in the negative minimum at 222 nm which then remained largely unchanged

on addition of higher equivalents. A $\frac{1}{3} \text{ Gd} + \text{MB1-1S} \rightleftharpoons \frac{1}{3} \text{ Gd}(\text{MB1-1S})_3$ binding model was used to analyse the data, giving an average association constant ($\log K_a$) of 4.4 ± 0.6 . This can be compared to the previously investigated MB1-1 where $\log K_a = 4.9 \pm 0.6$. Due to the negligible change in molar ellipticity of MB1-1L on addition of Gd(III), a binding constant could not be extrapolated.

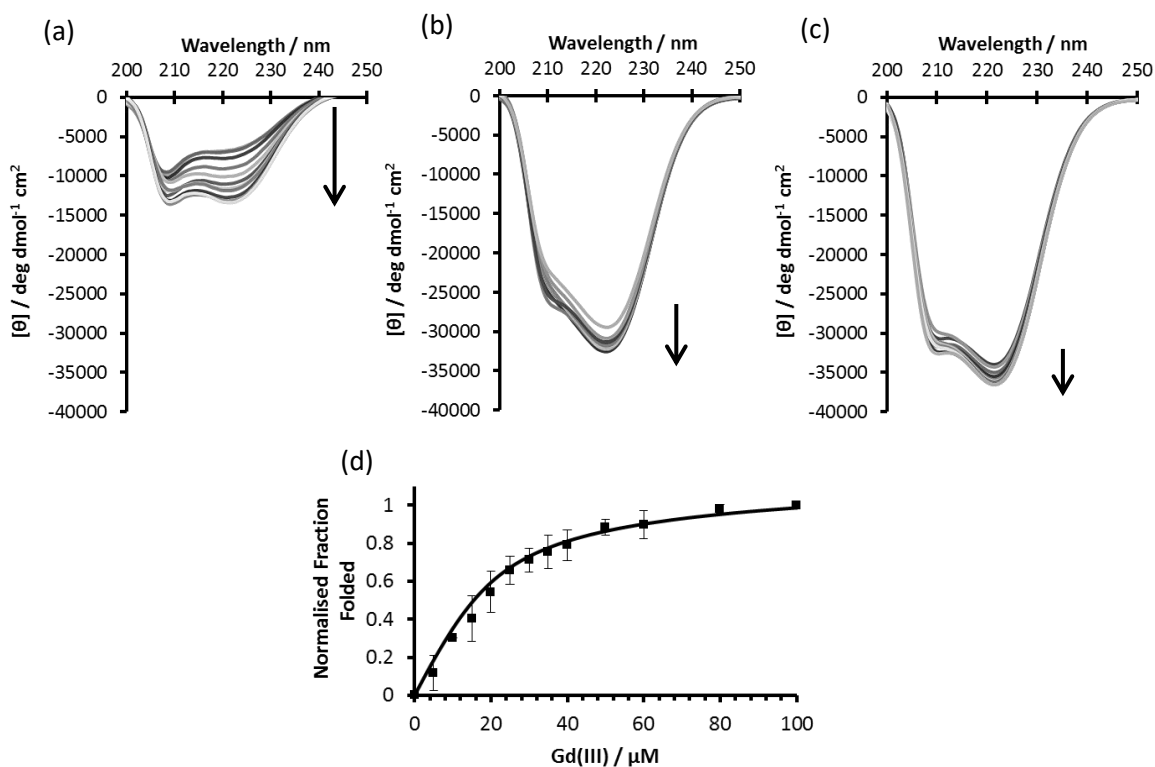


Figure 3.3: CD spectra of 100 μM (a) MB1-1S, (b) MB1-1 and (c) MB1-1L in the presence of increasing aliquots of Gd(III) in 10 mM HEPES buffer pH 7.0. (d) The normalised fraction folding of MB1-1S, analysed using a $\text{MB1-1S} + \frac{1}{3} \text{ Gd(III)} \rightleftharpoons \frac{1}{3} (\text{Gd}(\text{MB1-1S})_3)$ binding model, allowed for the calculation of a binding constant. Error bars are standard deviation for $n=3$ experiments.

It was previously reported by Berwick and co-workers that MB1-1 was the most well folded of the coiled coils which feature the Asn_3Asp_3 Gd(III) binding site (metallo $83 \pm 7\%$ folded)⁹⁵ and reasoned that the fifth heptad may not be essential. MB1-1S, which contains only four heptads, was found to be largely unfolded in the apo state (no more than 20% based

on the CD molar ellipticity at 222 nm), which only increased to 33% on addition of GdCl₃, suggesting that the 5th heptad is essential for a well folded coiled coil.

3.3.2 Ln(III) Binding

TbCl₃ titrations were monitored directly by luminescence. Due to Tb(III)'s low-lying excited states, which allow for emission in the visible spectrum, it can be used as a model for Gd(III) luminescence. A solution of 30 μM MB1-1L monomer was excited at 280 nm, and the emission spectrum monitored from 455 - 700 nm. Similar spectra were recorded on addition of aliquots of TbCl₃ (1 mM stock), and displayed the characteristic Tb(III) emission peaks at 490, 545, 585, 620, and 650 nm, see Figure 3.4(c). These increased in intensity on addition of up to one equivalent of Tb(III) per three strands of MB1-1L.

The region from 530 – 560 nm was integrated and plotted as a function of Tb(III) concentration. A $\frac{1}{3} \text{ Tb} + \text{MB1-1L} \rightleftharpoons \frac{1}{3} \text{ Tb}(\text{MB1-1L})_3$ binding model was used to interpret the data, giving an association constant ($\log K_a$) of 5.0 ± 0.2 . The experiment was repeated with MB1-1S giving a $\log K_a$ of 4.6 ± 0.2 and can be compared to the previously investigated MB1-1 for which a $\log K_a$ of 5.3 ± 0.1 was calculated, with the spectra shown in Figure 3.4.

Tb(III) luminescence experiments provide important insight into Ln(III) coordination chemistry. For MB1-1 and MB1-1L the data was consistent with one Ln(III) ion per trimer saturating the binding site with the same affinity (within error). This suggests binding affinity is independent of peptide length. It is important to note that this affinity ($\log K_a$ of 5.0) is significantly lower than current clinically adopted MRI CAs ($\log K_a$ of 18.8⁷¹), and hence, an improvement in K_a would be required prior to translation into a clinical setting.⁹⁵

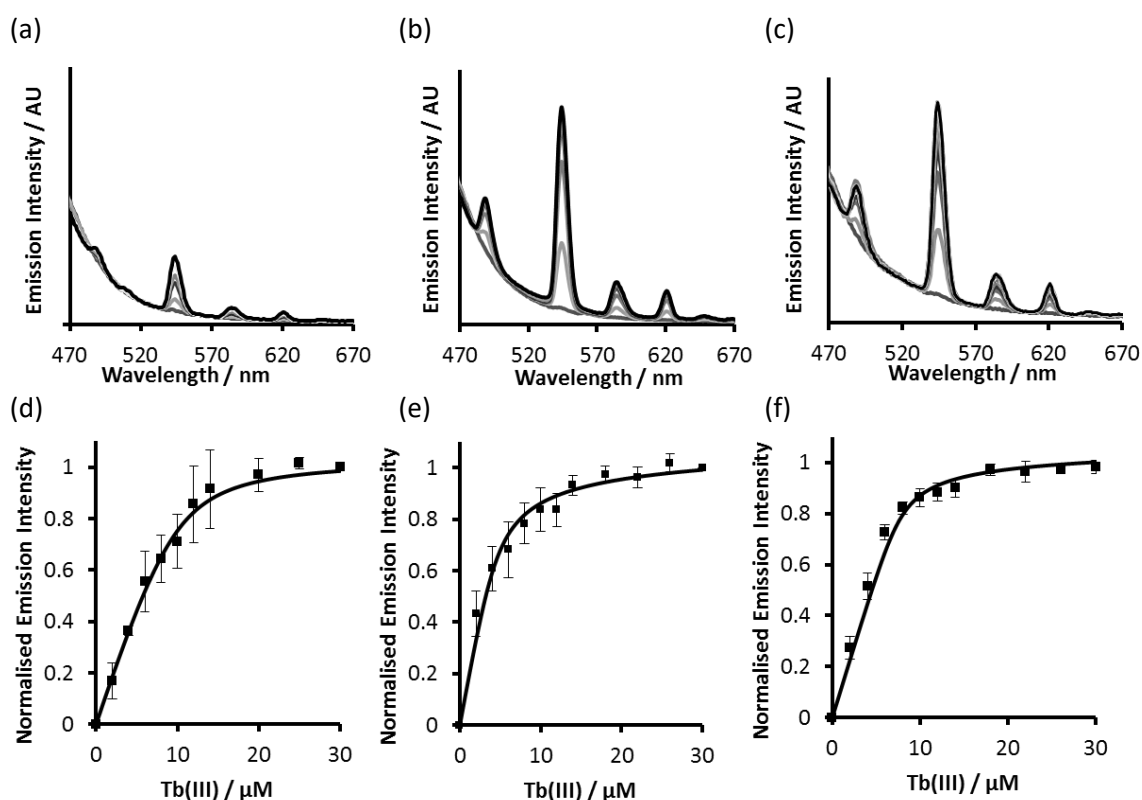


Figure 3.4: Emission profile of (a) MB1-1S, (b) MB1-1 and (c) MB1-1L recorded in the presence of increasing aliquots of Tb(III) in 10 mM HEPES buffer pH 70, using a $\lambda_{\text{exc}} = 280$ nm. The normalised integration of the 545 nm peak analysed using a peptide + $\frac{1}{3}$ Gd(III) \leftrightarrow $\frac{1}{3}$ (Gd(peptide)₃) binding model, allowed for the calculation of a binding constant for (d) MB1-1S (e) MB1-1 and (f) MB1-1L.

Error bars are standard deviation for n=3 experiments.

For the metallo MB1-1S system, the lack of substantial folding recorded in the CD experiments was accompanied by only a small luminescence enhancement on addition of Tb(III). Although this is consistent with some binding, this could be non-specific, including to Glu residues intended for salt bridge formation, some of which are located in close proximity to the Trp sensitiser. The binding constant is similar to that of the longer peptides, despite the fact that MB1-1S is poorly folded.

3.3.3 Peptide Stability

CD spectroscopy was used to compare the stability of MB1-1S, MB1-1 and MB1-1L, by both thermal and chemical denaturation. 30 μM solutions of peptide monomer in the absence and presence of 10 μM GdCl_3 were subjected to a gradual increase in temperature from 25 to 85°C, and the CD signal at 222 nm recorded as an indication of peptide folding, with the data shown in Figure 3.5.

The MB1-1S apo peptide was found to be only 20% folded at 25°C, which remained unchanged over the measured temperature range and is more consistent with the signal contribution of an unstructured peptide. The metallo MB1-1S complex was 29% folded at 25°C and decreased in folding to 20% at 85°C. In contrast, MB1-1L decreased in folding by approximately 30% (from 83% to 58% apo and 86% to 58% metallo) when the temperature reached 85°C, but never reached an unfolding baseline. When comparing MB1-1L to MB1-1, the thermal unfolding profiles show a gradual decrease in folding over a 60°C range. Importantly both the $\text{Gd}(\text{MB1-1})_3$ and $\text{Gd}(\text{MB1-1L})_3$ complexes remain largely folded at biologically relevant temperatures (37°C).

When analysing peptide stability, it can be concluded that MB1-1S has poor stability with respect to thermal unfolding studies, which show it to be entirely unfolded even in the presence of $\text{Gd}(\text{III})$, at 55°C. In MB1-1S, the binding site is located at the N-terminus. This was previously found to be the most tolerated position for the binding site and yielded the most folded five heptad coiled coil.⁹⁵ In MB1-1S, the destabilising effect of the Asn and Asp layers, which interrupt two heptads, cannot be overcome by the remaining two intact heptads. It can be concluded that a minimum of five heptads are required for the folding of coiled coils which feature a Asn_3Asp_3 binding site, even in the presence of $\text{Ln}(\text{III})$. Intriguingly, all of the $\text{Ln}(\text{III})$ coiled-coils that have been reported to date consist of five heptads, which may imply

that the fifth heptad is required to overcome the destabilising negative charges of the Ln(III) binding site.^{80,81,95,97,114} These findings are somewhat in contrast with other metallo coiled-coils, including the work of Pecoraro and co-workers who have found that Cys₃ binding sites for Hg(III) and Cd(III) coordination are well tolerated within coiled coils consisting of four heptads, and that metal binding can even induce folding for shorter peptides consisting of three heptads.^{91,130}

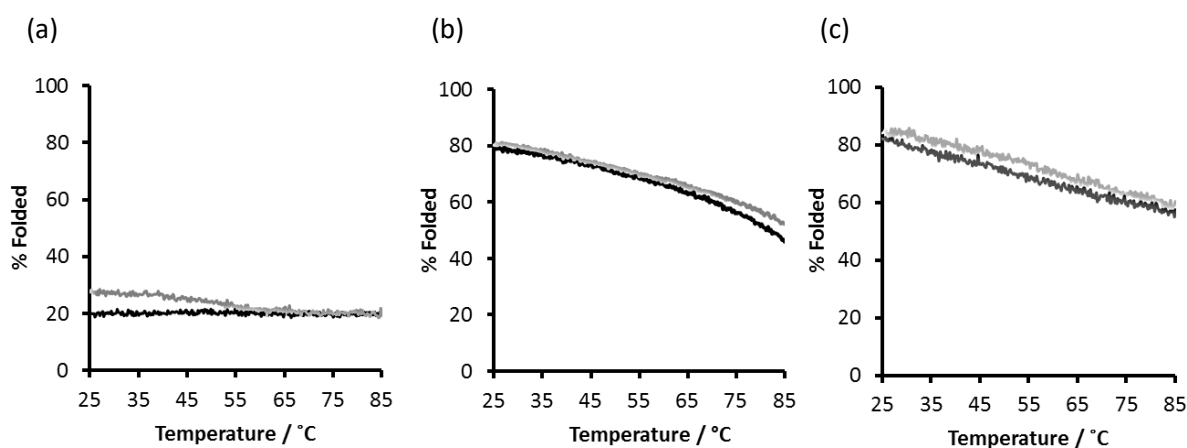


Figure 3.5: Percentage folded data from CD thermal unfolding of 30 μM (a) MB1-1S, (b) MB1-1 and (c) MB1-1L monomer in the absence (dark) and presence (light) of 10 μM GdCl_3 in 10 mM HEPES buffer pH 7.0.

Chemical denaturation showed the folding of MB1-1L, and the previously investigated MB1-1, to decrease in the presence of 6 M guanadinium hydrochloride (Gua-HCl), when monitored by CD, as shown in Figure 3.6. When the Gua-HCl concentration increased, a decrease in signal at 222 nm was observed. This occurred in solutions containing 30 μM peptide monomer, in both the absence and presence of 10 μM GdCl_3 . A difference in percentage folding between the two peptides was observed at 6 M Gua-HCl with MB1-1 being completely unfolded (17%) in the apo and metallo complexes whilst MB1-1L remained somewhat folded (38%).

A two-state equilibrium model between folded trimer and unfolded monomer was used to interpret the data. Extrapolation of the data yielded free energies of folding, ΔG°_{H2O} , of 18.2 ± 3.5 kcal mol⁻¹ and 21.6 ± 2.5 kcal mol⁻¹ for apo MB1-1 and MB1-1L, and 17.8 ± 1.5 kcal mol⁻¹ and 21.8 ± 5.6 kcal mol⁻¹ for Gd(MB1-1)₃ and Gd(MB1-1L)₃, respectively, displaying no increase in stability, within the error of the experiment.

The ΔG°_{H2O} data for MB1-1 and MB1-1L suggests that the additional 6th heptad does not induce further coiled coil stability in the apo or metallo systems. However, in the work by other groups it has been reported to enhance stability with respect to denaturation, by 5-9 kcal mol⁻¹.^{71,109}

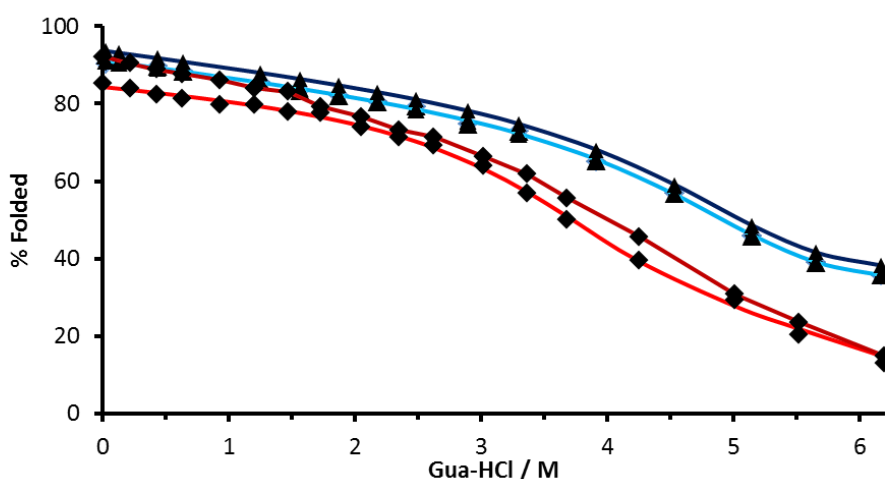


Figure 3.6: Percentage folded data from CD chemical unfolding of 30 μ M MB1-1 (diamond, red) and MB1-1L (triangle, blue) monomer in the absence (light) and presence (dark) 10 μ M GdCl₃, in 10 mM HEPES pH 7 buffer. Concentration of Gua-HCl was increased between 0 and 6 M and the signal at 222 nm monitored.

3.3.4 Ca(II) Displacement

Many Ln(III) binding sites evolve from native Ca(II) binding sites and although not designed for Ca(II), it was of interest to see if Ca(II) could bind or displace Ln(III) from the site. This is of particular significance due to the large quantities of Ca(II) in the body .

First a sample of 30 μM peptide monomer was run with integration of the spectra giving a base value for 0% Tb(III) binding. 10 μM Tb(III) was added to the above sample and left to equilibrate for 20 minutes before measuring. Integration of this spectrum gave a value representative of 100% Tb(III) binding. Ca(II) in aliquots of 10 μM , 100 μM , 1 mM and 10 mM was added to individual samples and left to equilibrate for 20 minutes. By integrating each spectrum and comparing to the 0% and 100% Tb(III) binding controls, the percentage of Tb(III) binding could be calculated for each sample. The average of three experiments with standard deviation error bars is shown in Figure 3.7. A decrease in Tb(III) binding was observed for all three peptides on addition of Ca(II). The largest decrease was observed for MB1-1S, which could be due to its unfolded structure and the increased accessibility of the Ln(III) binding site. Both MB1-1 and MB1-1L showed a negligible reduction in Tb(III) binding when there was a 1:1 ratio of Tb(III):Ca(II) and a 10 - 30% reduction after the addition of 100 μM Ca(II) (1:10 ratio). This increased to a maximum of 80% displacement on addition of 10 mM Ca(II).

This amount of displacement could be due to the binding site being positioned at the N-terminus of the coiled coil, making it more labile compared to if it was in the middle heptads. This could be concerning as it demonstrates that Gd(III) could be displaced by Ca(II) in the body, causing the release of highly toxic Gd(III). This, along with the binding constants, shows that the stability of the complex needs to be improved before the use of these probes *in vivo*. This could be achieved by cross linking the peptide strands so that Gd(III) is held more tightly in place within the Ln(III) binding site.

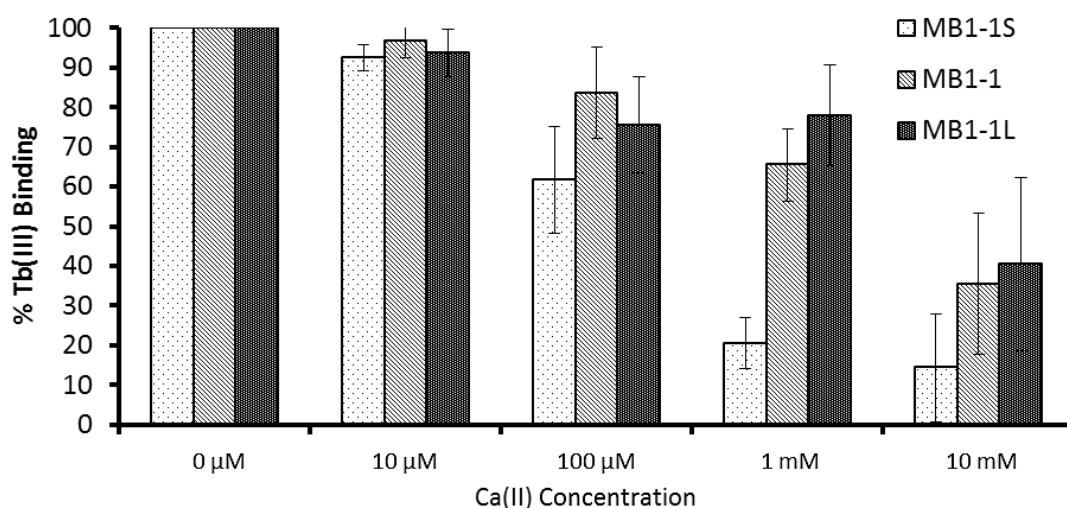


Figure 3.7: Bar chart showing percentage of Tb(III) remaining bound following Ca(II) displacement studies with MB1-1S, MB1-1 and MB1-1L. 30 μM peptide monomer and 10 μM Tb(II), in 10 mM HEPES buffer pH 7.0, in the presence of 10 μM, 100 μM, 1 mM and 10 mM Ca(II).

3.3.5 Water Coordination

The coordination environment of the metallo peptides was characterised further by establishing the amount of inner-sphere water coordinated to Tb(III) when bound to MB1-1S, MB1-1 and MB1-1L. Tb(III) luminescence decay lifetimes in H₂O and D₂O were used to probe the amount of inner-sphere water coordinated to Tb(III) when bound to MB1-1S and MB1-1L, with the data shown in Figure 3.8. The luminescence lifetime decays of MB1-1S and MB1-1L at 545 nm were recorded as 1.4 ± 0.2 ms in H₂O and 0.7 ± 0.3 ms in D₂O for MB1-1S and 1.5 ± 0.3 ms in H₂O and 0.6 ± 0.2 ms in D₂O for MB1-1L.

In order to correct for the contribution of outer sphere water, the Parker-Beeby equation¹¹⁶ was applied and it was found that primary water coordination remains largely unchanged for the three peptides ($q = 3.5 \pm 0.5$, 3.1 ± 0.2 ⁹⁵ and 3.7 ± 0.7 , for MB1-1S, MB1-1 and MB1-1L, respectively).

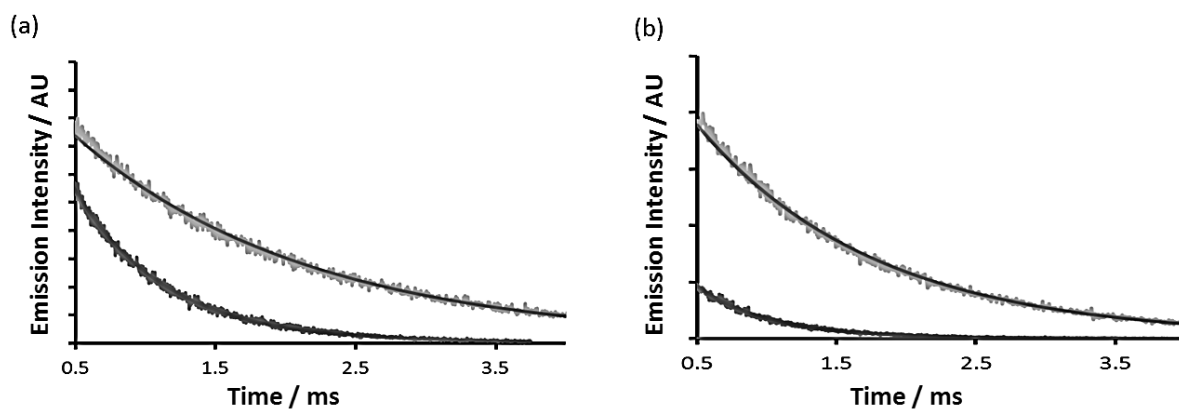


Figure 3.8: Representative decay profiles of Tb(III) emission at 545 nm for 100 μM peptide monomer (a) MB1-1S and (b) MB1-1L on addition of 10 μM of Tb(III) in 10 mM HEPES buffer pH 7.0, recorded in both H₂O (light) and D₂O (dark) fit to a mono-exponential decay allowing for calculation of q values.

The similar hydration states of MB1-1 and MB1-1L are proposed to be due to the fact that the addition and removal of a heptad at the C-terminus does not have a significant impact on coiled-coil stability, Ln(III) affinity and coordination chemistry, and is unlikely to impact on water penetration and coordination. As the additional heptad has been introduced at the C-terminus, and the Tb(III) binding site is located at the N-terminus, it is unlikely that the binding site will be sensitive to subtle structural changes at the C-terminus (*c.a.* 5 nm away). Despite MB1-1S being unfolded in the metallo form, the q value remains the same, within error, as the two longer peptides.

3.3.6 Relaxivity and MRI Contrast Agent Efficiency

In order to establish if changing the length of the peptide affects relaxivity, the longitudinal (T_1) and transverse (T_2) relaxation times of water protons were investigated at 7 T and 1 T, in the presence of increasing concentrations of Gd(MB1-1S)₃, Gd(MB1-1)₃ and Gd(MB1-1L)₃, with the data shown in Figures 3.9 and 3.10, respectively.

An increase in the concentration of the Gd(III) complex leads to a decrease in both the T_1 and T_2 relaxation times for all peptides. The relaxivities were found to be (r_1) 11.4 ± 1.5 and (r_2) $71.0 \pm 3.6 \text{ mM}^{-1} \text{ s}^{-1}$ for MB1-1S and (r_1) 10.9 ± 0.8 and (r_2) $81.8 \pm 5.4 \text{ mM}^{-1} \text{ s}^{-1}$ for MB1-1L at 7 T. These can be compared to the values previously reported for MB1-1 (r_1) 9.9 ± 1.5 and (r_2) $88.3 \pm 16.8 \text{ mM}^{-1} \text{ s}^{-1}$.⁹⁵ This demonstrated that the change in peptide length is not significant enough to cause in a change in relaxivity between MB1-1 and MB1-1L. The relaxivity of MB1-1S was lower than the two longer peptides, which may be due to the lack of folding.

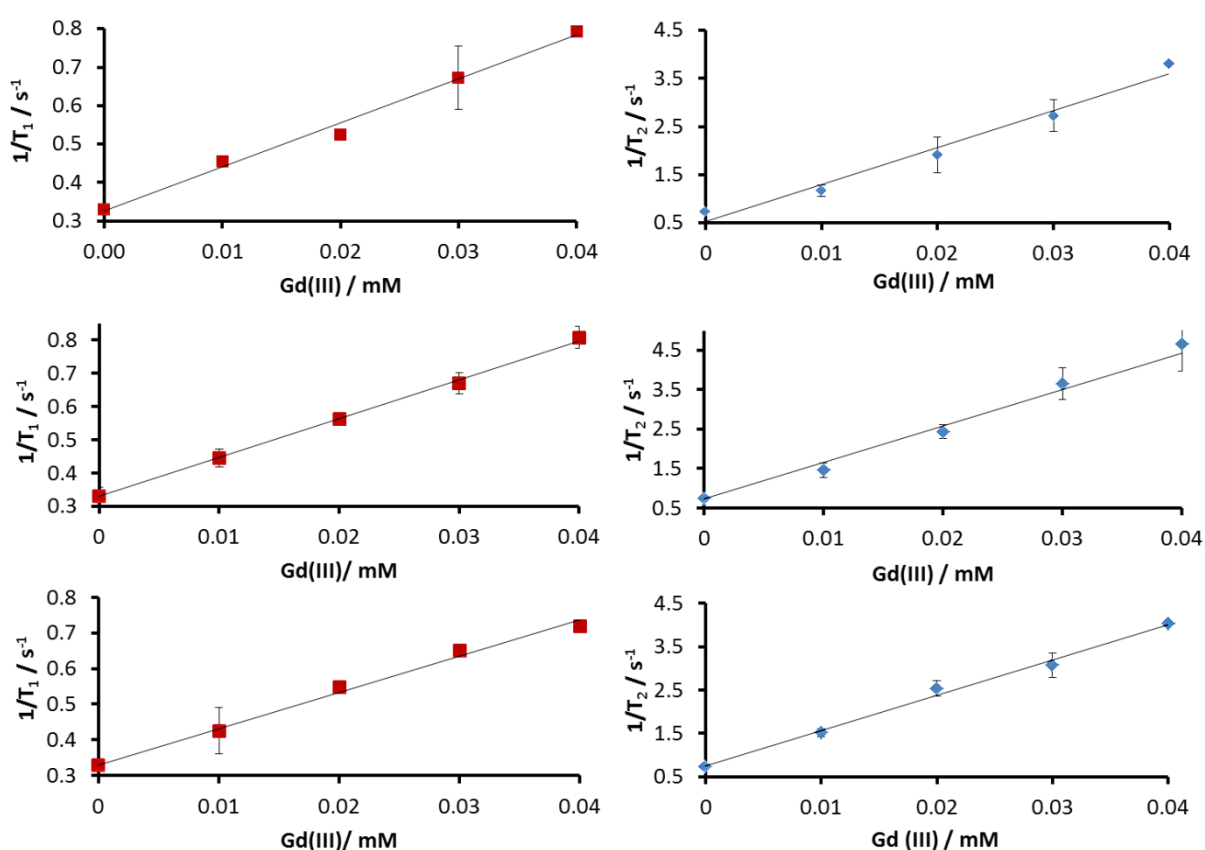


Figure 3.9: Relaxivity plots of relaxation rates showing reciprocal of relaxation time as a function of Gd(III) concentration for T_1 (left) and T_2 (right) for (top) MB1-1S, (middle) MB1-1⁹⁵ and (bottom) MB1-1L. All samples recorded at 7 T at 298 K in the presence of 10 mM HEPES buffer pH 7.0, with two equivalences of peptide trimer to Gd(III). Error bars show standard deviations from data repeated in triplicate.

T_1 and T_2 measurements were conducted at a lower field (1 T), for the two well-folded peptides (MB1-1 and MB1-1L), in order to assess if the effect of peptide size had more of an impact at lower field strengths. This is because rotational correlation time has previously been shown to have a larger impact on r_1 at low fields.⁴⁰ An increase in Gd(III) coiled-coil concentration led to relaxivities of (r_1) 64.3 ± 3.2 and (r_2) 87.6 ± 0.9 $\text{mM}^{-1} \text{s}^{-1}$ for MB1-1, and (r_1) 67.4 ± 4.2 and (r_2) 96.5 ± 3.2 $\text{mM}^{-1} \text{s}^{-1}$ for MB1-1L, with the data shown in Figure 3.10.

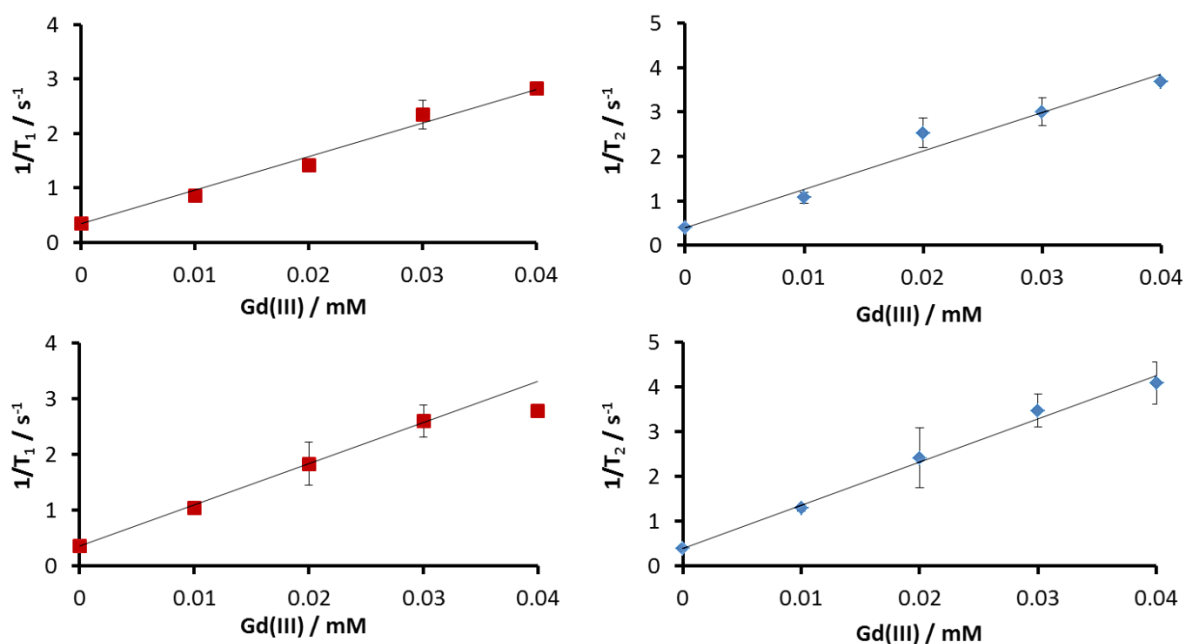


Figure 3.10: Relaxivity plots of relaxation rates showing reciprocal of relaxation time as a function of Gd(III) concentration for T_1 (left) and T_2 (right) for (top) MB1-1 and (bottom) MB1-1L. All samples recorded at 1 T at 298 K in the presence of 10 mM HEPES buffer pH 7.0, with two equivalences of peptide trimer to Gd(III). Error bars show standard deviation.

Again little difference is observed between $\text{Gd}(\text{MB1-1})_3$ and $\text{Gd}(\text{MB1-1L})_3$. When comparing relaxivity data at the lower, and more clinically relevant field strength (1 T) with the higher field strength (7 T), the most notable difference is that the longitudinal relaxivity (r_1) significantly increases (MB1-1 = 11.7 ± 1.5 to 64.3 ± 3.2 $\text{mM}^{-1} \text{s}^{-1}$, MB1-1L 10.9 ± 0.8 to 67.4 ± 4.2 $\text{mM}^{-1} \text{s}^{-1}$). It is well understood that r_1 typically increases at low fields for large complexes

with slow rotational correlation time.⁴⁰ For example, small and rapidly tumbling Gd(III) complexes, such as MS-325, show only a small increase in r_1 on lowering the field strength, from $5.2 \text{ mM}^{-1} \text{ s}^{-1}$ at 9.4 T to $8.3 \text{ mM}^{-1} \text{ s}^{-1}$ at 1.4 T. This is in contrast with the slow tumbling analogue formed on binding to HSA, where an increase from $7.2 \text{ mM}^{-1} \text{ s}^{-1}$ at 9.4 T to $24.3 \text{ mM}^{-1} \text{ s}^{-1}$ at 1.4 T is observed. This is due to molecular tumbling becoming more significant at low fields.⁴⁰ In contrast, r_2 remains largely unchanged with changing field strengths, and, if anything, increases with increasing field strength.^{40,46} This is because Gd(III) magnetises linearly and the susceptibility effects of Gd(III) are higher with increasing field strength and this results in greater r_2 at high fields.⁴⁰

3.3.7 Prediction of the Rotational Correlation Time

As part of a collaboration with Dr Smith, School of Maths, University of Birmingham, hydrodynamic calculations, based on the equations by Kim and Karrila,¹³¹ were performed to calculate a theoretical rotational correlation time of MB1-1S, MB1-1 and MB1-1L. This method has previously been used to model prolate spheroids and applied to the Olfactory Marker Protein, a globular protein, and a bacteriorhodopsin fragment in which all residues experience nanosecond timescale motions,^{132,133} and is described in more detail by Holde *et al.*¹³⁴ Rotational correlation times of 4.6, 6.9 and 10.0 ns were calculated for MB1-1S, MB1-1 and MB1-1L, respectively. This shows that the addition of a heptad theoretically increases the rotational correlation time by 2-3 ns. Relaxivity will reach a maximum when the correlation time is the inverse of the proton Larmor frequency. For a 1.5 T imaging spectrometer, as used clinically, the optimum τ_c is 2.5 ns and the optimum value for τ_m is about 10 ns.¹⁵ When comparing to the MB1 peptides, MB1-1L is closest to this optimum value for low field imaging.

3.3.8 Prediction of the Water Residence Time

Calculations derived from the SBM equations were written, as shown in Appendix A9, and run in MATLAB¹³⁵ for the two stable and well folded coiled-coils, MB1-1 and MB1-1L. The theoretical longitudinal relaxivity was plotted as a function of water residence time, for both low (1 T) and high field strengths (7 T), with the data shown in Figure 3.11. In addition to the rotational correlation time, relaxivity is dependent on how the Gd(III) ion interacts with water molecules, including the number of bound water molecules, the water residency time and the Gd-water distance.

From the previously described Tb(III) lifetime experiments, it is assumed that Gd(MB1-1)₃ and Gd(MB1-1L)₃ coordinate Gd(III) in a very similar fashion, having a very similar (within error) number of coordinated water molecules. The two metallo complexes are assumed to differ primarily in their rotational correlation time in solution. From the predictive plot shown in Figure 3.11, it is observed that when $r_1 = 11 \text{ mM}^{-1} \text{ s}^{-1}$ (7 T) and $r_1 = 65 \text{ mM}^{-1} \text{ s}^{-1}$ (1 T), (an average of what was as calculated for Gd(MB1-1)₃ and Gd(MB1-1L)₃ experimentally) the water residency time is either extremely short, or extremely long, being located on either extreme of the predictive curves. At 7 T the water residency time is calculated to be either 0.5 ns or 3000 ns for both Gd(MB1-1)₃ and Gd(MB1-1L)₃. At 1 T the water residency time is calculated to be either 6 ns or 500 ns for both Gd(MB1-1)₃ and Gd(MB1-1L)₃. The short values (0.5 and 6 ns) would be consistent with values reported for water coordinated to free Gd(III) in aqueous solution (1 ns)¹⁷, whereas the longer value is more in line with what has been reported for small molecule Gd(III) complexes, such as [Gd(DTPA)]²⁻ (gadopentetic acid/ Magnevist), bound to a protein complex (1000 ns).¹⁵

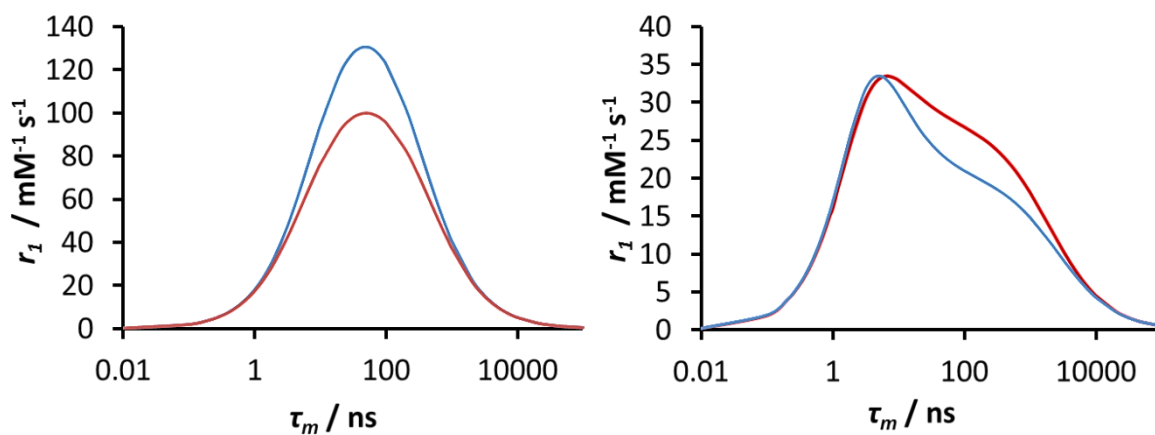


Figure 3.11: Effect on r_1 with changing water residency time τ_m (ns), for a $q=3$ system, on r_1 at field strengths of (a) 1 T and (b) 7 T, with rotational correlation times of 6.9 ns corresponding to MB1-1 (red) and 10.0 ns corresponding to MB1-1L (blue).

3.3.9 Experimental Water Residence Time in $\text{Gd}(\text{MB1-1})_3$

Variable temperature ^{17}O NMR is a technique used to provide information regarding water residence time and water exchange. The technique works by measuring the exchange rate of the oxygen atom of water and can provide information on the chemical exchange mechanism. Transverse relaxation rates are measured using a CPMG pulse sequence and the relaxation data interpreted using SBM theory and the Swift and Connick Equations.¹³⁶

In order to establish which scenario was most likely, as part of a collaboration with Dr. Ivanovic-Burmazovic at Friedrich-Alexander-Universität, Germany, ^{17}O NMR was used to calculate the water residence time for $\text{Gd}(\text{MB1-1})_3$ which was found to be very short (1.56 ns) and of the same order of magnitude as that measured for 9-coordinated $\text{Gd}(\text{III})$ aqua complex (1.02 ns). This is similar to the rapid water residency times (0.5 and 6 ns) predicted in Figure 3.11.^{20–22}

When looking at Figure 3.12, based on a fast water residency time of 1.56 ns, it is predicted that there will be very little difference in relaxivity of MB1-1 and MB1-1L at either 1 T or 7 T for the given rotational correlation times. In order to see a difference in relaxivity for

MB1-1 and MB1-1L it theoretically would be necessary to redesign the binding site to change the water residency time to between 7 – 300 ns. At a water residency time of 40 ns, it is calculated that the highest possible r_1 for this class of contrast agent will be observed at 1 T and the greatest difference between rotational correlation times of 6.9 and 10 ns will be observed at 7 T. Therefore, an analogue of MB1-1 with τ_m of 40 ns could be designed to achieve maximum r_1 at 1 T, and a difference in τ_R at both field strengths would be observed.

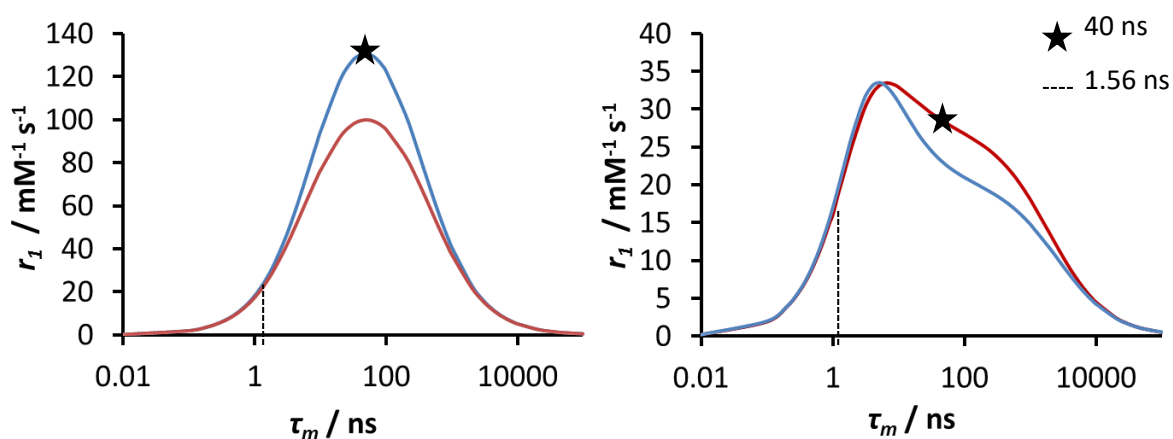


Figure 3.12: Effect on r_1 with changing water residency time τ_m (ns), for a $q=3$ system, on r_1 at field strengths of (a) 1 T and (b) 7 T, with rotational correlation times of 6.9 ns (red) and 10.0 ns (blue).

3.4 Conclusions

This study illustrates a number of key points about the MB1-1 series of Gd(III) coiled-coils. Firstly, a minimum of 5 heptads is required for successful coiled-coil folding, in the presence of a Ln(III) binding site. This is due to the de-stabilising nature of the negatively charged site being overcome with increased length. This was not achieved in MB1-1S where there were 4 heptads. For peptides consisting of 5 or 6 heptads, Ln(III) binding to a N-terminal site caused little change in structure, stability and coordination chemistry, as evident from CD and luminescence. This translated through to the MRI studies in which MB1-1 and MB1-1L exhibited the same r_1 and r_2 relaxivities at both 1 and 7 T. This study suggests that when considering the SBM equations the rotational correlation time is not the limiting factor for this

class of contrast agent at the magnetic field strengths used and as q remains constant, the water residency time must be limiting.

Water residency time was calculated using ^{17}O NMR and investigated using calculations to determine how relaxivity was affected when using different rotational correlation times. It was found that no difference in r_1 would be observed between MB1-1 and MB1-1L when $\tau_m = 1.56$ ns. By slowing τ_m to 40 ns it was predicted that a difference would be observed between the two peptides and r_1 would be at its maximum at 1 T. This could be further investigated using the MB1 series of peptides where the Ln(III) binding site is translated along the coiled coil, specifically with MB1-4 where $q = 2$. As the Ln(III) binding site is located further into the hydrophobic core, it would be predicted that the water residency time will be longer and may fall in the optimum window predicted in Figure 3.12. This will provide more information with regards to the importance of water residency time in this class of contrast agent and how it can impact relaxivity.

Chapter 4: Investigation of the Importance of Water

Coordination to the Exterior of a Coiled-Coil MRI Contrast

Agent

4.1 Introduction

In addition to inner-sphere water mechanisms, secondary sphere water mechanisms can contribute to relaxivity. This is defined as water which hydrogen bonds to inner-sphere water or the contrast agent (CA).⁴⁵ This second sphere is defined by the water residence time, which must be longer than the diffusional correlation time and can lead to a strong enhancement of the relaxivity of the CA.⁴⁵ Secondary sphere water is governed by the same parameters as inner-sphere water, as described by the SBM equations, and has previously been investigated using a number of different metal centres.¹³⁷⁻¹⁴⁰ The three defined hydration spheres (inner, secondary and outer) are compared in Figure 4.1.

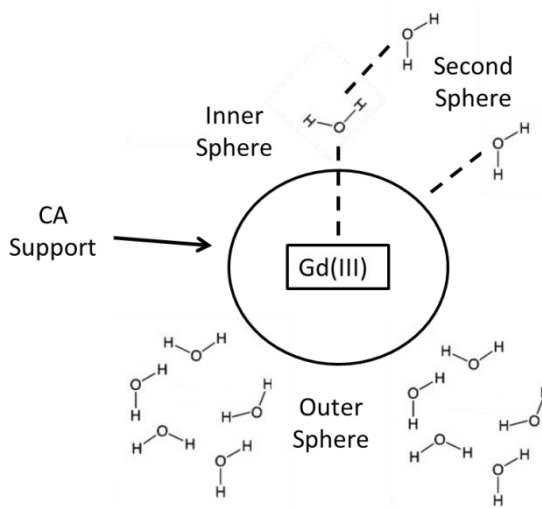


Figure 4.1: Schematic diagram to show the location of inner, second and outer sphere water molecules surrounding an MRI CA.

When investigating secondary sphere water for GdCAs there are three distinct features that must be considered for optimisation.⁴⁵ (1) The water residence time (τ_m) for current MRI CAs is two orders of magnitude longer than the optimal value. This is a major challenge for achieving high relaxivity.⁴⁵ (2) The metal to hydrogen distance (r_{MH}) values for inner-sphere water molecules show little variation amongst Ln(III) complexes with different charge, coordination number and hydration state. The distance of secondary sphere water is more varied and has previously been investigated between 3.2 and 4.5 Å. Due to the $1/r_{MH}^6$ dependence, control of this parameter is of high importance in order to obtain high relaxivities.⁴⁵ (3) Unlike in the inner-sphere, the number of water molecules located in the second sphere can increase without the number of donor atoms of the ligand changing and without hindering the stability of the complex.⁴⁵

Secondary sphere water plays a small role in the relaxivity of small molecule GdCAs, however, it is very important to consider for an accurate interpretation of relaxivity data and for a better understanding of the relationship between structure and relaxivity.⁴⁵ It has additionally been found that secondary sphere relaxivity has a direct impact on $q = 0$ complexes, such as MB1-2, where the relaxivity cannot be attributed to inner or outer sphere mechanisms. Instead it arises from exchangeable water in the second sphere.

There are a number of examples which highlight the importance of secondary sphere water, using a range of metals. Kushnir and Navon investigated water relaxation enhancement using Mn(II) bound to a series of macromolecules. They found an additional contribution to the inner-sphere r_1 mechanism, which dominated when analysed at high fields.¹³⁷ This additional contribution could not be explained by an inner or outer sphere mechanism. It was determined that the water molecules were located outside the inner-sphere with an average residency time of 0.3 ns, thus being defined as secondary sphere.¹³⁷ Oakes and Smith

investigated the relaxation properties of $[\text{Mn}(\text{EDTA})(\text{H}_2\text{O})]^{2-}$ and found secondary sphere contributions to be from four water molecules which were hydrogen bonded to four coordinated carboxylate groups. The metal-hydrogen distance was calculated to be 3.7 Å, close enough to have a significant impact on the overall relaxivity.¹³⁸ Merbach and co-workers reported a detailed computational and ^{17}O NMR investigation into the structure and dynamics of the second hydration sphere around a Cr(III) hexa-aqua ion. Thirteen water molecules were found to be located in the second sphere with an average lifetime of 128 ps, resulting in a large increase in relaxivity.^{139,140}

4.2 Aims

Secondary sphere water coordination was investigated with the MB1 peptide series. Through the careful selection of hydrogen bond acceptor groups on the ligand, there is the possibility to promote the formation of strong interactions between the CA and water, increase the number of water molecules located in the second hydration sphere and shorten their average distance from Gd(III), all attributing to an increase in relaxivity.⁴⁵ A peptide was designed, in order to compare to MB1-2,⁹⁷ with the potential to coordinate more water to its exterior. An increase in secondary sphere water coordination to the peptide exterior was hypothesised to result in an increase in relaxivity. By using a design where $q = 0$ any change to the relaxivity could be attributed to secondary sphere water interactions on the coiled-coil exterior. The peptides discussed in this chapter are the same length as MB1-1 in Chapter 3.

Table 4.1: Mo1-2 and MB1-2⁹⁷ peptide sequences. Additional lysine and glutamate residues in Mo1-2 are shown in bold and underlined.

| Peptide | Sequence |
|--------------|--|
| MB1-2 | Ac – G – IAAIEQK IAANEWK DAAIEQK IAAIEQK IAAIEQK – G – NH ₂ |
| Mo1-2 | Ac – G – <u>IKAIEEK</u> <u>IKENEWK</u> <u>DKAIEEK</u> <u>IKAIEEK</u> <u>IKAIEEK</u> – G – NH ₂ |

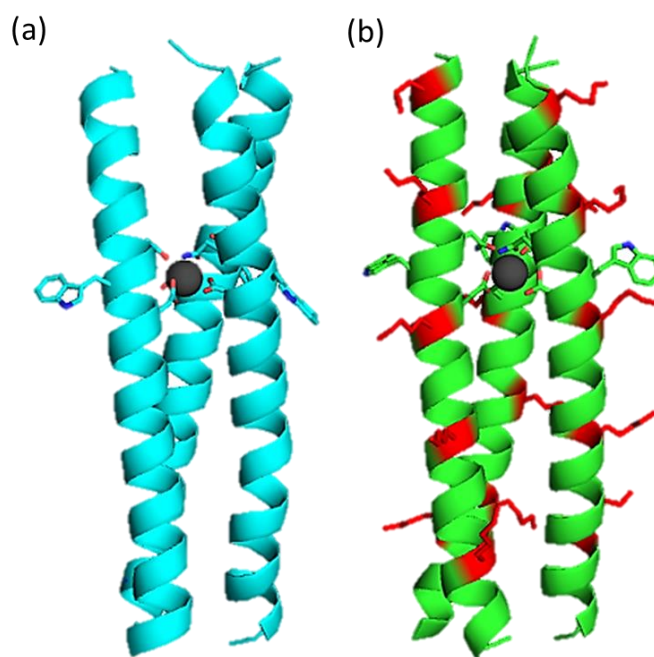


Figure 4.2: Schematic diagram of (a) MB1-2 and (b) Mo1-2. The peptide backbone is represented as a cartoon, binding site (Asn, Asp) and sensitiser (Trp) shown as sticks, additional Lys residues in Mo1-2 shown as red sticks and Ln(III) as a sphere.

The new peptide, Mo1-2, has additional lysine (K) residues, which have replaced alanine (A) residues, on its exterior in the **b** position, the sequence is compared to MB1-2 in Table 4.1 and the structures are compared in Figure 4.2. Mo1-2 was initially designed in collaboration with Muhammed Rassul as part of a PSIBS mini project. Alanine is known to be a helix-inducing amino acid, whereas lysine can hydrogen bond to water, has the ability to form salt bridges with polar amino acids on the other peptide chains within the coiled coil, and induces coiled-coil formation. Water can hydrogen bond to the NH_3^+ group of the lysine side chain, which could result in enhanced water coordination with the peptide, and has the potential for increased relaxivity. The glutamine (Q) residue at position **f** of the heptad was replaced with glutamate (E), in order to balance the charge of the lysine residues in the coiled coil. Polar residues such as glutamine and glutamate are known to help with solubility and can hydrogen bond to water through their polar side chains. The structures of these amino acids are shown in Figure 4.3.

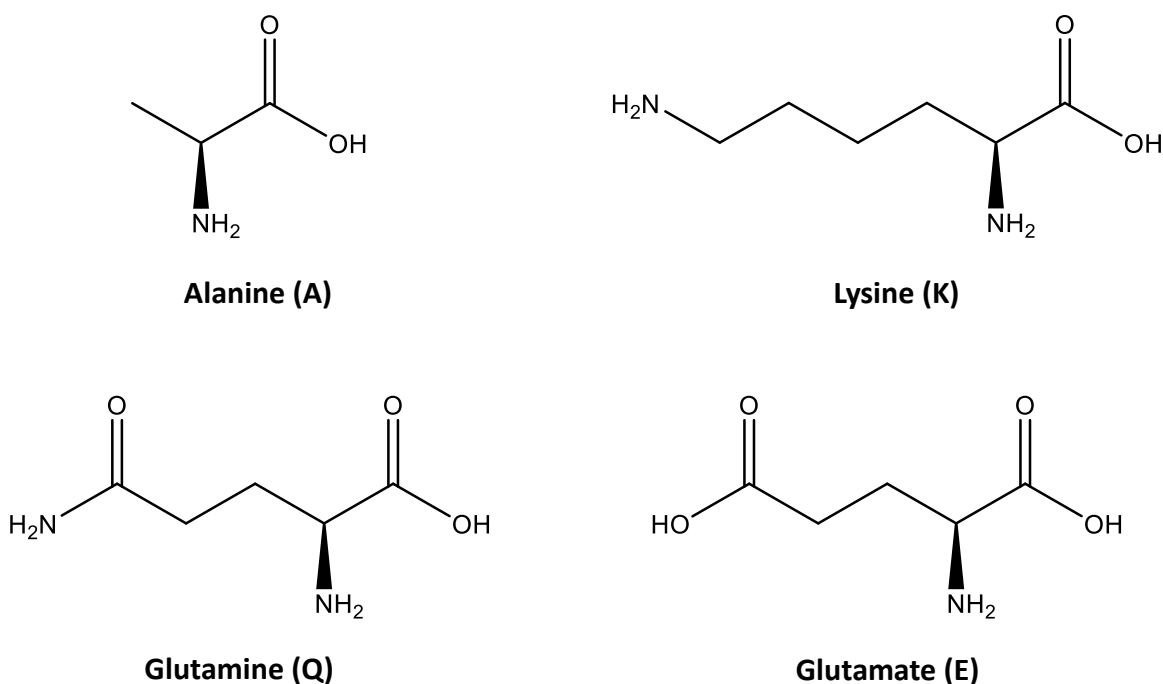


Figure 4.3: Amino acid substitutions in the newly designed Mo1-2 peptide.

A further consideration is the longer length of the lysine side chain, compared to that of alanine. Lysine has a number of rotamers which will increase the size of the major *b* axis (width), shown in Figure 4.4. This has the potential to reduce the rotational correlation time which in turn could increase the relaxivity. However, in this class of CA this would be unlikely as the rotational correlation time was concluded to not be a limiting factor in Chapter 3.

Secondary sphere water coordination in this chapter is described as water coordinated to the exterior of the coiled coil. It is important to consider that secondary sphere water can also be coordinated to the primary sphere water or within the hydrophobic core of the coiled coil. The location of the secondary sphere water coordinated to the exterior of Mo1-2 is much further away from Gd(III) than water coordinated to the primary sphere water, or within the hydrophobic core, which could mean it results in a smaller increase to relaxivity. The water residency time for secondary sphere water coordinated to the coiled-coil will be sufficiently faster than water coordinated to primary sphere water within the coiled-coil construct. This difference in water residency time will also impact how much the relaxivity will change.

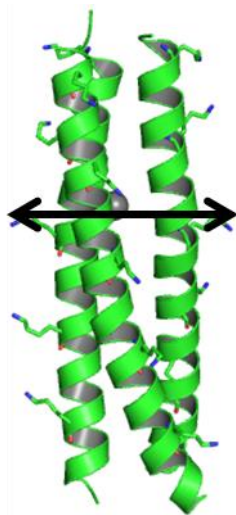


Figure 4.4: Introduction of lysine residues into a model of Mo1-2 increase the major *b* axis (shown in black). The peptide backbone is shown as a cartoon with the lysine residues displayed as sticks.

4.3 Results and Discussion

4.3.1 Secondary Structure

The secondary structure of Mo1-2 was experimentally determined using CD spectroscopy, with data shown in Figure 4.5. A 30 μM solution of Mo1-2 monomer forms a partially α -helical peptide, as is evident from the minimum at 208 and 222 nm in the CD spectrum. The intensity at 222 nm is consistent with a partially folded α -helical coiled-coil peptide ($\Theta_{222} = -9184 \text{ deg dmol}^{-1} \text{ cm}^2$, $27 \pm 4\%$). On addition of 10 μM GdCl_3 an increase in the intensity of the minimum at 222 nm is observed, with the spectrum now consistent with enhanced peptide folding ($\Theta_{222} = -22913 \text{ deg dmol}^{-1} \text{ cm}^2$, $66 \pm 8\%$).

This is very similar to the behaviour of MB1-2 where the intensity of the apo peptide represents some α -helical coiled-coil formation ($\Theta_{222} = -7460 \text{ deg dmol}^{-1} \text{ cm}^2$, $21 \pm 3\%$). On addition of 10 μM GdCl_3 the spectrum becomes more representative of a well folded coiled-coil ($\Theta_{222} = -21971 \text{ deg dmol}^{-1} \text{ cm}^2$, $62 \pm 3\%$). It can be concluded that the substitutions made to the coiled-coil exterior, caused no substantial change in folding, within the error of the

experiment. This is due to the Ln(III) binding site remaining in the same position within the hydrophobic core and the isoleucine residues that template the hydrophobic core remaining unchanged. A small decrease in folding could have been expected due to the strongly alpha-helix inducing alanine residues in MB1-2 being replaced with lysine residues, however, no change in folding was observed.

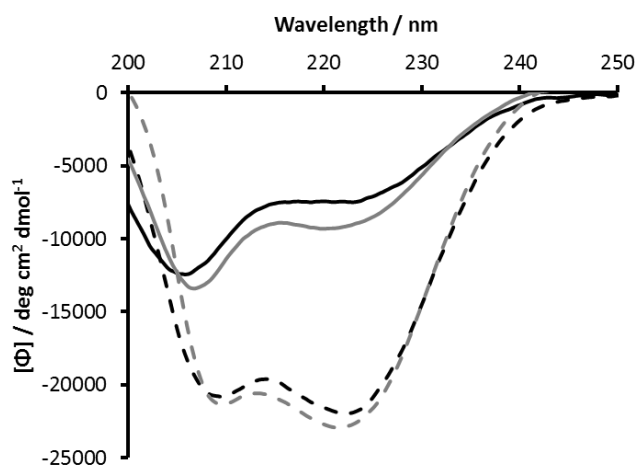


Figure 4.5: CD profile of 30 μM monomer peptide in the presence (dashed) and absence (solid line) of 10 μM GdCl_3 in 10 mM HEPES buffer pH 7.0, for MB1-2 (black line) and Mo1-2 (grey line).

4.3.2 Calculation of a Binding Constant using CD and Luminescence

Titration of aliquots of GdCl_3 into a 30 μM solution of Mo1-2 monomer were monitored by CD and led to a gradual increase in the signal at 222 nm which plateaued at higher equivalences, with the data shown in Figure 4.6. A $\frac{1}{3} \text{Gd} + \text{Mo1-2} \rightleftharpoons \frac{1}{3} \text{Gd}(\text{Mo1-2})_3$ binding model was used to interpret the data, giving an average association constant ($\log K_a$) of 5.3 ± 0.3 , however, it was found that the Mo1-2 data did not fit well to a 1:3 binding model.

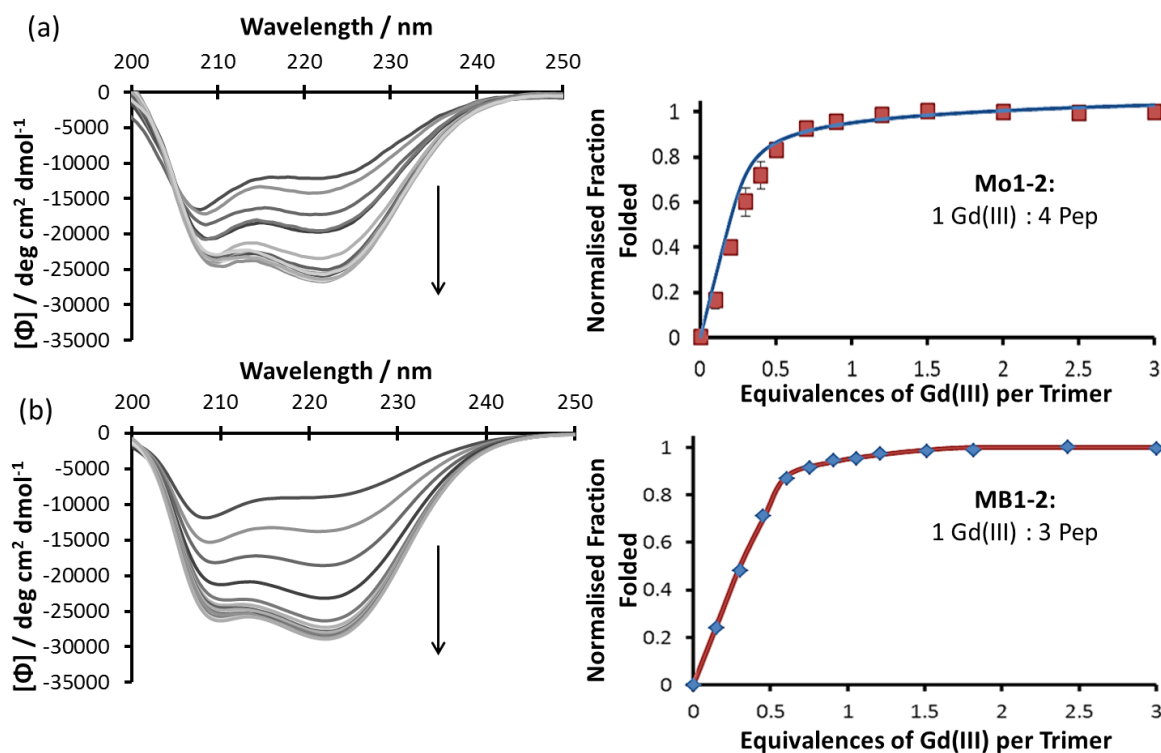


Figure 4.6: CD titration of 30 μM (a) Mo1-2, (b) MB1-2 with increasing aliquots of GdCl_3 in 10 mM HEPES buffer pH 7.0. The normalised fraction folding is shown to the right. Models for MB1-2 + $\frac{1}{3}\text{Gd(III)} \rightarrow \frac{1}{3}(\text{Gd}(\text{MB1-2})_3)$ and Mo1-2 + $\frac{1}{4}\text{Gd(III)} \rightarrow \frac{1}{4}(\text{Gd}(\text{Mo1-2})_4)$ were used, allowing the calculation of a binding constant. Error bars are standard deviation for $n=3$ experiments.

Because of this, 1:2 and 1:4 binding models were investigated. A binding constant for each stoichiometry was predicted, generating a theoretical fit, as shown in Figure 4.7. It was shown that the 1:4 prediction was the most similar to the experimental data. A 1:4 binding model was used to analyse the experimental data and yielded a $\log K_a$ of 4.0 ± 0.3 . It was unexpected that the new Mo1-2 peptide no longer had a 1:3 stoichiometry as no change to the trimeric inducing residues was made.

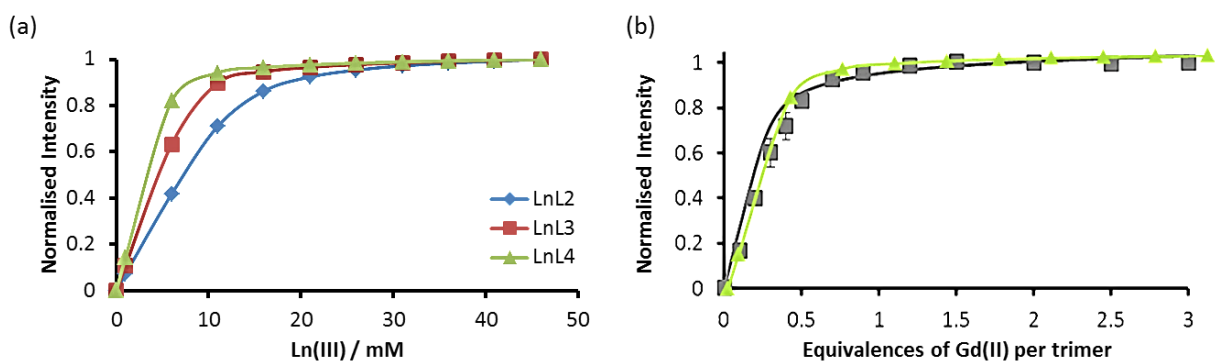


Figure 4.7: (a) Theoretical predictions for a 1:2, 1:3 and 1:4 stoichiometry, generated using ChemEQL Software.¹⁴¹ Ln(III) was used with ligands (L) with a -1 charge. An estimated binding constant of $\log K_a = 4.0$ was used in the calculation. (b) Overlay of 1:4 prediction (green) and experimental CD data (grey).

Tb(III) titrations were monitored directly by luminescence allowing for verification of the stoichiometry of Mo1-2, with the data shown in Figure 4.8. A solution of 30 μM Mo1-2 monomer was excited at 280 nm, and the emission spectrum monitored from 455 - 700 nm, with an increase in the intensity of the characteristic Tb(III) emission peaks displayed on the addition of Tb(III). The region from 530 – 560 nm was integrated and plotted as a function of Tb(III) concentration. A sharp increase followed by a plateau at a 1:4 equivalence was observed, representative of saturation of the binding site with Tb(III). A binding model of $\frac{1}{4} \text{Tb} + \text{Mo1-2} \rightleftharpoons \frac{1}{4} \text{Tb}(\text{Mo1-2})_4$ was used, giving an association constant ($\log K_a$) of 4.3 ± 0.6 . This can be compared to MB1-2 where $\log K_a$ was calculated to be 5.1 ± 0.2 using CD and 5.5 ± 0.2 using luminescence.

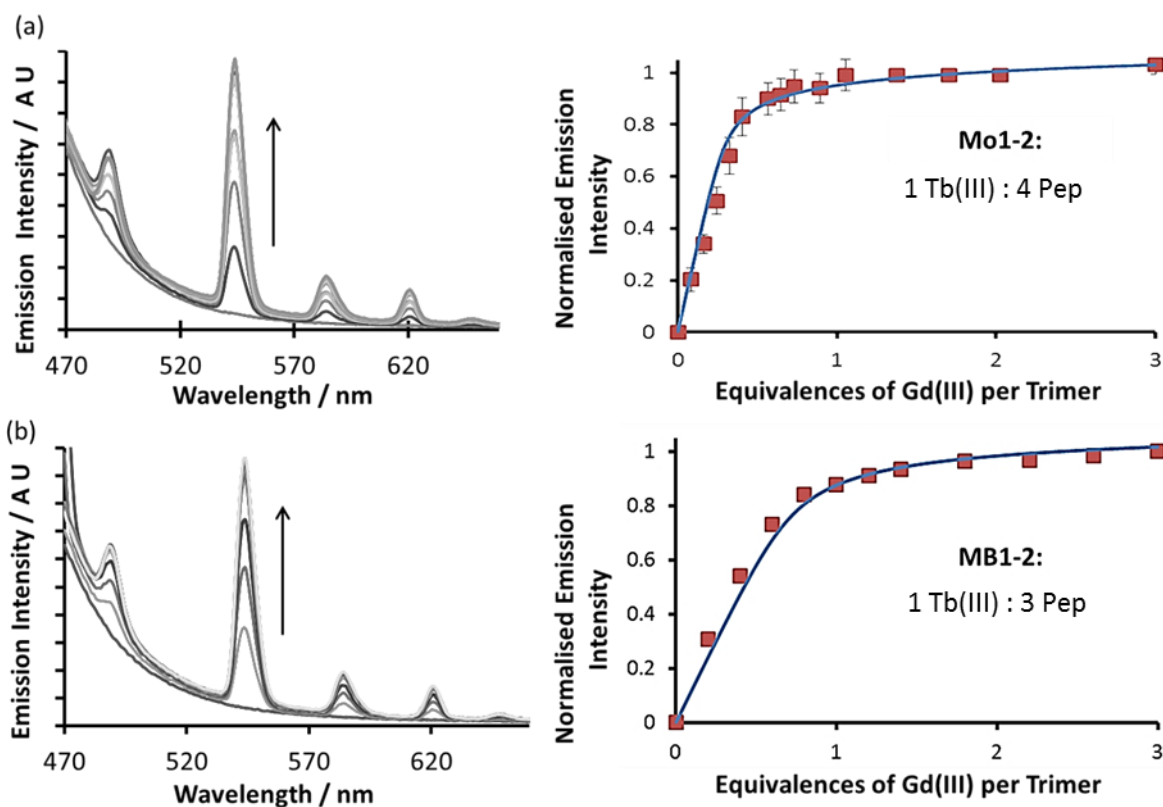


Figure 4.8: Emission profile of (a) Mo1-2 and (b) MB1-2 with increasing aliquots of Tb(III) ran in 10 mM HEPES buffer pH 7.0, using a $\lambda_{\text{exc}} = 280$ nm. The normalised integration of the 545 nm peak is shown to the right. MB1-2 + $\frac{1}{3}$ Gd(III) \leftrightarrow $\frac{1}{3}$ (Gd(MB1-2)₃) and Mo1-2 + $\frac{1}{4}$ Tb(III) \leftrightarrow $\frac{1}{4}$ (Gd(Mo1-2)₄) binding models allowed for the calculation of a binding constant. Error bars are standard deviation for n=3 experiments.

4.3.3 Determining the Oligomeric State of Mo1-2

Due to the discrepancy in fitting the binding curve of Mo1-2, analytical ultracentrifugation (AUC) was used to determine the mass and stoichiometry of the metallo complex, with the data collected as part of a collaboration with Dr Adams at the University of Nottingham and the data shown in Figure 4.9. A weighted average of 11.6 ± 0.2 kDa was calculated with a z-average of 14.2 ± 0.7 kDa. This is consistent with a system with a species of 8 kDa and 18 kDa, corresponding to a metallo dimer and tetramer in a ratio of 62% dimer and 38% tetramer. It is possible that these numbers are underestimates due to the effects of non-ideality, but this should not impact the result by a large margin.

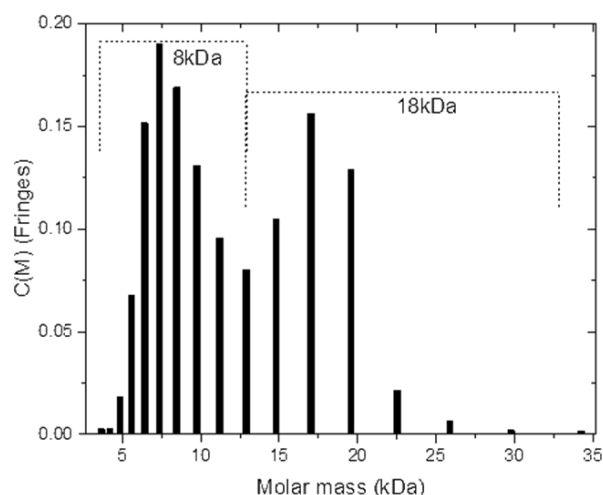


Figure 4.9: AUC data analysed by MULTISIG. The overall weight and z-averages are given as 11.4 kDa, 13.5 kDa. The distribution shows two species, one at 8 kDa and one at 18kDa, which matches closely to a dimer-tetramer system.

Coiled-coil peptide sequences consist of heptad repeats which contain two hydrophobic positions (**a** and **d**).⁸⁴ These residues have the ability to determine the stoichiometry of the coiled coil.¹⁴² Alber and co-workers investigated the change in structure of derivatives of the GCN4 leucine zipper when sets of buried residues (**a** and **d** position) in the peptide sequence were altered and found that dimer, trimer and tetramer structure could be formed.⁸⁴ The occurrence of isoleucine at the **a** position and leucine at the **d** position of the heptad repeat was found to favour the formation of a dimer, whereas the reverse arrangement resulted in a tetrameric peptide. It was found that an even distribution of isoleucine, where it is positioned at both the **a** and **d** positions, resulted in a trimer.^{84,86} In the Mo1-2 peptide isoleucine is positioned at the **a** and **d** position in four of the heptads with a substitution for asparagine in the **d** position of the second heptad and aspartate in the **a** site of the third heptad in order to form the Ln(III) binding site. From this amino acid configuration we would predict the formation of a trimer. The same substitution is made in MB1-2 where a trimer is known to form.

In addition to leucine and isoleucine, polar residues which are buried in the hydrophobic core of a coiled-coil peptide can play a significant role in defining the stoichiometry of the coiled coil. Two-stranded coiled-coils such as those in transcription regulators,⁸⁶ often contain at least one asparagine residue at position **a**, toward the centre of the sequence.^{86,87,142} Polar residues such as glutamine and threonine at positions **a** and **d** are also shown to favour trimer formation. In the Mo1-2 sequence, glutamine has been replaced with glutamate in the **f** sites. Glutamine is also present in the **e** position in both Mo1-2 and MB1-2. There is one asparagine in the **d** site of the third heptad which could signify for a dimeric structure, however, this same substitution occurs in the MB1-2 peptide where a trimer peptide is known to form.⁹⁷

The driving force for trimerisation can be described by the optimal organisation of side-chain–side-chain interactions of the heptad repeat. The motif incorporates networks of surface salt bridges and optimal internal hydrophobic packing interactions.⁸⁷ It was found that the same motif is present in intracellular, extracellular, viral and synthetic trimeric coiled coils. In MB1-2 and Mo1-2, glutamate is at position **e** and lysine at position **g** to promote the formation of inter-helical salt bridges, for stabilisation and trimeric formation.

The characteristic rules of coiled-coil formation developed in the 1990's have allowed for the development of pattern-based methods that predict the occurrence of a specific stoichiometry with a high degree of confidence.⁸⁷ These methods allow the user to input the primary structure of a coiled coil. The programme determines the stoichiometry based on the location of hydrophobic and hydrophilic amino acids as well as taking into account key features of all the amino acids present in the primary structure.

Investigation into the stoichiometry of coiled-coil peptides has been further undertaken by Woolfson and co-workers.^{143–148} This has included the development of a

number of algorithms, e.g. LOGICOIL¹⁴⁹ and SOCKET¹⁵⁰, which have the ability to identify coiled-coil domains in the structures of natural proteins. This has resulted in a database, CCPLUS,¹⁵¹ and Periodic Table of Coiled-Coil Structures¹⁵² which lists the natural coiled-coil domains from the Protein Data Bank. The rules for coiled-coil stoichiometry and folding are integrated into the database to provide a guide for *de novo* coiled-coil designs.

It was of interest to calculate what stoichiometry the Mo1-2 peptide would be predicted to be, using the rules for coiled-coil formation. LOGICOIL¹⁴⁹ analysis has the ability to determine the contribution of dimer, trimer and tetramer species. The algorithm uses information from over 90% of known coiled-coil structures.¹⁴⁹ The statistical method used in LOGICOIL (Bayesian variable selection) can be easily applied to predict coiled-coil oligomeric states, and also has the ability to account for higher order associations such as inter helical interactions.¹⁴⁹

Table 4.2: LOGICOIL predictions for MB1-2 and Mo1-2

| Peptide | Antiparallel dimer | Parallel dimer | Parallel Trimer | Parallel Tetramer |
|---------|--------------------|----------------|-----------------|-------------------|
| MB1-2 | 1.01 | 1.03 | 1.22 | 0.49 |
| Mo1-2 | 1.01 | 0.90 | 1.36 | 0.81 |

The results of the LOGICOIL analysis performed for Mo1-2 and MB1-2 are shown in Table 4.2. It was predicted that the most probable state of Mo1-2 would be a trimer with the second most probable being an antiparallel dimer. In comparison, it was predicted that MB1-2 was most likely to be a trimer with the second most probable structure being a parallel dimer.

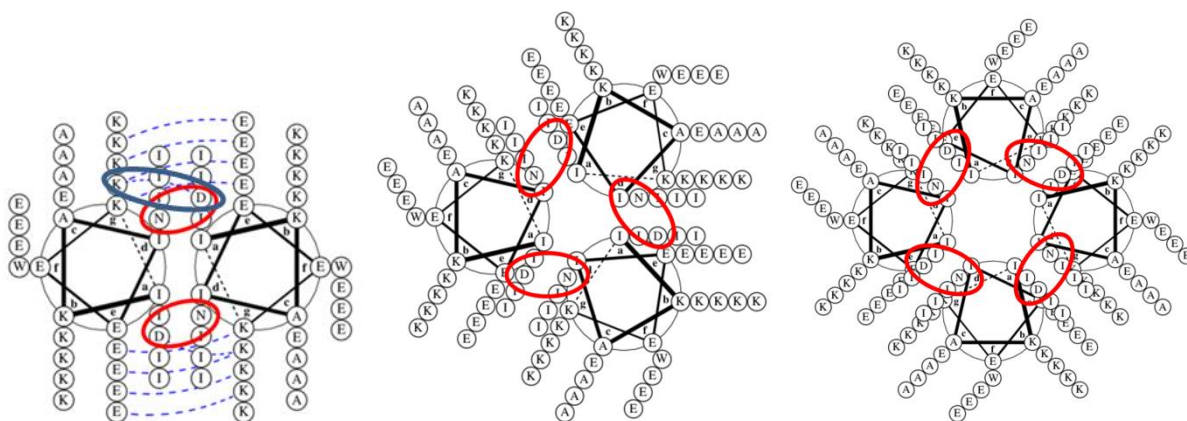


Figure 4.10: Parallel dimer, trimer and tetramer helical wheel diagrams for Mo1-2. The binding site amino acids are circled in red. Salt bridges are shown by blue dashed lines for the dimer structure and the salt bridge between aspartate and lysine is circled in blue. Figures generated using DrawCoil.

The stoichiometry of Mo1-2 was further investigated by drawing helical wheel structures, shown in Figure 4.10, it is possible to see the potential for the formation of a Ln(III) binding site in a dimer, trimer and tetrameric composition. Salt bridges are shown to form between the lysine residues at the **g** position and the glutamate residues at the **e** position in the dimer structure. Interestingly a salt bridge is also shown to form between the aspartate binding site residue at the **a** position and a lysine residue in the heptad above in the dimer structure. This could mean that the aspartate residue may no longer be involved in binding the Ln(III). It would be proposed that more water could coordinate to the Ln(III) in the dimeric structure, increasing the *q* value. This is because only three ligands are forming the Ln(III) binding site, one bi-dentate aspartate residues and two mono-dentate asparagine residues. If this is the case, it could result in a higher relaxivity. In the tetrameric structure, there are 12 possible donor atoms for Ln(III) binding. This would be likely to result in $q = 0$ as there are no free coordination sites for water if all peptide ligands are involved in Ln(III) binding.

4.3.4 Effect of Oligomeric State on the Rotational Correlation Time

By looking at the helical wheel diagrams in Figure 4.10 it is possible to see the potential for the formation of dimer and tetramer structures, which were shown to be present in the AUC analysis. From the LOGICOIL predictions and positions of the amino acids chosen in the Mo1-2 peptide we would still expect a trimer to form. This was further investigated using MD simulations. Simulations were conducted in triplicate, using AMBER, of Mo1-2 in a dimeric, trimeric and tetrameric structure with the 10 ns snapshot output compared in Figure 4.11.

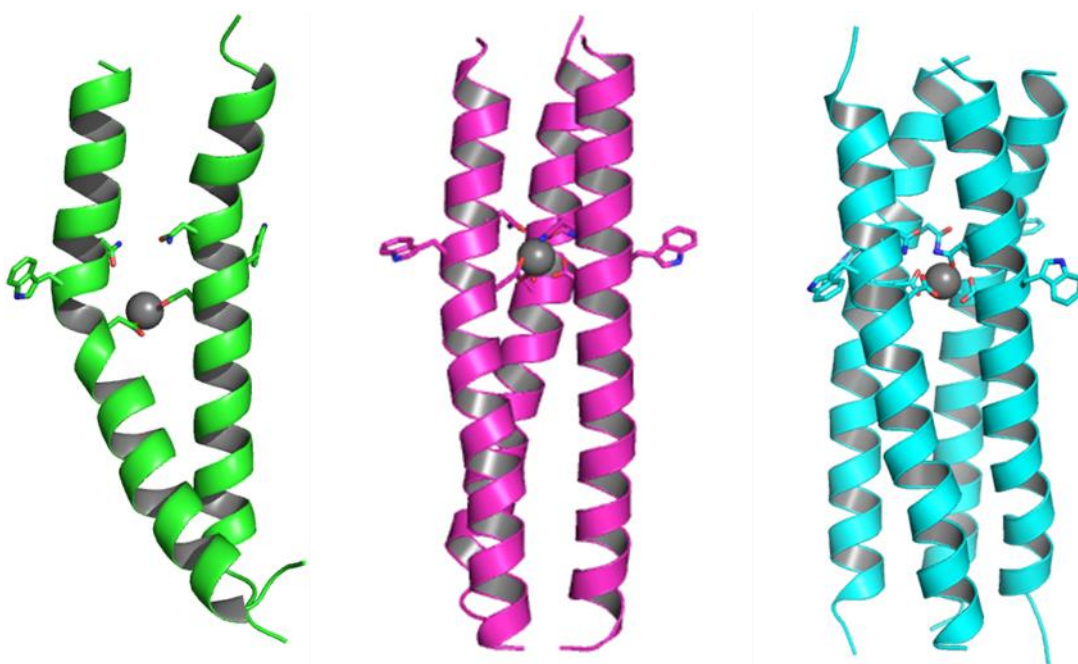


Figure 4.11: Schematic representation of a snapshot of a 10 ns MD simulations of Mo1-2 as a (a) dimer, (b) trimer and (c) tetramer. The peptide backbone is shown as a cartoon with the binding site amino acids and tryptophan sensitizer shown as sticks. The Gd(III) ion is shown as a grey sphere.

In the dimer simulation, only the four oxygen donor atoms from the aspartate residues are shown to be involved in Ln(III) binding. The Ln(III) is shown to be positioned outside of the hydrophobic core. This is different from the helical wheel diagram which showed that the aspartate residue would be involved in salt bridge formation rather than Ln(III) binding and

could allow for an increase in q . However, the helical wheel diagram is a much simpler depiction compared to MD simulations.

In the trimer, six oxygen atoms from the aspartate residues and three oxygen atoms from the asparagine residues are shown to be involved in Ln(III) coordination. This leaves three available binding sites for water coordination.

In the tetramer, the eight oxygen ligands from the four aspartate residues are shown to coordinate to the Ln(III) this leaves four coordination sites on the Ln(III) available for a water. The asparagine ligands although oriented towards the Ln(III), do not appear to take part in Ln(III) coordination.

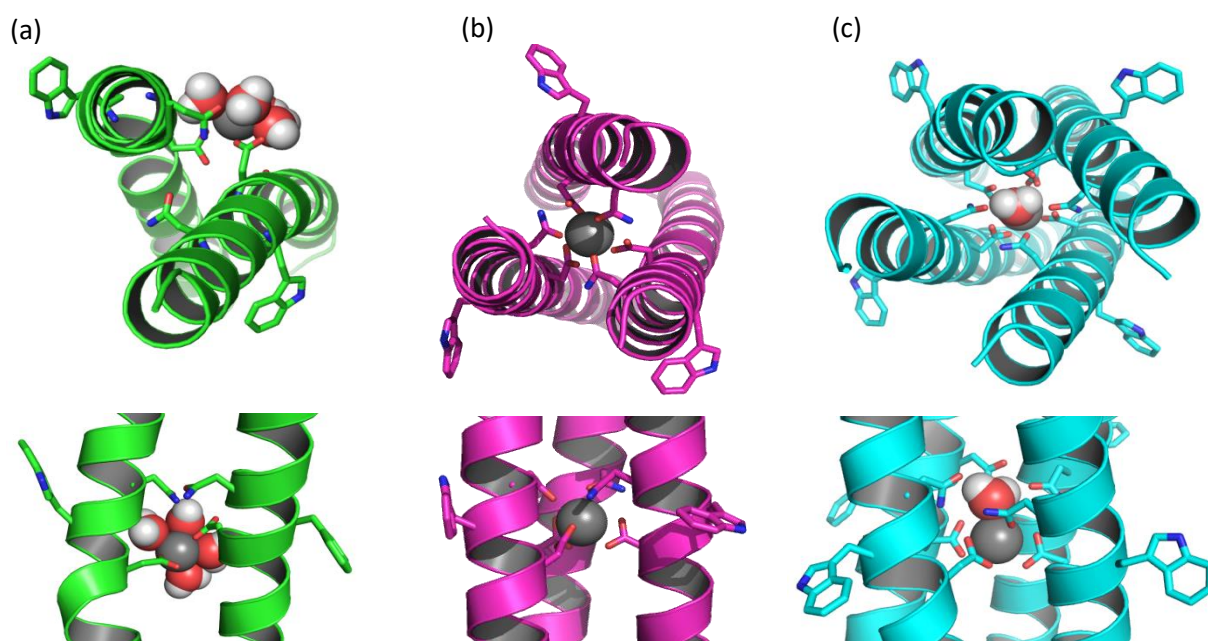


Figure 4.12: Snapshot of 10 ns MD simulations of Mo1-2 as a (a) dimer, (b) trimer and (c) tetramer.

The peptide backbone is shown as a cartoon with the binding site amino acids and tryptophan sensitizer shown as sticks. The Gd(III) ion is shown as a grey sphere and inner-sphere water shown as a red and white sphere.

When comparing water coordination to the Ln(III) in the MD simulations of the three systems, it was found that, after 10 ns, four water molecules were coordinated to the dimer, zero to the trimer and one to the tetramer, as shown in Figure 4.12. A q of four for the dimer would result in a dramatic increase in relaxivity compared to the trimer species with no inner-sphere water.

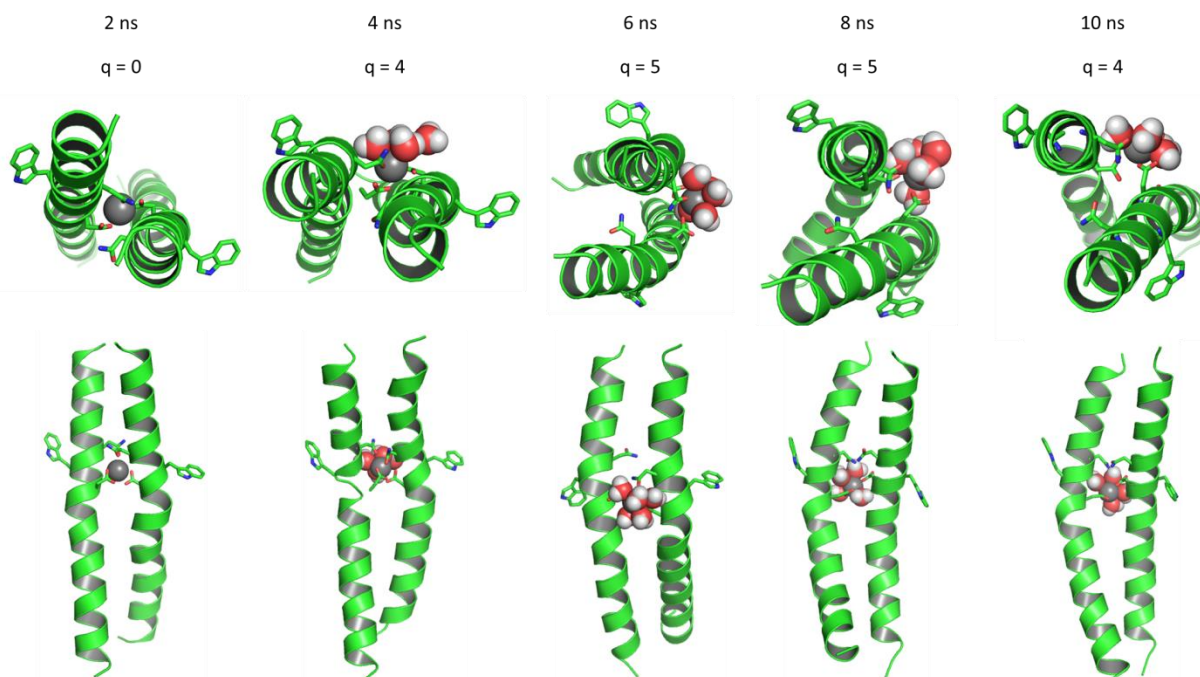


Figure 4.13: Top down and side on view of 2 ns snapshots of the MD simulation of the Mo1-2 dimer. The peptide is shown as a cartoon with the binding site and tryptophan residues shown as sticks. The Ln(III) is shown as a grey sphere and primary water is shown as red and white spheres.

Primary water coordination was further investigated for the dimer simulation, with snapshots shown in Figure 4.13. When analysing the snapshots taken every two nanoseconds, it was observed that at 2 ns the dimer species has q of zero and the Ln(III) is located in the centre of the isoleucine core. After 4 ns, the Ln(III) moves to the helical interface of the peptide, and locates itself between the two α -helices. Now q increases to five. This remains the same until 10 ns where q reduces to four, suggesting an inner-sphere water residency time of 6 ns. Throughout the 10 ns simulation, the four oxygen atoms from the two aspartate

residues are involved in Ln(III) coordination. From 2 ns to 6 ns one oxygen ligand from an asparagine residue coordinates to the Ln(III), this dissociates by 8 ns. Also observed over the 10 ns is distortion of the α -helix. This is most apparent at 4 ns where the peptide structure below the lanthanide binding site is no longer α -helical.

In the tetramer simulation (a snapshot shown in Figure 4.14) one inner-sphere water is coordinated to the Ln(III). This water molecule is present throughout the 10 ns simulation, suggesting an inner-sphere water residency time longer than 10 ns. This can be compared to the inner-sphere water residency time in MB1-1 which was experimentally determined to be 1.56 ns using ^{17}O NMR and calculated to be between 0.5 and 6 ns using the SBM equations. This could be due to the Ln(III) binding site being located further into the hydrophobic core. Additionally, one secondary sphere water molecule was coordinated to the primary sphere water which could provide an increase in relaxivity through the secondary sphere mechanism.

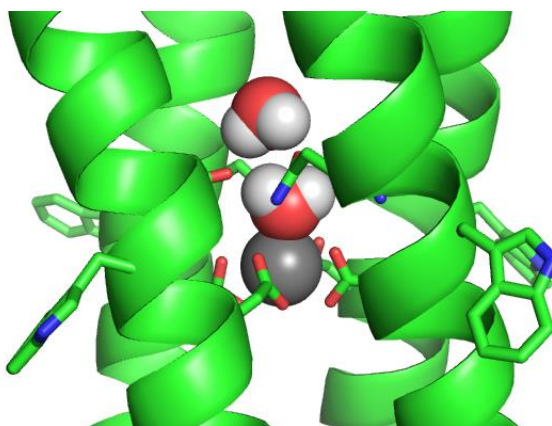


Figure 4.14: A snapshot at 10 ns of a hypothetical Mo1-2 tetramer. The peptide is shown as a cartoon and mesh, the binding site and tryptophan amino acids are shown as sticks, Ln(III) is shown as a grey sphere and the waters of interest are shown as red and white spheres.

To investigate the theoretical impact different peptide oligomers would have on relaxivity, due to changes in their dimensions and their rotational correlation times, the width

of the coiled coils, from the MD simulations was measured, and found to be $24.1 \pm 2.7 \text{ \AA}$ for the dimer, $23.3 \pm 2.1 \text{ \AA}$ for the trimer and $26.7 \pm 4.2 \text{ \AA}$ for the tetramer. The length of the three different stoichiometries remained the same (57 \AA). The rotational correlation time was then calculated for the changing width of the coiled coil using the same calculations as in Chapter 3, with the results plotted in Figure 4.15.

It was found that the rotational correlation time increased as the width of the coiled coil increased. For the dimer, trimer and tetramer it was found that the change in width had very little effect on the rotational correlation time, increasing it from 6 ns to 8 ns.

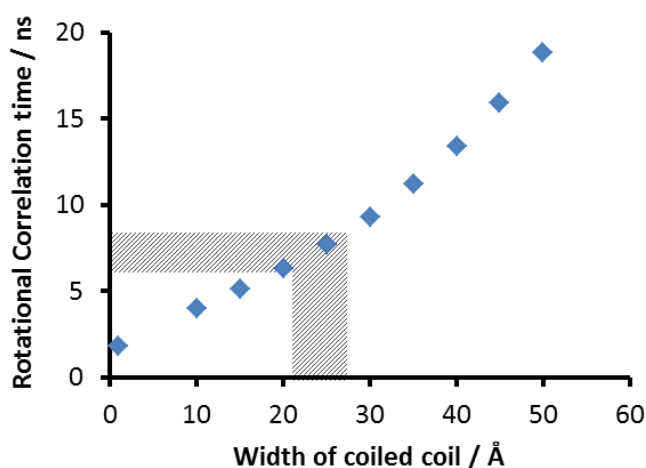


Figure 4.15: Predicated effect of changing the width of a coiled coil on the rotational correlation time. Highlighted area shows the change in width from 24.1 \AA to 26.7 \AA , corresponding to a change in rotational correlation time of 6 to 8 ns, calculated for a peptide length of 57 \AA .

The calculated rotational correlation times were then used to calculate the r_1 relaxivity, with the data shown in Figure 4.16. Four different q values were used as it was proposed from the MD simulations that $q = 4$ for the dimer, $q = 0$ for the trimer and $q = 1$ for the tetramer. As a value of 0 would return a null answer, intermediate values of 0.5 and 2 were also considered. It was found that no change in r_1 is observed when the rotational correlation time changes

between 6 and 8 ns, when calculated for each q value. An increase is observed up to 5 ns, but after this there is little change in r_1 for all q values.

These calculations demonstrate that the change in stoichiometry between a dimer, trimer and tetramer have very little effect on r_1 , if q remains the same. This is due to the small change in width only causing a change in the major b axis and the length (major a axis) remaining the same.

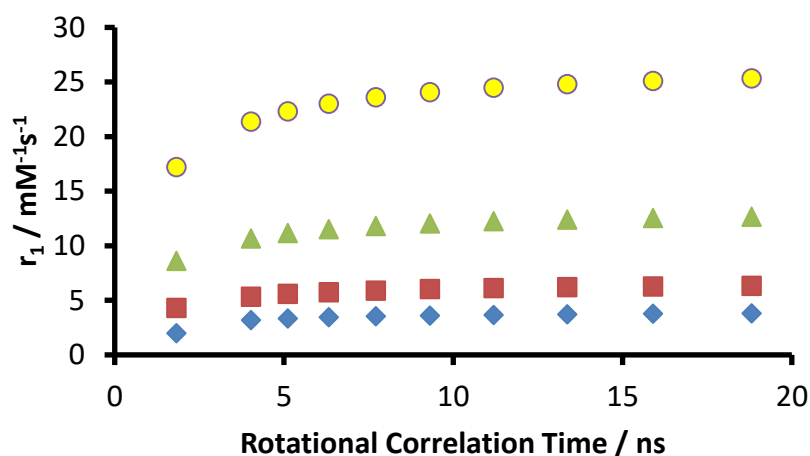


Figure 4.16: Predicted effect of changing the rotational correlation time on r_1 relaxivity for a $q = 0.5$ (blue), 1.0 (red), 2.0 (green) and 4.0 (yellow). Predictions made at 7 T, $\tau_m = 1.56$ ns, $r = 2.6$ nm.

To further investigate the importance of secondary sphere water coordination, the Mo1-2 peptide was characterised using CD, luminescence and MRI in order to determine the stability of the complex, quantify the amount of water coordinated to the Ln(III) when bound to the binding site and to determine the relaxivity. It was anticipated that this analysis would give further insight into the stoichiometry of the peptide as if experimentally $q = 1$ it would indicate the presence of a tetramer species with q values of more than one indicative of the presence of a dimer species.

4.3.5 Effect of Amino Acid Substitutions on Peptide Stability

CD spectroscopy was used to determine the chemical and thermal stability of Mo1-2, in comparison to MB1-2, with the data shown in Figure 4.17. Samples containing 30 μM of Mo1-2 monomer, in the absence and presence of 10 μM GdCl_3 , were subjected to a gradual increase in temperature from 25 to 85°C, and the CD signal at 222 nm was recorded as a measure of folding.

The apo peptide was 28% folded at 25°C and decreased to 18% folded at 85°C. The metallo complex was 63% folded at 25°C and decreased to 28% folded when the temperature reached 85°C. This is shown to be comparable to MB1-2 which in the apo peptide was 19% folded at 25°C and remained the same at 85°C. The metallo complex was 59% folded at 25°C and decreased to 28% folded when the temperature reached 85°C. This shows the stability for both peptides, in the apo and metallo complexes, is the same within the error of the experiment, indicating the change in exterior residues or change in stoichiometry did not impact peptide stability.

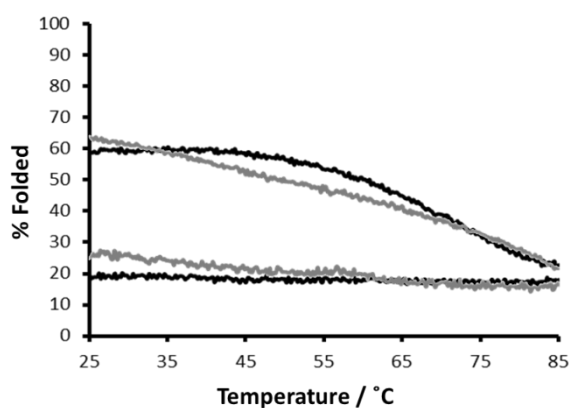


Figure 4.17: Change in percentage folded of 30 μM (black) MB1-2 and (grey) Mo1-2 monomer in the absence (dark) and presence (light) of 10 μM GdCl_3 in 10 mM HEPES buffer pH 7.0. % folded based on the CD signal at 222 nm.

Chemical denaturation showed the folding of Mo1-2 to decrease by 60% in the presence of 6 M guanadinium hydrochloride (Gua-HCl), when monitored by CD. A two-state equilibrium model between folded and unfolded was used to examine the peptide unfolding profiles. Extrapolation of the data gave free energies of folding, ΔG°_{H2O} , of 14.0 ± 2.3 kcal mol⁻¹ for the apo peptide, and 16.4 ± 0.8 kcal mol⁻¹ for the metallo complex. This can be compared to MB1-2 which gave ΔG°_{H2O} , of 12.7 ± 1.5 kcal mol⁻¹ for the apo peptide, and 15.3 ± 2.0 kcal mol⁻¹ for the metallo complex. ΔG°_{H2O} for both apo and metallo systems is the same, within the error of the experiment, for MB1-2 and Mo1-2. This shows that the modification of the exterior of the coiled coil, or the possible change in stoichiometry, has no noticeable influence on the stability of the peptide. Despite this, when comparing the trends of Mo1-2 and MB1-2 they were shown to be different, especially in the metallo system, as shown in Figure 4.18. In Gd(Mo1-2)₃ a sharp transition followed by a plateau at 3 M is observed. In comparison in Gd(MB1-2)₃ a slower transition occurs followed by a plateau at 4 M suggesting Gd(MB1-2)₃ is more stable. It was hypothesised that Mo1-2 would be more stable due to the presence of more side chains, lysine and glutamate, with the potential to form stabilising salt bridges across the coiled coil but this was not observed in this experiment.

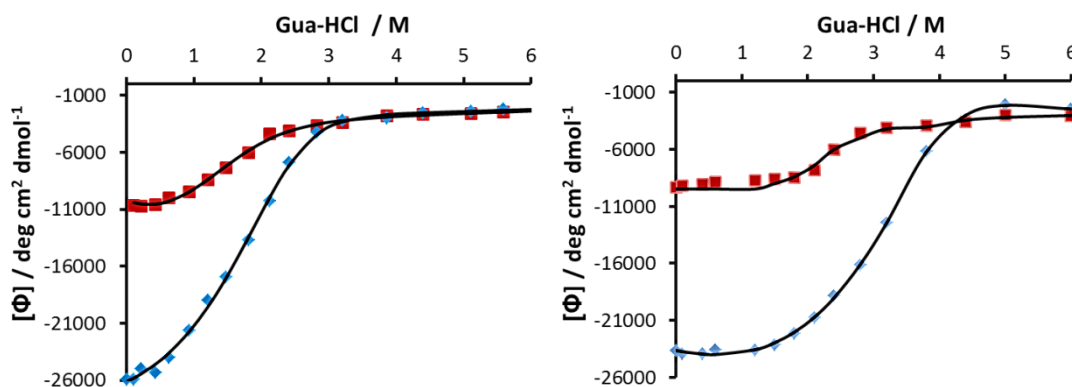


Figure 4.18: Change in molar ellipticity of 30 μ M (a) Mo1-2 and (b) MB1-2 monomer in the absence (red) and presence (blue) 10 μ M GdCl₃, in 10 mM HEPES buffer pH 7.0 as a function of [Gua-HCl]. Concentration of Gua-HCl was increased between 0 and 6 M and the signal at 222 nm monitored.

4.3.6 Computational Analysis of Water Coordination to the Peptide Exterior

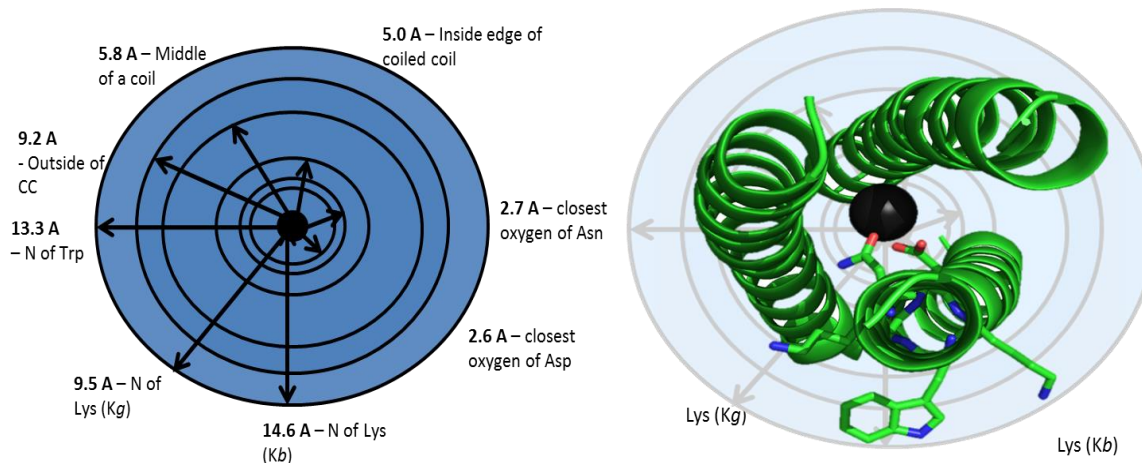


Figure 4.19: Schematic diagram to show the distances from the central Gd(III) to various locations within the Mo1-2 coiled coil. (a) Shows the distances of each point in the coiled coil measured from the Gd(III) ion and (b) shows how the coiled coil fits within these measurements.

In the work by Berwick and co-workers,^{95,97} the MB1-2 peptide was designed with a Ln(III) binding site positioned in the second and third heptads. The complex was reported to have $q = 0.0 \pm 0.1$ and a relaxivity of $4.1 \pm 1.2 \text{ mM}^{-1} \text{ s}^{-1}$ (r_1) and $24.4 \pm 2.6 \text{ mM}^{-1} \text{ s}^{-1}$ (r_2) at 7 T.⁹⁷ Here, outer sphere water coordination was considered to be the main contributing factor to relaxivity. MD simulations and computational analysis were used in order to analyse the secondary sphere water contribution to the peptide systems.

When analysing the 20 ns simulations of Mo1-2, lysine residues were measured to extend approximately 9.5 Å from the Gd(III) centre when in the **g** position (also present in MB1-2) and 14.6 Å in the **b** position (a new feature in Mo1-2), as shown in Figure 4.19. Water located around the lysine side chain was analysed in this system at a distance between 10 and 20 Å from the Gd(III) ion centre. It was calculated that Mo1-2 had 914 ± 24 water molecules located in this region compared to MB1-2 where there were 772 ± 25 , in the comparable simulation. The most dramatic difference between the two peptides was in the region between 16.1 and 20 Å, with the number of water molecules at each distance given in Table

4.3. When analysing the coiled-coil structure, this region is located directly around the NH_3^+ terminal group of the lysine residues. It is observed that more water is hydrogen bonded to the exterior of the peptide in Mo1-2 compared to the surface of MB1-2. The water molecules coordinated to the lysine residues of Mo1-2 are shown in Figure 4.20.

Table 4.3: Average number of water molecules at increasing distances from the coiled-coil peptide, calculated for Mo1-2 and MB1-2. Data shown is an average for three simulations and a standard deviation error.

| PEPTIDE | Distance / Å | | | | | | | | |
|---------|--------------|--------------|--------------|--------------|--------------|---------------|---------------|----------------|-----------------|
| | 2.1 - 3 | 3.1 - 4 | 4.1 - 5 | 5.1 - 6 | 6.1 - 7 | 7.1 - 10 | 10.1 - 13 | 13.1 - 16 | 16.1 - 20 |
| Mo1-2 | 1.0 ± 0 | 0.6 ± 0.5 | 0.1 ± 0.8 | 0.6 ± 0.9 | 2.3 ± 1.6 | 22.7 ± 3.4 | 93.3 ± 5.1 | 194.7 ± 7.7 | 656.1 ± 11.7 |
| MB1-2 | 1.0 ± 0.0 | 0.7 ± 0.5 | 2.3 ± 0.7 | 0.3 ± 0.7 | 3.3 ± 1.6 | 27.4 ± 2.7 | 97.8 ± 5.9 | 198.7 ± 8.5 | 475.5 ± 10.8 |

When looking at water closer to the coiled coil, more water is shown to be present in the MB1-2 simulation, between 2.1 and 5 Å distance from the Gd(III). This could indicate that in Mo1-2 the lysine residues, although polar and with the ability to hydrogen bond with water, are pushing the water molecules further away from the peptide and the paramagnetic Gd(III). This would increase the average Gd(III) to water distance resulting in a decrease in relaxivity, the opposite of the hypothesis.

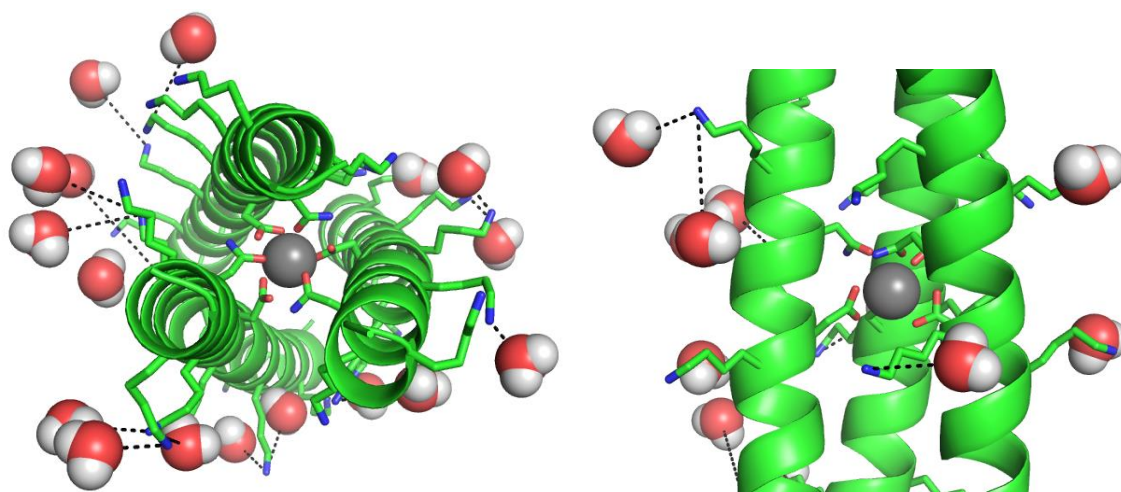


Figure 4.20: Pymol figures showing the coordination of water to lysine residues on the coiled-coil exterior. The peptide backbone is shown as a cartoon, the Ln(III) as a grey sphere, lysine residues and binding site residues as sticks and secondary sphere water as spheres.

4.3.7 Water Coordination

Calculating q from MD simulations can sometimes give different values to those obtained experimentally. This has previously been observed in the work by Berwick. Therefore, q was experimentally determined for the Mo1-2 system. Tb(III) luminescence lifetimes in H₂O and D₂O were used to probe the amount of inner-sphere water coordinated to the Tb(III) when bound to Mo1-2. The lifetime decays at 545 nm were measured as 0.6 ± 0.1 ms in H₂O and 0.4 ± 0.1 ms in D₂O with the decay shown in Figure 4.21. In order to correct for the contribution of outer sphere water, the Parker-Beeby equation¹¹⁶ was applied and it was calculated that less than one (0.6 ± 0.1) water was bound to Tb(III) in the metallo peptide complex. This can be compared to MB1-2 where zero waters are coordinated to the Tb(III) (0.0 ± 0.1).⁹⁷ A value of 0.6 ± 0.1 agrees with the MD simulations of the trimer and tetramer complexes where between zero and one water molecule was bound to the Ln(III).

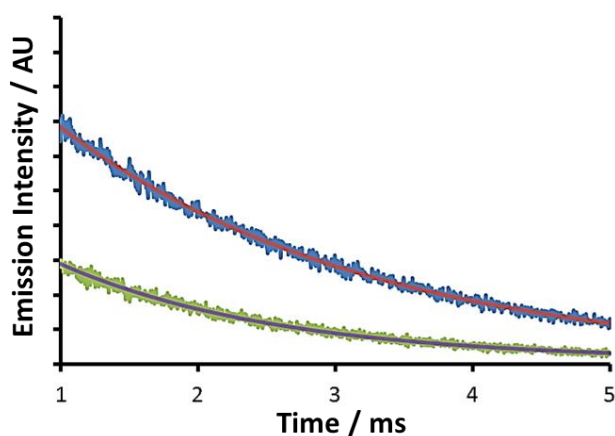


Figure 4.21: Decay profiles of Tb(III) emission at 545 nm for 100 μ M Mo1-2 monomer on addition of 0.3 equivalences of Tb(III) in 10 mM HEPES buffer pH 7.0, fit to a mono-exponential decay, in H₂O (dark) and D₂O (light) allowing for calculation of q values.

4.3.8 Relaxivity and Contrast Agent Efficiency

To determine the relaxivity of the $\text{Gd}(\text{Mo1-2})_3$, the longitudinal (T_1) and transverse (T_2) relaxation times were measured and compared to MB1-2, as shown in Figure 4.22. Double the concentration of peptide was used to ensure complete complexation of Gd(III) for if the complex was a dimer, trimer or tetramer. The longitudinal (r_1) and transverse (r_2) relaxivity, were found to be (r_1) 6.3 ± 2.3 and (r_2) $21.6 \pm 3.6 \text{ mM}^{-1} \text{ s}^{-1}$ respectively, compared to that of MB1-2 calculated to be (r_1) 4.6 ± 0.9 and (r_2) $21.3 \pm 1.2 \text{ mM}^{-1} \text{ s}^{-1}$ at 7 T.⁹⁷

T_1 and T_2 measurements were recorded at a lower field (1 T) in order to assess if the differences between Mo1-2 and MB1-2 were more apparent at lower field strengths (42.6 MHz (1 T)). This is because, when measuring at a lower field it is more sensitive to changes in the rotational correlation time and associated water dynamics.⁴⁰ This yielded relaxivities of (r_1) 16.7 and (r_2) 20.2 $\text{mM}^{-1} \text{ s}^{-1}$ for Mo1-2, and (r_1) 17.9 and (r_2) 20.7 $\text{mM}^{-1} \text{ s}^{-1}$ for MB1-2. Caution should be taken when drawing conclusions as only one experiment was performed. An increase in r_1 was observed when comparing 1 T and 7 T for both peptides. This is due to the slow rotational correlation time of the peptides and tumbling becoming more significant at low fields.⁴⁰ No significant differences in the longitudinal or transverse relaxation time were observed at either 1 T or 7 T. This means that the difference in q (0.6 vs 0.0) was not significant enough to cause an increase in relaxivity and any differences in secondary sphere water coordination, or in the stoichiometry of Mo1-2, had no significant effect on relaxivity.

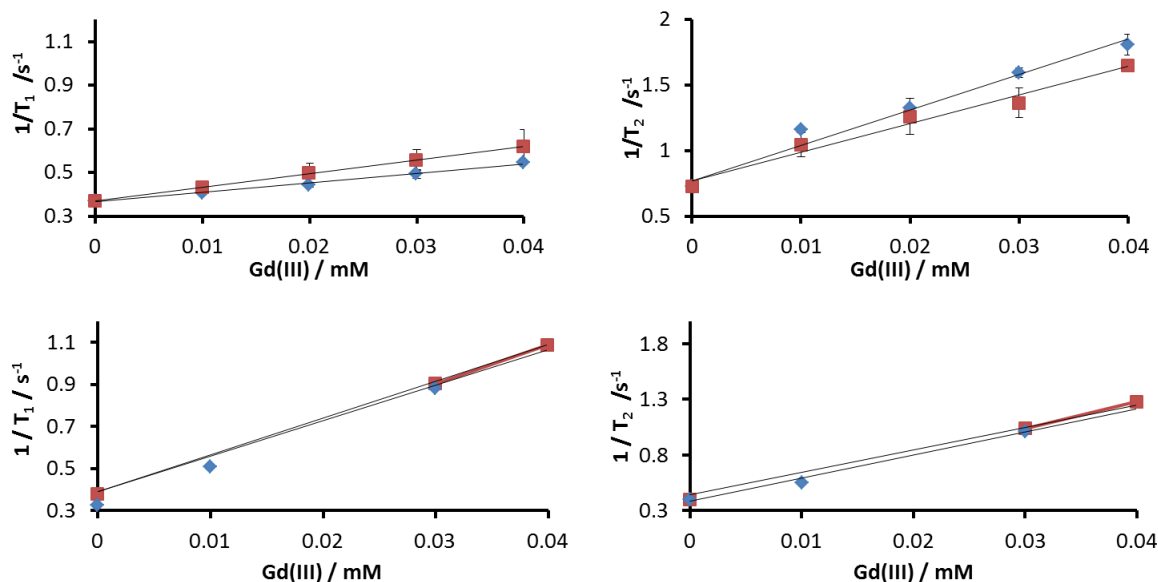


Figure 4.22: Relaxivity plots showing reciprocal of relaxation time as a function of Gd(III)

concentration for T_1 (left) and T_2 (right) at 7 T (top) and 1 T (bottom). Data is shown for Mo1-2 (grey) and MB1-2 (black). All samples recorded in the presence of 10 mM HEPES buffer pH 7.0, with an excess of peptide monomer compared to Gd(III). Error bars show data repeated in triplicate at 7 T, only one experiment was collected at 1 T.

4.4 Conclusions

In this chapter the effect of water coordination to the coiled-coil exterior on the relaxivity of Gd(III) binding peptides has been investigated. A new peptide, Mo1-2, was designed, synthesised and characterised and compared to the previously established MB1-2.

It was found that the addition of lysine residues on the peptide exterior had no effect on the stability of the peptide, despite additional polar groups being added to the peptide sequence with the ability to form stabilising interactions and predicted to increase the stability of the complex. Additionally, no change in relaxivity was observed, at low or high fields, despite more water being predicted to coordinate to the exterior of the peptide via the NH_3^+ groups of lysine. This water was too far from Gd(III) to result in a significant increase in relaxivity and no improvement in MRI CA potential was observed.

Interestingly, it was found that from CD and luminescence analysis, a 1:4 stoichiometry was observed for Mo1-2 compared to 1:3 for MB1-2. This was confirmed using AUC where a dimer: tetramer ratio of 62% dimer and 38% tetramer was determined. By analysing MD simulations and helical wheel diagrams it was found that both of these oligomers were possible due to salt bridging networks and the formation of an isoleucine core, despite the theory predicting a trimer. Luminescence lifetime experiments yielded $q = 0.6$, closer to the primary sphere water predictions for the trimer and tetramer species. Given more time, Mo1-2 would be further analysed using techniques such as Mass Spectrometry, ESR and NMRD in order to accurately determine the stoichiometry of the coiled coil.

Chapter 5: Investigating the Presence of Water Located in the Hydrophobic Core of a Coiled-Coil Peptide

5.1 Introduction

When considering the relaxivity potential of MRI contrast agents (CAs), it is essential to consider contributions from surrounding water molecules. These can be located in the inner-sphere (directly coordinated to Gd(III)), second sphere (coordinated to the primary water or CA support), or the outer sphere (water that diffuses close to the CA).¹⁹ The contribution of the solvent to the relaxation time can be improved by increasing the number and lifetime of water molecules located within each hydration sphere.

In Chapter 4, secondary sphere water was determined to be too far away, when coordinated to the exterior of the coiled coil, to impact relaxivity. In this chapter, the secondary sphere water located within the hydrophobic core and its effect on relaxivity was investigated. It was proposed that a water channel was present in the hydrophobic core of MB1-2 which would allow water to be closer to Gd(III) and this would have a greater effect on relaxivity.

In 1996, Hodges and co-workers first proposed that a cavity located within the hydrophobic core of a coiled-coil peptide could be used to accommodate water molecules.¹⁵³ This would result in a shorter Ln(III) – hydrogen distance (r_{MH}), compared to bulk water, hence increasing relaxivity (if the water residency time remained the same). The presence of a cavity was later confirmed by Pecoraro and co-workers in a coiled coil containing a Cd(II) thiolate binding site.^{154,155} Here, a L-leucine amino acid located directly above the cadmium binding site in the hydrophobic core of the coiled coil was replaced with a smaller, less sterically hindered alanine residue, and led to removal of the cavity and an increase in hydration state

(q) of cadmium.¹⁵⁶ It was also observed in the work by Pecoraro and co-workers that the presence of a cavity can force the metal binding site to adopt an undesirable trigonal pyramidal geometry.¹⁵⁴

The presence of cavities within the hydrophobic core of coiled coils can be highly destabilising, especially if the peptide is unable to repack its hydrophobic core to compensate for the cavity.¹¹⁴ It has been estimated that the introduction of a cavity can destabilise the peptide by approximately 2-5 kcal mol⁻¹, depending on the extent of repacking of the hydrophobic core.¹¹⁴ Additionally, the presence of disulphide bridges around the cavity site was shown to decrease the degree to which the peptide is destabilised.¹¹⁴

5.2 Aims

In the work by Berwick and co-workers,^{95,97} MB1-2 was designed with a Ln(III) binding site positioned in the second and third heptads, shown in Figure 5.1, with $q = 0.0 \pm 0.1$ and a relaxivity of (r_1) $4.1 \pm 1.2 \text{ mM}^{-1} \text{ s}^{-1}$ and (r_2) $24.4 \pm 2.6 \text{ mM}^{-1} \text{ s}^{-1}$ at 7 T.⁹⁷ Here, outer sphere water coordination was considered to be the main contributing factor to relaxivity. Upon further investigation into Berwick's 10 ns MD simulation of MB1-2 it was found that a water channel was present, which ran from the peptide exterior to above the Ln(III) binding site, which could allow water to get closer to Gd(III) than previously thought, shortening the Gd(III) - H₂O distance and increasing relaxivity. This was the first time water had been seen in this type of secondary sphere water environment in the MB1 peptides and presented an exciting opportunity to investigate the effect of water located in a channel.

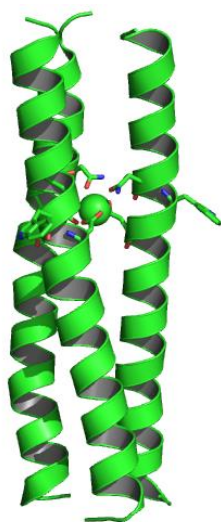


Figure 5.1: Schematic representation of MB1-2 after 20 ns of MD simulation with the peptide backbone shown as a cartoon, the Ln(III) metal as a sphere and binding site amino acids and the tryptophan sensitizer displayed as sticks.

In order to investigate the channel further, a new peptide was designed in which the water channel in MB1-2 would be blocked, so that no water could be located within the site. The design involved using a D-Isoleucine (D-Ile) to replace the L-isoleucine (L-Ile) residue in the α position immediately above the Ln(III) binding site; the isomers are shown in Figure 5.2. As the Ile side chain would now point towards the C-terminus, as opposed to towards the N-terminus for L-Ile, it was proposed that the channel would no longer be able to exist in the same position. D-amino acids have previously been used in *de novo* designed coiled-coils, due in part to their side chains having the same structure as their L-analogues.¹⁵⁷ Single amino acid substitutions have sometimes been shown to cause the formation of hairpin turns or stop the formation of an α -helix.¹⁵⁷⁻¹⁵⁹ When all the amino acids in a sequence have been changed to D-amino acids, a mirror structure has been observed. In other examples, it has previously been found that single, double and triple substitutions in α -helices can be tolerated within a coiled-coil structure.^{157,160}

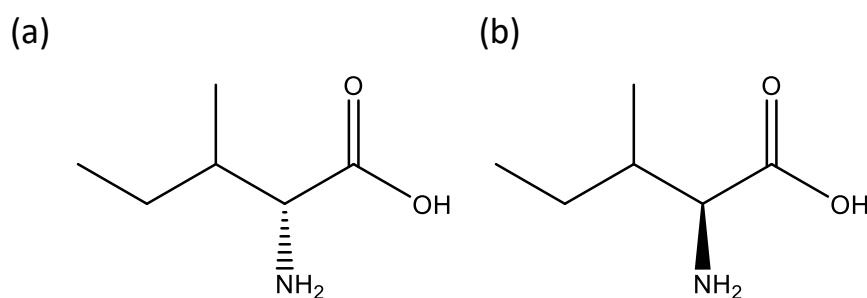


Figure 5.2: The (a) D- and (b) L- stereoisomers of isoleucine.

5.3 Results and Discussion

5.3.1 Investigation into Water Location in MB1-2

Further computational investigations into MB1-2 were completed. The simulation of MB1-2 was repeated and extended to 20 ns as it allowed the system to reach equilibrium. This was determined by counting the number of water molecules within 5 Å of the peptide backbone, with the data shown in Figure 5.3. By analysing the number of water molecules within this specified area it was calculated that this plateaued at 18 ns. It was concluded, that at this time point, the simulation has reached equilibrium.

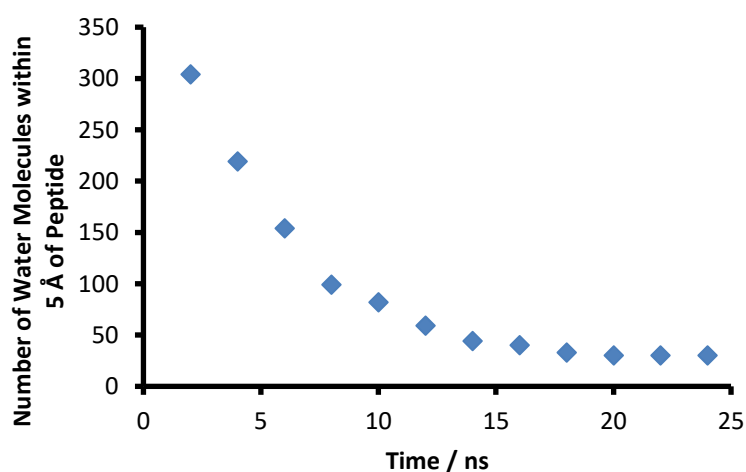


Figure 5.3: Quantification of water within 5 Å of Gd(MB1-2)₃ peptide measured as a function of time.

Equilibrium was reached after 18 ns, shown by the plateau of the curve.

When analysing the MB1-2 simulation, it was found that a water channel is present and remains throughout the simulation. The channel starts at the coiled-coil exterior at a distance of 9 Å from the Gd(III) and passes through the hydrophobic core of the peptide to the Gd(III) binding site. The channel allows water access in close proximity (defined as within 8 Å)¹²⁷ to the Ln(III) binding site, even allowing water molecules to interact directly to the inner-sphere water, and is predicted to result in an increase in water residence time compared to the bulk water. The increase in water residence time allows water to be influenced significantly by the paramagnetic Ln(III) before returning to the bulk water and has the potential to account for the relaxivity of the Gd(MB1-2)₃ complex, as experimentally $q = 0$. The simulations show one water molecule directly coordinated to the Ln(III), at a distance of 2.9 Å, despite a $q = 0$ being experimentally determined.⁹⁷ The water molecule is present after 2 ns of the simulation and remains coordinated to the Ln(III) throughout the 20 ns, indicating a water residence time of at least 18 ns.

The secondary sphere water molecules are shown to “queue up” in the channel and are directly hydrogen bonded to each other and to the inner-sphere water molecule, as shown in Figure 5.4(a). The secondary sphere water to Ln(III) distances are measured to be 5.0, 6.5, 9.2, 10.2 and 13.6 Å. After this distance, no water is directly interacting with water within the channel and so can be considered as outer sphere water.

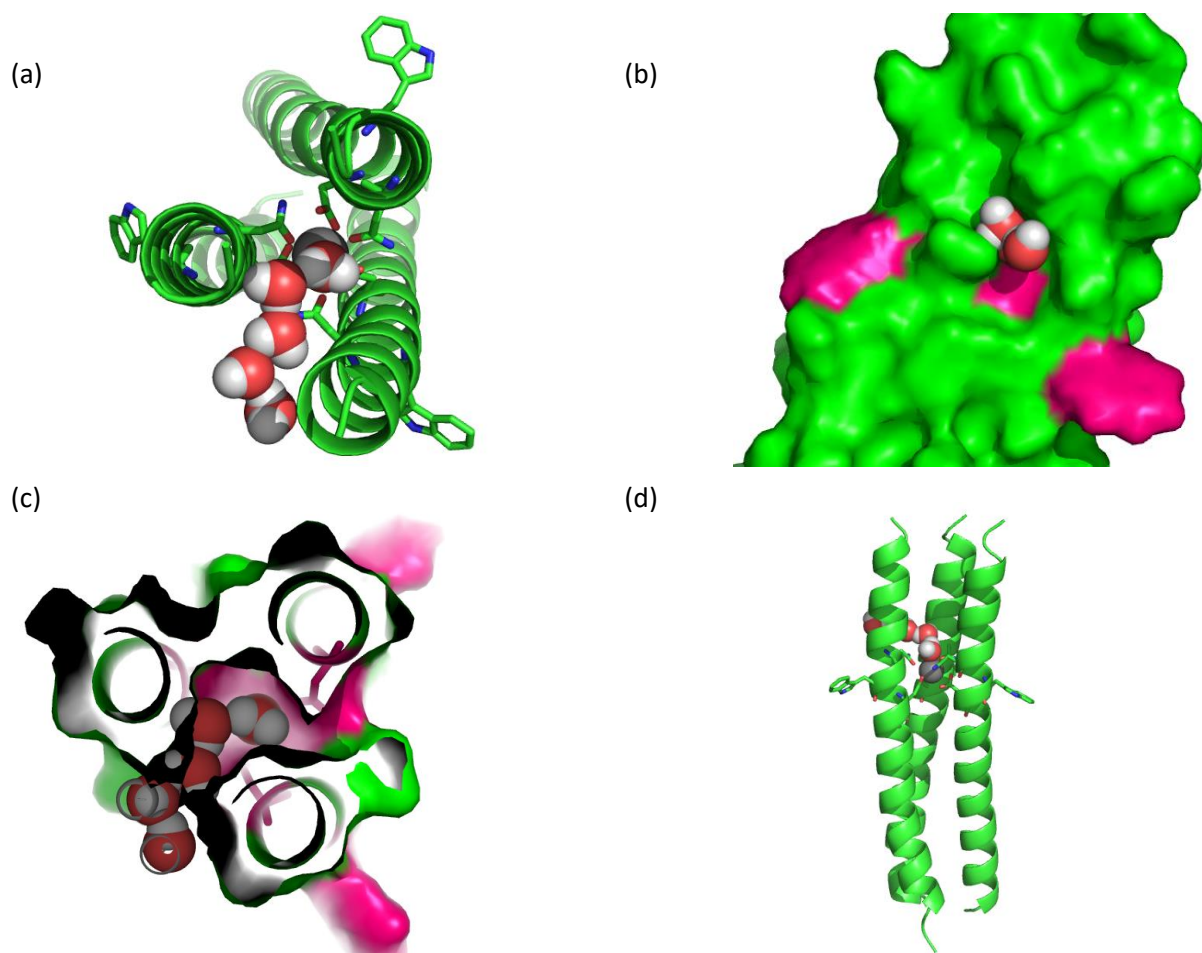


Figure 5.4 Schematic representation of Gd(MB1-2)₃ 20 ns MD simulation snapshot. Secondary sphere water molecules are shown located in a channel from the Gd(III) to the exterior of the coiled coil. The peptide backbone is shown as a cartoon, the Gd(III) metal as a grey sphere, the binding site amino acids and the tryptophan sensitiser displayed as sticks (and pink on the surface) and the secondary sphere water molecules are shown as red spheres. (a) Top down view showing secondary sphere water channel, (b) side view showing the entrance of the water channel from the coiled-coil exterior, (c) cross section view showing secondary sphere water located in the channel, (d) side view showing the binding site amino acids, Ln(III) and secondary sphere water.

5.3.2 Analysing Water Distances and SN1-2 Design

For water in the secondary sphere, relaxivity can be described by the same mechanisms used for inner-sphere water. The equation differs in that each water molecule

will have its own relaxation time and residency time.⁴⁰ The r'_{MH} is longer than for primary sphere water and the residency time τ'_m is shorter.⁴⁰

Equation 5.1:
$$r_i^{SS} = \frac{q'/[H_2O]}{T'_{im} + \tau'_m} \quad i = 1,2$$

By using Equation 5.1, it was calculated that a sharp decrease in r_1 is seen when the water distance increases from 2 to 8 Å, with water further than 8 Å barely contributing to relaxivity, as shown in Figure 5.5. This water is defined as in proximity to Gd(III). When considering the coiled coil, the outside of the alpha-helix backbone is approximately 9.2 Å from the Ln(III) centre, with the amino acid side chains extending to a maximum of 9.5 Å, illustrated in Figure 4.19. This indicates that any water present within the hydrophobic core of the coiled coil will have a substantial effect on relaxivity. Water molecules outside of the coiled-coil motif and coordinated to the exterior of the coiled coil will not have a significant influence on relaxivity. This could explain why no significant difference was observed between Mo1-2 and MB1-2 in Chapter 4.

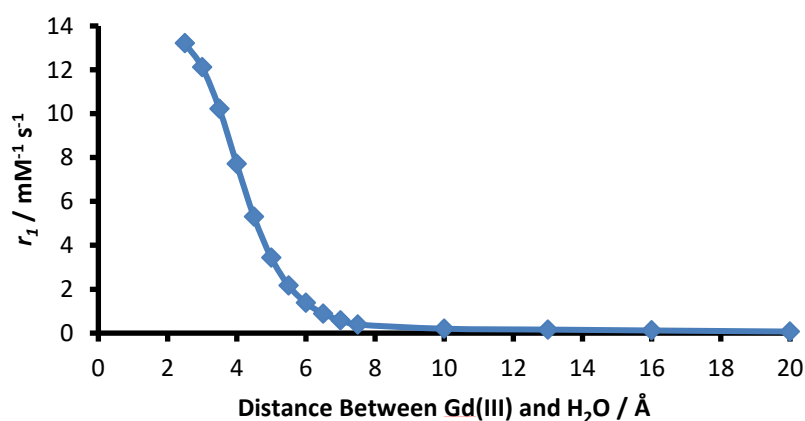


Figure 5.5: A graph to show the change in r_1 when the distance between Gd(III) and H₂O increases (7 T).

The contribution of each water molecule located in the channel in the MB1-2 simulation was calculated using Equation 5.1, with the values given in Table 5.1. A bulk water concentration $[\text{H}_2\text{O}]$ of 55.6 mol L^{-1} , τ_R of 6.6 ns and a τ'_m of 1 ns was used in the calculation. By adding the contributions of the secondary sphere water together an overall r_1 of $4.0 \text{ mM}^{-1} \text{ s}^{-1}$ was calculated, compared to the experimental value of $4.1 \pm 1.2 \text{ mM}^{-1} \text{ s}^{-1}$, showing all relaxivity for MB1-2 could be assigned to secondary sphere effects.

Table 5.1: Calculated secondary sphere water contributions to r_1 ; calculations are based on Equation 5.1 with a $q' = 1$ at each water distance. Water distances are measured from a 20 ns snapshot of the MB1-2 simulation.

| Water distance / Å | $r_1 / \text{mM}^{-1} \text{ s}^{-1}$ |
|--------------------|---------------------------------------|
| 5.0 | 3.10 |
| 6.5 | 0.73 |
| 9.2 | 0.10 |
| 10.2 | 0.05 |
| 13.6 | 0.01 |

The water channel in MB1-2 was found to be highly significant, as all water contributed to the relaxivity. It was of interest to examine what would happen if the water channel was blocked, as a proof of concept, and to better understand the role of secondary sphere water interactions. In order to try and block the water channel a new peptide, SN1-2, was designed. In this new peptide, D-Ile replaced the L-Ile located in the α position above the Ln(III) binding site, with the peptide sequence given in Table 5.2, where **X** represents D-Ile and the structure compared to MB1-2 in Figure 5.6.

Table 5.2: MB1-2 and SN1-2 peptide sequences used to investigate secondary sphere water interactions.

| Peptide | Sequence |
|---------|--|
| MB1-2 | Ac – G IAAIEQK IAANEWK DAAIEQK IAAIEQK IAAIEQK G – NH ₂ |
| SN1-2 | Ac – G IAAIEQK <u>X</u> AANEWK DAAIEQK IAAIEQK IAAIEQK G – NH ₂ |

It was proposed that the insertion of D-Ile above the binding site would block the water channel located above the Ln(III) binding site as the D-Ile side chains would point towards the C-terminus. This in turn would eliminate water in close proximity to Gd(III). MD simulations of SN1-2 were attempted using AMBER, as with previous peptides, in order to compare the structure with MB1-2. However, the D-Ile was not well tolerated in the equilibrium step of the simulation and the D-Ile would revert back to L-Ile, despite this not being possible physically. This was thought to be because of the sterics within the hydrophobic core and the hindrance of having a D-isomer surrounded by L-isomers in a tightly packed system. A number of techniques were used in order to try and stop this from happening; for example, using a lower density of water in the hydration box, manually reverting the amino acid back to the D-isomer after each step, and trying to fix the D-isomer in position. None of these techniques gave a result that was computationally accurate and could be critically compared to the 20 ns MB1-2, especially when considering the location of secondary sphere water. Further work could be undertaken to better understand the SN1-2 system using MD simulations. MD is only one way of analysing a peptide structure and often gives results which are different to those achieved using spectroscopic and analytical laboratory techniques. This has previously been observed by Berwick and co-workers where they observed $q = 1$ for MB1-2 using MD simulations and experimentally found it to be $q = 0$. Therefore, in this chapter blocking of the channel was quantified using experimental techniques such as determining the amount of inner-sphere water, and the water that contributes to q from outer sphere effects. The relaxivity of the new

peptide will be compared to MB1-2 and will be lower if the channel is blocked, due to the possibility that all of MB1-2 relaxivity being attributed to secondary sphere water coordination.

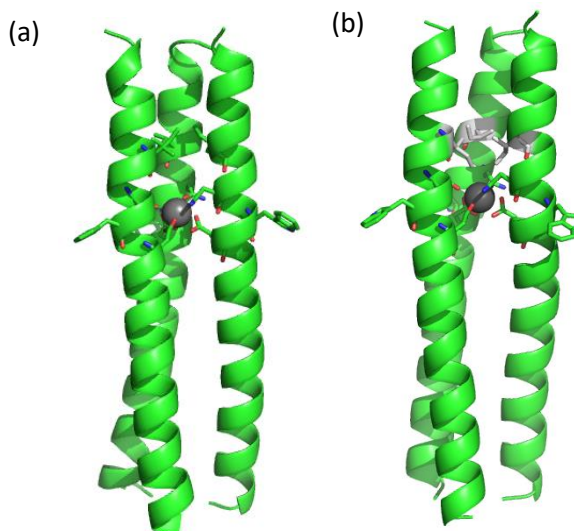


Figure 5.6: Schematic diagram of (a) MB1-2 and (b) SN1-2 with the peptide backbone shown as a cartoon, the Ln(III) metal as a sphere and binding site amino acids, Ile layer above the binding site and the tryptophan sensitizer displayed as sticks. The substitution for D-Ile is shown in grey in (b).

When analysing initial MD models of SN1-2 (post minimisation, pre equilibrium), it can be observed that the D-Ile substitution would block water access, as shown in Figure 5.7. Although further modelling was not possible, this initial structure gave an insight into the accessibility of the Ln(III) binding site of SN1-2 when compared to the secondary sphere water locations from the 20 ns MB1-2 simulation. D-Ile residues come within 4 Å of the Gd(III) ion and water is estimated to be blocked so that it can be no closer than 9 Å from Gd(III). The blocking of this water is expected to result in a decrease in relaxivity of $3.83 \text{ mM}^{-1} \text{ s}^{-1}$, using the data from Table 5.2.

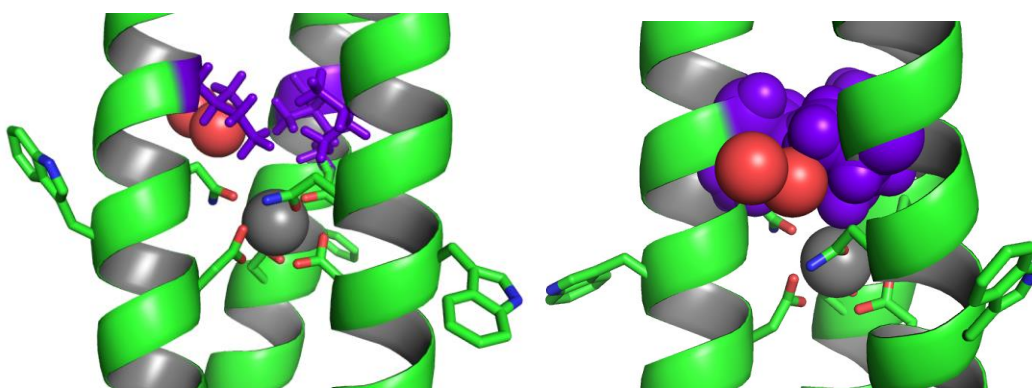


Figure 5.7: Initial MD model of SN1-2 overlaid with the secondary sphere water locations of MB1-2 shown as red spheres. (a) The substitution for D-Ile is shown as blue sticks and are shown to block the entry of secondary sphere water to the Ln(III) (b) D-Ile residues are shown as blue spheres and are shown to block the channel that was present in MB1-2, so that secondary sphere water cannot move in proximity to Ln(III). The peptide backbone is shown as a cartoon, the Ln(III) metal as a sphere and binding site amino acids and the tryptophan sensitizer displayed as sticks.

5.3.3 Secondary Structure

The secondary structure of SN1-2 was investigated using CD spectroscopy; with the spectra shown in Figure 5.8. A 30 μM solution of SN1-2 monomer, yields a CD spectrum representative of a poorly folded random coiled coil ($\Theta_{222} = -4900 \text{ dmol}^{-1} \text{ cm}^2$; $13 \pm 2\%$ folded). The addition of 10 μM GdCl_3 to the above sample leads to a spectrum representing enhanced coiled-coil folding with minimum at 208 and 222 nm ($\Theta_{222} = -10160 \text{ dmol}^{-1} \text{ cm}^2$; $26 \pm 1\%$ folded). This can be compared to MB1-2 which is poorly folded in the apo form ($21 \pm 3\%$ folded) and becomes well folded on the addition of 10 μM GdCl_3 ($62 \pm 3\%$ folded).⁹⁷

The poorly folded nature of the peptide could be due to the insertion of a D-amino acid into the hydrophobic core of the coiled coil. It has previously been shown, in the work of Pecoraro, that when a L-amino acid is substituted with a D-amino acid the ellipticity at 222 nm is still indicative of a right-handed α -helix, however, it decreases in intensity, suggesting a decrease in folding by around 40%.¹⁶¹ This is comparable to the decrease observed for SN1-2

compared to MB1-2. Within the hydrophobic core of the coiled coil, the amino acid side chains are closely packed and so an amino acid which is the opposite isomer has no room to sit, causing steric repulsion.

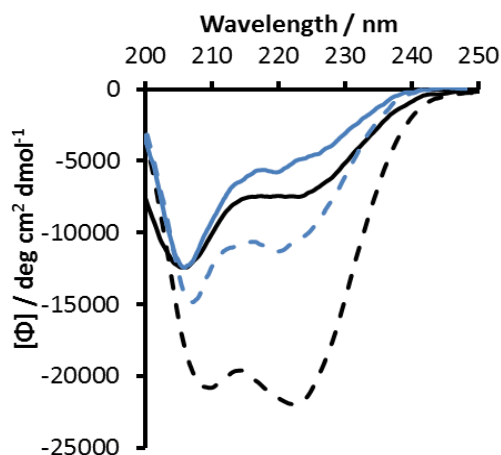


Figure 5.8: CD profile of 30 μM monomer peptide (blue) SN1-2 and (black) MB1-2 in the presence (dashed) and absence (line) of 10 μM GdCl_3 ran in 10 mM HEPES buffer pH 7.

Aliquots of GdCl_3 were titrated into a 30 μM solution of SN1-2 monomer and monitored by CD, initially leading to a gradual increase in the signal at 222 nm which plateaued at higher equivalents, as shown in Figure 5.9. A $\frac{1}{3} \text{Gd} + \text{SN1-2} \rightleftharpoons \frac{1}{3} \text{Gd}(\text{SN1-2})_3$ binding model was used, giving an average association constant ($\log K_a$) of 4.7 ± 0.2 . This can be compared to MB1-2 where a $\log K_a$ of 5.1 ± 0.2 was calculated. The binding constants are the same for SN1-2 and MB1-2, within the error of the experiment, suggesting that despite SN1-2 being less folded, the introduction of D-Ile has little impact on Ln(III) binding. This could be expected as there has been no change made to the binding site amino acids and only one substitution to the amino acids in the sequence.

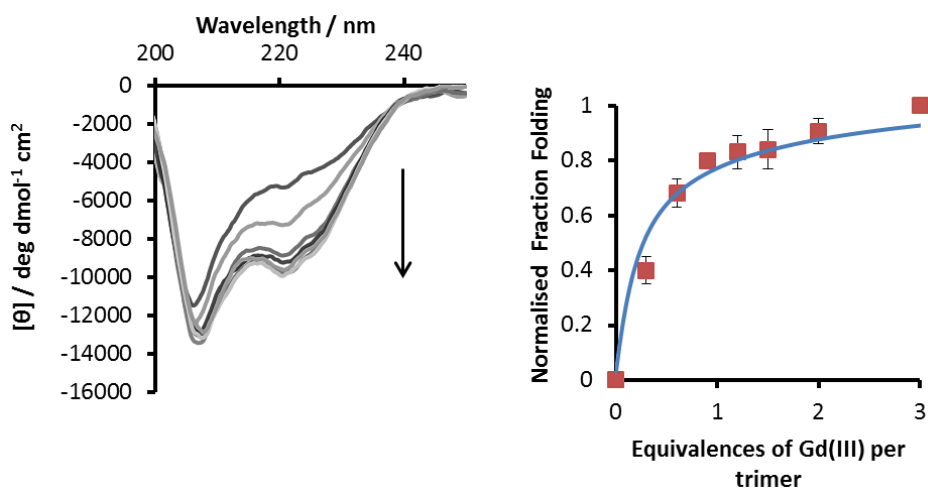


Figure 5.9: (a) CD spectra of 30 μM SN1-2 in the presence of increasing aliquots of Gd(III) in 10 mM HEPES buffer pH 7.0. (b) The normalised fraction folding of SN1-2 and using a peptide + $\frac{1}{3}$ Gd(III) \leftrightarrow $\frac{1}{3}$ (Gd(Peptide)₃) model allowed for the calculation of a binding constant. Error bars are standard deviation for n=3 experiments.

5.3.4 Tb(III) Binding and Luminescence

TbCl₃ titrations were monitored directly by luminescence in order to further investigate Ln(III) binding, with the spectra shown in Figure 5.10. A solution of 30 μM SN1-2 monomer was excited at 280 nm and the emission spectrum monitored from 455 - 700 nm. Similar spectra were recorded on addition of aliquots of TbCl₃. A $\frac{1}{3}$ Tb + SN1-2 \leftrightarrow $\frac{1}{3}$ Tb(SN1-2)₃ binding model was used to interpret the data, giving an association constant ($\log K_a$) of 4.7 ± 0.4 . This can be compared to the previously investigated MB1-2 for which a $\log K_a$ of 5.5 ± 0.2 was calculated. This shows the same trend as the CD titrations and represents no significant difference in Ln(III) binding between the two peptides, despite the fact that SN1-2 is poorly folded in both the apo and metallo complexes and MB1-2 is well folded on addition of Gd(III).

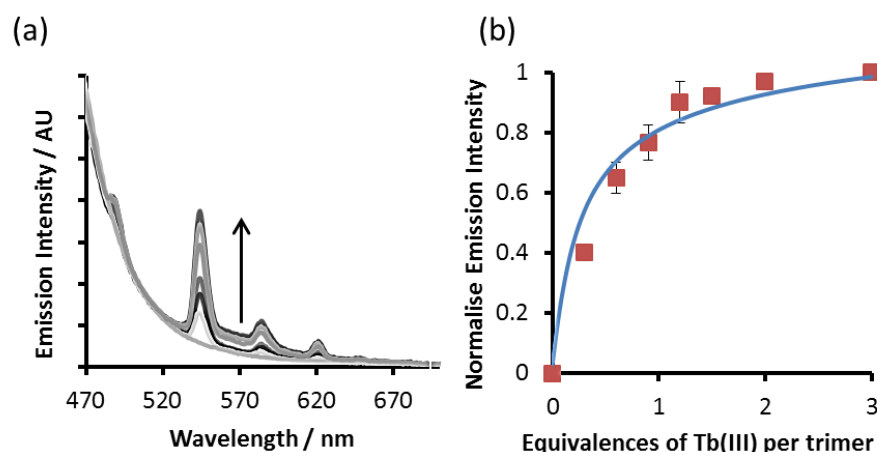


Figure 5.10: (a) Emission profile of SN1-2 with increasing aliquots of Tb(III) ran in 10 mM HEPES pH 7, using a $\lambda_{\text{exc}} = 280$ nm. (b) The normalised emission, fitting data for a peptide + $1/3$ Gd(III) \Leftrightarrow $1/3$ (Gd(Peptide)₃) allowing the calculation of a binding constant. Error bars are standard deviation for n=3 experiments.

5.3.5 Water Coordination

When calculating water coordination to a Ln(III), two methods can be used. The Horrocks-Sudnick equation^{162,163} calculates the number of water molecules coordinated to the Ln(III). The Parker-Beeby equation¹¹⁶ allows for correction to remove any contribution from outer sphere water effects. By comparing q calculated from each of these equations, the contribution from outer sphere effects can be considered.

Luminescence lifetime decays in H₂O and D₂O were measured in order to quantify the amount of inner-sphere water coordinated to Tb(III) when bound to SN1-2. The lifetime decays at 545 nm were measured as 1.2 ± 0.0 ms in H₂O and 2.1 ± 0.1 ms in D₂O, with the decay curves shown in Figure 5.11. The inner-sphere water coordination was calculated as $q = 1.5 \pm 0.1$ using the Horrocks-Sudnick equation.^{162,163}

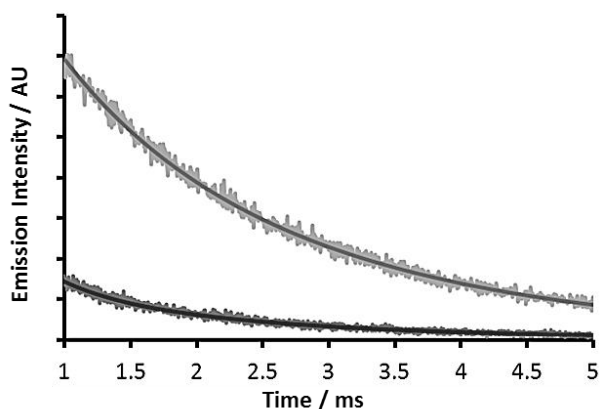


Figure 5.11: Decay profiles of Tb(III) emission at 545 nm for 100 μM SN1-2 monomer on addition of 10 μM of Tb(III) in 10 mM HEPES buffer pH 7.0, fit to a mono-exponential decay for H_2O (light) and D_2O (dark) allowing for calculation of q values.

In order to correct for contributions from the outer sphere water, the Parker-Beeby equation¹¹⁶ was used, giving $q = 1.5 \pm 0.1$. This can be compared to the previously reported MB1-2 of $q = 0.4 \pm 0.1$ using the Horrocks-Sudnick equation 0.0 ± 0.1 using the Parker-Beeby equation.⁹⁷ As the Horrocks-Sudnick and Parker-Beeby equations gave the same q for SN1-2, it could be considered that all water is inner-sphere and there are no outer sphere contributions. The increase in water coordination in SN1-2, compared to MB1-2, could be attributed to the lack of folding shown in the CD spectra. Even in the presence of Ln(III), the complex was only $26 \pm 1\%$ folded. This could mean that the binding site is more accessible to water, allowing more water to coordinate to Ln(III) compared to MB1-2; if this was the case one may expect q to be even higher.

5.3.6 Relaxivity and MRI Contrast Agent Efficiency

The relaxivity of SN1-2 was investigated and the longitudinal (T_1) and transverse (T_2) magnetic resonance relaxation times of protons measured, with the relaxivity plotted in Figure 5.12. The measurements were made using CPMG and inversion recovery pulse sequences, with increasing concentrations of $\text{Gd}(\text{SN1-2})_3$ at 300 MHz (7 T). The inverse relaxation times

were plotted as a function of Gd(III) concentration and yielded relaxivities of $r_1 = 9.1 \pm 0.9$ and $r_2 = 39.7 \pm 2.8 \text{ mM}^{-1} \text{ s}^{-1}$ compared to 4.6 ± 0.9 and $21.3 \pm 1.2 \text{ mM}^{-1} \text{ s}^{-1}$ for MB1-2.

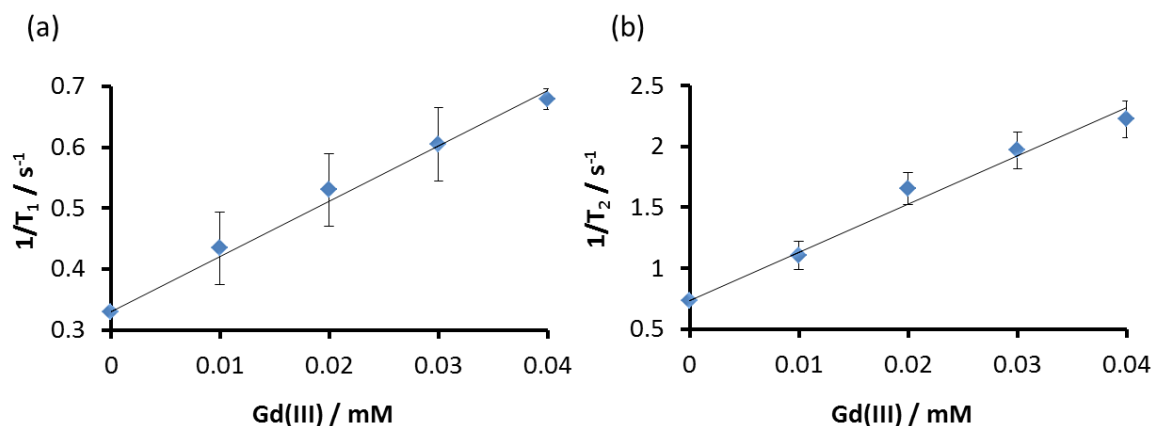


Figure 5.12: Relaxivity plot showing reciprocal of relaxation rate as a function of Gd(III) concentration for (a) T_1 and (b) T_2 for SN1-2. All samples recorded at 7 T at 298 K in the presence of 10 mM HEPES buffer pH 7.0, with two equivalences of peptide trimer per Gd(III). Error bars show standard deviation for data repeated in triplicate.

The increase in r_1 and r_2 for SN1-2 compared to MB1-2 can be attributed to the increase in q from 0.0 ± 0.1 to 1.5 ± 0.1 . Due to the lack of folding of SN1-2, which is thought to be responsible for the increase in water coordination, it was not possible to answer the hypothesis that insertion of a D-Ile above the binding site would block the water channel present in MB1-2. Because of this a new peptide was designed which would compensate for the destabilising nature of the D-Ile.

5.3.7 SN1-3L and MB1-3L Peptide Design

As shown in Chapter 3, the addition of one heptad to a five heptad trimeric coiled-coil has no significant effect on peptide folding, water coordination, or relaxivity when the binding site is at the N-terminus. A new peptide, SN1-3L, was designed with an additional heptad at the N-terminus of the SN1-2 coiled coil. It was hypothesised that the additional 7 amino acids would “zip up” the top of the peptide, forming a well-folded, stable coiled-coil

peptide, whilst allowing the D-Ile residue to block the water channel. The addition of a heptad results in an increase in the number of stabilising hydrophobic layers and salt bridges. The Ln(III) binding site is now in the third and fourth heptad so these two new peptides can also be compared to MB1-3 which has 5 heptads with the binding site in the third and fourth heptad, with data given in Table 1.3. MB1-3 is less folded than MB1-2 ($15 \pm 1\%$ apo and $41 \pm 4\%$ metallo) and the binding constant ($\log K_a = 5.2 \pm 0.36$), q (0.0 ± 0.1), and relaxivity ($r_1 = 4.0 \pm 1.0$ and $r_2 20.9 \pm 1.0 \text{ mM}^{-1} \text{ s}^{-1}$) are the same, within error.

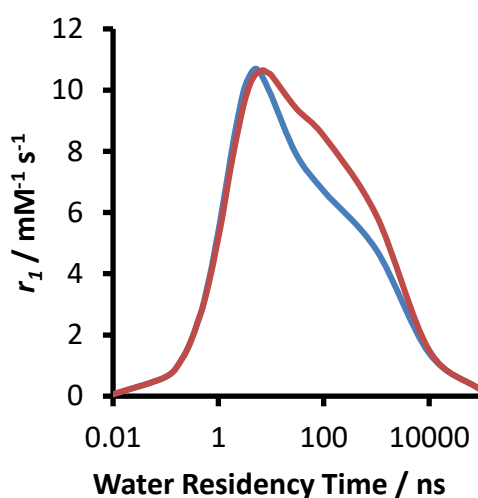


Figure 5.13: Effect of water residency time τ_m (ns), for a $q = 1$ system, on r_1 at field strengths of 7 T with rotational correlation times of 6.9 ns (corresponding to SN1-2 (blue)) and 10.0 ns) corresponding to SN1-3L (red)).

A comparison of the theoretical r_1 of SN1-2 and a new 6 heptad peptide (SN1-3L) was calculated using the SBM equations,^{20,21} represented in Figure 5.13. When calculated at 7 T, using $q = 1$ and a rotational correlation time of 6.9 ns for SN1-2 and 10.0 ns for SN1-3L, with a water residence time of 1 ns, the r_1 relaxivity was predicted to be the same for the two systems. The water coordination of SN1-2 is 1.5 and q for SN1-3L must be determined before accurate comparisons can be made as if q is higher, r_1 will also increase.

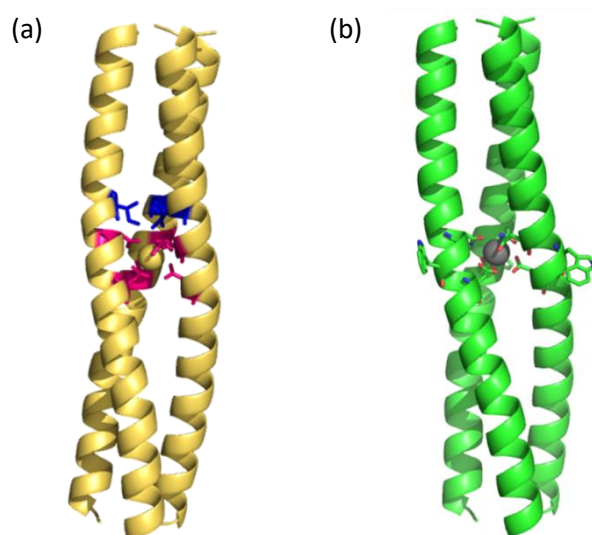


Figure 5.14: Schematic diagram of (a) SN1-3L and (b) MB1-3L with the peptide shown as a cartoon, the Ln(III) binding site amino acids as sticks, and metal ion as a sphere.

In order to reliably determine the influence of D-Ile within the new SN1-3L design, an analogous 6 heptad peptide with a L-Ile in place of the D-Ile was also synthesised, shown in Figure 5.14 and Table 5.3. This would allow any changes in secondary structure or relaxivity to be attributed to the addition of the D-Ile and blocking the channel, instead of due to the increase in peptide length, even though the addition of a heptad was shown not to have an impact when the binding site was located at the N-terminus.

Table 5.3: Peptide sequences used to investigate secondary sphere water interactions, where **X** = D-Ile and binding site amino acids are in bold.

| Peptide | Sequence |
|---------|---|
| MB1-2 | Ac – G IAAIEQK IAANEWK DAAIEQK IAAIEQK IAAIEQK G – NH ₂ |
| SN1-2 | Ac – G IAAIEQK X AANEWK DAAIEQK IAAIEQK IAAIEQK G – NH ₂ |
| SN1-3L | Ac – G IAAIEQK IAAIEQK X AANEWK DAAIEQK IAAIEQK IAAIEQK G – NH ₂ |
| MB1-3L | Ac – G IAAIEQK IAAIEQK IAANEWK DAAIEQK IAAIEQK IAAIEQK G – NH ₂ |

5.3.8 Secondary Structure

The secondary structure of SN1-3L and MB1-3L was investigated using CD spectroscopy, with the resulting spectra shown in Figure 5.15. 30 μM monomer solutions

yielded spectra consistent with a partially folded α -helical coiled-coil for SN1-3L ($\Theta_{222} = -8285$ deg dmol⁻¹ cm², 25 \pm 4 %) and a well folded α -helical coiled-coil for MB1-3L ($\Theta_{222} = -32696$ deg dmol⁻¹ cm², 73 \pm 4 %). The partial folding of SN1-3L is due to the insertion of a D-Ile in the hydrophobic core, and was also observed for SN1-2. Due to the extra length of the peptide an increase in folding compared to SN1-2 is observed.

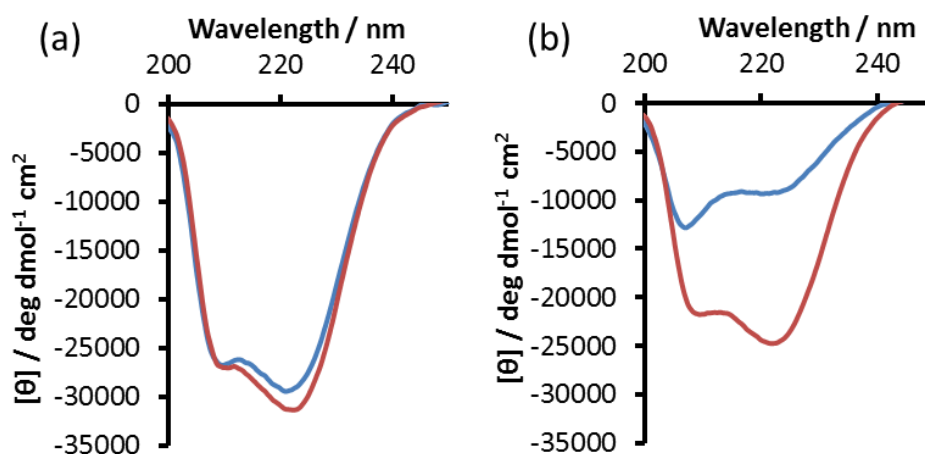


Figure 5.15: CD profile of 30 μ M monomer peptide (a) MB1-3L and (b) SN1-3L in the presence (red) and absence (blue) of 10 μ M GdCl₃ ran in 10 mM HEPES buffer pH 7.

The addition of 10 μ M GdCl₃ to SN1-3L led to an increase in signal at 222 nm, indicating the formation of a well folded α -helical coiled-coil ($\Theta_{222} = -24498$ deg dmol⁻¹ cm², 64 \pm 7 %), as shown in Figure 5.15. MB1-3L formed a well folded structure without the need for Ln(III) templating and so a negligible change was observed ($\Theta_{222} = -33363$ deg dmol⁻¹ cm², 77 \pm 4 %). In comparison to SN1-2, SN1-3L is a well folded coiled-coil upon Ln(III) addition and so can be used in order to test the proposed hypothesis of blocking the water channel above the Ln(III) binding site. Here, the additional heptad provides an increase in folding and compensates for the destabilising introduction of D-Ile.

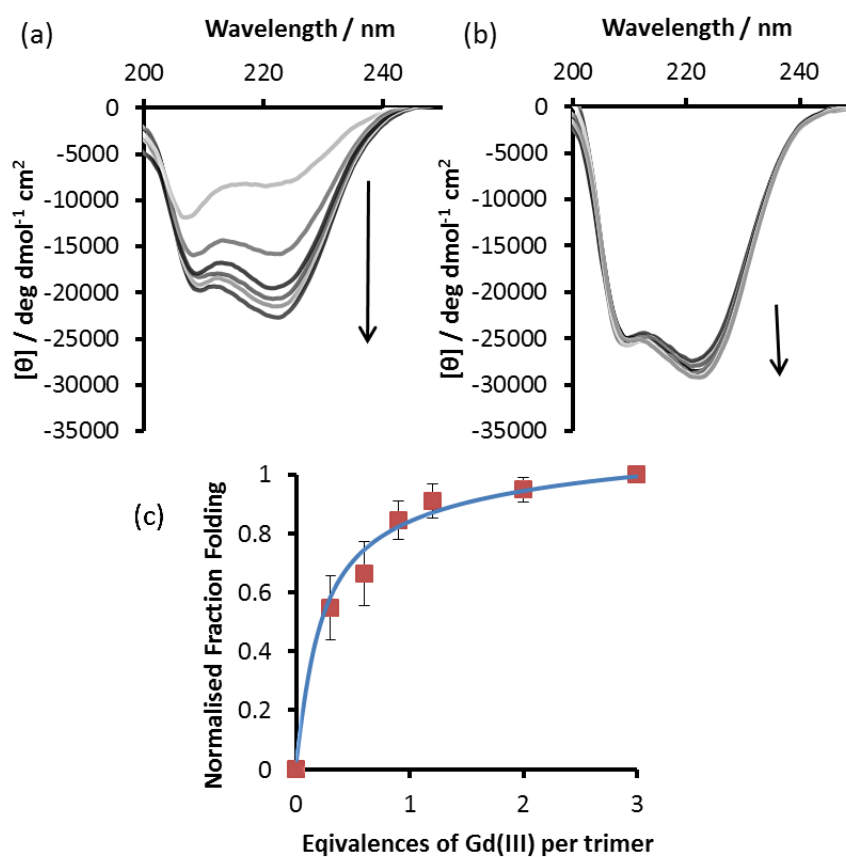


Figure 5.16: CD spectra of 30 μM (a) SN1-3L and (b) MB1-3L with increasing aliquots of Gd(III) in 10 mM HEPES buffer pH 7. (c) The normalised fraction folding is shown for SN1-3L fitting data for a $1/3$ peptide + Gd(III) \leftrightarrow $1/3$ (Gd(Peptide)₃) allowing the calculation of a binding constant. Error bars are standard deviation for n=3 experiments.

A titration of GdCl₃ into a 30 μM solution of peptide monomer was monitored by CD and led to a gradual increase in intensity at 222 nm which plateaued at one equivalence of Gd(III) per trimer for SN1-3L, as shown in Figure 5.16. A $1/3$ Gd + monomer \leftrightarrow $1/3$ Gd(monomer)₃ binding model was used to interpret the data, giving an average association constant ($\log K_a$) of 4.7 ± 0.2 for SN1-3L. In contrast, the analogous titration of GdCl₃ into MB1-3L, showed no significant change in folding, and a binding curve could not be extrapolated. The binding constant for SN1-3L was calculated to be the same as that for SN1-2 suggesting that the additional heptad did not influence the Ln(III) coordination environment. This would be expected as no change has been made to the binding site amino acids and it has been

shown previously with MB1-1 and MB1-1L that increasing the length of the peptide from 5 to 6 heptads has no impact on metal binding.

5.3.9 Tb(III) Binding and Luminescence

TbCl₃ titrations were monitored by luminescence, using the method previously described, with the spectra for SN1-3L and MB1-3L shown in Figure 5.17. Characteristic emission spectra were observed for both peptides with signal intensity increasing on addition of Tb(III) up to one equivalence of Tb(III) per trimer.

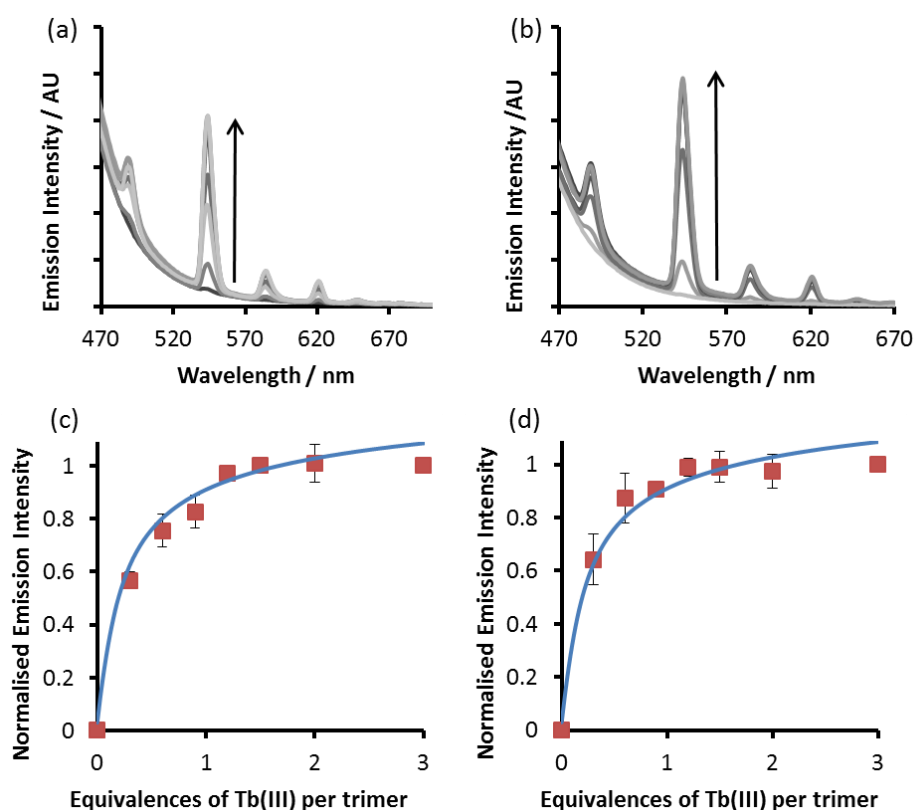


Figure 5.17: Emission profile of (a) SN1-3L and (b) MB1-3L with increasing aliquots of Tb(III) ran in 10 mM HEPES buffer pH 7, using a $\lambda_{\text{exc}} = 280$ nm. The normalised fraction folding is shown below. Fitting data for a $\frac{1}{3}$ peptide + Gd(III) \Leftrightarrow $\frac{1}{3}$ (Gd(Peptide)₃) is shown for (c) SN1-3L and (d) MB1-3L, allowing the calculation of a binding constant. Error bars are standard deviation for n=3 experiments.

A $\frac{1}{3}$ Tb + monomer \Leftrightarrow $\frac{1}{3}$ Tb(monomer)₃ binding model was used to interpret the data, giving an association constant ($\log K_a$) of 4.7 ± 0.5 for SN1-3L and 5.1 ± 0.7 for MB1-3L.

The binding constants for SN1-3L and MB1-3L are the same, within the error of the experiment, compared to SN1-2, MB1-2 and MB1-3. This suggests that the addition of a heptad, to both systems, has caused no change in Ln(III) binding.

5.3.10 Thermal Stability

CD spectroscopy was used to compare the stability of the three new peptides, SN1-2, SN1-3L and MB1-3L, by thermal denaturation, as shown in Figure 5.18. This was conducted to see if the introduction of D-Ile would affect the overall stability of the peptide. It has previously been shown that the introduction of a single D-amino acid can decrease stability by 1 kcal mol⁻¹,¹⁶¹ however removal of a cavity can increase stability by 2-5 kcal mol⁻¹. 30 μM solutions of peptide monomer in the absence and presence of 10 μM GdCl₃, were subjected to a gradual increase in temperature from 25 to 85°C, and the CD signal at 222 nm recorded as an indication of peptide folding.

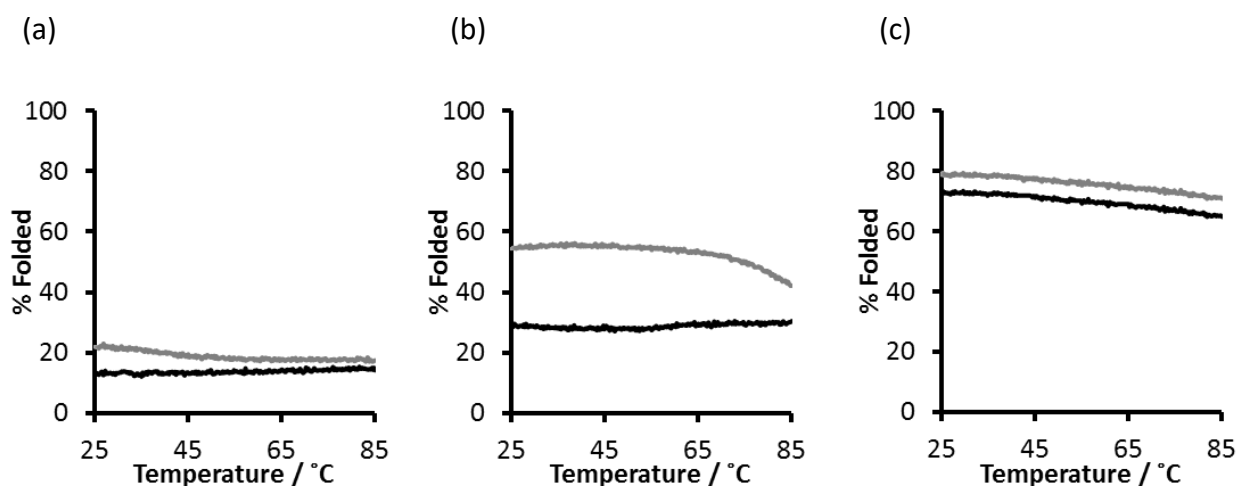


Figure 5.18: Percentage folded data from CD thermal unfolding of 30 μM (a) SN1-2 (b) SN1-3L and (c) MB1-3L monomer in the absence (dark) and presence (light) of 10 μM GdCl₃ in 10 mM HEPES buffer pH 7.0, based on the CD signal at 222 nm.

SN1-2 in the apo and metallo complex was found to be 12% and 22% folded at 25°C, respectively, and stayed largely the same over the measured temperature range. In contrast,

SN1-3L remained at 30% folded in the apo form and decreased in folding from 55% to 42% in the metallo complex but did not become completely unfolded as evidenced by the lack of baseline for the unfolding transition. MB1-3L decreased from 75% folded at 25°C to 65% folded at 85°C in the apo system and 80% to 75% in the metallo complex but remained folded at physiological temperatures.

It can be concluded that SN1-2 has poor stability with respect to thermal unfolding studies, which show it to be entirely unfolded even in the presence of Gd(III). This is vastly different to MB1-2, with the comparable spectra shown in Figure 5.19, suggesting that the insertion of D-Ile into a 5 heptad peptide results in a dramatic decrease in stability. The stability increases for the longer, more folded metallo complexes and MB1-3L was found to be considerably more stable than SN1-3L in both the apo and metallo complex. This suggests that the addition of a D-Ile in both the 5 heptad and 6 heptad peptides results in a decrease in peptide thermal stability. When comparing the spectra of SN1-2 and SN1-3L, SN1-3L appeared to be more stable, despite the fact that the binding constant was calculated to be the same and $\text{Gd}(\text{SN1-3L})_3$ was well folded at physiological temperatures. It has previously been shown that the introduction of a single D-amino acid into a coiled coil consisting of all L-amino acids does not lead to major distortion of the α -helical backbone.¹⁵⁴ The extent to which D-amino acids destabilise the α -helix has been shown to be highly dependent on the size of the side chain, with b-branched amino acids such as Ile being the most destabilising as they are too big to fit into the available space in the hydrophobic core.^{114,154,155,161} The introduction of a single D-amino acid has been shown to destabilise the coiled coil by around 1 kcal mol⁻¹

1,161

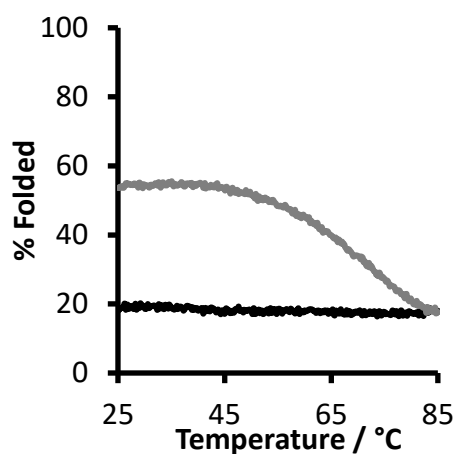


Figure 5.19: Percentage folded data from CD thermal unfolding of 30 μM MB1-2 in the absence (dark) and presence (light) of 10 μM GdCl_3 in 10 mM HEPES buffer pH 7.0, based on the CD signal at 222 nm.

5.3.11 Water Coordination

It was of interest to investigate whether the water channel present in MB1-2 had been blocked in SN1-3L. It was hypothesised that by adding an extra heptad above the binding site, the peptide would be more folded than SN1-2 (as demonstrated by CD) and the D-Ile would block the water channel above the Ln(III) binding site. Luminescence lifetime decays were performed in H_2O and D_2O , with the decay shown in Figure 5.20. The lifetime decays at 545 nm were measured as 2.0 ± 0.0 ms in H_2O and 2.2 ± 0.1 ns in D_2O for SN1-3L and 1.8 ± 0.3 ms in H_2O and 2.4 ± 0.1 ns in D_2O for MB1-3L. This yielded $q = 0.2 \pm 0.1$ for SN1-3L and $q = 0.5 \pm 0.3$ for MB1-3L, using the Horrocks-Sudnick equation¹⁶². When correcting for outer sphere water, using the Parker-Beeby equation¹¹⁶, it was calculated that $q = 0.1 \pm 0.1$ for SN1-3L and $q = 0.2 \pm 0.1$ for MB1-3L.

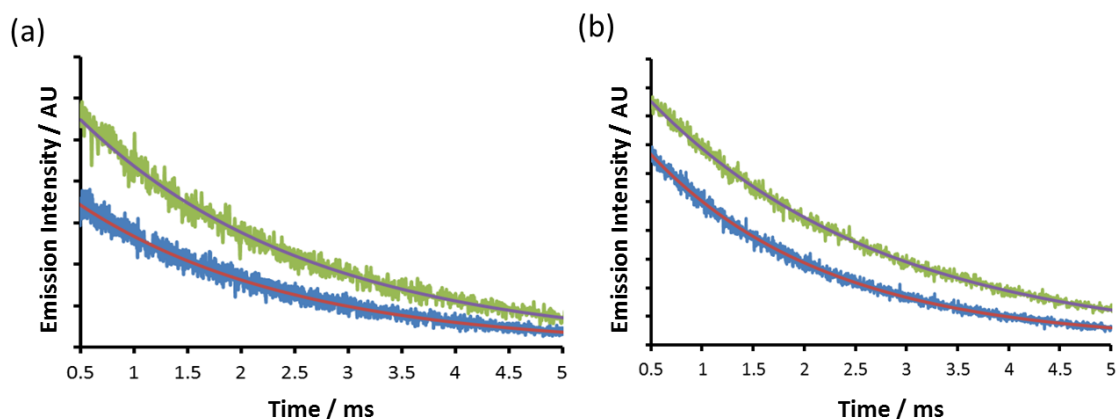


Figure 5.20: Decay profiles of Tb(III) emission at 545 nm for 100 mM monomer of (a) SN1-3L (b) MB1-3L on addition of 0.3 equivalences of Tb(III) in 10 mM HEPES buffer, pH 7.0, data recorded in H₂O (light) and D₂O (dark) and fit to a mono-exponential decay for allowing for calculation of q values.

It was calculated that q was the same for SN1-3L and MB1-3L, within the error of the experiment, when using both the Horrocks-Sudnick and Parker-Beeby equations. This could indicate that the insertion of a D-Ile above the binding site has no effect on the water channel present and no effect on secondary sphere water coordination, or that removing the channel has no effect on inner-sphere water coordination. Additionally, q is found to be lower for the two longer peptides than for SN1-2 which could be attributed to the well folded nature of these metallo peptides compared to SN1-2. However, q for SN1-3L and MB1-3L is the same as MB1-2. This shows the addition of a heptad had no effect on water coordination, as was previously demonstrated with MB1-1 and MB1-1L. This result does not allow conclusions to be drawn on the absence or presence of the water channel and so further investigations are required.

5.3.12 Relaxivity and MRI Contrast Agent Efficiency

It was hypothesised that the relaxivity of SN1-3L would be the same as that of MB1-3L due to the same q but any secondary sphere effects may become apparent by an increase

in relaxivity for MB1-3L. The r_1 and r_2 relaxivities were calculated to be (r_1) 6.3 ± 0.3 and (r_2) $26.8 \pm 2.2 \text{ mM}^{-1} \text{ s}^{-1}$ for SN1-3L and (r_1) 7.9 ± 1.1 and (r_2) $23.2 \pm 3.4 \text{ mM}^{-1} \text{ s}^{-1}$ for MB1-3L at 7 T, with the data shown in Figure 5.21.

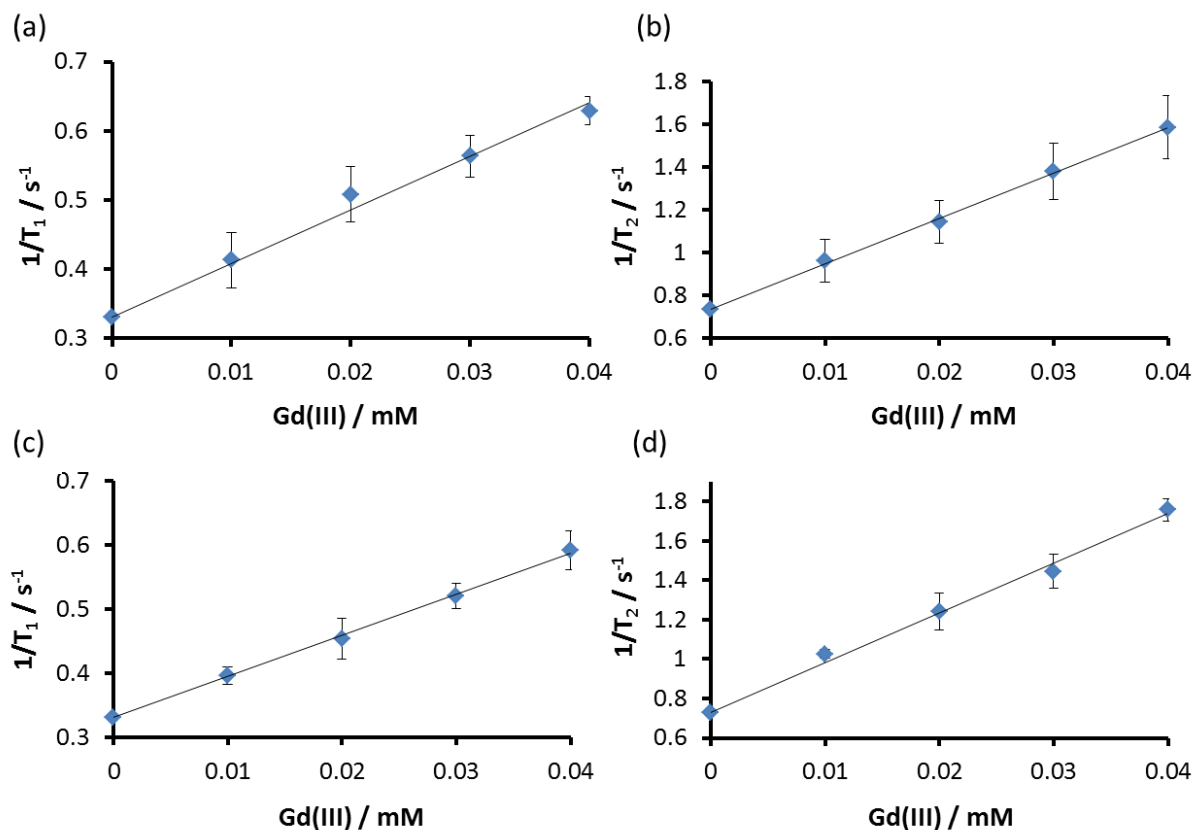


Figure 5.21: Relaxivity plot showing reciprocal of relaxation time as a function of Gd(III)

concentration for T_1 (left) and T_2 (right) for (top) MB1-3L and (bottom) SN1-3L. All samples recorded at 7 T at 298 K in the presence of 10 mM HEPES buffer pH 7.0, with two equivalences of peptide trimer to Gd(III). Error bars show standard deviation from data repeated in triplicate.

No significant difference in r_1 or r_2 was observed between SN1-3L and MB1-3L, which would be expected as q is the same, within error, for the two peptides. This meant that any differences in secondary sphere effects were not significant enough to be observed by a change in relaxivity at 7 T. The relaxivity for both peptides was found to be the same as MB1-2 and MB1-3, within the error of the experiment, suggesting again that the rotational

correlation time has little impact on relaxivity for this class of contrast agent, under these experimental conditions. The results of this experiment meant that a conclusion could not be made regarding the removal of the water channel.

5.4 Conclusions

In this chapter the presence of a water channel observed in the MD simulations of MB1-2 was investigated. The MD simulation was extended to 20 ns and repeated in triplicate in order to further analyse the MB1-2 structure. It was determined that the relaxivity of MB1-2 could be attributed to the presence of a water channel located directly above the Ln(III) binding site which allowed water molecules to sit in proximity (within 8 Å) to Ln(III). This was experimentally investigated through the use of a D-Ile located directly above the Ln(III) binding site with the hypothesis that this would block the water channel, limiting the access to water. This would be accompanied by a decrease in relaxivity and would provide an important insight into the mechanism of relaxivity for when $q = 0$ and allow for a proof of concept into secondary sphere water.

Three new peptides were synthesised. SN1-2 consisted of 5 heptad repeats with D-Ile located above the Ln(III) binding site. The peptide was insufficiently folded resulting in water accessing the unstructured metal binding sites and so could not be used for meaningful comparison. Two further peptides, MB1-3L and SN1-3L, consisting of 6 heptad repeats, showed an increase in peptide folding compared to MB1-2 and SN1-2. SN1-3L had a D-Ile above the metal binding site and MB1-3L was used as a control with an L-Ile in the same position. Both peptides were well folded and had no water located in the inner-sphere, directly coordinated to the Ln(III). Relaxivity data showed SN1-3L and MB1-3L to have the same r_1 and r_2 relaxivity, within error.

Through the use of a D-Ile, in SN1-2, the water channel located in MB1-2 appeared to be blocked in initial MD simulations. Further work could be completed in order to provide further insight into SN1-2 and SN1-3L systems, using MD simulations, to visualise the presence or absence of a channel within the hydrophobic core.

When comparing SN1-3L and MB1-3L experimentally, no significant difference was observed in q and there was no change in relaxivity suggesting that the water channel had not been blocked and water was still able to be located in proximity to Gd(III). Alternatively, the channel had been blocked in both peptides and so the secondary sphere water effects were the same in both systems.

Chapter 6: Investigating the Introduction of Ln(III) Coiled Coils into Biological Systems

6.1 Introduction

Magnetic resonance imaging (MRI) is a widely used clinical imaging technique which provides contrast without using ionising radiation.¹⁶⁴ MRI has major advantages for soft tissue imaging as it is non-invasive, non-ionising, can penetrate optically opaque systems and has no apparent side effects.³³ The ability to capture information from multiple planes deep within a patient and excellent soft tissue contrast have contributed to the development of MRI as a powerful imaging tool.³³

MRI contrast agents (CA) are used annually in approximately 30 million procedures, with more than 300 million procedures performed to date.¹⁶⁵ Lauterbur and co-workers were the first to demonstrate the effectiveness of using paramagnetic CAs to improve tissue contrast in MRI.² All clinically approved Gd(III) contrast agents (GdCAs) are based on small molecules with relaxivity (r_1 and r_2) of around 4-6 mM⁻¹ s⁻¹.¹⁶⁴ The first GdCAs, Magnevist [Gd(DTPA)]²⁻ and Dotoram [Gd(DOTA)], were extracellular fluid agents, followed by those designed for specific tissue types, for example, liver and gastrointestinal imaging.¹⁶⁶

Most GdCAs are approved at a dose of 0.1 mmol Gd/kg, with kg referring to the weight of the patient, and for MR angiography studies double this dose is sometimes used.^{28,39} Newer agents, such as Gadofosvest, are approved at lower doses (0.03 mmol/kg).¹⁶⁷ The dose administered will impact exposure and elimination times. GdCA kinetics exhibit a distribution phase followed by an elimination phase, as shown in Figure 6.1. If the dose is lowered by a factor of three, the exposure is reduced, as the area under the curve for plasma elimination becomes smaller. If the dose remains the same but the elimination and distribution becomes

longer then the area under the curve will be larger and the patient will be exposed to Gd(III) for longer.³⁵ This occurs in renally impaired patients, such as those with Nephrogenic Systemic Fibrosis (NSF). For clinically approved GDCAs, there is no intracellular distribution around the body, apart from sometimes in the liver.³⁶

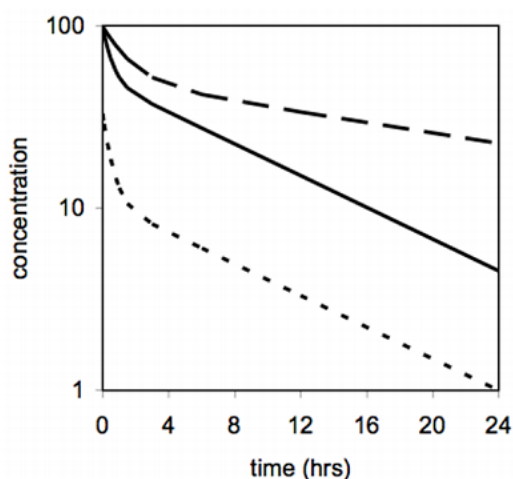


Figure 6.1: Graph to show the effect of dose and half time on Gd(III) exposure to the patient. The dotted line represents compound administered at 0.3 x dose for the same GdCA represented by the solid line. The dashed line shows the effect of a 3 x longer half-life, compared to the same dose of the solid line, for example in a renally impaired patient. Figure reproduced with permission from Aime, S.; Caravan, P. J. *Magn. Reson. Imaging* 2009, 30 (6), 1259–1267.

Following the injection of a GdCA into a patient, the compound distributes in the blood and extracellular space. The terminal half-life for blood elimination is about 1.5 hours for patients with normal renal function.^{35,36} Preclinical animal studies indicate that GdCAs currently on the market are excreted rapidly and intact.³⁵ As GdCAs are exclusively eliminated by the kidneys.¹⁶⁸ In patients who suffer from renal diseases, for example NSF, the half-life of GdCA elimination can increase from hours to days depending on the severity of the disease.^{168,169} This slow removal of Gd(III) can result in deposition of Gd(III) in the brain, skin and internal organs.^{168,170,171} Pharmacokinetic studies in patients with NSF show the complete

removal of the GdCA after 7 days. In healthy patients this will have occurred within 12 hours.^{35,172,173}

It is still not established if the Gd(III) retained in patients with renal disease is coordinated, as part of the CA, or has dissociated from the complex. It could dissociate from the CA and be present as an insoluble inorganic deposit such as the carbonate or phosphate salt. It could also be present in the binding site of calcium binding proteins.^{174,175} It has been reported that Gd(III) can replace Ca(II) in proteins resulting in inhibition of protein function, for example in Ca(II) carrier proteins in cell membranes.³⁵

Experiments of GdCA stability in human serum showed that 20% of Gd(III) was released from Gadoversetamide (Optimark) and Gadodiamide (Omniscan) after 15 days at pH 7.4 and 37°C, structures shown in Figure 6.2.¹⁷⁶ This suggests that patients suffering from renal disease could be exposed to free Gd(III) if Gadoversetamide or Gadodiamide were administered.³⁵

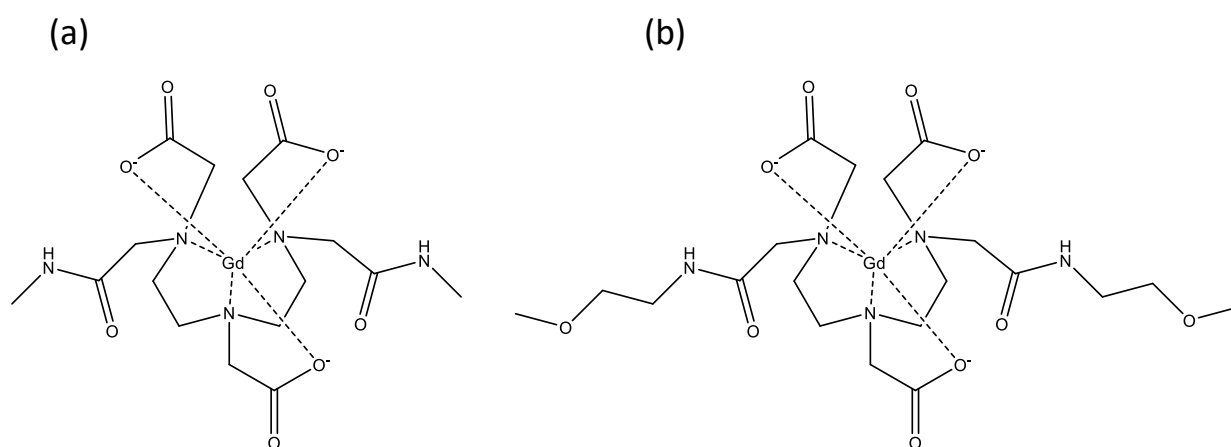


Figure 6.2: Structures of clinical MRI CAs; (a) Gadoversetamide (Optimark) and (b) Gadodiamide (Omniscan).

Metals with a high affinity for a Gd(III) binding site can increase transmetalation, for example Zn(II), Cu(II) or Fe(III). It is well established that Gd(III) release increases with

decreasing pH. Therefore, the rate of Gd(III) release will be enhanced in areas of low pH, for example in the renal proximal tubes.

When comparing small molecule CAs to peptide-based designs, peptides sometimes face challenges regarding metal selectivity and pharmacokinetic stability. One peptide-based MRI CA (ProCA32) is highly selective, has high relaxivities (both r_1 and r_2) and has the appropriate liver retention time and distribution for MR imaging.¹⁶⁴ ProCA32 was developed by converting a natural Ca(II) binding protein, parvalbumin, into a Gd(III) binding protein which is also PEGylated. This is the first of its kind to report an increase in relaxivity (r_1 of $33.4 \text{ mM}^{-1} \text{ s}^{-1}$ and r_2 $44.6 \text{ mM}^{-1} \text{ s}^{-1}$ of at $37 \text{ }^\circ\text{C}$ and 1.4 T) without compromising metal binding stability, selectivity and pharmacokinetics, with the Gd(III) binding affinity comparable to that of DTPA.¹⁶⁴

6.2 Aims

In this chapter two peptides, MB1-1 and MB1-2, were investigated for their potential use in biological systems. As the peptides have different positions of the Ln(III) binding site and different amounts of inner-sphere water coordination, $q = 3$ and 0 respectively, it was of interest to investigate how this would affect the extent of transmetalation. Transmetalation, in MB1-1 and MB1-2, was investigated using a number of biologically relevant metals and under physiological buffer conditions. Finally, two cell lines were treated with $\text{Gd}(\text{MB1-1})_3$ at MRI relevant concentrations in order to assess the toxicity of the metallo complex.

6.3 Results and Discussion

6.3.1 Displacement of Ln(III) with Medically Relevant Metals

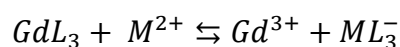
NSF, a disease which results in renal failure, can be linked to the use of GdCA.^{37,177} One hypothesis to explain this is the dissociation of Gd(III) from its support. Many studies have

been performed *in vivo* and *in vitro* in an attempt to determine the extent and mechanism of dissociation. It has been determined that there are three dissociation mechanisms between Gd(III) and its chelate with dechelation and transmetalation being the most common.^{30,34}

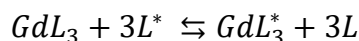
(1) Dechelation due to:



(2) Transmetalation of Gd(III) by an endogenous metal, especially, Ca(II), Cu(II) and Zn(II) corresponding to the reaction:



(3) Ligand exchange *via* the reaction:



It has been previously reported that a Gd/phosphate ratio of 1:100 will result in phosphate-induced gadolinium release by ligand exchange when using Gadodiamide (Omniscan),³⁴ structure shown in Figure 6.2(b). The presence of cations such as Ca(II), Cu(II) and Zn(II) has been shown to accelerate the release kinetics of gadolinium, either by catalysing ligand exchange or by inducing transmetalation.³⁴

By comparing MB1-1 and MB1-2, the effect of Ln(III) binding site position, and *q* value, on transmetalation could be investigated. It was hypothesised that MB1-2 would have less transmetalation due to the Ln(III) binding site sitting deeper into the hydrophobic core and being less accessible to competing metals.

Luminescence was used to determine the extent of transmetalation with Na⁺, K⁺, Ca²⁺ and Zn²⁺. In each experiment, the sample was excited at 280 nm and the emission spectrum monitored from 455 - 700 nm. The spectra were then integrated between 530 – 560 nm. Tb(III) was used as a model for Gd(III), as described in previous experiments.

First a sample of 30 μM peptide monomer was run with integration of the spectra giving a base value for 0% Tb(III) binding. 10 μM Tb(III) was added to the above sample and left to equilibrate for 20 minutes before measuring. Integration of this spectrum gave a value for 100% Tb(III) binding. Each metal (NaCl, KCl, CaCl_2 and ZnCl_2) was added to individual samples and left to equilibrate for 20 minutes, in aliquots of 10 μM , 100 μM , 1 mM and 10 mM. By integrating each spectra and comparing to the 0% and 100% Tb(III) binding controls, the percentage of Tb(III) binding could be calculated for each sample. The average of three experiments with standard deviation error bars is shown in Figure 6.3.

It can be observed that the singly charged metals (Na(I) and K(I)), shown in Figure 6.3(a) and 6.3(b), result in very little transmetalation in either the MB1-1 or the MB1-2 system, even at 1000 equivalences of metal compared to Tb(III) concentration. In comparison, a displacement of approximately 20% was observed with Ca(II) and Zn(II) in the MB1-1 system at 100 μM , shown in Figure 6.3(c) and 6.3(d). This increased to 30% and 90% transmetalation for 1 mM and 10 mM Zn(II) and 30% and 60% transmetalation for Ca(II), respectively. In comparison, little transmetalation occurred in MB1-2 with 20-40% displacement occurring at 10 mM and little change at lower concentrations.

The Asn_3Asp_3 Ln(III) binding site, located in the hydrophobic core of the coiled coil is designed to accommodate metals with a 3^+ charge, in part due to the 3^- charge associated with the binding site residues. The size and number of ligands makes the site ideal for Ln(III) binding. In MB1-1, the binding site sits at the top of the coiled coil and can be thought of as more accessible and more dynamic than the MB1-2 site which is located a heptad further into the hydrophobic core of the coiled coil. On addition of the biologically relevant metals described above, an increase in transmetalation was observed in the MB1-1 system, illustrated by a decrease in Tb(III) emission. This could be due to the positioning of the MB1-1

site as it is easier to access and is more dynamic. As it is positioned at the top of the coiled coil it has the ability to bind a metal using only some of the potential ligands whilst still maintaining a folded coiled-coil structure. Despite the charge of the binding site not being overcome by the biologically relevant metals, it was observed that the binding site will still accommodate the biological metal in preference to Tb(III) at high concentrations.

In comparison, there is less transmetalation occurring in the MB1-2 system (maximum of 40%) independent of which metal is used. This could be due to the binding site now being buried in the hydrophobic core of the coiled coil making it less accessible to competing metals. Furthermore, the apo-MB1-2 system is unfolded and the peptide requires Ln(III) binding to form a well folded coiled coil.

In both systems, as the destabilising charge of the binding site is not overcome by the metals used, it is less favourable for them to bind compared with Tb(III). When comparing the metals used in this study, it is observed that the 2⁺ metals have a higher potential for transmetalation compared to the 1⁺ metals. As the metal ions used are of a similar size, this is due to more of the destabilising charge of the binding site being overcome more by the 2⁺ metal ions, compared to the singly charged metals.

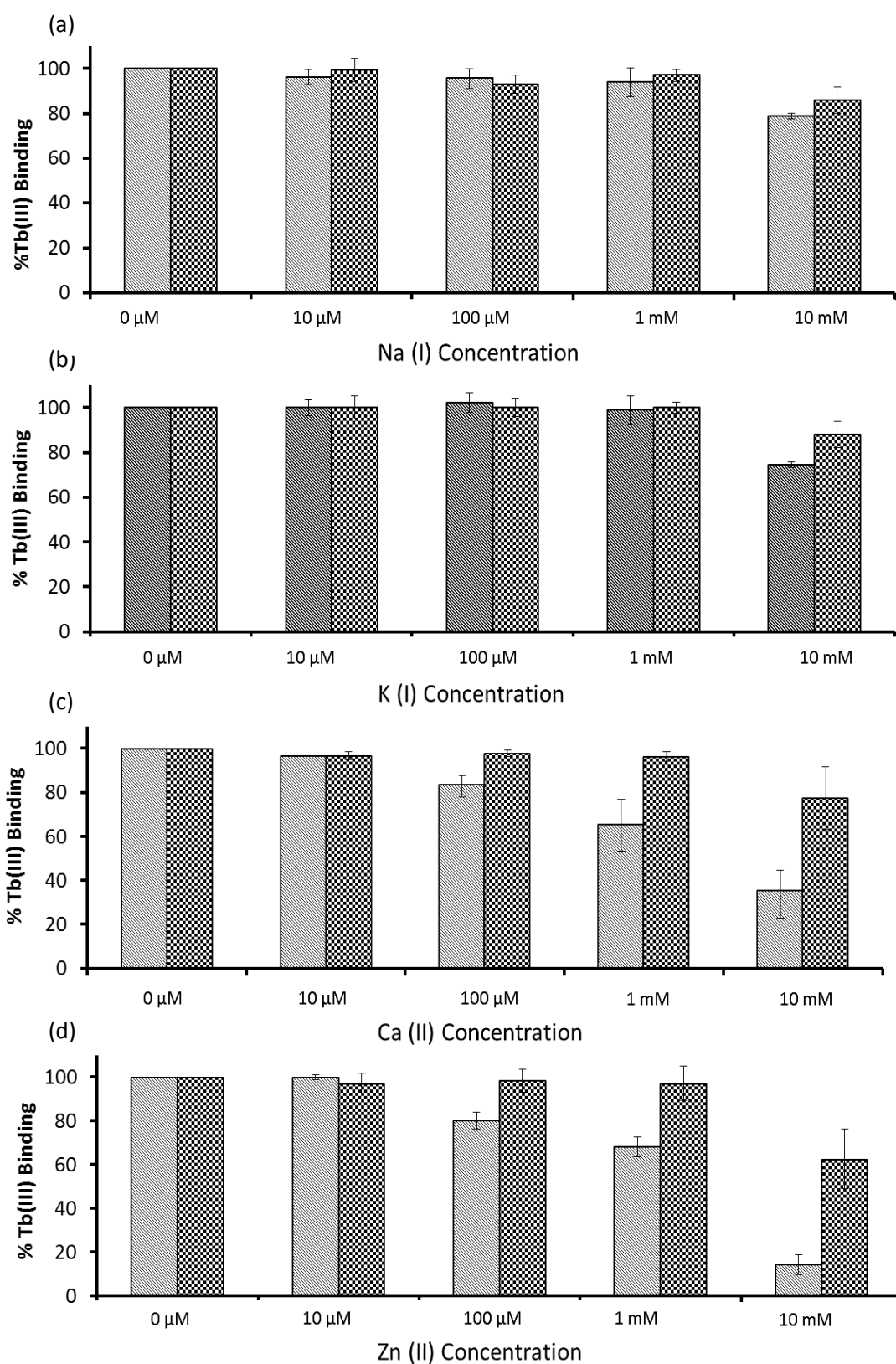


Figure 6.3: Graph to show the % of Tb(III) binding after the addition of physiological metals (a) Na(I), (b) K(I), (c) Ca(II), and (d) Zn(II) for MB1-1 (grey) and MB1-2 (hatched), 10 μ M Tb(III), in HEPES buffer pH 7.0.

6.3.2 Lanthanide Binding under Physiological Conditions

The experiment shown in Figure 6.3 was conducted at pH 7.0 at micro- and milli-molar concentrations. This gave results which can only be compared to other laboratory experiments and cannot be compared to physiological-type systems. Therefore, Tb(III) binding was investigated under physiological-type conditions, using PBS, as a prediction of the extent of dechelation and transmetalation that could occur *in vivo*.

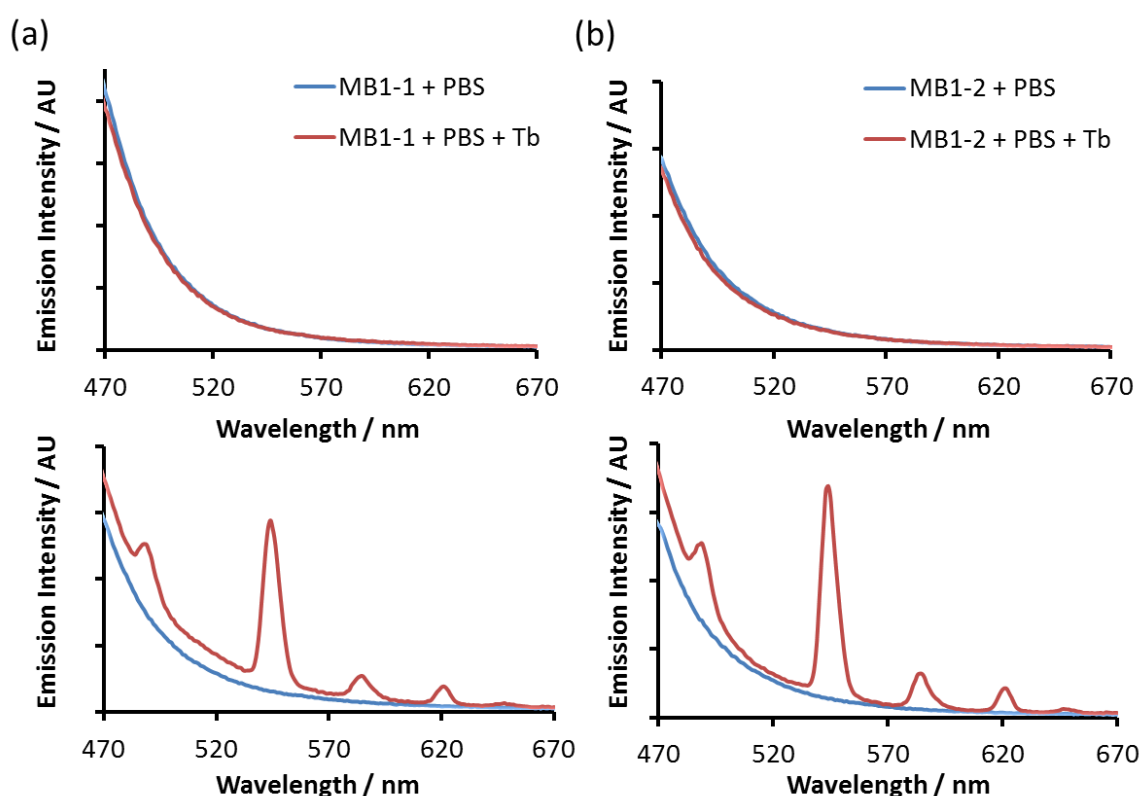


Figure 6.4: Emission profiles of 30 μM (a) MB1-1 and (b) MB1-2 in the absence (blue) and presence (red) of 10 μM Tb(III). Top spectra show experiment in PBS. Bottom spectra show experiments in 10 mM HEPES buffer pH 7.0.

Samples of 30 μM peptide monomer prepared in either HEPES buffer pH 7.0 or PBS were analysed before and after the addition of 10 μM Tb(III) (with an equilibration time of 20 minutes). As observed in Figure 6.4(a) and (b), no Tb(III) binding was observed in the presence of PBS for MB1-1 or MB1-2. In the analogous experiment, using HEPES buffer at pH 7.0, the

characteristic emission peaks are observed. A control experiment of 10 μM Tb(III) in either HEPES buffer pH 7.0 or PBS was also ran, as shown in Figure 6.5 (a) and (b). Here the characteristic peaks were observed but at much lower intensity compared to the peptide spectra due to no sensitisation taking place. Here the characteristic Tb(III) emission peaks are observed in both samples. This suggests that the Tb(MB1-1)₃ and Tb(MB1-2)₃ complexes are unable to form in the presence of PBS. This could be due to the PBS having a higher affinity for Tb(III) compared to the coiled-coil peptides and with the high concentration of PBS driving the formation of Tb-Phosphate complexes. It has previously been observed that a 1:100 ratio of Ln(III) to phosphate will result in phosphate induced Gd(III) release.³⁴ As Tb(III) is unable to bind to the coiled-coil peptide, no sensitisation of Tb(III) takes place and the emission peaks are not observed.

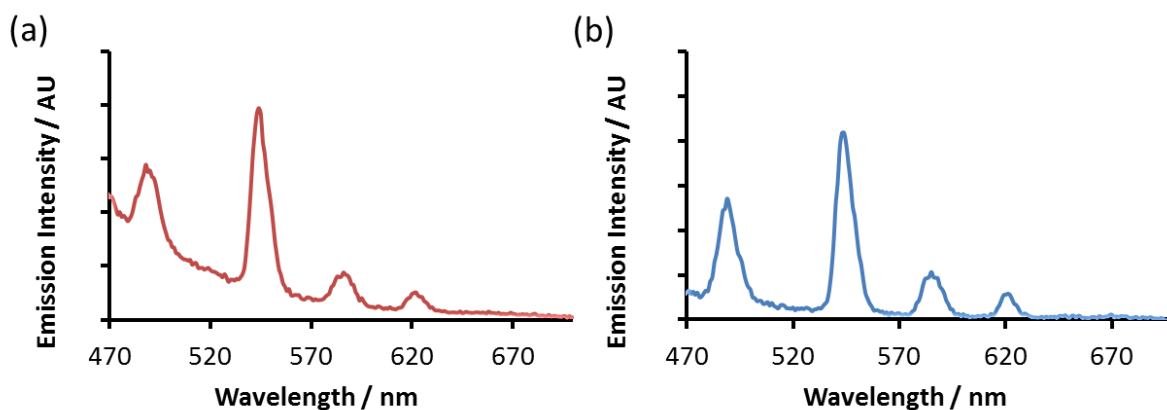


Figure 6.5: Emission profiles of 10 μM Tb(III) in (a) 10 mM HEPES buffer pH 7 and (b) PBS.

In order to investigate this further, Tb(III) binding was investigated using the individual components of PBS at their relevant concentrations and pH. Samples of 30 μM peptide monomer in HEPES buffer pH 7.0 were run, with integration of the spectra giving a value for 0% Tb(III) binding. 10 μM Tb(III) was added to each sample and left to equilibrate for 20 minutes. Integration of the spectra gave a value for 100% Tb(III) binding. Aliquots of the components of PBS (137 mM NaCl, 2.4 mM KCl, 10 mM Na₂HPO₄, 1.8 mM KH₂PO₄) were added

to separate samples of both MB1-1 and MB1-2 and left to equilibrate for 20 minutes. The samples were run and the integration of the spectra compared to the 0% and 100% values in order to give the percentage Tb(III) binding of the sample, with the data shown in Figure 6.6.

When analysing the MB1-1 system, it was found that a 70% decrease in Tb(III) binding was observed with NaCl and a 20% decrease in Tb(III) binding was observed with KCl. On addition of KH_2PO_4 and Na_2HPO_4 , no Tb(III) remained bound to the peptide complex. This is predicted to be due to the high concentration of phosphate present in the sample, compared to the concentration of peptide, which drives the formation of Tb(III) phosphate complexes, due to phosphate induced Tb(III) release from the Ln(III) binding site. Tb(III) phosphate complexes also have a higher association constant ($\log K_a = 6.4$) compared to the $\text{Tb}(\text{MB1-1})_3$ complex. Additionally the low pH of KH_2PO_4 (4.9) and high pH of Na_2HPO_4 (9.3) could destabilise the metallo complex by interfering with the hydrogen bonding network which stabilises the secondary and tertiary structure of the folded coiled coil.

The same is observed for the MB1-2 system. Transmetalation has less impact on the $\text{Tb}(\text{MB1-2})_3$ system due to the binding site being located in the second and third heptad of the coiled coil, making it less accessible to competing ions. Despite this, on addition of KH_2PO_4 and Na_2HPO_4 all Tb(III) has dechelated from the peptide system and no binding was observed. This shows that the presence of phosphate is highly destabilising for the $\text{Tb}(\text{peptide})_3$ complex.

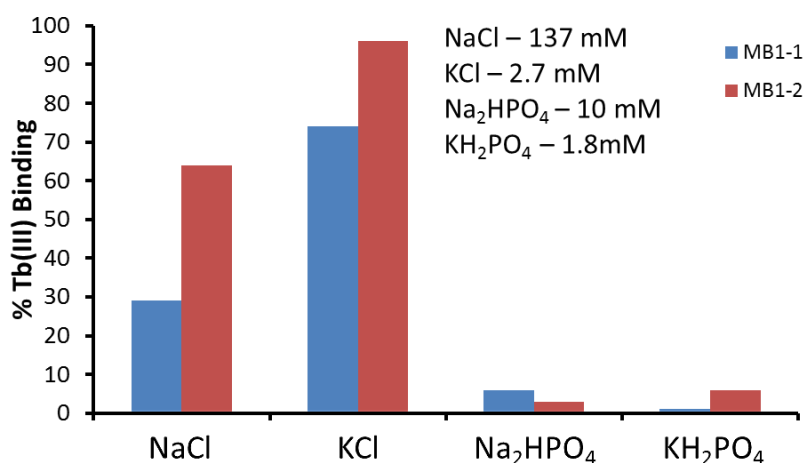


Figure 6.6: A graph to show the % Tb(III) binding in samples containing 30 μ M (blue) MB1-1 and (red) MB1-2 in the respective components of PBS.

6.3.3 Initial Cell Toxicity Testing

In order to continue investigating the behaviour of MB1-1 in physiological systems, preliminary cell studies were undertaken. Cell health can be monitored using a number of different techniques.¹⁷⁸ Plasma membrane integrity, DNA synthesis, enzyme activity, ATP presence and cellular reducing conditions are well known indicators of cell viability.^{137,179,180}

Cell testing was conducted as part of a collaboration with Dr De Cogan at the University of Birmingham Medical School. Apo-MB1-1 and Gd(MB1-1)₃ were used for the cell studies as it is the peptide complex with the highest relaxivity (both r_1 and r_2). It was previously observed that Tb(III) transmetalation and ligand exchange occurred in mock physiological conditions. Therefore, Gd(III) transmetalation may be observed in the *in vivo* cell studies with cell death occurring if Gd(III) is released.

An initial investigation was undertaken using Hela cells. Cells were seeded with increasing concentrations of MB1-1 (0.02, 0.04 and 0.06 mM) and a 0.01 mM Gd(MB1-1)₃ complex was used, the same concentration of Gd(III) as in CA used in the clinic. A blank containing no peptide or GdCl₃ and a 0.01 mM Gd(III) control were also investigated.

24 hours after seeding, the number of cells was counted using a haemocytometer with the processed data shown in Figure 6.7. No significant decrease in cell number was observed for the three apo-peptide concentrations and the Gd(MB1-1)₃ compared to the blank. A significant decrease in cell number was observed with the Gd(III) control, showing cell death occurred when in the presence of free Gd(III). This experiment showed that at a clinically relevant concentration of 0.01 mM, the Gd(MB1-1)₃ complex displayed no toxic effect in the HeLa cell line after 24 hours. This could imply that the Gd(III) remains complexed and is not free in solution. In healthy patients complete GdCA removal will occur within 12 hours suggesting at a concentration of 0.01 mM, Gd(MB1-1)₃ would display no toxic effects in a healthy patient. This is not the same as what was observed in the transmetalation studies where Gd(III) was shown to no longer be complexed. Because of this, further cell studies were undertaken.

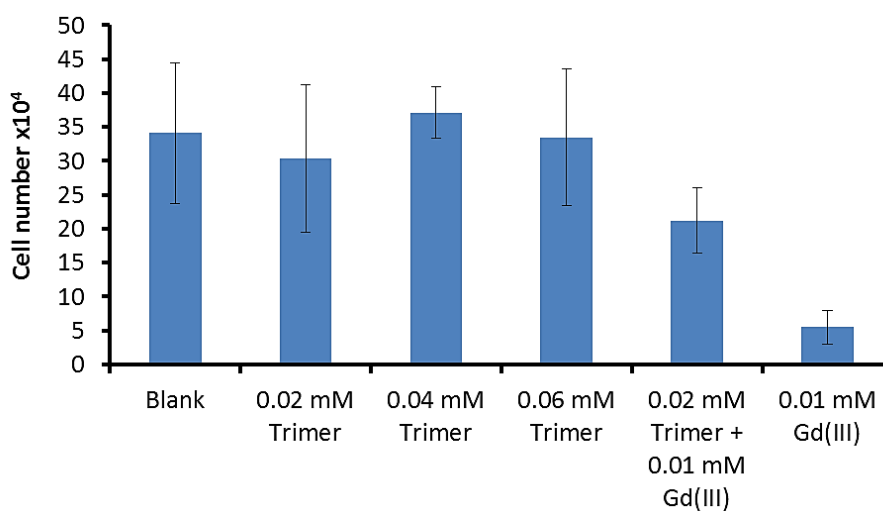


Figure 6.7: HeLa cells incubated with varying concentrations of MB1-1 and one metallo peptide complex after 24 hours incubation time. A blank and a Gd(III) control were also used. Error bars show standard deviation for the experiment.

6.3.4 Investigation of MB1-1 in Cancerous Brain Cells

Hela cells are often used for preliminary cell work as they are easy to cultivate and difficult to infect. It was next of interest to investigate brain cells as a more relevant model for MRI use in the human body. $\text{Gd}(\text{MB1-1})_3$ is non-targeting so a specific tissue type for this CA could not be selected. One of the most common uses of clinical MRI is imaging the brain, and monitoring cancerous brain tissue.¹³⁸⁻¹⁴⁰ Therefore, brain cells were chosen for the next stage of the biological experiments. Brain cells differ from other cells in a number of ways, most importantly in their function. Neurons produce electrical impulses to transfer information. Glial cells work to support neurons by protecting them with a buffer and nutritional support.

Cancerous human brain cells were incubated with increasing concentrations of MB1-1 and $\text{Gd}(\text{MB1-1})_3$, with the processed data shown in Figure 6.8. A $\text{Gd}(\text{III})$ control of 0.03 mM is shown in black and shows a significant decrease in cell number over the seven days, indicating cell death when in the presence of free $\text{Gd}(\text{III})$. The blank control is shown in grey and shows little decrease in cell number over time.

After one day of incubation, the apo peptide samples showed little difference in cell number compared to the blank control, within the error of the experiment. The 0.02 mM $\text{Gd}(\text{MB1-1})_3$ sample showed the same as the blank control, representing no cell death due to the peptide complex. The 0.04 mM $\text{Gd}(\text{MB1-1})_3$ sample showed an increase in cell number, however, this was not thought to be significant.

After three days, the apo peptide samples and the 0.02 mM $\text{Gd}(\text{MB1-1})_3$ sample showed no significant difference to the blank control, representative of no cell death due to addition of the peptide complex. The 0.04 mM $\text{Gd}(\text{MB1-1})_3$ sample was significantly lower and closer to that of the $\text{Gd}(\text{III})$ control. This could mean that $\text{Gd}(\text{III})$ has dissociated from the peptide and is in the toxic, aqueous form.

After seven days of incubation only the lowest peptide concentration of 0.02 mM was shown to be statistically the same as the blank control. The higher concentrations of peptide, 0.04 and 0.06 mM, showed a significant decrease in cell number, attributed to cell death, and were closer in cell number to the toxic Gd(III) control. Both Gd(MB1-1)₃ samples showed a reduction in cell number, similar to that of the Gd(III) control.

This experiment shows the metallo complex to be toxic to the human brain cancer cells after seven days of incubation. This is most likely due to the transmetalation of Gd(III) by biological metals and phosphate in the cell media, as predicted in the initial cell studies using PBS. The apo peptide was also shown to contribute to cell death after seven days, even though no Gd(III) was present in the sample. This result comes from only one set of experiments and so further investigations into the toxicity of both the apo and metallo complexes should be completed to provide a better understanding of the system.

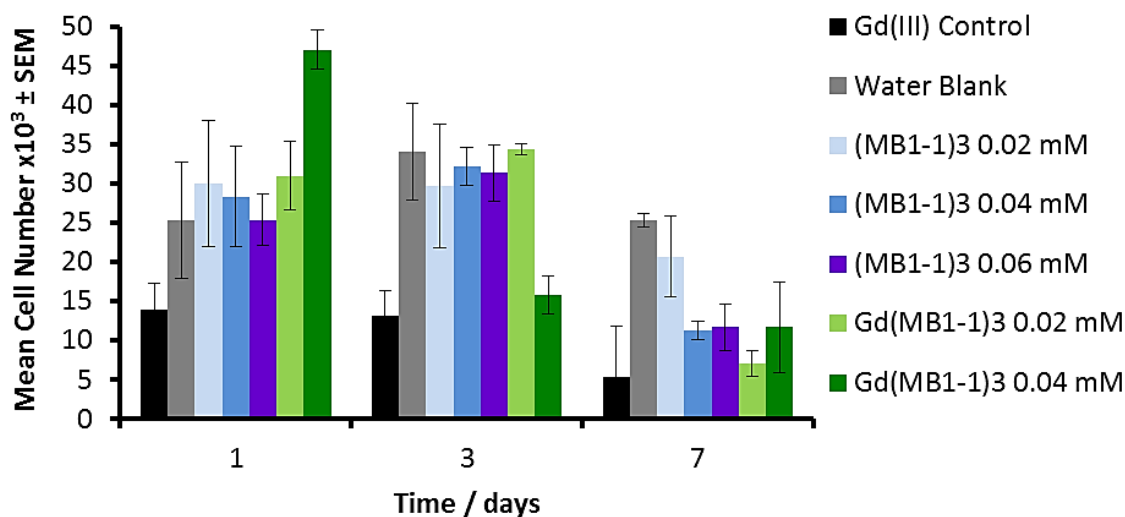


Figure 6.8: Human brain cancer cells incubated with varying concentrations of MB1-1 (blue) and Gd(MB1-1)₃ (green) monitored over 1,3 and 7 days. A blank control is shown in black and a Gd(III) control shown in grey. Error bars show standard deviation for the experiment.

6.4 Conclusions

In this chapter, $\text{Gd}(\text{MB1-1})_3$ and $\text{Gd}(\text{MB1-2})_3$ were subjected to transmetalation studies using biologically relevant metals. It was observed that the Ln(III) located within the binding site in the hydrophobic core of the coiled coil was displaced by Ca(II), Zn(II), K(I) and Na(I). Transmetalation was more apparent in the MB1-1 system as the binding site is more accessible and dynamic at the top of the coiled coil. The metals with a 2⁺ charge were shown to cause more transmetalation compared to the metals with a 1⁺ charge. This is thought to be due to the higher charge being closer to that required to neutralise the 3⁻ charge of the coiled coil.

PBS was used as a preliminary test to mimic a biological system and no $\text{Tb}(\text{MB1-1})_3$ or $\text{Tb}(\text{MB1-2})_3$ formation was observed. This could be due to the binding affinity of Tb(III) binding to phosphate being higher than that of the peptide complex, or that the phosphate ligand disrupts the coordination of the binding site so that Tb(III) can no longer bind. Phosphate was also been seen to induce Ln(III) release from the binding site. This was observed when investigating $\text{Tb}(\text{peptide})_3$ binding in the presence of Na_2HPO_4 and KH_2PO_4 and it was found that no $\text{Tb}(\text{peptide})_3$ was present in the sample.

Finally, preliminary cell studies were under taken. It was found that MB1-1 and $\text{Tb}(\text{MB1-1})_3$ did not display any toxic effect after 24 hours in initial studies using Hela cells. When human brain cells were used, a decrease in cell number was observed for the apo and metallo peptide complexes after seven days. From this preliminary biological study, it can be concluded that currently the $\text{Gd}(\text{MB1-1})_3$ system is far from suitable for progression to clinical trials. The binding constant is very low for an MRI CA and a significant amount of transmetalation occurs when in the presence of biological metals and phosphate. Most importantly, a dramatic reduction in cell number was observed when human brain cells were

incubated with the metallo complex. Future work for this CA must focus on enhancing metal binding and decreasing the potential for transmetalation.

Chapter 7: Concluding Remarks and Future Work

7.1 Conclusions

In this thesis the MB1 series of peptides has been interrogated to better understand the mechanism by which contrast is achieved and thereby offering the opportunity to generate new systems with enhanced relaxivity. The SBM equations^{20,21} were used as a guideline for optimisation of the CA. Rotational correlation time, inner-sphere water residency time and secondary sphere water dynamics were investigated. Primary sphere water coordination has previously been investigated by Berwick where they found that an increase in q results in an increase in relaxivity in this class of contrast agent.⁹⁵

Rotational correlation time was explored using a series of three peptides of differing lengths (MB1-1S, MB1-1 and MB1-1L). It was found that, when using the MB1-1 peptide sequence, a minimum of five heptads are required for adequate peptide folding and stability. The increase from five to six heptads had little effect on peptide folding, q or relaxivity, indicating that the rotational correlation time is not the dominating factor for this series of peptide-based CAs. It was also found that water residence time has a large impact on the predicted relaxivity of $\text{Gd}(\text{MB1-1})_3$ and could be limiting the effect of changing the rotational correlation time. The water residency time is currently very fast for $\text{Gd}(\text{MB1-1})_3$ but by slowing this to approximately 40 ns an increase in relaxivity would be observed and any changes in rotational correlation time would have a more significant impact.

The effect of water coordination to the coiled-coil exterior on the relaxivity of $\text{Gd}(\text{III})$ binding peptides was investigated through the design of Mo1-2. It was found that the addition of lysine residues on the peptide exterior had no effect on the folding or stability of the peptide. Additionally, no change in relaxivity was observed, at low or high fields. Secondary

sphere water coordinated to the peptide exterior was too far from Gd(III) to impact relaxivity. Interestingly, tetramer and dimer stoichiometries were observed for Mo1-2, confirmed using AUC and further analysed using MD. Luminescence lifetime experiments yielded $q = 0.6$, agreeing with trimer and tetramer stoichiometries.

Secondary sphere water coordination and dynamics were further examined in Chapter 5. By using MD simulations, it was found that a water channel was present in the hydrophobic core of Gd(MB1-2)₃ allowing water to come within close proximity (8 Å) to the Ln(III). It was hypothesised that by using D-Ile the channel would be blocked and no water would be located in the second sphere and the relaxivity would decrease. This was investigated as a proof of concept and to better understand the importance of secondary sphere water interactions. SN1-2 was designed, based on MB1-2, with D-Ile above the Ln(III) binding site. Gd(SN1-2)₃ was unfolded and so could not be used to test the hypothesis. Two peptides consisting of 6 heptads, MB1-3L and SN1-3L were analysed and were both well folded on addition of Gd(III). The relaxivity of both peptides was shown to be the same as MB1-2. This was concluded to be because that the water channel had not been blocked and water was still able to be located in proximity to Gd(III), or because, the channel had been blocked in both SN1-3L and MB1-3L and so the secondary sphere water effects were the same in both systems.

Finally, transmetalation studies were conducted with MB1-1 and MB1-2. It was found that less transmetalation occurred when the Ln(III) binding site was located further into the hydrophobic core due to poor accessibility. Two cell lines were subsequently incubated with MB1-1 and Gd(MB1-1)₃. It was found that the cell number decreased substantially after three and seven days when treated with Gd(MB1-1)₃. Because of this, improvements to metal stability and transmetalation would need to be made before the peptide could progress further in biological studies.

Overall it can be concluded that rotational correlation time and secondary sphere water interactions are not the limiting factor for the relaxivity of this class of contrast agent under these experimental conditions. Inner-sphere water coordination has previously been shown to have a significant impact on relaxivity, through translating the Ln(III) binding site along the coiled coil. Further investigations into changing the water residency time may also prove the preliminary conclusion that it has a significant impact on relaxivity for this class of contrast agent.

7.2 Future Work

7.2.1 Use of Alternative Lanthanides for MRI PARACEST

CEST and PARACEST imaging are methods being used more and more in clinical MRI imaging.^{181,182} Both of these methods use lanthanides, but not Gd(III), in order to reduce the signal of bulk water, providing negative contrast.^{182,183} By applying a pre-saturation pulse at the resonance frequency of an exchanging proton site, the saturated spin is transferred to bulk water by chemical exchange.¹⁸⁴ This is dependent on the number of exchanging protons, the water exchange rate, and the properties of the chosen lanthanide. Most commonly Dy(III), Tb(III), Yb(III) and Eu(III) are used.^{185,186} The MB1-1 and MB1-2 peptides display enhanced folding in the presence of Ln(III) in a 1:3 metal to peptide monomer concentration, as displayed in Figure 7.1. Initial T_1 and T_2 measurements using these Ln(III) showed little promise with $r_1 = 0 \text{ mM}^{-1} \text{ s}^{-1}$ and r_2 of between 5 and 20 $\text{mM}^{-1} \text{ s}^{-1}$ in both MB1-1 and MB1-2, with the r_2 data shown in Figure 7.2. It would next be of interest to determine the CEST and PARACEST potential of these systems.

(a)

(b)

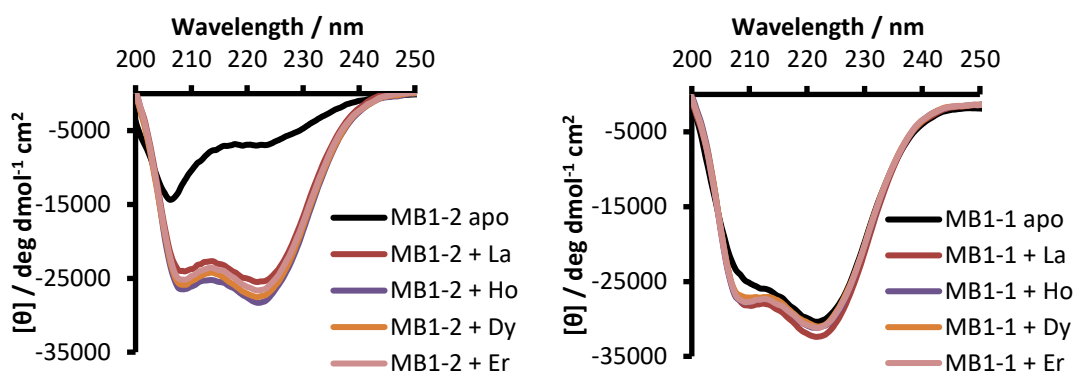


Figure 7.1: CD profile of 30 μM monomer (a) MB1-1 and (b) MB1-2 in the absence (black) and presence of 10 μM Ln(III) in 10 mM HEPES buffer pH 7.0.

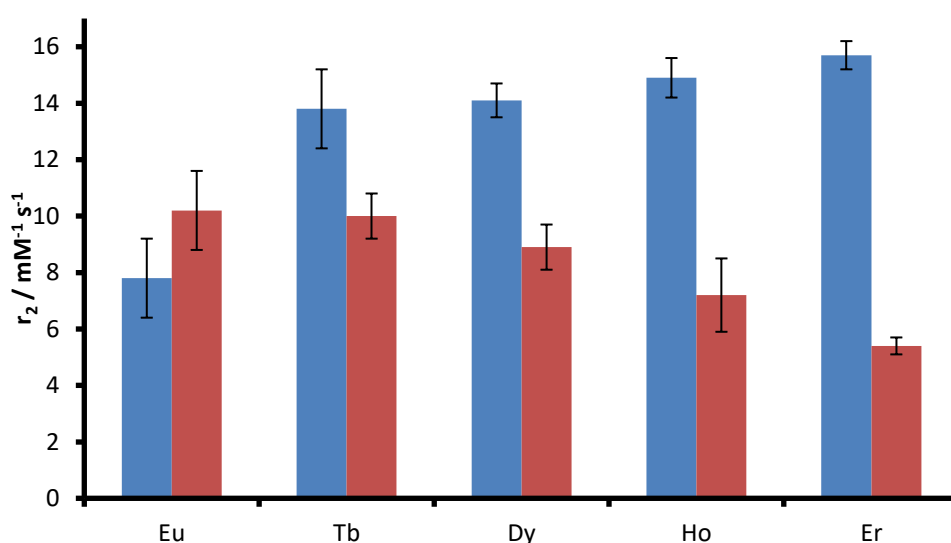


Figure 7.2: Processed preliminary data to compare the r_2 data for (blue) MB1-1 and (red) MB1-2 with a series of Ln(III).

7.2.2 Mn(II) MRI Contrast Agents

Due to the toxicity of Gd(III) in current MRI CAs, and reports of metal pooling in the brain, research has become more focussed on the use on Manganese.^{40,66–70} Mn(II) has all the attractive attributes of Gd(III); long electronic relaxation time, high spin quantum number, fast water exchange, but with increased stability.⁶⁶ The MB1-1 and MB1-2 peptides have shown promising binding potential with Mn(II), however, the binding constant was found to be lower

than that with Gd(III) ($\log K_a = 2.5 \pm 0.4$) with 1000 μM required to cause a change in peptide folding with a 30 μM monomer peptide solution, with the CD spectra shown in Figure 7.3.

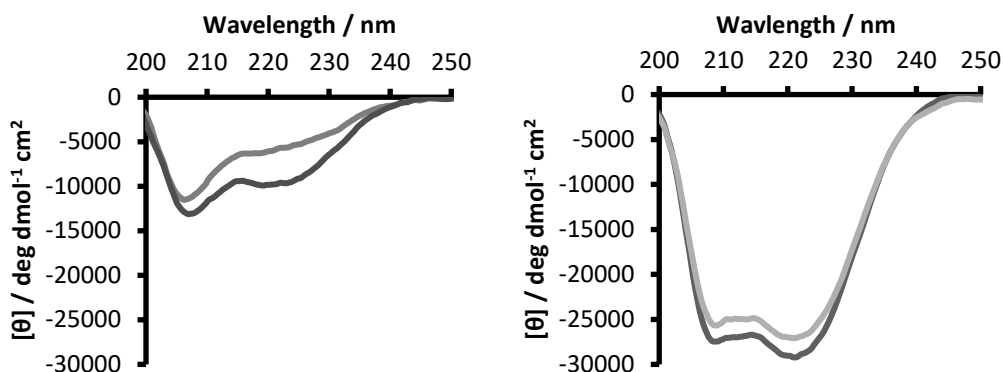


Figure 7.3: CD profile of 30 μM monomer peptide (a) MB1-2 and (b) MB1-1 in the presence (black) and absence (grey) of 1000 μM Mn(III) in 10 mM HEPES buffer pH 7.0.

7.2.3 Improvement in Binding Constant

As shown in the initial cell studies conducted with MB1-1, the stability of the metallo peptide needs to be greatly improved before translating to further cell studies. Once improved, the peptide complex could be adapted to MRI biological concentrations in order to perform further *in vivo* studies. The stability and binding constant could be increased by crosslinking the peptide strands of the coiled coil through Lys residues at the peptide termini in order to trap Gd(III) within the hydrophobic core of the coiled coil.

Chapter 8: Materials and Methods

8.1 Materials

Fluorenylmethoxycarbonyl (Fmoc) protected amino acids, dimethylformamide (DMF), N,N,N',N'-tetramethyl-O-(1H-benzotriazol-1-yl)uronium hexafluorophosphate (HBTU) synthesis grade N,N-dimethylformamide (DMF) and 20% piperidine in DMF premix, were purchased from Pepceuticals Ltd. Rink amide 4-methylhydrlamine (MBHA) resin, diisopropylethylamine (DIPEA), N-methylpyrrolidone (NMP), 20% piperidine in DMF, hydroxybenzotriazole (HoBT), N,N-diisopropylethylamine (DIPEA) and dichloromethane (DCM) and trifluoroacetic acid (TFA) were purchased from AGTC Bioproducts Ltd. Triisopropylsilane (TIPS), xylenol orange sodium salt, and trifluoroacetic acid (TFA) were purchased from Acros Organics. Diethyl ether, acetic anhydride, acetic acid, GdCl₃·6H₂O and TbCl₃·6H₂O were obtained from Sigma Aldrich. Urea (>99% purity), guanadinium hydrochloride, glacial acetic acid, HPLC grade water and acetonitrile, sodium hydroxide, sodium chloride, 2-[4-(2-hydroxyethyl)piperazin-1-yl]ethanesulfonic acid (HEPES), glacial acetic acid and ethylenediaminetetraacetic acid (EDTA) were purchased from Fisher Scientific Ltd. D₂O (99.9% purity) was purchased from VWR. All water except that used for HPLC was ultrapure grade obtained from a Millipore Elix-Gradient A10 system.

8.2 Peptide Synthesis and Purification

All peptides reported were synthesised on a CEM Liberty Blue automated peptide synthesiser on a 0.25 mmol scale using a rink amide MBHA resin (0.368 g, 0.68 meqg⁻¹) using standard Fmoc-amino acid solid-phase synthesis protocols.⁹⁹

An inert N₂ atmosphere was used for all automated synthesis and DMF was used as the main solvent. All Fmoc amino acids (0.2 M) used in the automated synthesis were dissolved in DMF.

The resin was swollen in DMF (10 ml) for 20 minutes before being loaded onto the synthesiser. Deprotection of Fmoc group from each amino acid was performed using 20% piperidine in DMF with 0.1 M HoBT. An initial deprotection step (10 mL, 60 W, 75°C, 30 s) was followed by a main deprotection (10 mL, 60 W, 75°C, 180 s). Coupling to the next Fmoc amino acid was achieved using 0.5 M HBTU in DMF (activator) and 2 M DIPEA (34.8 mL) in NMP (activator base), in a 1:5:5:10 molar ratio of resin : amino acid : activator : activator base, using standard microwave conditions.

After each deprotection step, the reaction vessel was washed with DMF (3 x 5 min, 5 sec drain time). After the first amino acid coupling the reaction vessel was washed with DMF (1 x 5 mL, 5 sec drain time). This was followed by (2 x 5 mL, 5 sec drain time) after the second coupling in addition to the two standard manifold washes (2 x 4 mL DMF, 5 sec drain time)

A single coupling programme was used apart from for the final two heptads which were double coupled (30 W, 75°C, 600 sec) and both of the terminal Glycine residues were double coupled using a 10 min coupling (30 W, 75°C, 600 sec).

After all couplings and the final N-terminal deprotection, the resin was washed and transferred to a 50 mL falcon tube and swollen in DMF (15 mL) for 20 mins. The resulting peptide was acetylated whilst still on the resin using 20% acetic anhydride (4 mL), 20% DIPEA (4 mL) in DMF (20 mL) for 30 minutes, whilst being stirred. The peptide on resin was washed with DCM (15 mL) and diethyl ether (15 mL) and air dried for one hour.

Cleavage occurred under a nitrogen atmosphere, with stirring, using a TFA cocktail which contained 2.5% TIPS (0.5 mL), 2.5% H₂O (0.5 mL) and 95 % TFA (19 mL) for three hours. The resin was removed, filtered and washed with TFA (10 mL). The filtrate was reduced in volume (to approx. 10 mL) by blowing N₂ over the solution and the peptide was precipitated out using a 10 times excess of cold diethyl ether and stored in the freezer for one hour.

The crude peptide was collected by centrifugation (Eppendorf centrifuge 5702 with rotor A-4-38 and rotational speed of 4400 rpm, 10 minutes) and the diethyl ether removed. The peptide was dissolved in 50% water, 50% acetonitrile solution and filtered (33 mm with 0.45 µm pore size).

The crude peptides were purified by preparative reverse phase HPLC using a Phenomenex Synergi C18 column. A linear gradient from 20% to 70% MeCN (+ 0.05% TFA) and water (+ 0.05% TFA) over 40 minutes was used with a flow rate of 10 mL /min. Detection wavelengths of 210 nm and 280 nm were used.

The pure peptide was reduced under vacuum and characterised using analytical RP-HPLC with a Phenomenex Synergi C18 column (1.00 ml/min flow rate), and by MALDI-TOF mass spectrometry (MALDI Micro MX Mass Spectrometer) with a 0.04 M sinapinic acid matrix. Peptide yields were calculated to be between 12-25%. The peptide spectra are shown in the Appendix.

8.3 Sample Preparation and Concentration Determination

Stock solutions of GdCl₃ and TbCl₃ (1 mM) were freshly prepared in deionized water and their concentrations determined, in triplicate, using a xylenol orange and EDTA titration, as reported by Fedeli and co-workers.¹⁸⁷

Peptide stock solutions were freshly prepared and concentrations determined in triplicate on a Shimadzu 1800 UV spectrometer. Spectra were recorded in single beam mode with a medium speed (slit width 1.0 nm, data interval 1.0 nm, scan range 420-260 nm) in a 1 cm, 700 μL quartz cuvette. The stock concentration of peptide (~ 1 mg per 100 μL ultrapure water) was calculated using the tryptophan absorbance at 280 nm ($\epsilon_{280} = 5690 \text{ M}^{-1}\text{cm}^{-1}$). A 5 μL aliquot of peptide stock was added to 695 μL of 6 M urea so that the peptide was fully unfolded. A blank containing 695 μL of 6 M urea and 5 μL ultrapure water was prepared as a baseline. All solutions were centrifuged (Eppendorf MiniSpin, 45° fixed-angle rotor F-45-12-11, rotational speed of 13,400 rpm, 3 minutes) and left to equilibrate for 10 min before recording. The corrected absorbance was calculated by subtracting the baseline at 400 nm from the Trp peak at 280 nm. The concentration of peptide monomer was calculated using Equation 2.2

LnCl_3 concentrations were determined in triplicate using a xyenol orange indicator and EDTA titration with standard Ln^{3+} solutions, following a standard procedure reported by Fedeli and coworkers.¹⁸⁷

8.4 Circular Dichroism (CD) Spectroscopy

CD spectra of 30 μM peptide monomer solutions were recorded in the absence and presence of 10 μM GdCl_3 , in 10 mM HEPES buffer pH 7.0, in a 1 mm path length, 300 μL , quartz cuvette on a Jasco J-715 spectropolarimeter. The optical chamber was purged and kept under inert N_2 during the experiments. Scans were recorded from 300 – 200 nm with a 200 nm/min scan rate and a 1 nm bandwidth and 1 sec response. Baseline correction was applied for all samples. All samples were left to equilibrate for 10 minutes before recording.

The observed ellipticity in millidegrees was converted into molar ellipticity, (Θ) , which is reported in units of $\text{deg dmol}^{-1} \text{ cm}^2$. The percentage folding of the peptide sample was $\sim 146 \sim$

calculated using the theoretical maximum ellipticity value of each peptide at 222 nm, based on previous methods.¹¹⁰ The values reported are based on an average of three repeats, and the standard deviations reported accordingly.

The fraction folded, f , is related to the observed ellipticity, Θ_{obs} , molar ellipticity of the apo peptide, Θ_{apo} , and the molar ellipticity of the metallo peptide, Θ_{met} at 222 nm, as given in Equation 8.1.

Equation 8.1:

$$f = \frac{\Theta_{obs} - \Theta_{apo}}{\Theta_{met} - \Theta_{apo}}$$

Gd(III) titrations were performed on addition of aliquots of a 1 mM stock solution of GdCl₃ in HEPES buffer pH 7.0. Each sample was left to equilibrate for 10 minutes. The resulting data was fit using DynaFIT Software (Biokin Ltd, Massachusetts) to a $1/3 M + L \rightleftharpoons 1/3 (ML_3)$ binding model, to determine the binding constant. Titrations were carried out in triplicate with the standard deviation error reported.

Chemical unfolding data was recorded of a 30 μ M peptide monomer solution in 10 mM HEPES buffer pH 7.0, in the absence and presence of 10 μ M GdCl₃, by monitoring the molar ellipticity at 222 nm as a function of increasing Gua-HCl concentration (from 0 to 7 M) in a 1 mm pathlength quartz cuvette. The Gibbs free energy was calculated by fitting to a two-state equilibrium model, folded to three monomers, using a nonlinear least squares fitting. The script was adapted from previous work by Buer *et al*,¹⁸⁸ written in MATLAB, and shown in Appendix A10.

Thermal unfolding spectra were collected using a Jasco Peltier Temperature accessory from 25 – 85 °C, using a temperature gradient of 0.7 °C min⁻¹, in a 1 cm cuvette, monitoring the signal at 222 nm.

Thank you to Professor Hannon, School of Chemistry, University of Birmingham, for use of the instrument.

8.5 Luminescence

Luminescence spectra were recorded using a 1 cm path length quartz cuvette and an Edinburgh Instruments Fluorescence FLS90 system fitted with a 450 W Xenon arc lamp and a Hamamatsu R928 photomultiplier tube. The emission monochromator was fitted with two interchangeable gratings blazed at 500 nm and 1200 nm and the data was collected using F900 spectrometer analysis software.

30 μM peptide monomer solutions in 10 mM HEPES buffer pH 7.0 were analysed on the addition of aliquots of a 1 mM stock solution of TbCl_3 in 10 mM HEPES buffer pH 7.0. Solutions were excited at 280 nm and emission scanned from 455-750 nm using a 455 nm long pass filters. Spectra were corrected for instrument response (grating/PMT) in all cases. The change in emission intensity was calculated by integrating the Tb(III) peak at 545 nm and normalizing it using the apo peptide spectrum. All experiments were repeated in triplicate to calculate an average and standard deviation error.

Tb(III) luminescence titrations were analysed using Equation 8.2 where f is the normalised emission intensity, related to the observed emission intensity, I , emission intensity of the apo peptide, I_a , and the emission intensity of the metallo peptide, I_m , integrated between 530-560 nm.

Equation 8.2:
$$f = \frac{I - I_a}{I_m - I_a}$$

A binding constant was determined using DynaFIT Software (Biokin Ltd, Massachusetts) and a $1/3 \text{ M} + \text{L}_3 \rightarrow 1/3 (\text{ML}_3)$ binding model. Titrations were carried out in triplicate with the standard deviation error reported.

Tb(III) lifetimes in D₂O and H₂O were experimentally determined for Tb(peptide)₃ by analysing solutions of 10 μM TbCl₃ and 100 μM MB1-1L in 10 mM HEPES buffer pH 7.0, using a μF flash lamp light source (50 Hz), collecting over a 10 ms range, with a lamp trigger delay of 0.1 ms. Data was fit to mono-exponential decay kinetics using the Kaleidagraph software package and the Marquardt-Levenburg linear least squares algorithm, where I and I_0 are the emission intensity at time t and $t=0$ and τ is the lifetime, as given in Equation 8.3. By using the observed lifetime, the number of coordinated water molecules can be calculated using the Horrocks-Sudnik equation, or the Parker-Beeby equation which allows for outer sphere water effects to be taken into account.^{116,162} Data was collected in triplicate with standard deviation errors given.

Equation 8.3:
$$I_t = I_0 \exp(-t/\tau)$$

Thank you to Professor Pikramenou, School of Chemistry, University of Birmingham, for use of the instrument.

8.6 NMR Spectroscopy

High field NMR relaxation data was collected using a Bruker DMX 300 spectrometer, with a 7 T vertical wide-bore superconducting magnet, which operates at a proton resonance frequency of 300.13 MHz, using a 25 mm 1H radio frequency (RF) coil. The 90° and 180° pulses were optimised for each sample (approximately 8 μs and 14 μs respectively). The spectrometer was controlled using a Linux workstation operating XWIN-NMR, version 3.5, and ParaVision version 3.0 software. An imaging method was used to collect T_1 and T_2 data with all experiments recorded at 293 ± 0.3 K. T_1 and T_2 maps of water protons in phantom samples (consisting of 6 x 3 mm NMR tubes positioned in a Teflon sample holder) were acquired using a Rapid Acquisition with Relaxation Enhancement (RARE) spin-echo imaging sequence. Horizontal images were acquired with a 10 mm slice thickness, using a 25 by 25 mm field of

view, 64 x 64 pixel matrix. A spectral width of 10,000 Hz, receiver gain of 45.2, repetition time of 15 s and an echo time of 2.2 ms were used with 2 signal averages. An excitation pulse and refocusing pulse of 512 μ s were also used. T_1 relaxation maps were produced from a series of 33 spin echo images with varying T_1 inversion recovery delays from 5×10^{-3} - 11 s and RARE factor of 8. T_2 relaxation maps were produced from 121 echo images with echo times from 10 - 1280 ms and a RARE factor of 1. All experiments were collected in triplicate to calculate an average and standard deviation error. Experiments were analysed using Prospa Software (Magritek, Wellington, New Zealand) and Kaleidagraph Software (Synergy Software, Pennsylvania, USA), where the relaxation time for each concentration was taken from the average value from the pixels within the sample. The relaxivity for each sample was calculated from the gradient of a plot of r_1 or r_2 Vs GdCl_3 concentration.

Low field relaxivity data was collected at the University of Durham as part of a RSC sponsored collaboration. A Spinsolve Carbon benchtop NMR (Magritek, Wellington, New Zealand), fitted with a 1 T permanent magnet, and functioning at a proton resonance frequency of 43 MHz with a 5 mm RF coil was used. The data was collected using automated 90° and 180° radio frequency pulses. T_1 relaxation data was collected using two scans with a 3.2 s acquisition time. A repetition time of 15 s was selected with a maximum inversion time of 10 s, with the experiment being made up of 21 data points. T_2 relaxation data was collected using 4 scans with a 3.2 s acquisition time. An experiment repetition time of 7 s was used with a 2 ms echo time and a maximum total echo time of 2 s made up of 10 data points. All experiments were repeated in triplicate in order to calculate an average and standard deviation error.

Metallo-peptide samples were made in a 1:2 Gd(III):trimer ratio, in 10 mM HEPES buffer pH 7.0, to ensure >99% complexation of Gd(III). $\text{Gd}(\text{peptide})_3$ solutions containing 2.5,

5, 7.5, 10, 15, 20, 30 and 40 μM GdCl_3 and 2 equivalents of peptide trimer (0.5:1 GdCl_3 :peptide trimer), were prepared in 10 mM HEPES buffer pH 7.0. A measurement of each peptide concentration was repeated in triplicate in order to calculate an average and standard deviation error. 10 mM pH 7.0 HEPES and 0.1 mM GdCl_3 in 10 mM HEPES pH 7.0 samples were used as controls.

8.7 Molecular Dynamics Simulations

All peptide models were built using Insight II (Biosym/MSI, San Diego California).⁹⁷ The peptides were solvated using a TIP3P water solvent model with a water box 15 Å larger than the peptide in all directions. No counter ions were required as the metallo peptide is neutral. Minimisation and MD simulations were performed using AMBER v8.9¹⁸⁹ with a ff03 force field. Gd(III) ions were input as spheres with a charge of +3 and Van der Waals parameters (MOD4 RE format in Amber), radius = 1.7131 Å (radius) and well depth = 0.4598. The first step of the simulation involved a minimisation step where the peptide was subjected to 100,000 cycles of conjugate gradient minimisation. Secondly a 500 ps equilibrium step took place at 300 K, with constant volume and periodic boundary conditions. Data gathering ran for 20 ns at 300 K, with constant volume and periodic boundary conditions, taking snapshots every 10 ps.

MD simulations were initially analysed using Visual Molecular Dynamics software¹⁹⁰ and viewed using PyMol.¹⁹¹ Further analysis was completed using the Ptraj command in AMBER. This allowed for in depth analysis into individual water molecules, their distance from Gd(III) and their movements during the simulation. Analysis into water within the primary and secondary water spheres could also be conducted.

8.8 Cell Culture

Toxicity experiments were performed as part of a collaboration with Dr De Cogan at the University of Birmingham Medical School.

All cell culture techniques were performed under a sterile tissue culture hood (Gelaire BSB 4a laminar flow hood; Gelaire Pty Ltd, Australia). Cancer cell lines were cultured at 37°C in a humidified CO₂ incubator (MCO-17AIC; SANYO, Osaka, Japan (UK)) at 5% CO₂. All solutions and equipment were bought sterile or sterilized by autoclave when required.

HeLa carcinoma cells (PHE) (Purchased from Public Health England Culture Collections (PHECC), London UK) and human astrocytoma cells (human patient, University of Birmingham Medical School) were cultured at 37°C in 5% (v/v) CO₂ atmosphere in T₇₅ culture flasks (Invitrogen, UK) containing Dulbecco's Modified Eagle's Medium (DMEM, Sigma Aldrich, UK) supplemented with 10% Fetal Bovine Serum (FBS) (Sigma Aldrich, UK) and 1% penicillin and streptomycin (Sigma Aldrich, UK).

Adherent cells were grown to confluence and passaged using a standard trypsin-EDTA (0.25%:0.2%) protocol (Invitrogen, UK). This protocol consisted of removal of the cell culture media by aspiration, washing of the cell monolayer with PBS, removal of PBS and the addition of 1-2 mL trypsin into the container. The culture was then incubated for 2-5 mins at 37 celsius in 5% (v/v) CO₂ until cells are rounded and in suspension. The trypsin reaction was halted by the addition of fresh media and cells were diluted as necessary for experiments. Suspension cells were maintained at 2x10⁵ cells/mL and passaged by media splitting.

A 48 well plate was prepared using 10,000 cells per well (~100 µL), cell media (150 µL) containing DMEM supplemented with 10% FBS, 1% penicillin and 1% streptomycin, and

varying concentrations of apo and metallo MB1-1, as shown in Table 8.1. A blank and 0.03 mM GdCl₃ control were also used.

After an incubation period of 24 hours, 3 days or 7 days, a 50 µL sample was taken from each cell and the number of cells calculated using a haemocytometer. By counting the number of cells in each well, a mean and standard deviation for each concentration could be calculated. This process was repeated at each time point.

Table 8.1: Cell tray set up form MB1-1 cell culture experiments.

| | | | | | | | |
|-------|---------------------------------|-----------------------------------|---------------------------------|-----------------------------------|---------------------------------|-----------------------------------|------------------------------|
| BLANK | 0.02 mM (MB1-1) ₃ | 0.02 mM Gd(MB1-1) ₃ | 0.04 mM (MB1-1) ₃ | 0.04 mM Gd(MB1-1) ₃ | 0.06 mM (MB1-1) ₃ | 0.06 mM Gd(MB1-1) ₃ | 0.03 mM GdCl ₃ |
| BLANK | 0.02 mM Apo | 0.02 mM Metallo | 0.04 mM Apo | 0.04 mM Metallo | 0.06 mM Apo | 0.06 mM Metallo | 0.03 mM Gd(III) |
| BLANK | 0.02 mM Apo | 0.02 mM Metallo | 0.04 mM Apo | 0.04 mM Metallo | 0.06 mM Apo | 0.06 mM Metallo | 0.03 mM Gd(III) |
| BLANK | 0.02 mM Apo | 0.02 mM Metallo | 0.04 mM Apo | 0.04 mM Metallo | 0.06 mM Apo | 0.06 mM Metallo | 0.03 mM Gd(III) |
| BLANK | 0.02 mM Apo | 0.02 mM Metallo | 0.04 mM Apo | 0.04 mM Metallo | 0.06 mM Apo | 0.06 mM Metallo | 0.03 mM Gd(III) |
| BLANK | 0.02 mM Apo | 0.02 mM Metallo | 0.04 mM Apo | 0.04 mM Metallo | 0.06 mM Apo | 0.06 mM Metallo | 0.03 mM Gd(III) |

References

- (1) Hornak, J. P. *The Basics of MRI*; Interactive Learning Software, Henrietta, NY, 1996.
- (2) Lauterbur, P. C. *Nature* **1973**, *242*, 190–191.
- (3) Gaynora, D.; Griffith, D. M. *Dalt. Trans.* **2012**, *41*, 13239–13257.
- (4) Webb, A. G. *Introduction to Biomedical Imaging*; Wiley-IEEE Press: New York, 2003.
- (5) Atkins, P.; Overton, T.; Rouke, J.; Weller, M. *Shriver and Atkins' Inorganic Chemistry*, 4th Edition.; Oxford University Press: Oxford, 2006.
- (6) Elbanowski, M.; Mąkowska, B. *J. Photochem. Photobiol. A Chem.* **1996**, *99* (23), 85–92.
- (7) Heffern, M. C.; Matosziuk, L. M.; Meade, T. J. *Chem. Rev.* **2014**, *114* (8), 4496–4539.
- (8) Ward, M. D. *Coord. Chem. Rev.* **2010**, *254* (21–22), 2634–2642.
- (9) Jones, J. *Amino Acid and Peptide Synthesis*; Oxford University Press: Oxford, 2002.
- (10) Kodaria, C.; Brito, H.; Eoetonio, E.; Felinto, M.; Malta, O.; Brito, G. *J. Braz. Chem. Soc.* **2004**, *15* (6), 890–896.
- (11) Bloch, F.; Hansen, W. W.; Packard, M. *Phys. Rev.* **1946**, *70* (7), 474–485.
- (12) Purcell, E. M.; Torrey, H. C.; Pound, R. V. *Phys. Rev.* **1946**, *69* (1), 37–38.
- (13) Friebolin, H. *Basic One and Two Dimensional NMR Spectroscopy*, 5th Edition.; WILEY-VCH; Virginia, 2005.
- (14) Jacques, V.; Desreux, J. *Top. Curr. Chem.* **2002**, *221*, 1–24.
- (15) Caravan, P.; Ellison, J.; McMurry, T.; Lauffer, R. *Chem. Rev.* **1999**, *99*, 2293–2352.
- (16) Aime, S.; Botta, M.; Terreno, E. *Adv. Inorg. Chem.* **2005**, *57*, 173–237.
- (17) Fatin-Rouge, N.; Toth, E.; Meuli, R.; Bunzil, J. C. *J. Alloys Compd.* **2004**, *374* (1), 298–302.
- (18) Lowe, M. *Aust. J. Chem.* **2002**, *55*, 551.
- (19) Jacques, V.; Dumas, S.; Sun, W. C.; Troughton, J. S.; Greenfield, M. T.; Caravan, P. *Invest. Radiol.* **2010**, *45* (10), 613–624.
- (20) Solomon, I. *Phys. Rev.* **1955**, *99*, 559–565.
- (21) Bloembergen, N.; Morgan, L. O. *J. Chem. Physics* **1961**, *34*, 842–850.
- (22) Gueron, M. *J. Magn. Reson.* **1975**, *19*, 55–66.
- (23) Aime, S.; Batsanov, A. S.; Botta, M.; Howard, J. A. K.; Parker, D.; Senanayake, K.; Williams, G. *Inorg. Chem.* **1994**, *33*, 4696–4706.
- (24) Freed, J. *J. Chem. Phys.* **1978**, *68*, 4934–4939.
- (25) Xu, Q.; Zhu, L.; Yu, M.; Feng, F.; An, L.; Xing, C.; Wang, S. *Polymer (Guildf).* **2010**, *51* (6), 1336–1340.
- (26) Carr, D. H.; Brown, J.; Bydder, G. M.; Steiner, R. E.; Weinmann, H. J.; Speck, U.; Hall, A. S.; Young, I. R. *Am. J. Roentgenol.* **1984**, *143* (2), 215–224.
- (27) Callaghan, P. T. *Principles of Nuclear Magnetic Resonance Microscopy*; Oxford University Press: Oxford, 1991.
- (28) Weinmann, H. J.; Ebert, W.; Misselwitz, B.; Schmitt-Willich, H. *Eur. J. Radiol.* **2003**, *46* (1), 33–44.
- (29) Himes, N.; Min, J. Y.; Lee, R.; Brown, C.; Shea, J.; Huang, X.; Xiao, Y. F.; Morgan, J. P.; Burstein, D.; Oettgen, P. *Magn. Reson. Med.* **2004**, *52* (5), 1214–1219.
- (30) Port, M.; Idee, J.; Medina, C.; Robic, C.; Sabatou, M.; Corot, C. *Biometals* **2008**, *21*, 469–490.
- (31) Stezokowski, J.; Hoard, J. *Isr. J. Chem.* **1984**, *24*, 323–334.
- (32) Weisman, G.; Reed, D. *J. Org. Chem.* **1996**, *61* (51), 5186–5187.
- (33) Shahbazi-Gahrouei, D. *J. Res. Med. Sci.* **2009**, *14* (3), 141–147.
- (34) Robic, C.; Catoen, S.; Goltstein, D.; Idee, J.; Port, M. *Biometals* **2011**, *24*, 759–768.
- (35) Aime, S.; Caravan, P. *J. Magn. Reson. Imaging* **2009**, *30* (6), 1259–1267.
- (36) Ramalho, J.; Semelka, R. C.; Ramalho, M.; Nunes, R. H.; AlObaidy, M.; Castillo, M. *Am. J. Neuroradiol.* **2016**, *37* (7), 1192–1198.
- (37) Zou, Z.; Lin, M. *Indian J. Dermatol.* **2007**, *52*, 125–130.
- (38) Aime, S.; Botta, M.; Fasano, M.; Terreno, E. *Chem. Soc. Rev.* **1998**, *27*, 19–29.
- (39) Caravan, P. *Chem. Soc. Rev.* **2006**, *3*, 512–523.

- (40) Caravan, P.; Farrar, C. T.; Frullano, L.; Uppal, R. *Contrast Media Mol. Imaging* **2009**, *4* (2), 89–100.
- (41) Zech, S. G.; Sun, W. C.; Jacques, V.; Caravan, P.; Astashkin, A. V.; Raitsimring, A. M. *Chem Phys Chem* **2005**, *6*, 2570–2577.
- (42) Ferreira, M. F.; Martins, A. F.; Martins, J. A.; Ferreira, P. M.; Toth, E.; Geraldles, C. F. G. C. *Chem. Commun.* **2009**, *42*, 6475–6477.
- (43) Werner, E. J.; Avedano, S.; Botta, M.; Hay, B. P.; Moore, E. G.; Aime, S.; Raymond, K. N. *J. Am. Chem. Soc.* **2007**, *129*, 1870–1871.
- (44) Chen, J. W.; Belford, R. L.; Clarkson, R. B. *J. Phys. Chem. A* **1998**, *102*, 2117–2130.
- (45) Botta, M. *Eur. J. Inorg. Chem.* **2000**, *3*, 399–407.
- (46) Sherry, D.; Wu, Y. *Curr. Opin. Chem. Biol.* **2013**, *17*, 167–174.
- (47) Xu, J.; Franklin, S.; Whisenhunt, D.; Raymond, K. *J. Am. Chem. Soc.* **1995**, *117*, 7245–7246.
- (48) Nwe, K.; Bryant, L.; Brechbiel, M. *Bioconjug. Chem.* **2010**, *21*, 1014–1017.
- (49) Hermann, P.; Kotez, J.; Kubicek, V.; Lukes, I. *Dalt. Trans.* **2008**, *23*, 3027–3047.
- (50) Rudovský, J.; Cígler, P.; Kotek, J.; Hermann, P.; Vojtíšek, P.; Lukeš, I.; Peters, J. A.; Vander Elst, L.; Muller, R. N. *Chem. Eur. J.* **2005**, *11* (8), 2373–2384.
- (51) Lebduskova, P.; Hermann, P.; Helm, L.; Toth, E.; Kotek, J.; Binnemans, K.; Rudovsky, J.; Lukes, I.; Merbach, A. E. *Dalt. Trans.* **2007**, *4*, 493–501.
- (52) Stachura, M.; Chakraborty, S.; Gottberg, A.; Ruckthong, L.; Pecoraro, V. L.; Hemmingsen, L. *J. Am. Chem. Soc.* **2017**, *139* (1), 79–82.
- (53) Strauch, R.; Mastarone, D.; Sukerkar, P.; Song, Y.; Ipsaro, J.; Meade, T. *J. Am. Chem. Soc.* **2011**, *133*, 16346–16349.
- (54) Song, Y.; Xu, X.; MacRenaris, K.; Zhang, X.-; Mirkin, C.; Meade, T. *Angew. Chem Int. Ed.* **2009**, *48*, 9143–9147.
- (55) Chan, K.; Bara, S.; Botta, M.; Wong, W. *J. Inorg. Biochem.* **2004**, *98*, 677–682.
- (56) Fisher, M.; Vogtle, F. *Chem. Int. Ed.* **1999**, *38*, 885–905.
- (57) Pierre, V.; Botta, M.; Raymond, K. *J. Am. Chem. Soc.* **2005**, *127*, 504–505.
- (58) Lipari, G.; Szabo, A. *J. Am. Chem. Soc.* **1982**, *104*, 4546–4559.
- (59) Bulte, J. W. M.; Wu, C.; Brechbiel, M.; Brooks, R.; Vymazal, J.; Holla, M.; Frank, J. *Investig. Radiol.* **1998**, *33* (11), 841–845.
- (60) Vymazal, J.; Bulte, J. W. M.; Frank, J. A.; Chiro, G. Di; Brooks, R. A. *J. Magn. Reson. Imaging* **1993**, *3* (4), 637–640.
- (61) Keller, K.; Fossheim, S.; Koenig, S. *Investig. Radiol.* **1998**, *33*, 835–842.
- (62) Zhang, Y.; Vijayaragavan, V.; Da, G.; Bhakoo, K.; Tan, T. *Eur. J. Inorg. Chem.* **2012**, *12*, 2044–2048.
- (63) Vuong, Q.; Van Doorslaer, S.; Bridot, J. L.; Argante, C.; Alejandro, G.; Hermann, R.; Disch, S.; Mattea, C.; Stapf, S.; Gossuin, Y. *Magn. Reson. Mater. Physics, Biol. Med.* **2012**, *25* (6), 467–478.
- (64) Norek, M.; Pereira, G. A.; Geraldles, C. F. G. C.; Denkova, A.; Zhou, W.; Peters, J. A. *J Phys Chem C* **2007**, *111*, 10240–10246.
- (65) Deo, A.; Fogel, M.; Cowper, S. E. *Clin J Am Soc Nephrol* **2007**, *2*, 264–267.
- (66) Gale, E. M.; Atansavoa, I. P.; Blasi, F.; Ay, I.; Caravan, P. *J. Am. Chem. Soc.* **2015**, *137*, 15548–15557.
- (67) Hamm, B.; Vogl, T. J.; Branding, G.; Schnell, B.; Taupitz, M.; Wolf, K. J.; Lissner, J. *Radiology* **1992**, *182* (1), 167–174.
- (68) Vogl, T. J.; Hamm, B.; Schnell, B.; McMahon, C.; Branding, G.; Lissner, J.; Wolf, K. J. *J. Magn. Reson. Imaging* **1993**, *3* (1), 51–58.
- (69) Gallez, B.; G, B.; Swartz, H. M. *Magn. Reson. Med.* **1996**, *35* (1), 14–19.
- (70) Ni, Y.; Petré, C.; Bosmans, H.; Miao, Y.; Grant, D.; Baert, A.; Marchal, G. *Acad. Radiol.* **1997**, *38* (4), 700–707.
- (71) Cacheris, W. P.; Quay, S. C.; Rocklage, S. M. *Magn. Reson. Imaging* **1990**, *8* (4), 467–481.
- (72) Opsahl, L. R.; Uzgiris, E.; R, V. D. *Acad. Radiol.* **1995**, *2* (9), 762–767.
- (73) Jaccard, H.; Mieville, P.; Cannizzo, C.; Mayer, C.; Helm, L. *J. Inorg. Chem.* **2014**, *19*, 149–159.

- (74) León-Rodríguez, L. M. De; Ortiz, A.; Weiner, A. L.; Zhan, S.; Kovacs, Z.; Kodadek, T.; Sherry, A. D. *J. Am. Chem. Soc.* **2002**, *124*, 3514–3515.
- (75) Bull, S. R.; Guler, M. O.; Bras, R. E.; Meade, T. J.; Stupp, S. I. *Nano Lett.* **2005**, *5*, 1–4.
- (76) Bryson, J. W.; DeGrado, W. F. *Science.* **1995**, *270*, 935–941.
- (77) Cordes, M. H. J.; Davidson, A. R.; T, S. R. *Curr. Opin. Struct. Biol.* **1996**, *6*, 3–10.
- (78) Schneider, J. P.; Lombardi, A.; DeGrado, W. F. *Fold. Des.* **1998**, *3* (2), 29–40.
- (79) Regan, L.; DeGrado, W. F. *Science.* **1988**, *241*, 976–978.
- (80) Kohn, W. D.; Kay, C. M.; Hodges, R. S. *J. Pept. Res.* **1998**, *51* (1), 9–18.
- (81) Kashiwada, A.; Ishida, K.; Matsuda, K. *Bull. Chem. Soc. Jpn.* **2007**, *80* (11), 2203–2207.
- (82) McLachlan, A. D. *J. Mol. Biol.* **1978**, *124* (1), 297–304.
- (83) Cohen, C.; Parry, D. A. D. *Proteins* **1990**, *7*, 1–15.
- (84) Harbury, P. B.; Zhang, T.; Kim, P. S.; Alber, T. *Science.* **1993**, *262*, 1401–1407.
- (85) Betz, S. F.; Fairman, R.; O’Neil, K. T.; Lear, J. D.; DeGrado, W. F. *Phil. Trans. R. Soc. B.* **1995**, *348*, 81–88.
- (86) Parry, D. A. D.; Fraser, R. D. B.; Squire, J. M. *J. Struct. Biol.* **2008**, *163* (3), 258–269.
- (87) Kammerer, R. A.; Kostrewa, D.; Progius, P.; Honnappa, S.; Avila, D.; Lustig, A.; Winkler, F. K.; Pieters, J.; Steinmetz, M. O. *Proc. Natl. Acad. Sci. U. S. A.* **2005**, *102* (39), 13891–13896.
- (88) O’Shea, E. K.; Klemm, J. D.; Klm, P. S.; Alber, T. *Science.* **1991**, *254*, 539–544.
- (89) Harbury, P. B.; Kim, P. S.; Alber, T. *Nature* **1994**, *371*, 80–83.
- (90) Harding, M. M.; Nowicki, M. W.; Walkinshaw, M. D. *Crystallogr. Rev.* **2010**, *16*, 247–302.
- (91) Peacock, A. F. A.; Iranzo, O.; Pecoraro, V. L. *Dalt. Trans.* **2009**, *13*, 2271–2280.
- (92) Dokmsnic, I.; Sikie, M.; Tomie, S. *Acta Cryst. D* **2008**, *64*, 257–263.
- (93) Dieckmann, G. R.; Pecoraro, V. L. *J. Am. Chem. Soc.* **1997**, *119*, 6195–6196.
- (94) Nakagawa, T.; Mitsui, R.; Tani, A.; Sasa, K.; Tashiro, S.; Iwama, T.; Hayakawa, T.; Kawai, K. *PLoS One* **2012**, No. 7, e50480.
- (95) Berwick, M. R.; Slope, L. N.; Smith, C. F.; King, S. M.; Newton, S. L.; Gillis, R. B.; Adams, G. G.; Rowe, A. J.; Harding, S. E.; Britton, M. M.; Peacock, A. F. A. *Chem. Sci.* **2016**, *7*, 2207–2216.
- (96) Kashiwada, A.; Hiroaki, H.; Kohda, D.; Nango, M. *J. Am. Chem. Soc.* **2000**, 212–215.
- (97) Berwick, M. R.; Lewis, D. J.; Jones, A. W.; Parslow, R. A.; Dafforn, T. R.; Cooper, H. J.; Wilkie, J.; Pikramenou, Z.; Britton, M. M.; Peacock, A. F. A. *J. Am. Chem. Soc.* **2014**, *136* (4), 1166–1169.
- (98) Merrifield, R. B. *J. Am. Chem. Soc.* **1963**, *85* (14), 2149–2154.
- (99) Chan, W. C.; White, P. D. *Fmoc Solid Phase Peptide Synthesis: A Practical Approach*; Oxford University Press: New York, 2000.
- (100) Collins, J. M.; Leadbeater, N. E. *Org. Biomol. Chem.* **2007**, *5* (8), 1141–1150.
- (101) Rizzolo, F.; Testa, C.; Lambardi, D.; Chorev, M.; Chelli, M.; Rovero, P.; Papini, A. M. *J. Pept. Sci.* **2011**, *17* (10), 708–714.
- (102) Doig, A. J.; Baldwin, R. L. *Protein Sci.* **1995**, *4*, 1325–1336.
- (103) Gault, V. A.; McClenaghan, N. H. *Understanding Bioanalytical Chemistry: Principles and Applications*; Wiley-Blackwell: Oxford, 2009.
- (104) Conlon, J. M. *Nat. Protoc.* **2007**, *2* (1), 191–197.
- (105) Imoto, T.; Yamada, H. *Mol. Cell Biochem.* **1983**, *51*, 111–121.
- (106) Fenn, J. B.; Mann, M.; Meng, C. K.; Wong, S. F.; Whitehouse, C. M. *Science.* **1989**, *246* (4926), 64–71.
- (107) Aebbersold, R.; Mann, M. *Nature* **2003**, *422* (6928), 198–207.
- (108) Creighton, T. E. *Protein Structure: A practical approach*, 2nd Edition.; Oxford University Press: New York, 1997.
- (109) Ghosh, D.; Lee, K.; Demerler, B.; Pecoraro, V. L. *Biochemistry* **2005**, *44*, 10732–10740.
- (110) Myers, J. K.; Pace, N. C.; Scholtz, J. M. *Proc. Natl. Acad. Sci.* **1997**, *94*, 2833–2837.
- (111) Theory of Protein CD.
- (112) Cooper, T. M.; Woody, R. W. *Biopolymers* **1990**, *30*, 657–676.
- (113) Kelly, S. M.; Proce, N. C. *Biochim. Biophys. Acta - Mol. Cell Res.* **1997**, *1338*, 161–185.
- (114) Kohn, W. D.; Hodges, R. S. *J. Am. Chem. Soc.* **1998**, *16*, 379–389.
- (115) Lakowicz, J. R. *Principles of Fluorescence Spectroscopy*, 3rd Edition.; Springer: New York, 2006.

- (116) Beeby, A.; Clarkson, I. M.; Dickins, R. S.; Faulkner, S.; Parker, D.; Royle, L.; de Sousa, A. S.; Williams, G.; Wood, M. *J. Am. Chem. Soc.* **1999**, *2*, 493–503.
- (117) Claridge, T. *High-resolution NMR techniques in organic chemistry*, 1st Edition.; Pergamon: Oxford, 1999.
- (118) Britton, M. M. *Chem. Soc. Rev.* **2010**, *39* (11), 4036–4043.
- (119) Haacke, M.; Brown, R. W.; Thompson, M. R.; Venkatesan, R. *Magnetic Resonance Imaging: Physical Principles and Sequence Design*; New York, 1999.
- (120) Hennig, J.; Nauerth, A.; Freidburg, H. *Magn. Reson. Med.* **1986**, *3*, 823–833.
- (121) Servant, A.; Jacobs, I.; Bussy, C.; Fabbro, C.; da Ros, T.; Pach, E.; Ballesteros, B.; Prato, M.; Nicolay, K.; Kostarelos, K. *Carbon N. Y.* **2016**, *97*, 126–133.
- (122) Sitharaman, B.; Kissell, K. R.; Hartman, K. B.; Tran, L. A.; Baikalov, A.; Rusakova, I.; Sun, Y.; Khant, H. A.; Ludtke, S. J.; Chiu, W.; Laus, S.; Toth, E.; Helm, L.; Merbach, A. E.; Wilson, L. J. *Chem. Commun.* **2005**, *31*, 3915–3917.
- (123) Bryant, L. H.; Brechbiel, M. W.; Wu, C.; Bulte, J. W.; Herynek, V.; Frank, J. A. J. *J. Magn. Reson. Imaging* **1999**, *9* (2), 348–352.
- (124) Sirlin, C. B.; Vera, D. R.; Corbeil, J. A.; Caballero, M. B.; Buxton, R. B.; Mattrey, R. F. A. *Acad. Radiol.* **2004**, *11* (12), 1361–1369.
- (125) Anderson, E. A.; Isaacman, S.; Peabody, D. S.; Wang, E. Y.; Canary, J. W. Kirshenbaum, K. *Nano Lett.* **2006**, *6* (6), 1160–1164.
- (126) Strijkers, G. J.; Mulder, W. J.; van Heeswijk, R. B. Frederik, P. M.; Bomans, P.; Magusin, P. C.; Nicolay, K. *MAGMA* **2005**, *18* (4), 186–192.
- (127) Lauffer, R. B. *Chem. Rev.* **1987**, *87*, 901–927.
- (128) Franano, F. N.; Edwards, W. B.; Welch, M. J.; Brechbiel, M. W.; Gansow, O. A.; Duncan, J. R. *Magn. Reson. Imaging* **1995**, *13*, 201–214.
- (129) Yang, J. J.; Yang, J.; Wei, L.; Zurkiya, O.; Yang, W.; Li, S.; Zou, J. *J. Am. Chem. Soc.* **2008**, *130*, 9260–9267.
- (130) Dieckmann, G. R.; McRorie, D. K.; Lear, J. D.; Sharp, K. A.; DeGrado, W. F.; Pecoraro, V. L. *J. Mol. Biol.* **1998**, *280* (5), 897–912.
- (131) Kim, S.; Karrila, S. J. *Microhydrodynamics - Principles and Selected Applications*; Dover Publications Inc: New York, 1991.
- (132) d’Auvergne, E. J.; Gooley, P. R. *J. Biomol. NMR* **2007**, *40* (2), 107–119.
- (133) d’Auvergne, E. J.; Gooley, P. R. *J. Biomol. NMR* **2008**, *40* (2), 121–133.
- (134) Holde, K. E.; Johnson, W. C.; Ho, P. S. *Principle of Physical Biochemistry*; Prentice Hall Inc: New Jersey, 1998.
- (135) MATLAB 6.1, 2000.
- (136) Swift, T. J.; Connick, R. E. *J. Chem. Phys.* **1962**, *37* (2), 307–320.
- (137) Wei, G.-X.; Campagna, A. N.; Bobek, L. A. *J. Antimicrob. Chemother.* **2006**, *57* (6), 1100–1109.
- (138) Ogawa, S.; Lee, T. M.; Kay, A. R.; Tank, D. W. *Proc. Natl. Acad. Sci.* **1990**, *87* (24), 9868–9872.
- (139) Claussen, C.; Laniado, M.; Kazner, E.; Schörner, W.; Felix, R. *Neuroradiology* **1985**, *27* (2), 164–171.
- (140) Ward, K. M.; Aletras, A. H.; Balaban, R. S. *J. Magn. Reson.* **2000**, *143* (1), 79–87.
- (141) Muller, B. ChemEQL Version 3.2, 2015.
- (142) Ciani, B.; Bjelić, S.; Honnappa, S.; Jawhari, H.; Jaussi, R.; Payapilly, A.; Jowitt, T.; Steinmetz, M. O.; Kammerer, R. A. *Proc. Natl. Acad. Sci.* **2010**, *107* (46), 19850–19855.
- (143) Woolfson, D. In *Fibrous Proteins: Structures and Mechanisms*; Springer International Publishing: New York, 2017; pp 35–61.
- (144) Fletcher, J.; Harniman, R.; Barnes, F.; Boyle, A.; Collins, A.; Mantell, J.; Sharp, T.; Antognozzi, M.; Booth, P.; Linden, N.; Miles, M.; Sessions, R.; Verkade, P.; Woolfson, D. *Science*. **2013**, *340*, 595–599.
- (145) Thomson, A.; Wood, C.; Burton, A.; Bartlett, G.; Sessions, R.; Brady, R.; Woolfson, D. *Science*. **2014**, *346*, 485–488.
- (146) Wood, C.; Bruning, M.; Ibarra, A.; Bartlett, G.; Thomson, A.; Sessions, R.; Brady, R.; Woolfson, D. *Bioinformatics* **2014**, *30*, 3029–3035.

- (147) Bromley, E.; Channon, K.; Moutevelis, E.; Woolfson, D. N. *ACS Chem. Biol.* **2008**, *3* (1), 38–50.
- (148) Woolfson, D. N.; Bartlett, G. J.; Burton, A. J.; Heal, J. W.; Niitsu, A.; Thomson, A. R.; Wood, C. W. *Curr. Opin. Struct. Biol.* **2015**, *33*, 16–26.
- (149) Vincent, T. L.; Green, P. J.; N, W. D. *Bioinformatics* **2012**, 69–76.
- (150) Walshaw, J.; Woolfson, D. N. *J. Mol. Biol.* **2001**, *307* (5), 1427–1450.
- (151) Testa, O.; Moutevelis, E.; Woolfson, D. *Nucleic Acids Res* **2009**, *37*, 315–322.
- (152) Woolfson, D.; Moutevelis, E. *J. Mol. Biol.* **2009**, *385*, 726–732.
- (153) Monera, O. D.; Sonnichsen, F. D.; Hicks, L.; Kay, C. M.; Hodges, R. S. *Protein Eng.* **1996**, *9*, 353–362.
- (154) Lee, K.-H.; Matzapetakis, M.; Mitra, S.; Marsh, E. N. G.; Pecoraro, V. L. *J. Am. Chem. Soc.* **2004**, *126* (30), 9178–9179.
- (155) Lee, K.-H.; Cabello, C.; Hemmingsen, L.; Marsh, E. N. G.; Pecoraro, V. L. *Angew. Chem Int. Ed.* **2006**, *45* (18), 2864–2868.
- (156) Pace, C. N.; Scholtz, J. M. *Biophys. J.* **1998**, *75* (1), 422–427.
- (157) Peacock, A. F. A.; Hemmingsen, L.; Pecoraro, V. L. *Proc. Natl. Acad. Sci.* **2008**, *105* (43), 16566–16571.
- (158) Wendt, H.; Berger, C.; Baici, A.; Thomas, R. M.; Bosshard, H. R. *Biochemistry* **1995**, *34* (12), 4097–4107.
- (159) Krause, E.; Beyermann, M.; Dathe, M.; Rothmund, S.; Bienert, M. *Analytical Chem.* **1995**, *67* (2), 252–258.
- (160) Durani, S. *Acc. Chem. Res.* **2008**, *41*, 1301–1308.
- (161) Peacock, A. F. A.; Stuckey, J. A.; Pecoraro, V. L. *Angew. Chem Int. Ed.* **2009**, *48*, 7371–7374.
- (162) Horrocks, W. D. J.; Sudnick, D. *J. Am. Chem. Soc.* **1979**, *101* (2), 334–340.
- (163) Horrocks, W.; Sudnick, D. *Acc. Chem. Res.* **1981**, *14*, 394–392.
- (164) Xue, S.; Yang, H.; Qiao, J.; Pu, F.; Jiang, J.; Hubbard, K.; Hekmatyar, K.; Langley, J.; Salarian, M.; Long, R. C.; Bryant, R. G.; Hu, X. P.; Grossniklaus, H. E.; Liu, Z.-R.; Yang, J. J. *Proc. Natl. Acad. Sci.* **2015**, *112* (21), 6607–6612.
- (165) Lohrke, J.; Frenzel, T.; Endrikat, J.; Alves, F. C.; Grist, T. M.; Law, M.; Lee, J. M.; Leiner, T.; Li, K.-C.; Nikolaou, K.; Prince, M. R.; Schild, H. H.; Weinreb, J. C.; Yoshikawa, K.; Pietsch, H. *Adv. Ther.* **2016**, *33*, 1–28.
- (166) Oudkerk, M.; Sijens, P. E.; Van Beek, E. J.; Kuijpers, T. J. *Invest. Radiol.* **1995**, *30* (2), 75–78.
- (167) Shamsi, K.; Yucel, E. K.; Chamberlin, P. *Invest. Radiol.* **2006**, *41* (11), 822–830.
- (168) Roberts, D. R.; Lindhorst, S. M.; Welsh, C. T.; Maravilla, K. R.; Herring, M. N.; Braun, K. A.; Thiers, B. H.; Davis, W. C. *Invest. Radiol.* **2016**, *51* (5), 280–289.
- (169) Murata, N.; Gonzalez-Cuyar, L. F.; Murata, K.; Fligner, C.; Dills, R.; Hippe, D.; Maravilla, K. R. *Invest. Radiol.* **2016**, *51* (7).
- (170) Karabulut, N. *Diagnostic Interv. Radiol.* **2015**, *21* (4), 269–270.
- (171) Robert, P.; Violas, X.; Grand, S.; Lehericy, S.; Idée, J.-M.; Ballet, S.; Corot, C. *Invest. Radiol.* **2016**, *51* (2), 73–82.
- (172) Jenjob, R.; Kun, N.; Ghee, J. Y.; Shen, Z.; Wu, X.; Cho, S. K.; Lee, D. H.; Yang, S.-G. *Mater. Sci. Eng. C* **2016**, *61*, 659–664.
- (173) Kanal, E. *Magn. Reson. Imaging* **2016**, *34* (10), 1341–1345.
- (174) Bourne, G. W.; Trifaró, J. M. *Neuroscience* **1982**, *7* (7), 1615–1622.
- (175) Boland, L. M.; Brown, T. A.; Dingledine, R. *Brain Res.* **1991**, *563* (12), 142–150.
- (176) Frenzel, T.; Lengsfeld, P.; Schirmer, H.; Hutter, J.; Weinmann, H. J. *Invest. Radiol.* **2008**, *43* (12), 817–828.
- (177) Sieber, M. A.; Lengsfeld, P.; Frenzel, T.; Golfier, S.; Schmitt-Willich, H.; Siegmund, F.; Walter, J.; Weinmann, H. J.; Pietsch, H. *Eur. Radiol.* **2008**, *18* (10), 2164–2173.
- (178) Galluzzi, L.; Aaronson, S.; Abrams, J.; Alnemri, E.; Andrews, D.; Baehrecke, E.; Bazan, N.; Blagosklonny, M.; Blomgren, K.; Borner, C.; Bredesen, D.; Brenner, C.; Castedo, M.; Cidlowski, J.; Ciechanover, A.; Cohen, G.; De Laurenzi, V.; De Maria, R.; Deshmukh, M.; Dynlacht, B.; El-Deiry, W.; Flavell, R.; Fulda, S.; Garrido, C.; Golstein, P.; Gougeon, M.-L.; Green, D.; Gronemeyer, H.; Hajnoczky, G.; Hardwick, J.; Hengartner, M.; Ichijo, H.; Jaattela, M.; Kepp, O.;

- Kimchi, A.; Klionsky, D.; Knight, R.; Kornbluth, S.; Kumar, S.; Levine, B.; Lipton, S.; Lugli, E.; Madeo, F.; Malorni, W.; Marine, J.; Martin, S.; Medema, J.; Mehlen, P.; Melino, G.; Moll, U.; Morselli, E.; Nagata, S.; Nicholson, D.; Nicotera, P.; Nunez, G.; Oren, M.; Penninger, J.; Pervaiz, S.; Peter, M.; Piacentini, M.; Prehn, J.; Puthalakath, H.; Rabinovich, G.; Rizzuto, R.; Rodrigues, C.; Rubinsztein, D.; Rudel, T.; Scorrano, L.; Simon, H.; Steller, H.; Tschopp, J.; Tsujimoto, Y.; Vandenabeele, P.; Vitale, I.; Vousden, K.; Youle, R.; Yuan, J.; Zhivotovsky, B.; Kroemer, G. *Cell Death Differ.* **2009**, *16* (8), 1093–1107.
- (179) Schreer, A.; Tinson, C.; Sherry, J. P.; Schirmer, K. *Anal. Biochem.* **2005**, *344* (1), 76–85.
- (180) Byth, H. A.; Mchunu, B. I.; Dubery, I. A.; Bornman, L. *Phytochem. Anal.* **2001**, *12* (5), 340–346.
- (181) Liu, G.; Song, X.; Chan, K. W. Y.; McMahon, M. T. *NMR Biomed.* **2013**, *26* (7), 810–828.
- (182) Woods, M.; Woessner, D. E.; Sherry, A. D. *Chem. Soc. Rev.* **2006**, *35* (6), 500–511.
- (183) Vinogradov, E.; Sherry, A. D.; Lenkinski, R. E. *J. Magn. Reson.* **2013**, *229*, 155–172.
- (184) Suchý, M.; Li, A. X.; Liu, Y.; Feng, Q.; Bartha, R.; Hudson, R. H. E. *Can. J. Chem.* **2016**, *94* (8), 715–722.
- (185) Cakic, N.; Savic, T.; Stricker-Shaver, J.; Truffault, V.; Platas-Iglesias, C.; Mirkes, C.; Pohmann, R.; Scheffler, K.; Angelovski, G. *Chem. Commun.* **2016**, *52* (59), 9224–9227.
- (186) He, J.; Bonnet, C. S.; Eliseeva, S. V.; Lacerda, S.; Chauvin, T.; Retailleau, P.; Szeremeta, F.; Badet, B.; Petoud, S.; Toth, E.; Durand, P. *J. Am. Chem. Soc.* **2016**, *138* (9), 2913–2916.
- (187) Barge, A.; Cravotto, G.; Gianolio, E.; Fedeli, F. *Contrast Media Mol. Imaging* **2006**, *1*, 184–188.
- (188) Buer, B. *Design, Synthesis and Study of Fluorinated Proteins*, 2nd Edition.; Köhler, V., Ed.; Springer New York, 2014.
- (189) Case, D. A.; Berryman, J. T.; Betz, R. M.; Cerutti, D. S.; Cheatham, T. E.; Darden, T. A.; Duke, R. E.; Giese, T. J.; Gohlke, H.; Goetz, A. W.; Homeyer, N.; Izadi, S.; Janowski, P.; Kaus, J.; Kovalenko, A.; Lee, T. S.; LeGrand, S.; Li, P.; Luchko, T.; Luo, R.; Madej, B.; Merz, K. M.; York, D. M.; Kollman, P. A. AMBER 2015.
- (190) Humphrey, W.; Dalke, A.; Schulten, K. *J. Molec. Graph.* **1996**, *14*, 33–38.
- (191) The PyMOL Molecular Graphics System, Version 1.8 Schrödinger, LLC.

Appendix

Table A1: Molecular weights of each peptide and MALDI (M+H)⁺ data

Figure A2: MALDI mass spectrum and analytical HPLC of pure MB1-1S

Figure A3: MALDI mass spectrum and analytical HPLC of pure MB1-1

Figure A4: MALDI mass spectrum and analytical HPLC of pure MB1-1L

Figure A5: MALDI mass spectrum and analytical HPLC of pure MB1-2

Figure A6: MALDI mass spectrum and analytical HPLC of pure Mo1-2

Figure A7: MALDI mass spectrum and analytical HPLC of pure SN1-2

Figure A8: MALDI mass spectrum and analytical HPLC of pure SN1-3L

Figure A9: MALDI mass spectrum and analytical HPLC of pure MB1-3L

Appendix A10: MATLAB script for relaxivity calculations

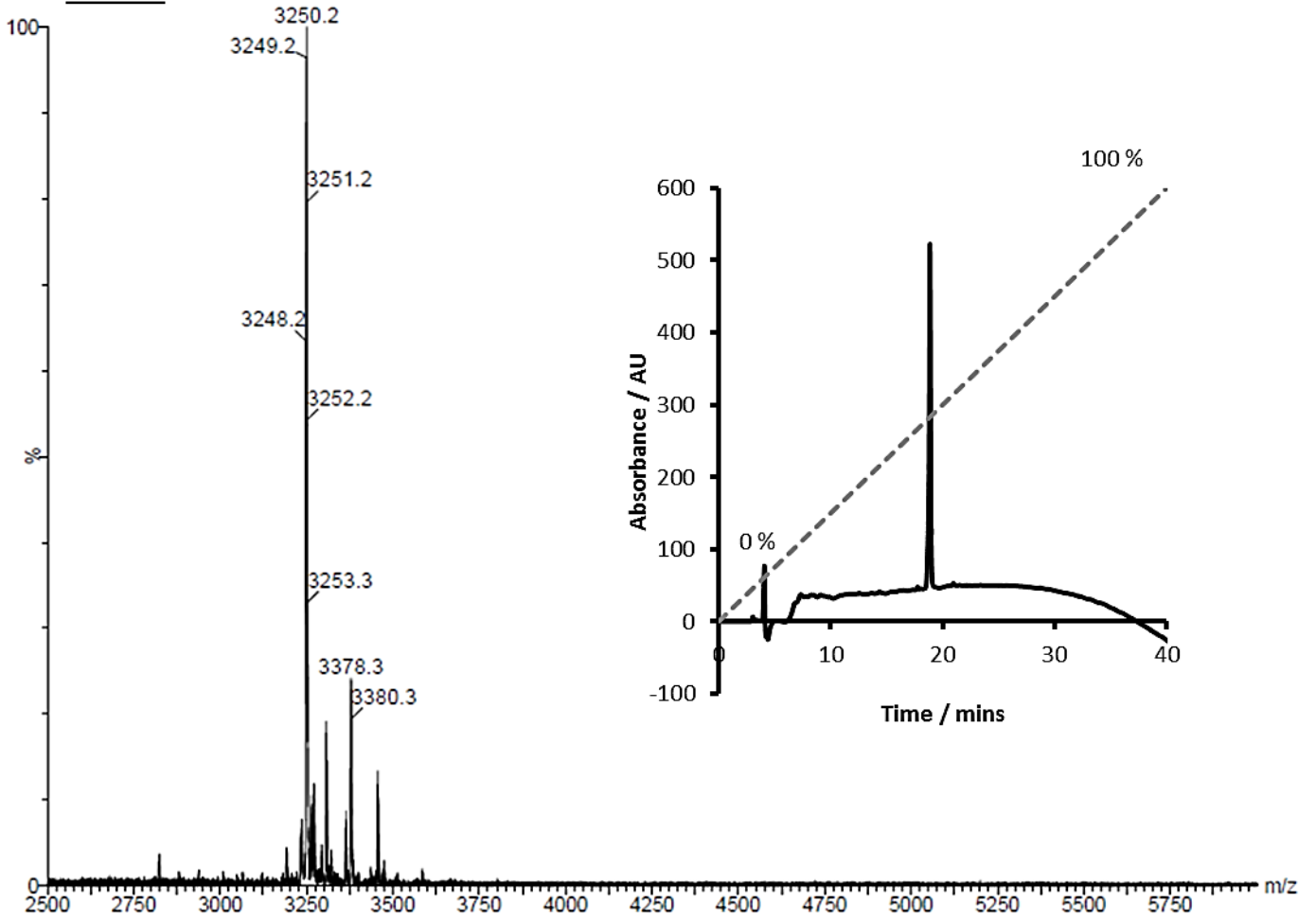
Appendix A11: MATLAB script for calculation ΔG

Table A1: Molecular weights of each peptide and MALDI (M+H)⁺ Ion Mass

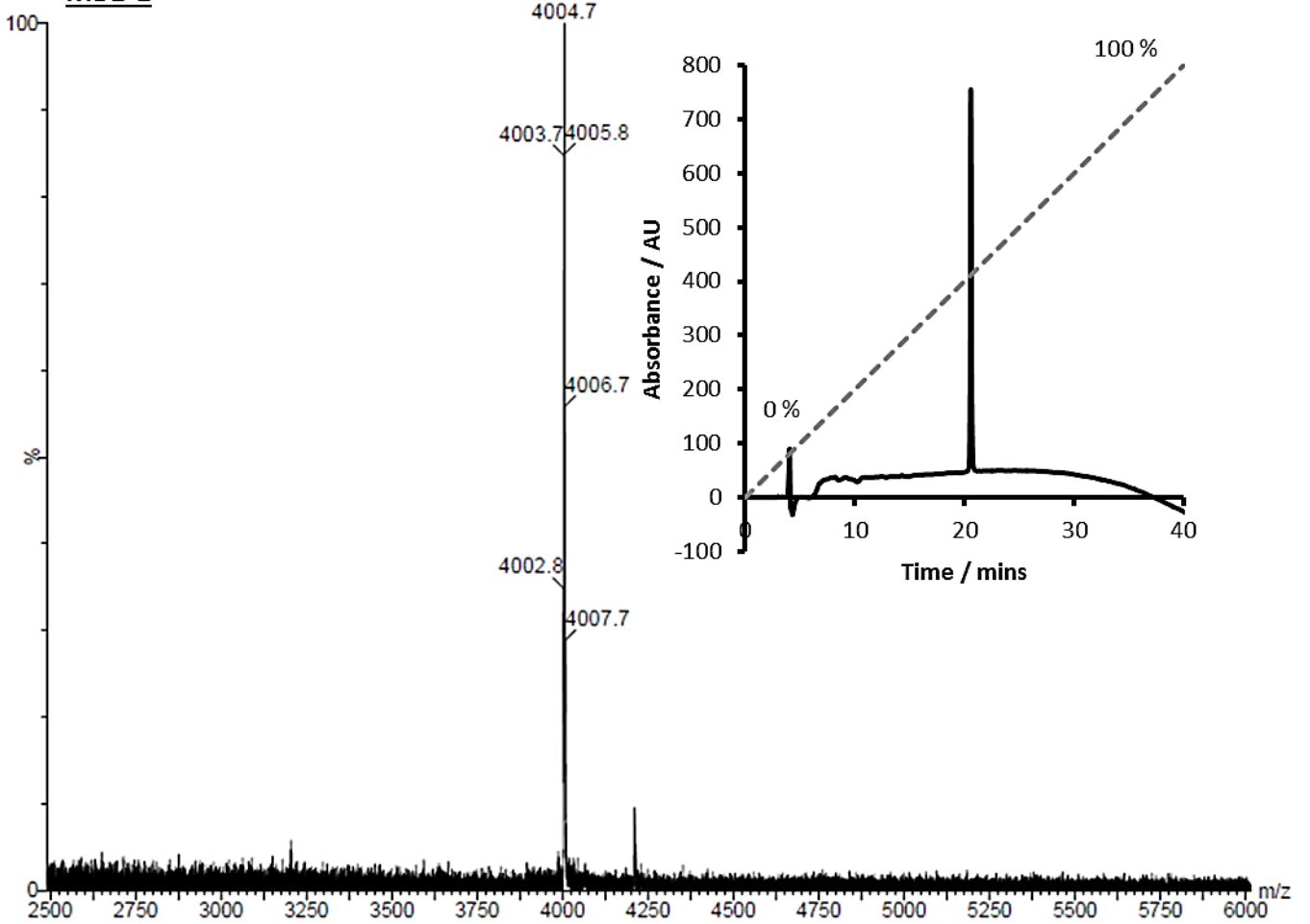
| Peptide Name | Sequence | Molecular Weight (Calculated) | Observed MALDI (M+H) ⁺ Ion Mass |
|---------------|---|-------------------------------|--|
| MB1-1S | Ac – G – IAANEWK DAAIEQK IAAIEQK IAAIEQK – G – NH ₂ | 3250 | 3250 |
| MB1-1 | Ac – G – IAANEWK DAAIEQK IAAIEQK IAAIEQK IAAIEQK – G – NH ₂ | 4004 | 4005 |
| MB1-1L | Ac – G – IAANEWK DAAIEQK IAAIEQK IAAIEQK IAAIEQK IAAIEQK – G – NH ₂ | 4758 | 4755 |
| MB1-2 | Ac – G – IAAIEQK IAANEWK DAAIEQK IAAIEQK IAAIEQK – G – NH ₂ | 4004 | 4005 |
| Mo1-2 | Ac – G – IKAIEEK IKENEWK DKAIEEK IKAIEEK IKAIEEK – G – NH ₂ | 4351 | 4352 |
| SN1-2 | Ac – G – IAAIEQK <u>X</u> AANEWK DAAIEQK IAAIEQK IAAIEQK – G – NH ₂ (<i>X = D-Ile</i>) | 4004 | 4003 |
| SN1-3L | Ac – G – IAAIEQK IAAIEQK <u>X</u> AANEWK DAAIEQK IAAIEQK IAAIEQK – G – NH ₂ (<i>X = D-Ile</i>) | 4758 | 4758 |
| MB1-3L | Ac – G – IAAIEQK IAAIEQK IAANEWK DAAIEQK IAAIEQK IAAIEQK – G – NH ₂ | 4758 | 4759 |

Impurities of higher mass than the peptide (M+H)⁺ peak are thought to be due to salt adducts.

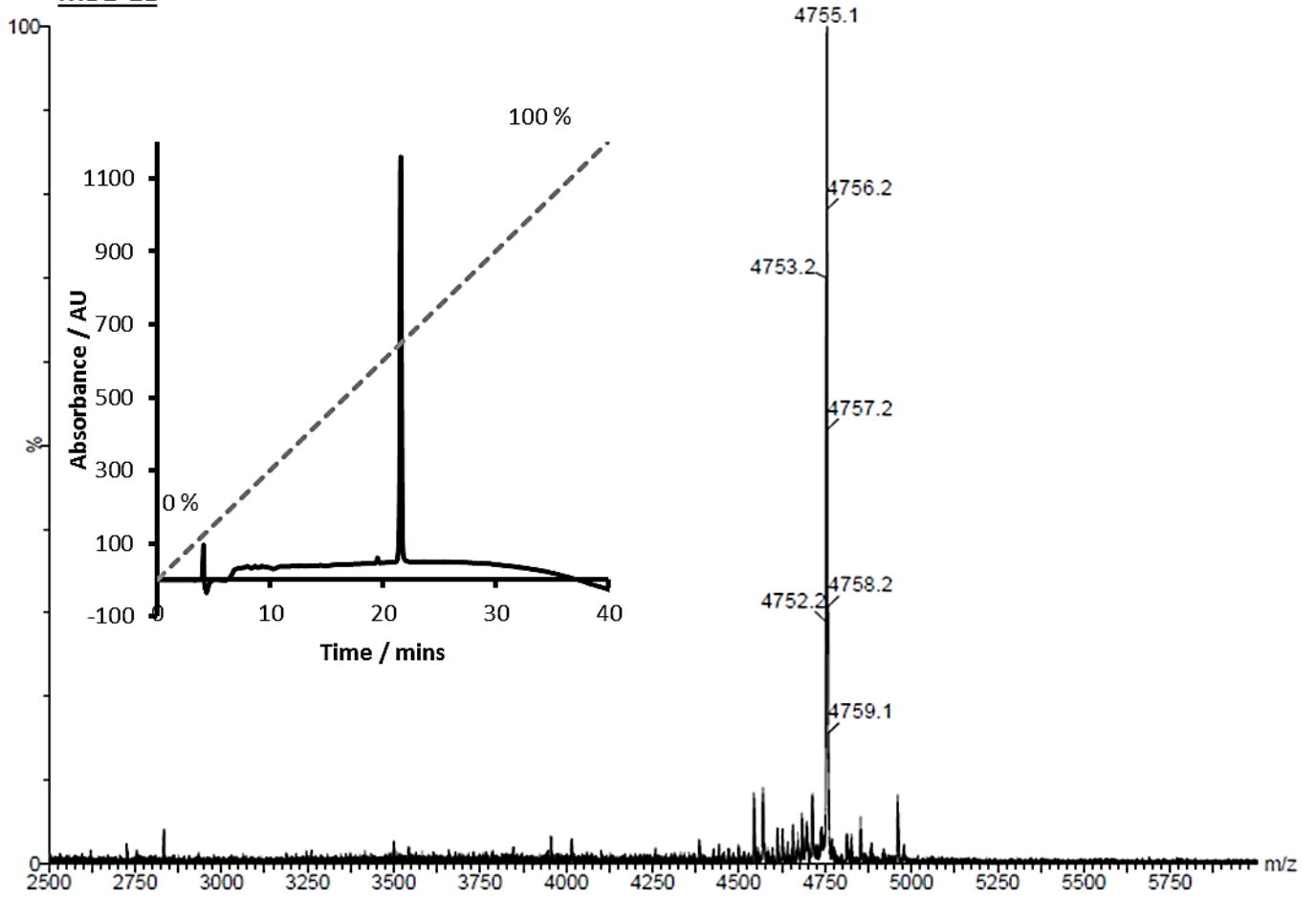
MB1-1S



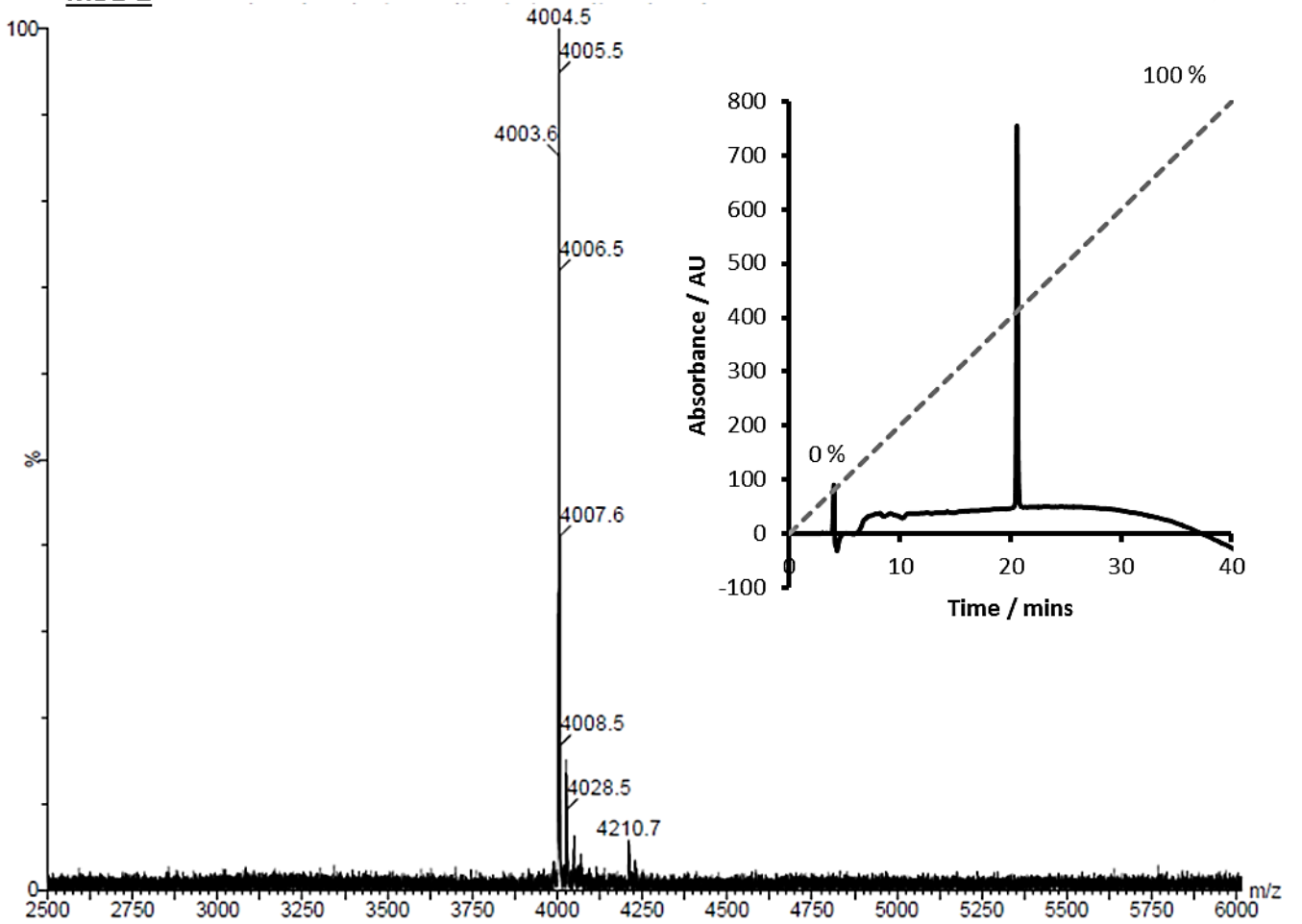
MB1-1



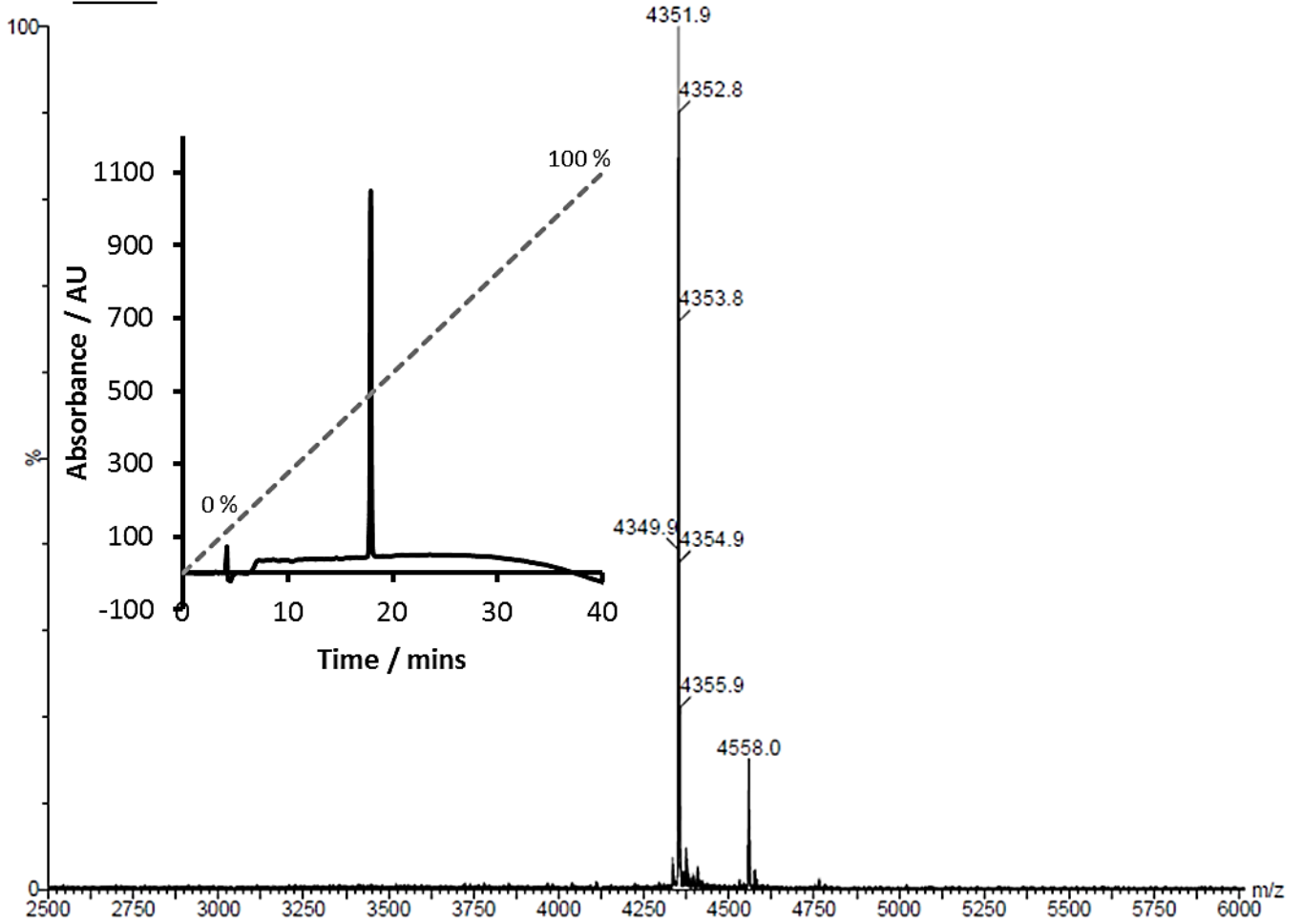
MB1-1L



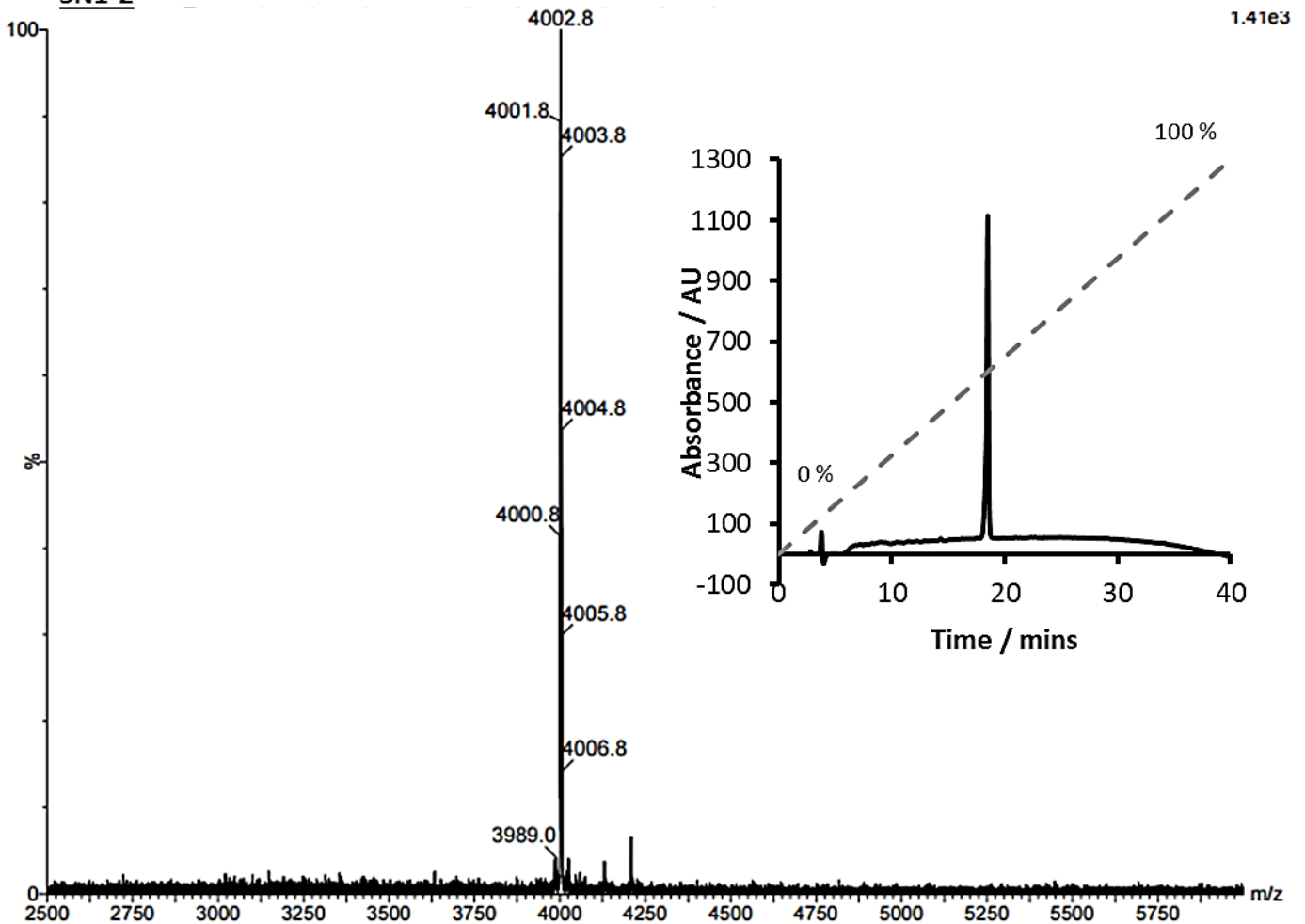
MB1-2



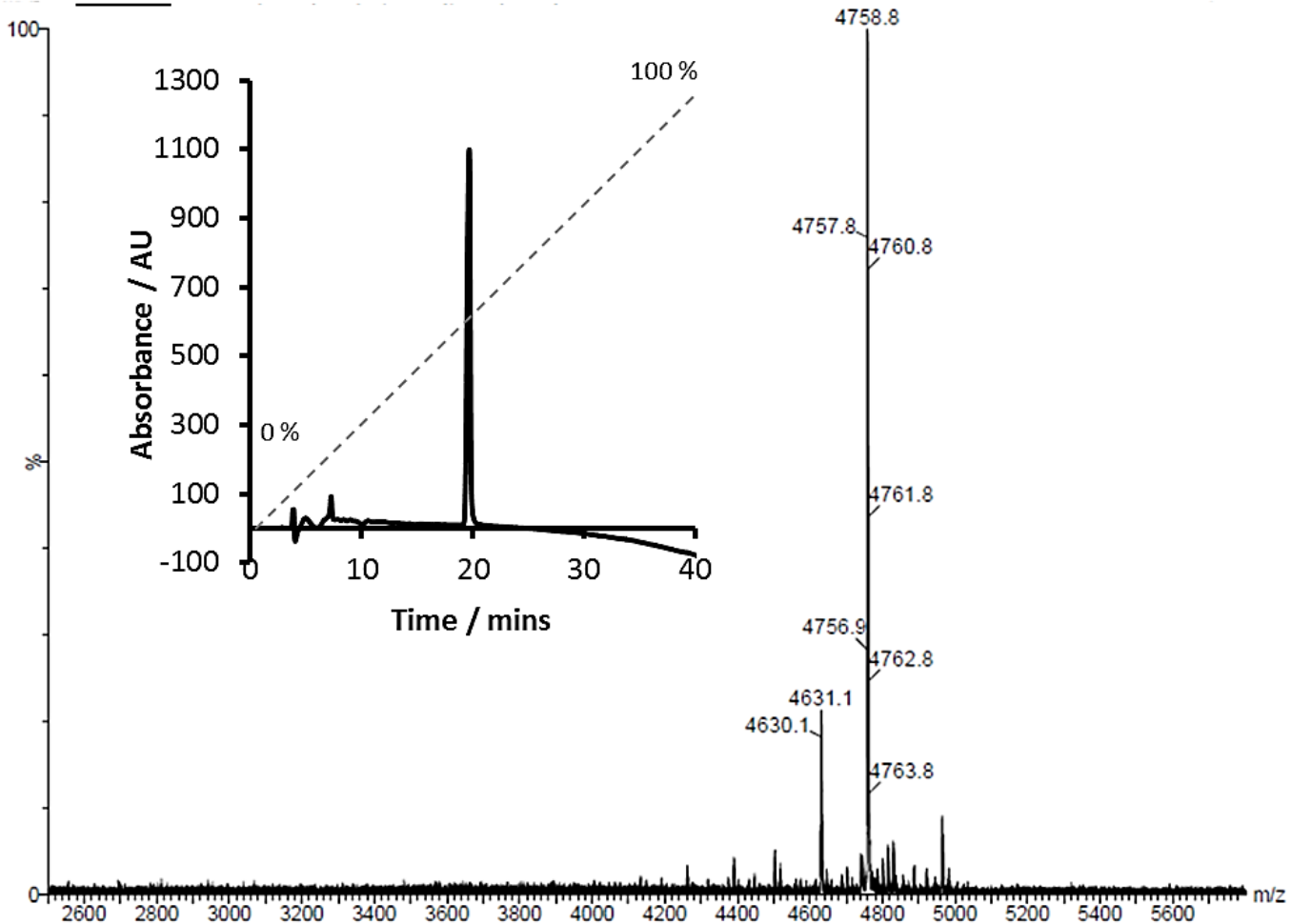
Mo1-2



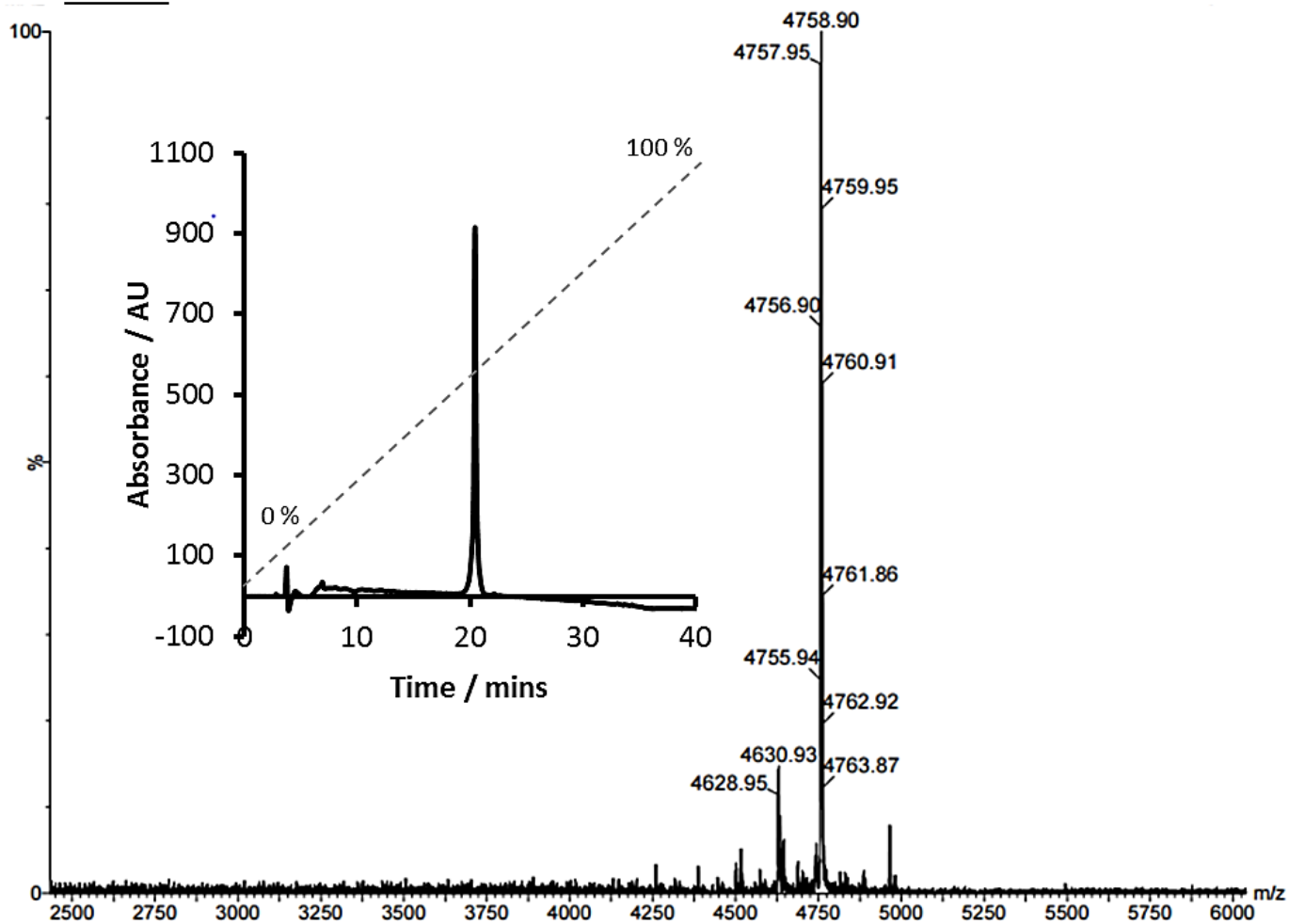
SN1-2



SN1-3L



MB1-3L



Appendix A10: MATLAB Script for Relaxivity Calculations

% This code is to determine r1 using a range of MRI constants and variables
% You can change the variables below to make the calculation specific for your CA
% This can be used for inner-sphere or secondary sphere calculations by changing r6

%% Variables

% q = number of coordinated waters

q = 3;

% H2O = concentration of water (Constant)

H2O = 55.6;

% m = water residence time

tm = 1.56E-09;

%u = permittivity of vacuum (Constant)

u = 8.854e-21;

%YH = magnetogyric ratio

YH = 2.678e8;

%g = g-factor

g = 2;

% uB = Bohr magneton (Constant)

uB = 9.274e-21;

% s = spin quantum number

s = 7/2;

%r6 = ion-proton distance

r = 2.6e-9;

%WH = Larmor frequency of proton

WH = 2.98e8;

%tR = rotational correlation time

tR = 6.8e-9; %MB1-1S

%tR = 8.4e-9; %MB1-1

%tR = 10e-9; %MB1-1L

%% Calculation

%tC = total rotational correlation time

tC = 1./ (1/tR + 1./tm);

T1m = 1./ ((2/15)*(u/(4*pi)).*((YH^2 * g^2 * uB^2 * s*(s+1))/(r^6)).* ((3.*tC)/(1+ WH^2 .* tC.^2)));

%R1 = (q ./ H2O) ./ (T1m + tm);

%r1 = R1 / 1000

Appendix A11: MATLAB Script for Calculating ΔG

% This code is to determine deltaG using Gua-HCl unfolding data.

% This code will produce a curve of the data and fit the data to give a curve and a value for deltaG

%% Change these parameters

n = 3; % monomer to n-mer folding

P = 30e-6; % free monomer concentration in M

T0 = 298.15; % temperature in K

% Save data in two columns (Concentration of Gua-HCl, Ellipticity)

%%

R = 8.3145; % Ideal gas constant

data = [Gua-HCl, Ellipticity]

%data = uiimport;

%data = data.data;

Den = data(:,1);

Theta_Obsd = data(:,2);

K = @(b, Den) exp(-(b(1).*ones(length(Den),1)-b(2).*Den)./(R*T0));

U = @(b, Den) arrayfun(@(k) fzero(@(x) n*x^n+k*x-k*P, [0 P]), K(b, Den));

f = @(b, Den) (b(3).*ones(length(Den),1)+b(5).*Den).*U(b, Den)./P +

(b(4).*ones(length(Den),1)+b(6).*Den).*(P.*ones(length(Den),1)-U(b,Den))./P;

%%Initial Values Module

beta0 = zeros(6,1);

beta0(3) = max(Theta_Obsd)+1;

beta0(4) = min(Theta_Obsd)-1;

Utest = P.*(Theta_Obsd - (beta0(4).*ones(length(Theta_Obsd),1)))./(beta0(3)-beta0(4));

Ktest = n.*(Utest).^n./(P.*ones(length(Utest),1)-Utest);

DGtest = -R.*T0.*log(Ktest);

TestMat = ones(length(DGtest),2);

for i = 1:length(DGtest)

 TestMat(i,1) = 1;

 TestMat(i,2) = -Den(i);

end

ParaEst = linsolve(TestMat,DGtest);

beta0(1) = ParaEst(1);

beta0(2) = ParaEst(2);

[beta, r, J, COVB, mse, emi] = nlinfit(Den, Theta_Obsd, f, beta0);

% ci = nlparco(beta,r,'covar',COVB);

ci = nlparci(beta,r,'covar',COVB);